

## Durham E-Theses

---

*Numerical aspects of enriched and high-order  
boundary element basis functions for Helmholtz  
problems.*

GILVEY, BENJAMIN

### How to cite:

---

GILVEY, BENJAMIN (2021) *Numerical aspects of enriched and high-order boundary element basis functions for Helmholtz problems.*, Durham theses, Durham University. Available at Durham E-Theses Online: <http://etheses.dur.ac.uk/14240/>

### Use policy

---

The full-text may be used and/or reproduced, and given to third parties in any format or medium, without prior permission or charge, for personal research or study, educational, or not-for-profit purposes provided that:

- a full bibliographic reference is made to the original source
- a [link](#) is made to the metadata record in Durham E-Theses
- the full-text is not changed in any way

The full-text must not be sold in any format or medium without the formal permission of the copyright holders.

Please consult the [full Durham E-Theses policy](#) for further details.

# Numerical aspects of enriched and high-order boundary element basis functions for Helmholtz problems.

Ben Gilvey

Thesis submitted towards the  
degree of Doctor of Philosophy



School of Engineering and Computing Sciences  
Durham University  
United Kingdom

June 2021

Ben Gilvey

## Abstract

In this thesis several aspects of the Partition of Unity Boundary Element Method (PUBEM) are investigated, with novel results in three main areas:

1. Enriched modelling of wave scattering from polygonal obstacles. The plane waves are augmented by a set of enrichment functions formed from fractional order Bessel functions, as informed by classical asymptotic solutions for wave fields in the vicinity of sharp corners. It is shown that the solution accuracy can be improved markedly by the addition of a very small number of these enrichment functions, with very little effect on the run time.
2. High-order formulations. Plane waves are not the only effective means of introducing oscillatory approximation spaces. High-Order Lagrange polynomials and high-order Non-Uniform Rational B-Splines (NURBS) also exhibit oscillation and these are tested and compared against PUBEM. It is found that these high-order functions significantly outperform the corresponding low-order (typically quadratic) polynomials and NURBS that are commonly used, and that for large problems the highest order tested (11th) has potential to be competitive with PUBEM without the associated ill-conditioning.
3. Integration. The accuracy of PUBEM traditionally comes at the cost of the requirement to evaluate many highly-oscillatory integrals. Several candidate integration strategies are investigated with the aim of finding a robust, accurate and efficient approach. Schemes tested include the Filon and asymptotic methods, as well as the Method of Stationary Phase (MSP). Although these schemes are found to be spectacularly successful for many cases, they fail for a sufficient number of situations to cause a complete PUBEM analysis based on these methods to lack robustness. Conclusions are drawn about the effective use of more traditional quadrature for robust implementations.

# Declaration

The work in this thesis is based on research carried out in the Computational Mechanics Group, Department of Engineering, Durham University. No part of this report has been submitted elsewhere for any other degree or qualification and it is all my own work unless referenced to the contrary in the text. Parts of this work have been published in the following:

## Journal articles

- Gilvey, B. D., Trevelyan, J. and Hattori, G., 2020. Singular enrichment functions for Helmholtz scattering at corner locations using the Boundary Element Method. *International Journal for Numerical Methods in Engineering*, 121(3), pp.519-533.
- Gao, J., Condon, M., Iserles, A., Trevelyan, J. and Gilvey, B., 2021. Quadrature methods for highly oscillatory singular integrals. *Journal of Computational Mathematics*, 39(2), pp.227-260.
- Gilvey, B. D. and Trevelyan, J. 2021. A comparison of high-order and plane wave enriched BEM basis functions for Helmholtz problems. *Engineering Analysis with Boundary Elements*, 122, pp.190-201.

## Conference papers

- Gilvey, B.D., Wagner, G.A., Trevelyan, J., Seaïd, M. and Gao, J., 2017. Evaluation of highly oscillatory integrals in the Partition of Unity BEM for wave simulations in 2D, *in Proceedings of the 25th Conference on Computational Mechanics (UKACM)*. University of Birmingham, 11-13 April. Birmingham : University of Birmingham, pp.305-308.
- Gilvey, B.D., Wagner, G.A., Trevelyan, J., Seaïd, M. and Gao, J., 2017. Application of Filon-type methods to highly oscillatory integrals arising from the Partition of Unity BEM for 2D wave scattering simulations, *in Proceedings of the Eleventh UK Conference on Boundary Integral Methods (UKBIM 11)*. Nottingham Trent University, 10-11 July. Nottingham : Nottingham Trent University, pp.72-79.
- Gilvey, B.D., Hattori, G., Trevelyan, J., 2019. Singular enrichment functions for Helmholtz scattering by polygonal objects, *in Proceedings of the 12th UK Conference*

*on Boundary Integral Methods (UKBIM12)*. Oxford Brookes University, 8-9 July. Oxford : Oxford Brookes University, pp.1-8.

- Gilvey, B.D., Trevelyan, J., 2019. Numerical treatment of highly oscillatory PUBEM integrals, *in Proceedings of the 12th UK Conference on Boundary Integral Methods (UKBIM12)*. Oxford Brookes University, 8-9 July. Oxford : Oxford Brookes University, pp.25-31.

Copyright © 2021 by Ben Gilvey.

The copyright of this thesis rests with the author. No quotations from it should be published without the author's prior written consent and information derived from it should be acknowledged.

# Acknowledgements

I would like to express my deepest gratitude to my supervisor Prof. Jon Trevelyan. Jon gave me the opportunity to undertake the research that formed this thesis and supported me throughout. Jon is kind and patient, along with being a true expert in numerical methods; I could not imagine a better supervisor. During my time at Durham I have learned a lot from Jon, both inside and outside of academia.

I would also like to thank my family for the emotional support and patience that has been invaluable during my doctoral studies.

Finally, I would like to acknowledge the funding awarded to me from Durham University and the Engineering and Physical Sciences Research Council.

Ben Gilvey

Durham, June 2021

# Contents

Abstract	
Declaration	ii
Acknowledgements	iv
Contents	v
List of Figures	viii
List of Tables	xiii
Acronyms	xiv
<b>1 Introduction</b>	<b>1</b>
1.1 Thesis statement . . . . .	2
1.2 Outline of this thesis . . . . .	2
<b>2 Theory of acoustics</b>	<b>4</b>
2.1 The Helmholtz equation . . . . .	4
2.2 Fundamental solutions . . . . .	5
2.3 Numerical solution . . . . .	6
<b>3 Boundary Element Method</b>	<b>8</b>
3.1 Background . . . . .	8
3.2 Interior domains . . . . .	9
3.3 Exterior domains . . . . .	12
3.4 Discretisation . . . . .	15
3.5 PUBEM . . . . .	19
3.5.1 Background . . . . .	19
3.5.2 Derivation . . . . .	20
3.5.3 Exact geometry representation . . . . .	22
<b>4 Integration</b>	<b>23</b>
4.1 Overview . . . . .	23
4.1.1 Traditional quadrature . . . . .	23
4.2 BEM integrals . . . . .	24
4.3 PUBEM integrals . . . . .	26
4.3.1 Sub-divided integration . . . . .	27

4.3.2	Split Telles scheme . . . . .	29
4.4	Computation of error . . . . .	31
4.4.1	Error in PUBEM integrals . . . . .	31
4.5	Integration schemes for highly oscillatory integrals . . . . .	33
4.5.1	PUBEM integral . . . . .	34
4.5.2	In the absence of stationary points . . . . .	36
	Straight line case . . . . .	36
	Asymptotic method . . . . .	36
	Filon method . . . . .	38
	Comparison . . . . .	41
	Circular arc case . . . . .	43
4.5.3	Stationary point cases . . . . .	45
	Filon method . . . . .	46
	Numerical example . . . . .	51
	Method of stationary phase . . . . .	53
	Straight line case . . . . .	53
	Targeted Gauss-Legendre . . . . .	60
4.5.4	Problems with using integration schemes for highly oscillatory in- tegrals . . . . .	61
	Non-stationary cases . . . . .	61
	Stationary point cases . . . . .	64
4.6	Gauss-Legendre tailored for PUBEM integrals . . . . .	69
4.6.1	Straight line element . . . . .	69
4.6.2	Scattering by a square . . . . .	73
4.6.3	Circular arc element . . . . .	73
4.6.4	Scattering from a circle . . . . .	76
4.6.5	Scattering by a capsule . . . . .	82
4.6.6	Conclusion . . . . .	82
4.7	Summary . . . . .	83
<b>5</b>	<b>Singular enrichment functions for wave scattering by polygons</b>	<b>85</b>
5.1	Introduction . . . . .	85
5.2	XBEM formulation . . . . .	87
5.3	PUXBEM formulation . . . . .	88
5.4	Modified basis functions . . . . .	89
	5.4.1 Square scattering object . . . . .	92
	Use of blending functions . . . . .	95
	Accuracy locally at a corner . . . . .	96
	Conditioning . . . . .	98
	Single degree of freedom per Bessel function . . . . .	99
	5.4.2 Multiple square scattering . . . . .	101
	5.4.3 Triangular scattering object . . . . .	103
5.5	Conclusions . . . . .	104

<b>6</b>	<b>High-order basis functions</b>	<b>107</b>
6.1	Introduction . . . . .	107
6.1.1	Lagrange basis . . . . .	108
6.1.2	NURBS . . . . .	108
6.1.3	Plane waves. . . . .	112
6.2	Numerical testing . . . . .	112
6.2.1	Implementation . . . . .	112
6.2.2	Scattering by a cylinder . . . . .	113
6.2.3	Scattering by three cylinders . . . . .	116
6.2.4	Plane wave propagating along the length of a duct . . . . .	120
	Pollution error in the duct. . . . .	122
6.3	Conclusions . . . . .	125
<b>7</b>	<b>Optimal selection of basis for PUBEM</b>	<b>126</b>
7.1	Varying $k$ . . . . .	127
7.2	Varying the number of degrees of freedom . . . . .	128
7.3	Comparison . . . . .	128
7.4	Conclusion . . . . .	133
<b>8</b>	<b>Conclusions and further work</b>	<b>134</b>
8.1	Conclusions . . . . .	134
8.1.1	Integration schemes for PUBEM . . . . .	134
8.1.2	Singular basis functions for scattering from corners . . . . .	135
8.1.3	High-order Lagrange and NURBS schemes . . . . .	135
8.1.4	Optimal selection of basis functions for PUBEM . . . . .	136
8.2	Recommendations for further work . . . . .	136
8.2.1	Integration . . . . .	136
8.2.2	Singular enrichment functions . . . . .	137
8.2.3	High-order basis functions . . . . .	137
8.2.4	Optimal selection of basis functions for PUBEM . . . . .	137
	<b>Appendices</b>	<b>138</b>
	<b>A Stationary points algorithm</b>	<b>139</b>
	<b>B Method of Fundamental Solutions</b>	<b>144</b>
	<b>C Quantification of errors</b>	<b>146</b>
	<b>References</b>	<b>147</b>

# List of Figures

3.1	Interior domain $\Omega_f$ with boundary $\Gamma$ and point $p$ surrounded by a circle of radius $\epsilon$ . . . . .	10
3.2	Interior domain $\Omega_f$ with point $p$ located on the boundary $\Gamma$ . . . . .	11
3.3	Example angles on which a collocation point may sit. The angle on the left would result in $c(p) = \frac{1}{4}$ , the angle in the middle would result in $c(p) = \frac{1}{2}$ and the angle on the right would result in $c(p) = \frac{3}{4}$ . The analysis domain is shown un-shaded. . . . .	12
3.4	Generic scattering object where $\Omega_s$ is the domain of the scatterer, $\Omega_f$ is the fluid domain, $\Gamma$ is the boundary of the scatterer, $\phi^{inc}$ is the incident wave and $\Gamma_\infty$ represents the boundary at infinity. . . . .	14
3.5	Generic scattering object discretised into quadratic elements with 3 nodes per elements and the parametric variable $\xi$ . . . . .	16
3.6	Quadratic Lagrangian shape functions. . . . .	18
3.7	Quadratic PUBEM element with $M = 4$ showing the parametric variable $\xi$ . . . . .	21
4.1	Example BEM discretisation (1) and PUBEM discretisation (2). . . . .	28
4.2	Comparison of the real and imaginary parts of a BEM integrand (left) and the real and imaginary parts of a PUBEM integrand (right). Both corresponding to the first element of the respective BEM and PUBEM discretisations of the unit square, both of which with a collocation point at $(0, 1)$ , $k = 500$ . . . . .	28
4.3	Wave sub-divided into integration cells of length $\frac{\lambda}{4}$ using a coordinate change to $\zeta$ . . . . .	29
4.4	(left) $L^2$ relative error $\epsilon$ (in $\phi$ over $\Gamma$ ) vs. $\tau$ for three test cases having $\pm 0.1\%$ , $1\%$ , or $2\%$ injected into the integrals; $k = 25$ . (right) $L^2$ relative error $\epsilon$ (in $\phi$ over $\Gamma$ ) vs. $k$ for three test cases having $\pm 0.1\%$ , $1\%$ , or $2\%$ injected into the integrals; $\tau \approx 5$ . Notably, as can be s . . . . .	32
4.5	Error in the asymptotic approximation of $H_1^{(1)}(kr)$ , using (4.46) with only the first two terms in the series, for small $k$ and $r$ , wherein $k$ is the wavenumber and $r$ is distance from the Hankel source point. . . . .	35
4.6	Variables used to define source point location. . . . .	36
4.7	(left) Integrand in the absence of stationary points with $k = 100$ , $\phi = 60^\circ$ , $x_p = 0.5$ , $y_p = 2.5$ . (right) Integrand containing a stationary point with $k = 100$ , $\phi = 60^\circ$ , $x_p = 3$ , $y_p = 3$ . . . . .	37
4.8	Relative error for a non-stationary case using the Asymptotic method with the 1st derivative (blue) and with the 2nd derivative (red). . . . .	42

4.9	Location of source point $p$ and field point $q$ relative to the circular arc element (of radius $R$ and spanning between the $x$ and $y$ axes) which can be thought of as forming one quarter of a unit circle scattering object. . . . .	43
4.10	Mapping of $\theta_q \mapsto \xi$ for the circular arc element spanning between the $x$ and $y$ axes which can be thought of as forming one quarter of a unit circle scattering object. . . . .	44
4.11	Source point locations which result in a stationary point within the interval of integration (yellow) and source point locations which result in a stationary point laying outside of the interval of integration (blue). Results are obtained by setting $\bar{\phi} = \pi/2, x_e = 4$ and varying $\theta$ and $r$ . . . . .	47
4.12	Polarity definition for $g'(\xi)$ for an arbitrary fixed $\phi$ and a flat straight line element, shown at $\theta = \phi$ and $\theta = -\phi$ . Positive and negative areas indicate the areas in which the $g'(\xi)$ will be positive or negative respectively, thus, $g'(\xi)$ behaves monotonically either side of a stationary point. . . . .	48
4.13	Hermite polynomial fit. . . . .	52
4.14	$L^2$ error for a first order stationary point Filon scheme (blue), a second order scheme (red) and a third order scheme (orange). . . . .	52
4.15	Smooth blending functions for including the end point contributions to the MSP formulation. . . . .	54
4.16	$L_2$ error for the integral containing the $N_2$ shape function, and a comparison of the $L_2$ error of the integral containing the $N_1$ shape function evaluated with and without including the end point contributions. . . . .	56
4.17	$L_2$ error incurred by MSP for stationary points $\xi^*$ located across a straight line flat element for a range of $k$ . . . . .	57
4.18	Trigonometric shape functions. . . . .	58
4.19	Test elements from a circular scattering object with trigonometric support. . . . .	59
4.20	Relative error in the integration over the trigonometric support of the shared node between element 1 and 2 plotted against $k$ . . . . .	60
4.21	Window functions for targeted Gauss-Legendre. . . . .	61
4.22	(left) Example of a window function and associated integrand for $N_2$ with a stationary point at $\xi = 0$ , (right) $L_2$ error vs. $\bar{\rho}$ for the same case. . . . .	62
4.23	$L_2$ error for the $N_1$ and $N_2$ shape functions using targeted Gauss-Legendre integration with $\bar{\rho} = 0.2$ and $\delta = 0.15$ . . . . .	62
4.24	Regions of relative error $\epsilon$ for second order asymptotic method integrals with varying $r_0$ and $\theta$ , $k = 100$ ; yellow regions show $\epsilon < 0.001$ , blue regions show stationary point locations, and the white regions show near-stationary locations wherein $\epsilon > 0.01$ . . . . .	63
4.25	$L_2$ error for the $N_2$ case (left) and the $N_1$ case (right), both with $\bar{\phi} = \frac{\pi}{18}$ , $k = 500$ , $\bar{\rho} = 0.2$ , $\delta = 0.15$ , varying $\theta$ and $r_0$ . . . . .	64
4.26	Relative error using a second order Asymptotic scheme with $\theta$ and $r$ varying for the case when $x_e = 4$ and $\bar{\phi} = \frac{\pi}{3}$ . . . . .	65
4.27	Relative error using a second order Asymptotic scheme with $\theta$ and $r$ varying for the case when $x_e = 4$ and $\bar{\phi} = \frac{\pi}{3}$ . . . . .	65
4.28	Integrands resulting from different combinations of $x_e$ and $k$ . . . . .	66
4.29	Relative error in matrix terms for a circular scattering object, $k = 100\pi, E = 4$ and $M = 157$ . . . . .	67
4.30	$g(\xi)$ and the resulting integrand for a near stationary case. . . . .	68

4.31	$ Log_{10}(\epsilon) $ for a straight line element having having the starting point $(x_s, y_s) = (0, 0)$ and end point $(x_e, y_e) = (1, 0)$ , $\theta = 10^\circ$ , $r_0 = 1$ , $\bar{\phi} = 60^\circ$ and $k = 100$ . . . . .	70
4.32	$ Log_{10}(\epsilon) $ for a straight line element having having the starting point $(x_s, y_s) = (0, 0)$ and end point $(x_e, y_e) = (1, 0)$ , $\theta = 10^\circ$ , $r_0 = 1$ , $\bar{\phi} = 60^\circ$ and $k = 1 - 1000$ . . . . .	71
4.33	$ Log_{10}(\epsilon) $ for a straight line element having the starting point $(x_s, y_s) = (0, 0)$ and end point $(x_e, y_e) = (1, 0)$ , $0 < \bar{\phi} < 360^\circ$ , $r_0 = 1 - 10$ . . . . .	72
4.34	$ Log_{10}(\epsilon) $ for a straight line element having having the starting point $(x_s, y_s) = (0, 0)$ and end point $(x_e, y_e) = (4, 0)$ , $\theta = 90^\circ$ , $r_0 = 4$ , $0 < \bar{\phi} < 360^\circ$ and $k = 100$ . . . . .	74
4.35	$ Log_{10}(\epsilon) $ for a square scattering object, $k = 20$ . . . . .	75
4.36	$ Log_{10}(\epsilon) $ scaled for a square scattering object, $k = 20$ . . . . .	75
4.37	$Log_{10}(\epsilon)$ for a circular arc element, with a unit radius, of length $\frac{\pi}{4}$ spanning from the positive $x$ -direction to the positive $y$ -direction and having $x_p, y_p = (10, 10)$ , $R = 1$ , $\bar{\phi} = 60^\circ$ and $k = 100$ . . . . .	76
4.38	$Log_{10}(\epsilon)$ for a circular arc element spanning from $(-1, 0)$ to $(0, 1)$ and having $(x_p, y_p) = (10, 10)$ , $R = 1$ , $0 < \bar{\phi} < 360^\circ$ and $k = 100$ . . . . .	77
4.39	$Log_{10}(\epsilon)$ for a circular scattering object, $k = 50$ . . . . .	78
4.40	$Log_{10}(\epsilon)$ scaled for a circular scattering object, $k = 50$ . . . . .	79
4.41	Absolute error in matrix terms for scattering by a circle, with $E = 4$ , $M = 32$ and $k = 50$ . . . . .	80
4.42	Relative error in matrix terms for scattering by a circle, with $E = 4$ , $M = 32$ and $k = 50$ . . . . .	81
4.43	Capsule geometry. . . . .	82
4.44	(left) Real part of the total potential, (right) absolute value of total potential. Capsule scatterer for the case $k = 50$ . . . . .	83
5.1	(left) Real part of the total potential, (right) absolute value of total potential. Unit square scatterer for the case $k = 50$ . . . . .	86
5.2	Polar coordinate system local to a corner. . . . .	90
5.3	Bessel functions with $n = 1-6$ , $\alpha = \frac{2}{3}$ and $k = 20$ . . . . .	90
5.4	Internal point locations for a square scattering object. . . . .	92
5.5	$L^2$ relative error $\epsilon$ vs. DoF, $k = 20$ . . . . .	93
5.6	$L^2$ relative error vs. $k$ using 128 DoF. . . . .	94
5.7	(left) Hermite blending function, (right) Blended Bessel function with $n = 1$ , $k = 20$ and $\alpha = \frac{2}{3}$ . . . . .	96
5.8	Relative error vs. DoF for $\gamma = 1$ , varying $\beta$ where $L$ is the element length. . . . .	97
5.9	Relative error vs. $k$ using 128 DoF, varying $\beta$ where $L$ is the element length. . . . .	97
5.10	Internal point locations for single square scattering object. . . . .	98
5.11	Relative error vs. $\gamma$ using 128 DoF. . . . .	99
5.12	Condition number $\kappa$ of the $H$ matrix vs. degrees of freedom. . . . .	100
5.13	Relative error vs. DoF using a single DoF per $\psi_2$ , marked <i>1DoF</i> and using a DoF for each edge. The single DoF results were obtained using 124 DoF and the two DoF results used 128 DoF. . . . .	100
5.14	Internal point locations for the two square scattering arrangement. . . . .	102

5.15	Real part of total potential field resulting from a configuration of two squares being impinged by an $\phi_{inc} = \frac{\pi}{4}$ .	102
5.16	$L_2$ norm vs. DoF at internal points around two square scattering objects, where $\gamma = 0.01$ .	103
5.17	Internal point locations for single triangular scattering object.	104
5.18	Relative error vs. DoF for a triangular scattering object with $\gamma = 0.1$ , $k = 2$ .	105
5.19	Relative error vs. DoF for a triangular scattering object with $\gamma = 0.1$ , $k = 20$ .	105
6.1	Lagrangian basis functions with $a, b, c$ and $d$ showing $S = 3, 6, 9$ and $12$ respectively.	109
6.2	NURBS basis functions with all weights $w_j = 1$ ; $a, b, c$ and $d$ show $J = 3, 6, 9$ and $12$ respectively.	111
6.3	(left) Real part of the total potential, (right) absolute value of total potential, for scattering by a unit cylinder, $k = 2\pi$ .	114
6.4	$L^2$ relative error $\epsilon$ vs. $N_d$ for scattering by a unit cylinder, $k = 2\pi$ .	114
6.5	(Left) Condition number $\kappa$ vs. $N_d$ for Lagrange basis, (Right) Condition number $\kappa$ vs. $N_d$ for NURBS basis, for scattering by a unit cylinder, $k = 2\pi$ .	116
6.6	PUBEM $L^2$ relative error $\epsilon$ and condition number $\kappa$ for scattering by a unit cylinder, $k = 2\pi$ .	117
6.7	$L^2$ relative error $\epsilon$ for scattering by a unit cylinder, with $N_d \in 220-224$ .	117
6.8	(left) Real part of the total potential, (right) absolute value of total potential, for scattering by three unit cylinders, $k = 4\pi$ .	118
6.9	$L^2$ relative error $\epsilon$ vs $N_d$ (per cylinder) for scattering by three unit cylinders, $k = 4\pi$ .	119
6.10	(Left) Condition number $\kappa$ vs. $N_d$ for Lagrange basis, (Right) Condition number $\kappa$ vs. $N_d$ for NURBS basis, for scattering by three unit cylinders, $k = 4\pi$ .	119
6.11	PUBEM $L^2$ relative error $\epsilon$ and condition number $\kappa$ for scattering by three unit cylinders, $k = 4\pi$ .	120
6.12	Duct boundary conditions and domain.	121
6.13	$L^2$ error $\epsilon$ vs. $N_d$ per side for a travelling wave in a duct, $k = 4\pi$ .	122
6.14	(left) Condition number $\kappa$ for the Lagrange and NURBS basis, (right) Condition number $\kappa$ and $L^2$ error $\epsilon$ for the plane wave basis, for a travelling wave in a duct, $k = 4\pi$ .	123
6.15	(left) Local error $\epsilon_1$ for the Lagrange basis, (right) Local error $\epsilon_1$ for the NURBS basis for a travelling wave in a duct having $L = 54.4$ , $f = 750Hz$ , and including 1632 degrees of freedom on each long side.	124
6.16	Local error $\epsilon_1$ for the PUBEM basis for a travelling wave in a duct having $L = 54.4$ , $f = 750Hz$ , and including 1632 degrees of freedom on each long side.	125
7.1	$L^2$ relative error epsilon and the corresponding condition number $\kappa$ , for basis functions of order $p = 0$ .	127
7.2	$L^2$ relative error epsilon and the corresponding condition number $\kappa$ , for basis functions of order $p = 1$ .	128

7.3	$L^2$ relative error epsilon and the corresponding condition number $\kappa$ , for basis functions of order $p = 2$ . . . . .	129
7.4	$L^2$ relative error epsilon and the corresponding condition number $\kappa$ , for basis functions of order $p = 3$ . . . . .	129
7.5	$L^2$ relative error epsilon and the corresponding condition number $\kappa$ , for basis functions of order $p = 4$ . . . . .	130
7.6	$L^2$ relative error $\epsilon$ and the resulting condition number $\kappa$ vs. $N_d$ for discretisations including a total number of elements $E = 2, 4, 8, 16$ . $k = 50$ and $N_d$ is increased by increasing $M$ , $p = 0$ . . . . .	130
7.7	$L^2$ relative error $\epsilon$ and the resulting condition number $\kappa$ vs. $N_d$ for discretisations including a total number of elements $E = 2, 4, 8, 16$ . $k = 50$ and $N_d$ is increased by increasing $M$ , $p = 1$ . . . . .	131
7.8	$L^2$ relative error $\epsilon$ and the resulting condition number $\kappa$ vs. $N_d$ for discretisations including a total number of elements $E = 2, 4, 8, 16$ . $k = 50$ and $N_d$ is increased by increasing $M$ , $p = 2$ . . . . .	131
7.9	$L^2$ relative error $\epsilon$ and the resulting condition number $\kappa$ vs. $N_d$ for discretisations including a total number of elements $E = 2, 4, 8, 16$ . $k = 50$ and $N_d$ is increased by increasing $M$ , $p = 3$ . . . . .	132
7.10	$L^2$ relative error $\epsilon$ and the resulting condition number $\kappa$ vs. $N_d$ for discretisations including a total number of elements $E = 2, 4, 8, 16$ . $k = 50$ and $N_d$ is increased by increasing $M$ , $p = 4$ . . . . .	132
7.11	$L^2$ relative error $\epsilon$ vs. $k$ for the most accurate example for each $p$ taken from the above results (left). $L^2$ relative error $\epsilon$ vs. $N_d$ for the most accurate example for each $p$ taken from the above results (right). . . . .	133
B.1	MFS source point $\bar{\alpha}$ and sample point $\bar{\beta}$ , where $\bar{r}$ is the Euclidian distance between them. . . . .	145

# List of Tables

4.1	Solution time in seconds and relative error $\epsilon$ . . . . .	42
4.2	Time taken in seconds to evaluate varying ranges of integrals along with average relative error $\epsilon$ . . . . .	43
4.3	Solution time in seconds for Gauss-Legendre and for 3 Filon stationary point Filon schemes wherein the subscript (1, 2, 3) refers to the number of derivatives taken at end point and stationary point locations. . . . .	51
4.4	$L_2$ error for circular scattering object, $k = 50$ , $E = 4$ , $M = 32$ . . . . .	79
4.5	$L_2$ error for circular scattering object, $k = 50$ , $E = 4$ , $M = 32$ . . . . .	81
4.6	$L_2$ error for circular scattering object, $k = 60 - 100$ , $E = 4$ , $M = 38 - 64$ . . . . .	81
4.7	$L_2$ relative error $\epsilon$ for scattering by a capsule, $R = 1$ $k = 50$ , $E = 8$ , $M = 32$ . . . . .	82
5.1	Relative error $\epsilon$ using 128 DoF for $\gamma = 1-5$ . . . . .	94
6.1	Relative error $\epsilon$ with $M = 1$ using only a single element per side, $k = 4\pi$ . . . . .	122
6.2	Condition number $\kappa$ for the duct with $L = 54.4m$ , $W = 0.2m$ and $f = 750Hz$ . . . . .	124

# Acronyms

<b>BIE</b>	Boundary Integral Equation
<b>NDT</b>	Non-Destructive Testing
<b>SONAR</b>	SOund Navigation And Ranging
<b>HIFU</b>	High-Intensity Focused Ultrasound
<b>EMAT</b>	Electro Magnetic Acoustic Transducer
<b>MsT</b>	Magnetostrictive Transducer
<b>FEM</b>	Finite Element Method
<b>BEM</b>	Boundary Element Method
<b>NURBS</b>	Non-Uniform Rational B-Splines
<b>PUBEM</b>	Partition of Unity Boundary Element Method
<b>BBFEM</b>	Bernstein-Bézier Finite Element Method
<b>CAD</b>	Computer Aided Design
<b>IGAFEM</b>	Isogeometric Finite Element Method
<b>PUFEM</b>	Partition of Unity Finite Element Method
<b>PWDG</b>	Plane-Wave Discontinuous Galerkin Method
<b>UVWF</b>	Ultra-Weak Variational Formulation
<b>IGABEM</b>	Isogeometric Boundary Element Method
<b>CHIEF</b>	Combined Helmholtz Integral Equation Formulation
<b>SVD</b>	Singular Value Decomposition
<b>FCC</b>	Filon-Clenshaw-Curtis Method
<b>MSP</b>	Method of Stationary Phase
<b>IGA</b>	Isogeometric Analysis
<b>XIBEM</b>	eXtended Isogeometric Boundary Element Method

**XBEM**            eXtended Boundary Element Method  
**PUXBEM**        Partition of Unity eXtended Boundary Element Method

# Chapter 1

## Introduction

Acoustic wave propagation is a rich field of study, with many engineering applications, such as, Non-Destructive Testing (NDT), medical diagnostics ultrasound, SOund Navigation And Ranging (SONAR) and High-Intensity Focused Ultrasound (HIFU). Each of these methods employ transducers to generate acoustic signals which are to be transmitted into a domain of interest.

In the early 1900s, long before ultrasound became commonplace, SONAR was implemented on ocean liners (following the Titanic disaster) to detect hazards, and then submarines during the second world war; during this time, transducer designs improved and piezoelectric transducers were developed. Following this improvement, ultrasonic transducers were applied to NDT which typically involved pulsing ultrasonic waves into a given material, and receiving return signals that have been reflected from artifacts. The artifacts could be defects, such as cracks in the material or simply geometric properties which can be used to characterise the material. Since the advent of NDT, vast improvements have been made, for example, in the design of powerful transducers, such as: the Electro Magnetic Acoustic Transducer (EMAT) which generates Lorentz force to induce acoustic waves within a given medium; and, the Magnetostrictive Transducer (MsT) which employs the Wiedemann effect to generate acoustic waves. These designs are capable of generating horizontal shear waves which are non-dispersive within waveguides such as pipes and rods.

Following SONAR and NDT was the use of Ultrasound for medical imaging, becoming popular in the second half of the 20th century as a non-invasive method of diagnosis. By the 21st century, real-time 3D imaging of the human body was possible. More recently, extensive research is being performed into High-Intensity Focused Ultrasound (HIFU), which can be used to focus ultrasound waves on a cancerous region, such as a tumour. The purpose of this focusing is to heat up and destroy the tumour, with minimal damage to the surrounding healthy tissue. Such non-invasive techniques have obvious benefit over surgical intervention.

With all of these applications (although, specifically in the medical contexts), it is of great use to produce numerical models which can indicate the outcome of a given transducer design and placement, for example. A known issue is the fact that in many of these contexts, the wavelength  $\lambda$  is very small in relation to the artifacts from which the waves reflect. This causes difficulty for traditional numerical methods, such as the Finite Element Method (FEM) and the Boundary Element Method (BEM), as typically a fixed number of degrees of freedom are required per wavelength; thus, if there are many wavelengths in a domain then many degrees of freedom will be required which results in computational expense. Many numerical methods have been developed with the aim of ameliorating the computational cost required to solve high-frequency problems. Examples of such methods are the Partition of Unity Boundary Element Method (PUBEM) which is an enriched variant of BEM and high-order BEM which is introduced in this thesis and employs high-order basis functions.

## 1.1 Thesis statement

Broadly, the aim of this thesis is to explore numerical aspects of enriched and high-order boundary element basis functions. The enriched methods tested employ the plane-wave basis of the Partition of Unity Boundary Element Method with the addition of singular Bessel functions. The high-order bases include: Lagrange polynomials, trigonometric functions and Non-Uniform Rational B-Splines (NURBS).

The purpose of testing PUBEM in this thesis, is to observe the behaviour of PUBEM for novel problems, including interior domains and scattering from corners. The aim is then to improve upon standard PUBEM by using additional enrichment. Further, it is well-known that PUBEM integrals can be highly-oscillatory, thus efforts are directed at developing a robust integration scheme. The purpose of the high-order testing is to determine if the benefits seen in high-order FEM are shared by BEM, and to offer a point of comparison for PUBEM.

The results obtained in this thesis were generated by codes written in MATLAB, by the author.

## 1.2 Outline of this thesis

Chapters 2 and 3 outline existing literature, whereas from Chapter 4 onward, novel work is presented. References to relevant literature are provided as required.

- **Chapter 2: Theory of acoustics** This chapter provides the starting point for numerical acoustics, wherein the Helmholtz equation is derived and numerical solution is discussed.

- **Chapter 3: Boundary Element Method** BEM is introduced in this chapter along with some relevant literature, then the Boundary integral equation is derived. Numerical solution of the Boundary Integral Equation is discussed, and PUBEM is presented.
- **Chapter 4: Integration** This chapter introduces numerical integration in the context of BEM, discussing some of the known challenges, such as, singular integrals. Following this, a large section is devoted to the, more challenging, PUBEM integrals. Multiple highly-oscillatory integration schemes are developed and tested, along with a study into the application of standard Gauss-Legendre.
- **Chapter 5: Singular enrichment functions for wave scattering by polygons** This chapter presents PUBEM and BEM test results for challenging cases of scattering by corners. An extended BEM scheme (XBEM) and an extended PUBEM scheme (PUXBEM) are presented, both of which include fractional-order Bessel functions as enrichment to improve accuracy at corner locations. XBEM and PUXBEM are tested on numerical examples of scattering by polygons.
- **Chapter 6: High-order basis functions** This chapter introduces high-order Lagrange functions and NURBS to solve multiple scattering problems and an example of a wave travelling along the length of a duct. The pollution effect is observed in the duct and results are compared with PUBEM.
- **Chapter 7: Optimal selection of basis for PUBEM** This chapter provides insight into the relationship between the number of elements employed  $E$  vs. the number of plane-waves included per node  $M$  in a PUBEM scheme.
- **Chapter 8: Conclusions and further work** This chapter outlines the successes the thesis, along with providing recommendation for future research.

# Chapter 2

## Theory of acoustics

### 2.1 The Helmholtz equation

As a sound wave travels through a compressible medium  $\Omega$ , disturbances in ambient pressure  $P$  and density  $\rho$  are caused. Knowledge of these changes may be combined with the particle velocity  $V$  in the equation of mass conservation

$$\frac{\partial P}{\partial t} + \rho c^2 \nabla \cdot V = 0, \quad (2.1)$$

wherein  $t$  represents time and  $c$  is the speed of sound, which is specific to the medium in which the sound is travelling. Using the same variables, we arrive at the linearised momentum equation

$$\rho \frac{\partial V}{\partial t} = -\nabla P. \quad (2.2)$$

Using (2.1) and (2.2) it is possible to produce the inhomogeneous linearised wave equation,

$$\rho \nabla \cdot \left( \frac{1}{\rho} \nabla P \right) - \frac{1}{c^2} \frac{\partial^2 P}{\partial t^2} = 0, \quad (2.3)$$

which reduces to the following for homogeneous media.

$$\nabla^2 P - \frac{1}{c^2} \frac{\partial^2 P}{\partial t^2} = 0, \quad (2.4)$$

where  $\nabla^2$  is known as the Laplacian operator. For the above equations  $P = P(\mathbf{p}, t)$  where  $\mathbf{p}$  represents locations within the domain of interest, i.e.  $\mathbf{p} \in \Omega$ . The work in this thesis restricts the analysis to time-harmonic cases, i.e. where the acoustic variation is sinusoidal at all locations with respect to time, that is

$$P = \phi(\mathbf{p}) e^{-i\omega t} \quad (2.5)$$

wherein  $\phi \in \mathbb{C}$  represents the amplitude of the variation in sound pressure or acoustic potential,  $i = \sqrt{-1}$ , and  $\omega$  is frequency. Inserting this definition in to (2.4) and (2.3) produces

$$\rho_a \nabla \cdot \left( \frac{1}{\rho_a} \nabla \phi \right) + k^2 \phi = 0, \quad (2.6)$$

for the case wherein the medium in which the sound waves propagate has inhomogeneous material properties, and

$$\nabla^2 \phi(\mathbf{p}) + k^2 \phi(\mathbf{p}) = 0, \quad \mathbf{p} \in \Omega \quad (2.7)$$

for the case wherein the medium in which the sound waves propagate has homogeneous material properties which is known as the Helmholtz equation where  $k$  is the wave number which is defined in terms of the wavelength  $\lambda$  as  $k = 2\pi/\lambda$ .

## 2.2 Fundamental solutions

Before deriving the Boundary Integral Equation (BIE) for Helmholtz problems the concept of fundamental solutions, also known as Green's functions is introduced. For the analysis carried out in this thesis the Green's functions  $G(\mathbf{p}, \mathbf{q})$  are found by solving the equation

$$\nabla^2 G(\mathbf{p}, \mathbf{q}) + k^2 G(\mathbf{p}, \mathbf{q}) = -\delta(\mathbf{p} - \mathbf{q}), \quad \mathbf{p}, \mathbf{q} \in \Omega \quad (2.8)$$

where the right-hand-side is a Dirac delta function which has singular point source locations  $\mathbf{p}$  and may be evaluated at any point  $\mathbf{q}$ . The Dirac delta function is equal to

$$\delta(\mathbf{p} - \mathbf{q}) = \begin{cases} +\infty, & \text{if } \mathbf{q} = \mathbf{p} \\ 0, & \text{otherwise} \end{cases}$$

and has the useful property

$$\int_{-\infty}^{+\infty} \delta(\mathbf{p} - \mathbf{q}) d\mathbf{q} = 1, \quad (2.9)$$

and

$$\int_{-\infty}^{+\infty} \delta(\mathbf{p} - \mathbf{q}) f(\mathbf{q}) d\mathbf{q} = f(\mathbf{p}). \quad (2.10)$$

Solving (2.8) in  $2D$  provides the following Green's function

$$G(\mathbf{p}, \mathbf{q}) = \frac{i}{4} H_0^{(1)}(kr), \quad (2.11)$$

and its derivative

$$\frac{\partial G(\mathbf{p}, \mathbf{q})}{\partial n(q)} = \frac{-ik}{4} H_1^{(1)}(kr) \frac{\partial r}{\partial n}, \quad (2.12)$$

where  $H_0^{(1)}$  is a Hankel function of the first kind and of order zero,  $H_1^{(1)}$  is a Hankel function of the first kind and of order one and  $r$  is the Euclidian distance between  $\mathbf{p}$  and  $\mathbf{q}$ . Hankel functions are defined as follows,

$$H_n^{(1)}(kr) = J_n(kr) + iY_n(kr), \quad (2.13)$$

$$H_n^{(2)}(kr) = J_n(kr) - iY_n(kr), \quad (2.14)$$

where (2.13) and (2.14) are Hankel functions of the first and second kind respectively with  $J_n(kr)$  and  $Y_n(kr)$  being Bessel functions of the first and second kind respectively.

## 2.3 Numerical solution

Analytical solutions for (2.7) exist, but typically for very simple problems, for example:  $1D$  problems, such as plane-wave propagation in one direction;  $2D$  problems, such as the well-known scattering by a cylinder or multiple cylinders, and  $3D$  problems, such as scattering by a sphere. Some examples of analytical solutions can be found in [1] and [2]. To solve more general Helmholtz problems though, a numerical method of solution is required; in this thesis (2.7) is solved numerically, using BEM and enriched versions of BEM. Naturally, as is the case with numerical methods generally, the solutions are approximate. Though, some analytical solutions are presented in this thesis because, particularly when looking at very refined numerical discretisations, it is helpful to have an exact solution to compare against. Notably, by considering the Helmholtz equation, time-domain methods are ruled-out, thus not considered in this thesis.

Whilst this thesis focuses on BEM-type methods, there are many alternate numerical methods that can be employed to solve the Helmholtz equation. An overview of such methods is provided in this section to highlight core themes, though this is not intended to be a complete or exhaustive list. For example, there are methods based on statistical energy descriptions [43], physical optics [44], and finite difference methods [42] which can be used with success for some acoustics problems, but for brevity, the following discussion is restricted to element based methods.

Perhaps the most well-known of the numerical methods is FEM, whereby a domain, over which a given differential equation is to be solved, is discretised into finite elements. The solution of the differential equation can then be approximated via basis functions over each element, the amplitudes of which are sought during the solution process. FEM is used in many fields of engineering and has been extensively tested in acoustics settings [3–9]. Typically, conventional FEM performs well for Helmholtz problems in the lower-frequency range, though as frequency increases, so do the number of elements required which can eventually become prohibitively large, as has been quantified [6, 10]. This problem is in part due to the pollution effect incurred by FEM [3, 4, 15–17], which is a

form of numerical dispersion, that progresses over a long distance. Notably, throughout this thesis, the term ‘high-frequency’ is used to refer examples wherein the wavelength  $\lambda$  is short relative to the size of the domain of interest. That is, for a problem to be considered high-frequency  $k$  does not necessarily need to be large, instead  $\lambda$  needs to be small relative to, for example, the boundary of the domain of interest.

To overcome the difficulties associated with using FEM for high-frequency Helmholtz problems, two main approaches exist. Firstly, high-order basis functions, i.e. increasing the order of the conventional (usually) low-order polynomial basis. Secondly, enriched methods (also known as Trefftz methods) whereby alternate basis functions are chosen which are all canonical solutions to the governing partial differential equation.

Some examples of successful higher-order basis schemes are the Bernstein and Lobatto polynomials [19, 20], which show promising results and are further explored as the Bernstein-Bézier Finite Element Method (BBFEM) [25] and spectral methods [21–24] which apply global, rather than local, basis functions. Another alternative to the conventional polynomial basis functions are Non-uniform Rational B-splines (NURBS) which are used to construct geometries in Computer Aided Design (CAD). Such geometries can be conveniently exported from CAD software and used as a discretisation means to form Isogeometric Finite Element Method (IGAFEM) [18].

Alternatively, enriched methods for Helmholtz problems typically take the form of wave-based methods, such as, [27–30, 36] wherein oscillatory functions are used to form the basis. Most relevant to this thesis is the Partition of Unity Method [31, 32] which forms the ground for methods such as the Partition of Unity Finite Element Method (PUFEM) [33–35]. Further, a number of discontinuous plane-wave enrichment schemes have also been presented, such as the Plane-Wave Discontinuous Galerkin Method (PWDG) [37, 38], the Discontinuous Enrichment Method (DEM) [39], and the Ultra-Weak Variational Formulation (UWVF) [40], which is compared with PUFEM in [41]. Comparisons of performance between wave-based FEM with high-order FEM schemes is made in [26].

# Chapter 3

## Boundary Element Method

In this section the Boundary Integral Equation (BIE) is derived for wave problems in interior domains and for exterior scattering problems in infinite domains.

### 3.1 Background

BEM [48] is an element-based method, so there are common features between FEM and BEM, such as use of piecewise (typically polynomial) basis functions to describe variation in acoustic potential over each element. Though FEM methods discussed in section 2.3 can involve a volumetric discretisation, i.e. a  $2D$  problem requires computation of area integrals, and a  $3D$  problem requires computation of volume integrals. Conversely, via the use of fundamental solutions and Green's second identity, as will be seen in section 3.2, BEM can reduce the dimensionality of a problem to be solved, i.e. a  $2D$  problem only requires computation of  $1D$  line integrals, and a  $3D$  problem only requires computation of  $2D$  surface integrals. Further to the benefit offered by the reduction in dimensionality, as is well-known, BEM proves very useful when considering Helmholtz scattering in infinite domains. This is because BEM will only require discretisation of the surface of a scattering object, and once the acoustic potential  $\phi$  has been computed over the surface of the object,  $\phi$  can be computed at any point within the infinite domain, using only the surface discretisation. Another benefit of BEM for problems in infinite domains due to the inclusion of Green's functions in the formulation is that the Sommerfeld radiation condition [55, 56] is automatically satisfied, i.e. nothing is reflected back from infinity. A corresponding FEM model would require discretisation of part of the unbounded domain, thus limiting the region over which acoustic potential can be evaluated; further, FEM would require artificial domain truncation along with some non-reflecting boundary conditions to simulate the Sommerfeld radiation condition.

As is the case with FEM, there exist modified versions of BEM which aim to speed up the solution or increase accuracy per degree of freedom. Often, the aim of these

modifications is to allow more efficient solution of high-frequency problems, which can be challenging for conventional BEM schemes. As a rule of thumb, conventional BEM requires 8-10 degrees of freedom per wavelength to achieve ‘engineering accuracy’ of 1%. Similarly to FEM, Trefftz based methods also provide benefit in BEM schemes, which will be discussed in section 3.5, but before moving on it is important to note that there are alternative BEM approaches such as fast multipole methods [57–60], low-rank matrix approximations [61] and use of optimised linear algebra routines [62]. Such methods aim to increase the efficiency with which a system of BEM equations is solved. Notably, BEM matrices are densely populated in comparison to FEM matrices. Another popular flavour of BEM is Isogeometric Boundary Element Method (IGABEM) [45–47], wherein, similarly to IGAFEM, NURBS are used as basis functions to describe both the variation in acoustic potential, and the geometry of the domain in which the governing equation is solved.

## 3.2 Interior domains

Consider an interior domain, containing a homogeneous medium wherein frequency dependent wave propagation is governed by the Helmholtz equation (2.7). Before moving on to the formulation, it is important to remember the nature of the fundamental solutions resulting from a point source, shown in (2.8). This is because in order to form the BIE it is necessary to exclude a small region surrounding the singular point source resulting from the fundamental solution. In  $2D$ , this excluded region is a circle with radius  $\epsilon$  and a sphere in  $3D$  with radius  $\epsilon$ . The domain, along with the associated boundaries and a point  $p$  are shown in Fig. 3.1.

Making use of Green’s second identity it is possible to write the following,

$$\begin{aligned} \int_{\Omega_f - \Omega_\epsilon} [\phi(\mathbf{q}) \nabla^2 G(\mathbf{p}, \mathbf{q}) - G(\mathbf{p}, \mathbf{q}) \nabla^2 \phi(\mathbf{q})] d\Omega \\ = \int_{\Gamma + \Gamma_\epsilon} \left( G(\mathbf{p}, \mathbf{q}) \frac{\partial \phi(\mathbf{q})}{\partial n(\mathbf{q})} - \phi(\mathbf{q}) \frac{\partial G(\mathbf{p}, \mathbf{q})}{\partial n(\mathbf{q})} \right) d\Gamma(\mathbf{q}), \quad \mathbf{p} \in \Omega_f. \end{aligned} \quad (3.1)$$

where  $\Omega_f$  is the fluid domain in which the sound will propagate,  $G(\mathbf{p}, \mathbf{q})$  is the fundamental solution from (2.11),  $\mathbf{p}$  is a vector of singular source point locations, each point associated with a fundamental solution and  $\mathbf{q}$  are ‘field’ points at which the fundamental solutions are evaluated,  $\phi(\mathbf{q})$  is the unknown acoustic potential and  $n(\mathbf{q})$  is an outward facing unit normal vector from  $\Omega_f$ . The singular points associated with the fundamental solutions are excluded from the domain of interest to allow the following.

$$\nabla^2 \phi(\mathbf{q}) + k^2 \phi(\mathbf{q}) = \nabla^2 G(\mathbf{p}, \mathbf{q}) + k^2 G(\mathbf{p}, \mathbf{q}) = 0, \quad \mathbf{p} \in \Omega_f \quad (3.2)$$

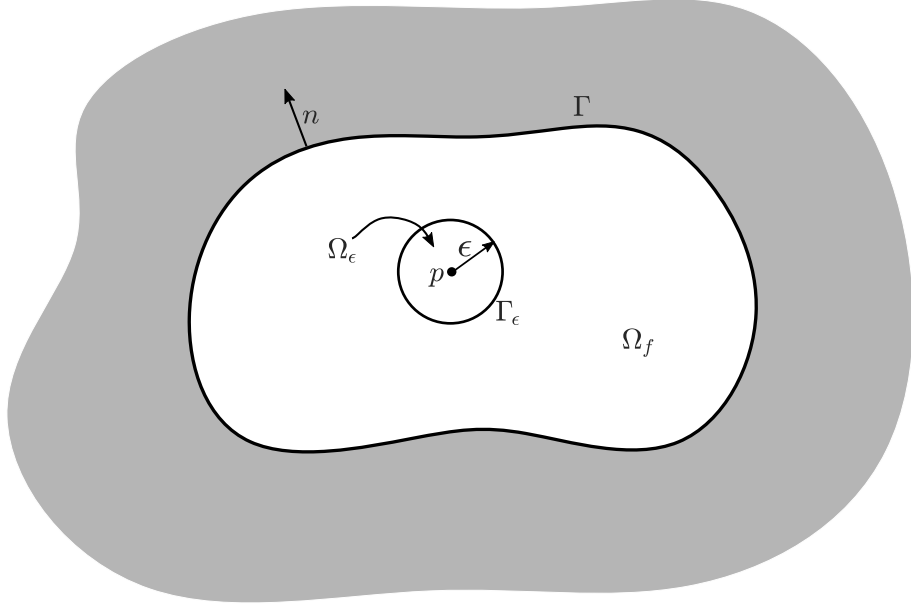


Figure 3.1: Interior domain  $\Omega_f$  with boundary  $\Gamma$  and point  $p$  surrounded by a circle of radius  $\epsilon$ .

which may be rearranged to provide

$$\begin{aligned} G(\mathbf{p}, \mathbf{q})\nabla^2\phi(\mathbf{q})+k^2\phi(\mathbf{q})G(\mathbf{p}, \mathbf{q}) \\ = \phi(\mathbf{q})\nabla^2G(\mathbf{p}, \mathbf{q}) + k^2\phi(\mathbf{q})G(\mathbf{p}, \mathbf{q}) = 0, \quad \mathbf{p} \in \Omega_f. \end{aligned} \quad (3.3)$$

The results of (3.3) may be inserted into (3.1) to produce

$$\begin{aligned} \int_{\Omega_f-\Omega_\epsilon} [\phi(\mathbf{q})\nabla^2G(\mathbf{p}, \mathbf{q})+k^2G(\mathbf{p}, \mathbf{q})\phi(\mathbf{q})]d\Omega \\ = \int_{\Gamma+\Gamma_\epsilon} \left( G(\mathbf{p}, \mathbf{q})\frac{\partial\phi(\mathbf{q})}{\partial n(\mathbf{q})} - \phi(\mathbf{q})\frac{\partial G(\mathbf{p}, \mathbf{q})}{\partial n(\mathbf{q})} \right) d\Gamma(\mathbf{q}), \quad \mathbf{p} \in \Omega_f, \end{aligned} \quad (3.4)$$

wherein the left-hand-side is certainly equal to zero due to (3.2), resulting in

$$\int_{\Gamma_s+\Gamma_\epsilon} \left( G(\mathbf{p}, \mathbf{q})\frac{\partial\phi(\mathbf{q})}{\partial n(\mathbf{q})} - \phi(\mathbf{q})\frac{\partial G(\mathbf{p}, \mathbf{q})}{\partial n(\mathbf{q})} \right) d\Gamma(\mathbf{q}) = 0, \quad \mathbf{p} \in \Omega_f. \quad (3.5)$$

It is clear from (3.5) that now only boundary integrals remain. To represent the boundary of the point source, it is necessary to take  $\epsilon \rightarrow 0$ . Therefore, the first integral over the boundary of the point source location  $\epsilon$  is

$$\lim_{\epsilon \rightarrow 0} \int_{\Gamma_\epsilon} G(\mathbf{p}, \mathbf{q})\frac{\partial\phi(\mathbf{q})}{\partial n(\mathbf{q})} d\Gamma(\mathbf{q}) = 0 \quad (3.6)$$

and the second is equal to the following

$$-\lim_{\epsilon \rightarrow 0} \int_{\Gamma_\epsilon} \phi(\mathbf{q}) \frac{\partial G(\mathbf{p}, \mathbf{q})}{\partial n(\mathbf{q})} d\Gamma(\mathbf{q}) = -\phi(\mathbf{p}), \quad (3.7)$$

which is known as the jump term.

$$-\phi(\mathbf{p}) + \int_{\Gamma} \left( G(\mathbf{p}, \mathbf{q}) \frac{\partial \phi(\mathbf{q})}{\partial n(\mathbf{q})} - \phi(\mathbf{q}) \frac{\partial G(\mathbf{p}, \mathbf{q})}{\partial n(\mathbf{q})} \right) d\Gamma(\mathbf{q}) = 0, \quad \mathbf{p} \in \Omega_f. \quad (3.8)$$

According to the above definitions, the source points  $\mathbf{p}$  are contained in the fluid domain  $\Omega_f$ , but it is necessary to move this to the boundary  $\Gamma$  in order to compute  $\phi(\mathbf{p}) \in \Gamma$  which will allow subsequent computation of acoustic potential at so-called field points which do not lie on the boundary. For a smooth scattering object this will half the jump term to provide the following updated version of (3.8).

$$\frac{-\phi(\mathbf{p})}{2} + \int_{\Gamma} \left( G(\mathbf{p}, \mathbf{q}) \frac{\partial \phi(\mathbf{q})}{\partial n(\mathbf{q})} - \phi(\mathbf{q}) \frac{\partial G(\mathbf{p}, \mathbf{q})}{\partial n(\mathbf{q})} \right) d\Gamma(\mathbf{q}) = 0, \quad \mathbf{p}, \mathbf{q} \in \Gamma. \quad (3.9)$$

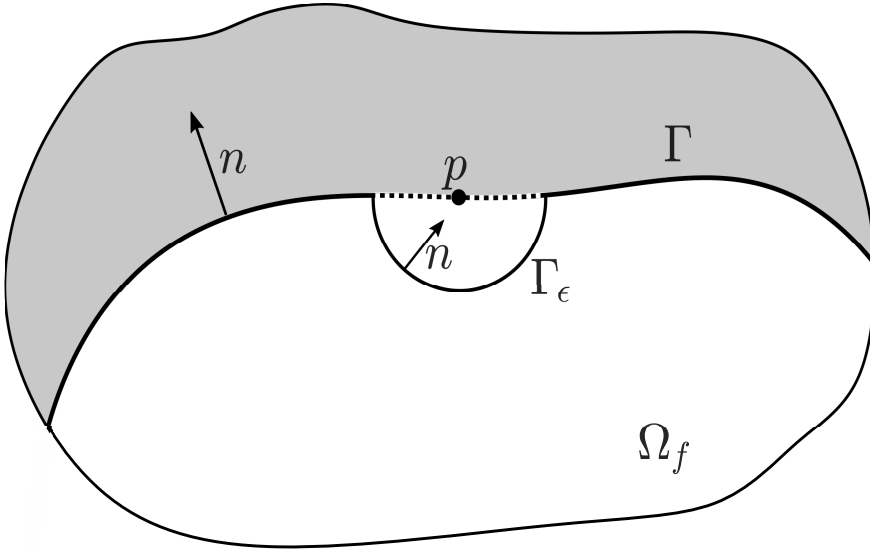


Figure 3.2: Interior domain  $\Omega_f$  with point  $p$  located on the boundary  $\Gamma$ .

This is shown in Fig. 3.2, where a single point  $p$  is located on the boundary  $\Gamma$ . The resulting equation is defined entirely over  $\Gamma$  thus reducing the dimensionality of the problem. As seen above, the jump term is halved on a smooth boundary, but this will not always be the case, such as for corner locations which will be encountered in this thesis. This requires the jump term to be multiplied by a new function  $c(\mathbf{p})$  which is dependent

on the geometry. By including  $c(\mathbf{p})$  and rearranging, (3.9) is generalised to produce

$$c(\mathbf{p})\phi(\mathbf{p}) + \int_{\Gamma} \phi(\mathbf{q}) \frac{\partial G(\mathbf{p}, \mathbf{q})}{\partial n(\mathbf{q})} d\Gamma(\mathbf{q}) = \int_{\Gamma} G(\mathbf{p}, \mathbf{q}) \frac{\partial \phi(\mathbf{q})}{\partial n(\mathbf{q})} d\Gamma(\mathbf{q}), \quad \mathbf{p}, \mathbf{q} \in \Gamma. \quad (3.10)$$

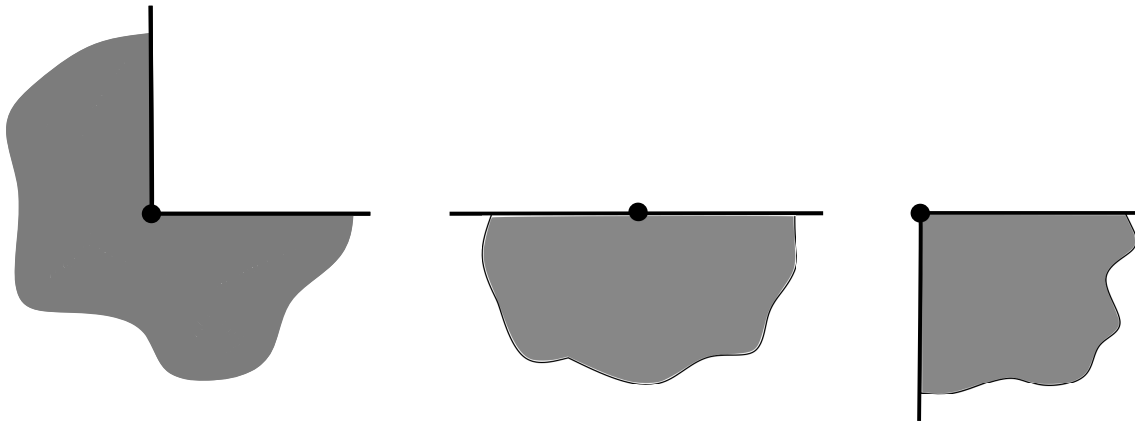


Figure 3.3: Example angles on which a collocation point may sit. The angle on the left would result in  $c(p) = \frac{1}{4}$ , the angle in the middle would result in  $c(p) = \frac{1}{2}$  and the angle on the right would result in  $c(p) = \frac{3}{4}$ . The analysis domain is shown unshaded.

wherein  $c(\mathbf{p})$  is a function of the angle subtended at points  $\mathbf{p}$ , which is illustrated in Fig. 3.3.

### 3.3 Exterior domains

Exterior scattering problems in infinite domains are a category in which BEM performs particularly favourably in, due to the fact that even though  $\Omega_f$  is infinite it is still possible to compute acoustic potential at any point, using only boundary integrals. Fig. 3.4 shows a generic scattering object which includes the same variables as for the interior problem but with the inclusion of an incident plane wave  $\phi^{inc}$  and a representation of a boundary at infinity, denoted  $\Gamma_\infty$ .

In order to apply the above formulation to exterior problems some minor modifications are required, the first of which is the Sommerfeld radiation condition, given by

$$\lim_{r \rightarrow \infty} |r|^{\frac{\bar{n}-1}{2}} \left( \frac{\partial \phi}{\partial |r|} - ik\phi \right) = 0, \quad (3.11)$$

where  $\bar{n}$  represents the dimension of the problem. This boundary condition does not result in a practical change in (3.10), but exists in the theoretical formulation, therefore is included here for completeness. From (3.11) the following relationship arises on  $\Gamma_\infty$ .

$$\frac{\partial \phi}{\partial |r|} = ik\phi, \quad (3.12)$$

which may be used in conjunction with the knowledge that

$$\frac{\partial \phi}{\partial |r|} = \frac{\partial \phi}{\partial n}, \quad (3.13)$$

which allows us to reformulate (3.10) over the boundary  $\Gamma_\infty$  to produce

$$\int_{\Gamma_\infty} ik\phi(\mathbf{q})G(\mathbf{p}, \mathbf{q})d\Gamma_\infty(\mathbf{q}) - \int_{\Gamma_\infty} \phi(\mathbf{q})\frac{\partial G(\mathbf{p}, \mathbf{q})}{\partial n(\mathbf{q})}d\Gamma_\infty(\mathbf{q}). \quad (3.14)$$

The fundamental solution in 2D (2.11) and its derivative (2.12) contain Hankel functions and are repeated here for convenience,

$$G(\mathbf{p}, \mathbf{q}) = \frac{i}{4}H_0^{(1)}(kr), \quad (3.15)$$

$$\frac{\partial G(\mathbf{p}, \mathbf{q})}{\partial n(\mathbf{q})} = \frac{-ik}{4}H_1^{(1)}(kr)\frac{\partial r}{\partial n}. \quad (3.16)$$

The asymptotic approximation of  $H_0^{(1)}$  and  $H_1^{(1)}$  at infinity are given by

$$H_0^{(1)}(kr) \sim \sqrt{\frac{2}{\pi kr}}e^{i(kr-\frac{\pi}{4})} \quad (3.17)$$

$$H_1^{(1)}(kr) \sim \sqrt{\frac{2}{\pi kr}}e^{i(kr-\frac{\pi}{4})} \quad (3.18)$$

therefore at infinity

$$H_1^{(1)}(kr) = -iH_0^{(1)}(kr), \quad (3.19)$$

which can be inserted into (3.14) to produce

$$\int_{\Gamma_\infty} \frac{k}{4}\phi(\mathbf{q})H_0^{(1)}d\Gamma_\infty(\mathbf{q}) - \int_{\Gamma_\infty} \frac{k}{4}\phi(\mathbf{q})H_0^{(1)}d\Gamma_\infty(\mathbf{q}), \quad (3.20)$$

thus removing any terms to be integrated over  $\Gamma_\infty$  which leaves (3.10) unchanged. Often, infinite domain problems are used to analyse the scattering of an incident wave from an obstacle, thus, the incident wave is included in (3.10) to produce the BIE for exterior scattering problems, as follows.

$$\begin{aligned} c(\mathbf{p})\phi(\mathbf{p}) + \int_{\Gamma_s} \phi(\mathbf{q})\frac{\partial G(\mathbf{p}, \mathbf{q})}{\partial n(\mathbf{q})}d\Gamma(\mathbf{q}) \\ = \int_{\Gamma_s} G(\mathbf{p}, \mathbf{q})\frac{\partial \phi(\mathbf{q})}{\partial n(\mathbf{q})}d\Gamma(\mathbf{q}) + \phi^{inc}(\mathbf{p}), \quad \mathbf{p}, \mathbf{q} \in \Gamma. \end{aligned} \quad (3.21)$$

Before moving on to the numerical solution of (3.10) using BEM, it is useful to consider

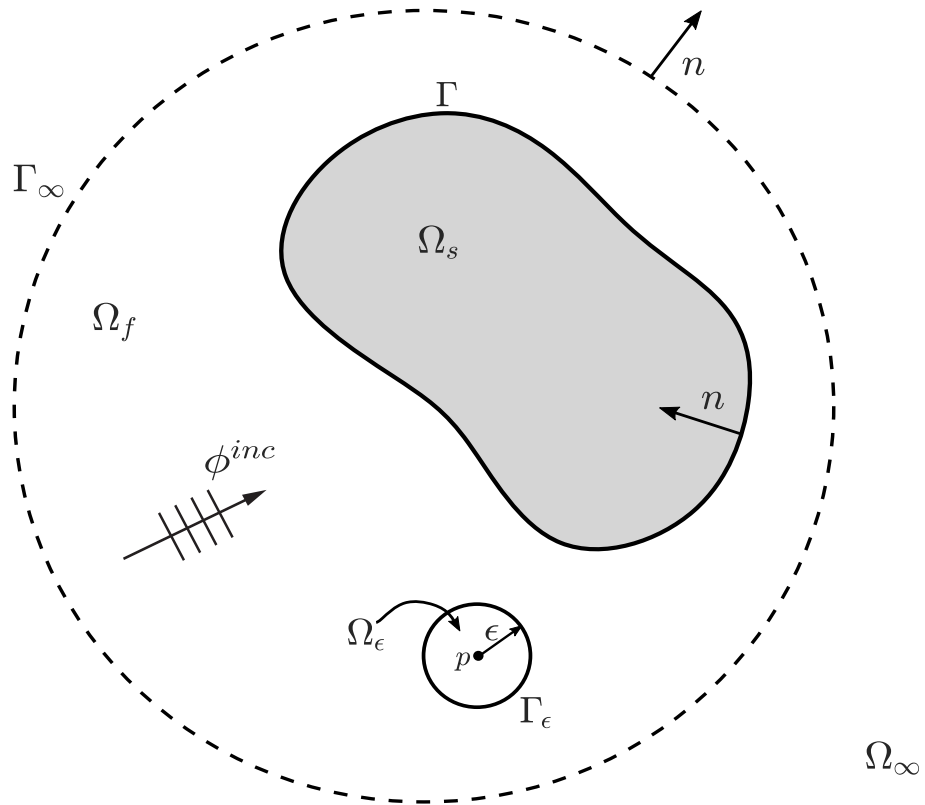


Figure 3.4: Generic scattering object where  $\Omega_s$  is the domain of the scatterer,  $\Omega_f$  is the fluid domain,  $\Gamma$  is the boundary of the scatterer,  $\phi^{inc}$  is the incident wave and  $\Gamma_\infty$  represents the boundary at infinity.

boundary conditions. The Robin boundary condition can be defined as

$$\frac{\partial\phi(\mathbf{q})}{\partial\mathbf{n}} = \alpha\phi(\mathbf{q}) + \beta, \quad q \in \Gamma \quad (3.22)$$

wherein  $\alpha$  and  $\beta$  are coefficients which may be varied depending on requirements. The Dirichlet condition can be defined as

$$\phi(\mathbf{q}) = g, \quad (3.23)$$

The ‘sound hard’ Neumann condition can be defined as follows

$$\frac{\partial\phi(\mathbf{q})}{\partial n(\mathbf{q})} = 0, \quad (3.24)$$

i.e.  $\alpha = \beta = 0$  in (3.22) though, the flexibility offered by the Robin condition is required for some interior problems considered in this thesis; thus, the Robin condition is applied to the BIE here, as follows,

$$\begin{aligned} c(\mathbf{p})\phi(\mathbf{p}) + \int_{\Gamma} \left[ \frac{\partial G(\mathbf{p}, \mathbf{q})}{\partial n(\mathbf{q})} - \alpha G(\mathbf{p}, \mathbf{q}) \right] \phi(\mathbf{q}) d\Gamma(\mathbf{q}) \\ = \int_{\Gamma} \beta G(\mathbf{p}, \mathbf{q}) d\Gamma(\mathbf{q}) + \phi^{inc}(\mathbf{p}), \quad \mathbf{p}, \mathbf{q} \in \Gamma. \end{aligned} \quad (3.25)$$

In the following section (3.25) is discretised for numerical solution.

### 3.4 Discretisation

In order to solve (3.25) numerically for general cases, the boundary  $\Gamma$  is divided into a total of  $E$  elements. Over each element the geometry, the acoustic potential  $\phi$  may be described in terms of a total  $J$  basis functions, commonly referred to as shape functions. These functions are defined in terms of a local coordinate  $\xi$ , over a given element  $e$  to provide a description of the geometry as

$$x = \sum_{j=1}^J x_j \Psi_j(\xi) \quad (3.26)$$

$$y = \sum_{j=1}^J y_j \Psi_j(\xi), \quad (3.27)$$

where  $x_i$  and  $y_i$  are local coordinates at nodal locations associated with element  $e$ .

A discretisation of a general scattering object is shown in Fig. 3.5 wherein each element is separated by straight lines, and each element contains 3 nodes. The choice of basis functions is discussed at length in chapters to follow, but for now the discretisation process

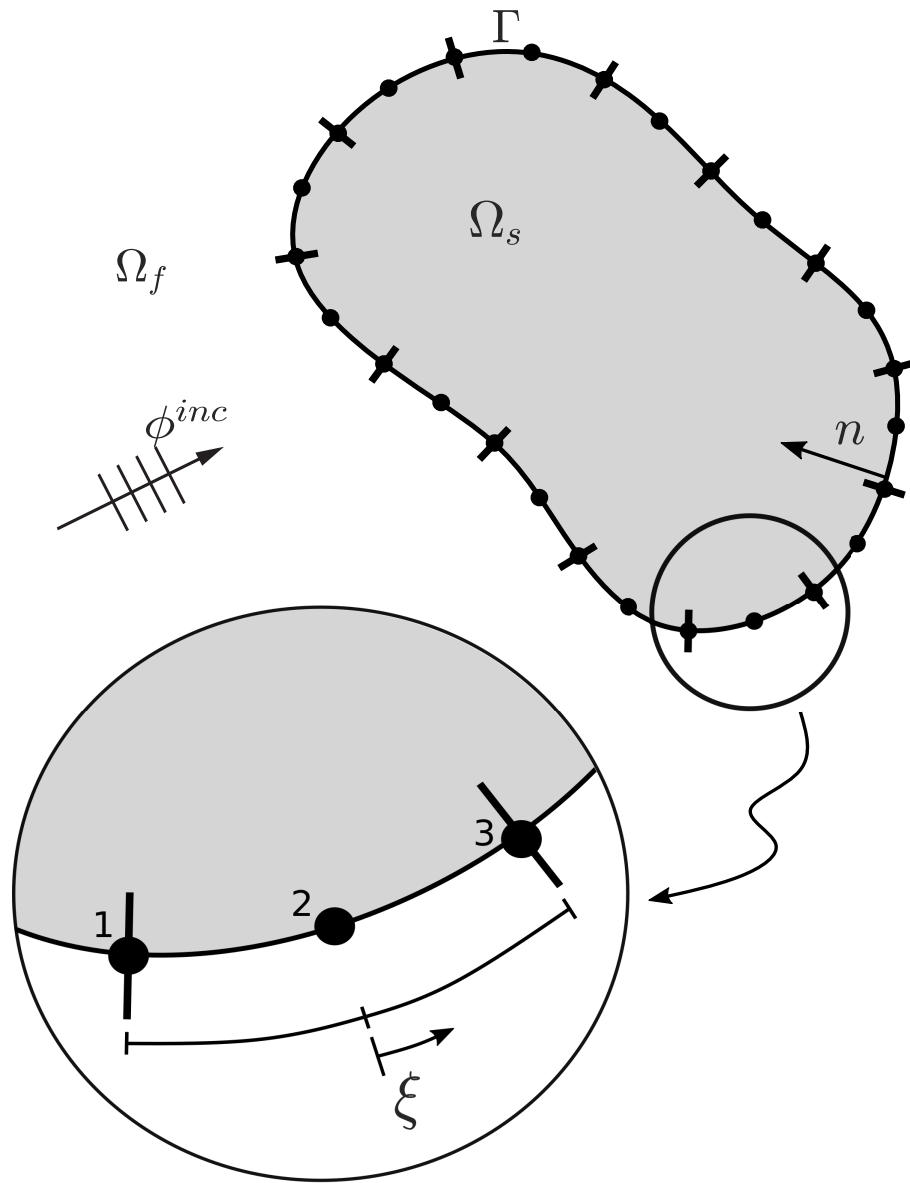


Figure 3.5: Generic scattering object discretised into quadratic elements with 3 nodes per elements and the parametric variable  $\xi$ .

is explained in terms of the commonly employed quadratic basis functions. For a quadratic element, the basis is given by

$$\Psi_1 = \frac{1}{2}\xi(\xi - 1) \quad (3.28)$$

$$\Psi_2 = (1 - \xi)(1 + \xi) \quad (3.29)$$

$$\Psi_3 = \frac{1}{2}\xi(\xi + 1), \quad (3.30)$$

where  $\xi \in [-1, 1]$ .  $\Psi_1, \Psi_2$  and  $\Psi_3$  are plotted in Fig. 3.6. Typically, the same basis functions used to describe the geometry are used to describe the acoustic potential  $\phi$ . This is referred to as an isoparametric formulation and produces the following expression for acoustic potential over an element,

$$\phi = \sum_{j=1}^J \phi_j \Psi_j(\xi). \quad (3.31)$$

In order to employ the local coordinate system which is a function of  $\xi$  over each element, a coordinate transformation is required. This results in a Jacobian of transformation which is defined as

$$J^e = \sqrt{\left(\frac{dx}{d\xi}\right)^2 + \left(\frac{dy}{d\xi}\right)^2}, \quad (3.32)$$

where, for example,  $dx/d\xi$  and  $dy/d\xi$  are as follows

$$\frac{dx}{d\xi} = \sum_{j=1}^J x_j \frac{d\Psi_j}{d\xi}, \quad (3.33)$$

$$\frac{dy}{d\xi} = \sum_{j=1}^J y_j \frac{d\Psi_j}{d\xi} \quad (3.34)$$

when basis functions  $\Psi_j$  are employed. It is now possible to produce the discretised form of (3.25) with  $E$  elements and  $J$  basis functions per element, given by

$$\begin{aligned} c(\mathbf{p})\phi(\mathbf{p}) + \sum_{e=1}^E \sum_{j=1}^J \int_{-1}^1 \left[ \frac{\partial G(\mathbf{p}, \mathbf{q})}{\partial \mathbf{n}} - \alpha G(\mathbf{p}, \mathbf{q}) \right] \Psi_j(\xi) J^e d\xi \phi_j^e \\ = \sum_{e=1}^E \int_{-1}^1 \beta G(\mathbf{p}, \mathbf{q}) J^e d\xi + \phi^{inc}(\mathbf{p}), \quad \mathbf{p}, \mathbf{q} \in \Gamma, \end{aligned} \quad (3.35)$$

in which  $\Psi_j$  denotes the basis functions,  $\phi_j^e$  represent the unknown nodal potential,  $J^e$  is the Jacobian of the geometric mapping  $(x, y) \rightarrow \xi$  and the conventional  $\xi \in [-1, 1]$

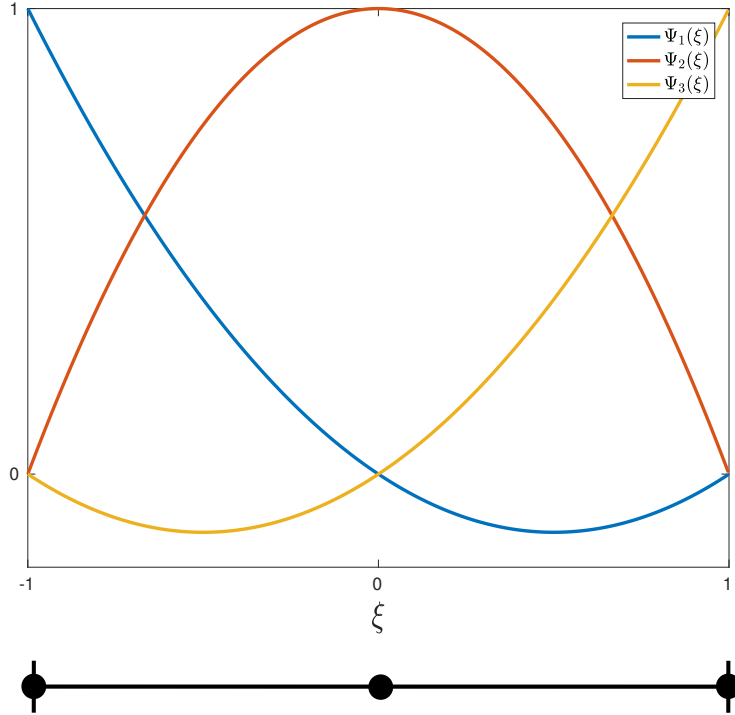


Figure 3.6: Quadratic Lagrangian shape functions.

is employed. Naturally, the Jacobian  $J^e$  is dependent on the geometric properties of the domain of interest. In certain examples, such as when considering straight line, or circular arc, elements,  $J^e$  will be a constant. In order to solve this equation, we must 'collocate' at points  $\mathbf{p}$  and integrate the resulting (3.35) over the boundary, which is performed element-by-element. For now, the collocation points  $\mathbf{p}$  will be equal to the nodal locations of the elements which is not mandatory but simplifies the interpolation process for  $\phi(\mathbf{p})$ . Non-nodal collocation will be required for a PUBEM formulation. The resulting linear system of equations in matrix form is given by,

$$\left[ \mathbf{C} + \mathbf{H} - \boldsymbol{\alpha}\mathbf{g} \right] \left\{ \boldsymbol{\phi} \right\} = \left\{ \boldsymbol{\beta}\mathbf{g} + \boldsymbol{\phi}^{inc} \right\}, \quad (3.36)$$

where  $\mathbf{C}$  contains the interpolations of  $c(\mathbf{p})\phi(\mathbf{p})$ ,  $\mathbf{H}$  and  $\boldsymbol{\alpha}\mathbf{g}$  contain the boundary integrals from the left hand side of (3.35),  $\boldsymbol{\phi}$  is the vector of unknown potentials,  $\boldsymbol{\beta}\mathbf{g}$  is a vector containing the boundary integrals from the right hand side of (3.35) and  $\boldsymbol{\phi}^{inc}$  is a vector of incident wave potential at collocation locations. The parameter used to define the number of degrees of freedom employed per wavelength is therefore

$$\tau = \frac{(J-1)E\lambda}{\tilde{p}}, \quad (3.37)$$

where  $\tilde{p}$  is the perimeter of the problem boundary i.e.  $\tilde{p} = \int d\Gamma$ . Naturally, solving (3.36)

recovers the unknown potential  $\phi$  at nodal locations, which may then be interpolated using (3.31) to determine  $\phi$  at non-nodal locations. Following this, recovery of the acoustic potential at points which are within the fluid domain (i.e. for  $\mathbf{p} \in \Omega_f$ ) wherein wave propagation is taking place is straightforward as the nodal potentials  $\phi$  are now known. This means that potential  $\phi$  at points  $\mathbf{p} \in \Omega_f$  may be obtained simply by performing the integration performed over the boundary (with the known values of  $\phi$  inserted into (3.35)).

Further, it is well known that solutions of (3.35) become non-unique at frequencies corresponding to the eigenfrequencies of the associated interior problem formed on the same boundary  $\Gamma$ . In the interest of simplicity, the Combined Helmholtz Integral Equation Formulation (CHIEF) [87] is employed here to overcome the system degeneracy. CHIEF requires additional collocation points located in the interior domain  $\Omega_s$  of the scattering object, resulting in an overdetermined system of equations, that requires an appropriate solver. It should be noted that there is a popular alternative method of Burton and Miller [88] which can be regularised as in [89, 90] reducing the hypersingular integrals to weakly singular.

## 3.5 PUBEM

### 3.5.1 Background

PUBEM is inspired by Trefftz methods, whereby the basis functions, in this case plane-waves, that are employed are chosen because they are known solutions of the governing equation. Though, PUBEM is not a true Trefftz method as the plane-waves are, typically, multiplied by polynomial shape functions. The result is a plane-wave basis, multiplied by interpolating functions that have the partition of unity property. This method was developed by Perrey-Debain et al.[49–51] and has been shown to greatly reduce the number of degrees of freedom required per wavelength to achieve engineering accuracy of 1%. In fact, the heuristic requirement of 8-10 degrees of freedom per wavelength (for conventional BEM) can be reduced to approximately 2.5 for a PUBEM scheme in the mid-high frequency range.

Typically the set of plane-waves of which the PUBEM basis is comprised propagate at equispaced angles with respect to one another. This even spread of plane-waves, if sufficient in number, allows solution of general problems which includes concave objects and reflections from multiple objects. This is noteworthy because there are more problem-specific enrichment methods wherein leading order behaviour is built-in to the enrichment [53, 54] to obtain extremely efficient and accurate solutions for certain classes of problem, for example, scattering by a single convex polygon.

### 3.5.2 Derivation

The derivation of PUBEM can follow the same path as for BEM, shown above, until it comes to selecting the basis functions. For this reason, the derivation provided here can proceed from (3.35). The same polynomial basis may be employed but enriched such that the unknown potential is written as a linear combination of plane waves propagating in different directions, i.e.

$$\phi = \sum_{j=1}^J \sum_{m=1}^M \Psi_j(\xi) A_{jm} e^{ik\mathbf{d}_{jm} \cdot \mathbf{q}}, \quad (3.38)$$

$$\mathbf{d}_{jm} = (\cos \bar{\phi}_{jm}, \sin \bar{\phi}_{jm}), \quad \bar{\phi}_{jm} = \frac{2\pi(m-1)}{M} \quad (3.39)$$

where  $A_{jm}$  are the unknown plane wave amplitudes,  $\mathbf{d}_{jm}$  are the direction vectors of the plane waves,  $i = \sqrt{-1}$  and  $M$  is the number of plane waves considered per node. Therefore the discretised form of (3.35) in a PUBEM setting becomes

$$\begin{aligned} c(\mathbf{p})\phi(\mathbf{p}) + \sum_{e=1}^E \sum_{j=1}^J \sum_{m=1}^M \int_{-1}^1 \left[ \frac{\partial G(\mathbf{p}, \mathbf{q})}{\partial \mathbf{n}} - \alpha G(\mathbf{p}, \mathbf{q}) \right] \Psi_j(\xi) e^{ik\mathbf{d}_{jm} \cdot \mathbf{q}} J^e d\xi A_{jm}^e \\ = \sum_{e=1}^E \int_{-1}^1 \beta G(\mathbf{p}, \mathbf{q}) J^e d\xi + \phi^{inc}(\mathbf{p}), \quad \mathbf{p}, \mathbf{q} \in \Gamma. \end{aligned} \quad (3.40)$$

Solving (3.40) results in a vector of unknown amplitudes  $A_{jm}$ , which can then be multiplied by the corresponding plane-waves to recover the unknown potential  $\phi$ . To compute the number of degrees of freedom per wavelength one must compute

$$\tau = \frac{(J-1)ME\lambda}{\tilde{p}}. \quad (3.41)$$

An example PUBEM element is shown in Fig. 3.7, with  $M = 4$  and  $J = 3$ . Additionally, for  $M > 1$  non-nodal collocation is required, which introduces some slightly more involved numerical treatment. For example,  $[\mathbf{C}]$  is now populated by interpolating between nodes and multiplying by the respective plane-waves.

It is well-known that the linear systems of equations resulting from enriched formulations can suffer from ill-conditioning [52]; in PUBEM, the ill-conditioning is mostly observed at large  $\tau$ . Such conditioning problems are expected because, as is well known, PUBEM performs optimally with a relatively coarse discretisation, i.e. using relatively large elements and large  $M$ . Therefore, when  $\tau$  is large, there are often many enrichment waves propagating at equispaced angles. That is, for any given enrichment wave, at any given node, the neighbouring enrichment waves will be propagating in substantially similar directions and therefore will result in substantially similar equations adjacent to one

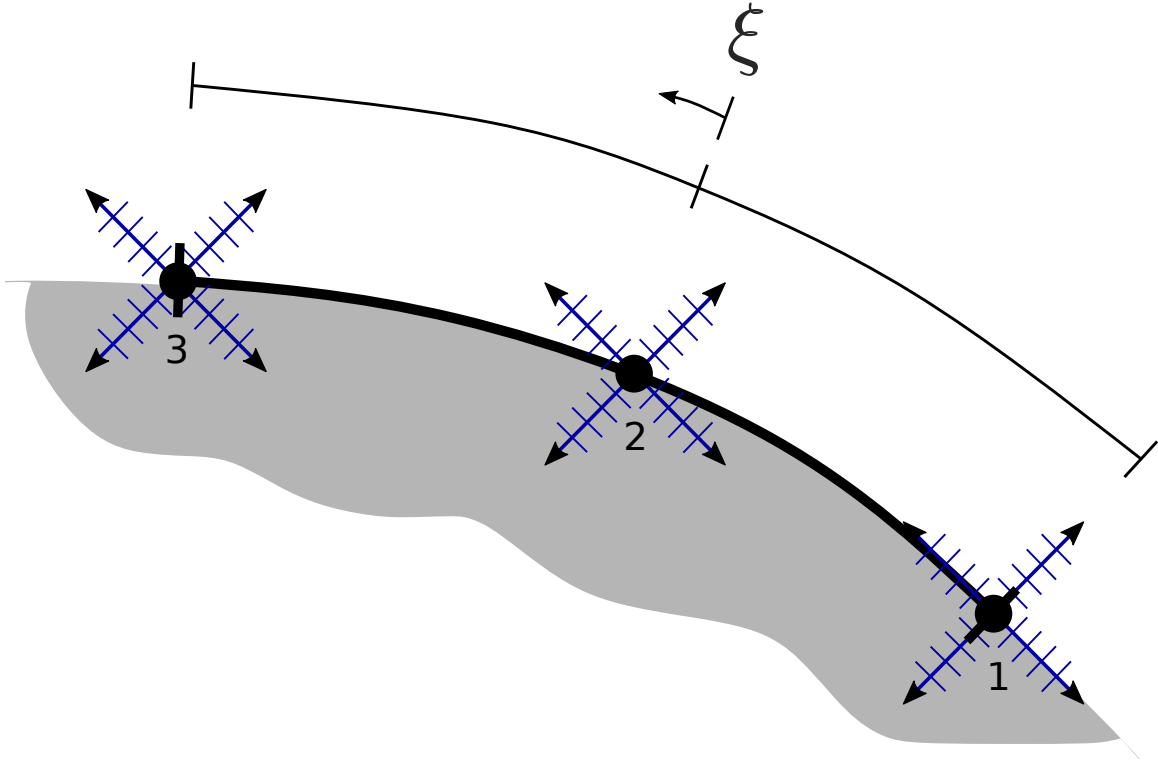


Figure 3.7: Quadratic PUBEM element with  $M = 4$  showing the parametric variable  $\xi$ .

another within the resulting system of equations. Naturally, such similarity between the equations, increases the condition number of the associated system of equations.

Typically, the conditioning of the PUBEM systems can be easily managed by controlling  $\tau$  and using a suitable method of solution [52], such as Singular Value Decomposition (SVD). Further, oversampling by adding a surplus of collocation points can also help to reduce the condition number of the resulting system of equations, though this was not required to produce the results shown in this thesis. Additionally, it is possible to perform the PUBEM enrichment in a Galerkin procedure, though in the current work the collocation form of BEM is employed, such that (3.40) is collocated at a sufficient number of points  $p$  to yield a solvable linear system.

When producing a BEM discretisation one must consider the accuracy required, which will inform the choice of  $\tau$ , which in turn will determine the number of elements required. Perhaps further decisions are required to select the type of basis function and the order of basis function to be employed. In PUBEM however, one must select the number of elements to use and the number of plane waves employed per node. To the authors' knowledge there has been no attempt to define an optimal combination of  $E$  and  $M$ . Chapter 7 of this thesis is devoted to providing insight into the relationship between  $E$  and  $M$ .

### 3.5.3 Exact geometry representation

For PUBEM simulations in particular, exact geometry representation is often required to unlock the full benefit of enrichment. This is because, as mentioned above, PUBEM performs optimally with a relatively coarse discretisation, i.e. using relatively large elements and large  $M$ . A coarse discretisation, with large relatively large  $M$ , may include many wavelengths within a single element.

The basis functions should be able to accurately represent the potential, but if the geometry is not exact, geometric errors can be injected into the solution. A common rule of thumb is that geometric details start to have a significant influence on wave scattering when their size grows to be similar to the wavelength (and larger). Since the element spans many wavelengths it is unlikely a simple quadratic description of the geometry will be sufficient. Additionally, the condition number for PUBEM matrices can be considerably larger than for standard BEM simulations, thus errors can be magnified which means it is important to populate the system matrices as accurately as possible.

# Chapter 4

## Integration

### 4.1 Overview

In order to populate the matrices  $[\mathbf{H}]$  and  $[\mathbf{G}]$  from (3.36) and (3.40) it is necessary to evaluate boundary integrals. This integration is performed numerically and often requires special treatment.

A brief primer on traditional quadrature is presented followed by discussion of the standard BEM integrals. Some more challenging cases such as singular integrals are covered before presenting the PUBEM integrals to highlight the difference between the two. The challenges of performing integration of highly-oscillatory PUBEM kernels are discussed at length, with some conventional methods presented. Following this, a number of methods are presented which aim to effectively integrate highly-oscillatory functions, each method is tested on PUBEM integrals. Finally, a more conventional sub-divided Gauss-Legendre integration scheme is tested, at length, on the PUBEM integrals.

#### 4.1.1 Traditional quadrature

In this section, standard integration techniques are presented, which are used to compute the integrals from (3.35). For a general case,

$$\int_a^b f(x)dx. \quad (4.1)$$

It is possible to perform the integration using a rudimentary Newton-Cotes scheme such as the composite trapezoidal method wherein an integral is approximated by sub-dividing the interval of integration into  $n$  sub-intervals of width  $h$ , as follows

$$\int_a^b f(x)dx \approx \frac{h}{2}f(a) + h \sum_{k=1}^{n-1} f(x + kh) + \frac{h}{2}f(b), \quad (4.2)$$

and approximating the integral over each sub-interval using a trapezoid. However, the dominant method used in FEM, BEM and for the majority of the results in this thesis is that of Gaussian-Legendre quadrature. This requires the integral of interest to be expressed as a weighted sum comprising the value of the integrand at specified sample points, multiplied by corresponding weights. The formula for a, general, ‘ $n$ ’ point quadrature scheme is given by

$$\int_a^b f(x)dx \approx \frac{b-a}{2} \sum_{i=1}^n w_i f\left(\frac{b-a}{2}x_i + \frac{a+b}{2}\right), \quad (4.3)$$

where  $x_i$  and  $w_i$  are the abscissas and weights respectively, for  $i = 1, \dots, n$ . The intention is to select appropriate  $x_i$  and  $w_i$  in order to create a scheme which is exact when approximating polynomials of degree  $2n - 1$  or less. There are a number of options for selecting appropriate  $x_i$  and  $w_i$ , but the integration performed for this thesis employs Gauss-Legendre quadrature, in which  $x_i$  are the roots of the  $n$ th Legendre polynomial, and the weights are provided by the following.

$$w_i = \frac{2}{(1-x_i)^2 [P'_n(x_i)]^2}. \quad (4.4)$$

As is shown in (3.35) the integrals are defined in terms parametric variable  $\xi \in [-1, 1]$ , which, due to its limits, allows us to write the Gauss quadrature scheme more compactly as

$$\int_{-1}^1 f(\xi)d\xi \approx \sum_{i=1}^n w_i f(\xi_i). \quad (4.5)$$

## 4.2 BEM integrals

From the the BIE in (3.35), there are three types of integral requiring evaluation, which are:

$$\int_{-1}^1 \frac{\partial G(\mathbf{p}, \mathbf{q})}{\partial \mathbf{n}} \Psi_j(\xi) J^e d\xi, \quad (4.6)$$

$$\int_{-1}^1 \alpha G(\mathbf{p}, \mathbf{q}) \Psi_j(\xi) J^e d\xi, \quad (4.7)$$

and

$$\int_{-1}^1 \beta G(\mathbf{p}, \mathbf{q}) J^e d\xi. \quad (4.8)$$

The first of which (4.6), in  $2D$ , can comfortably be computed using (4.5), but it is well-known that the Green's function

$$G(p, q) = \frac{i}{4} H_0^1(kr), \quad (4.9)$$

present in (4.7) and (4.8) is weakly singular as  $kr \rightarrow 0$ , which occurs when a collocation point lies within the interval of integration. This causes slow convergence using standard Gauss-Legendre integration. Naturally, this term is not included for the sound-hard scattering problems because, for Neumann problems,  $\alpha = 0$  but for problems in which the sound hard condition is not appropriate a 'Robin' boundary condition

$$\frac{\partial \phi(q)}{\partial \mathbf{n}} = \alpha \phi(q) + \beta, \quad q \in \Gamma, \quad (4.10)$$

is applied which introduces the requirement to compute the singular integrals relating to the  $\alpha$  and  $\beta$  terms. The approach taken in this thesis is to employ a Telles transformation [67]. This entails performing a coordinate transformation, as follows.

$$\xi(\gamma) = a\gamma^3 + b\gamma^2 + c\gamma + d. \quad (4.11)$$

If we define  $\bar{\xi}$  as the point at which  $f(\xi)$  becomes singular and enforce the following conditions.

$$\left. \frac{d\xi}{d\gamma} \right|_{\bar{\xi}} = 0 \quad (4.12)$$

$$\left. \frac{d^2\xi}{d\gamma^2} \right|_{\bar{\xi}} = 0 \quad (4.13)$$

$$\xi|_{\gamma=-1} = -1 \quad (4.14)$$

$$\xi|_{\gamma=1} = 1, \quad (4.15)$$

the constants  $a, b, c$  and  $d$  can be defined, as follows.

$$a = \frac{1}{Q} \quad (4.16)$$

$$b = \frac{-3\bar{\gamma}^2}{Q} \quad (4.17)$$

$$c = \frac{3\bar{\gamma}^2}{Q} \quad (4.18)$$

$$d = -b \quad (4.19)$$

where

$$Q = 1 + 3\bar{\gamma}^2. \quad (4.20)$$

The following relationship can be defined at the singular location.

$$\bar{\gamma} = \sqrt[3]{\bar{\xi}\xi^* + |\xi^*|} + \sqrt[3]{\bar{\xi}\xi^* + |\xi^*|} + \bar{\xi}, \quad (4.21)$$

where

$$\xi^* = \xi^2 - 1. \quad (4.22)$$

The result of this transformation is a new integral form,

$$\int_{-1}^1 f(\xi(\gamma)) \frac{d\xi}{d\gamma} d\gamma. \quad (4.23)$$

with a Jacobian, defined by

$$\frac{d\xi}{d\gamma} = \frac{3(\gamma - \bar{\gamma})^2}{1 + 3\bar{\gamma}^2}. \quad (4.24)$$

Due to (4.12) and (4.13) as  $\xi \rightarrow \bar{\xi}$  the Jacobian  $\frac{d\xi}{d\gamma} \rightarrow 0$ , which has a smoothing effect on the overall behaviour of the integrand. The result is an integral that can be evaluated using standard Gauss quadrature, because the integrand in (4.24) becomes regular since the Jacobian has cancelled the singularity. The third integral (4.8) is included for completeness, however, because (4.8) does not contain basis functions, it is not discussed further in this thesis. Though, naturally, (4.8) is integrated in the same way as (4.7).

### 4.3 PUBEM integrals

The focus of this section will be the evaluation of the highly oscillatory PUBEM integrals using approaches from the field of asymptotic analysis. Before these approaches are presented, some numerical aspects relating to Gauss quadrature and singular integration are discussed.

The PUBEM integrals mirror (4.6) and (4.7) but with the inclusion of plane-waves, as follows:

$$\int_{-1}^1 \frac{\partial G(\mathbf{p}, \mathbf{q})}{\partial \mathbf{n}} \Psi_j(\xi) e^{(ik\mathbf{d}\cdot\mathbf{q})} J^e d\xi, \quad (4.25)$$

and

$$\int_{-1}^1 G(\mathbf{p}, \mathbf{q}) \Psi_j(\xi) e^{(ik\mathbf{d}\cdot\mathbf{q})} J^e d\xi. \quad (4.26)$$

In order to increase the number of degrees of freedom for a standard BEM scheme, the

number of elements  $E$  is increased, but if PUBEM is employed there is the option to increase the number of plane waves included per node  $M$ . As soon as  $M > 1$ , it becomes necessary to collocate at non-nodal locations. It is common to employ a relatively coarse discretisation [63, 64], using large elements, and increasing  $M$  to achieve greater accuracy per degree of freedom. This introduces extra requirements for the numerical solution, such as:

- 1 Sub-divided integration
- 2 Split Telles scheme

These requirements will be briefly discussed here, before moving on to the alternative integration schemes, but first a simple example is presented to highlight the difference between BEM and PUBEM integrals. Fig. 4.1 exemplifies BEM and PUBEM discretisation of a unit square scattering object wherein the BEM discretisation is shown with 10 elements per side and the PUBEM discretisation is shown with a single element per side. A typical 2D BEM discretisation, using quadratic elements would require 8-10 degrees of freedom per wavelength, i.e.  $\tau = 8-10$  which is usually achieved by selecting an appropriate number of elements, whereas a typical 2D PUBEM discretisation would require  $\tau \approx 2.5$ .

As  $k$  increases, the PUBEM elements shown in Fig. 4.1 could remain the same size, i.e.  $E$  does not change, but  $M$  increases; whereas, in the BEM discretisation the elements would need to reduce in size, to maintain an appropriate  $\tau$ . Fig. 4.2 shows BEM and PUBEM integrands associated with the same unit square example, wherein the bottom left hand corner of the square is located at  $(0, 0)$ ,  $k = 500$ , and the first element of the discretisation starts at  $(0, 0)$  and runs in the positive  $x$ -direction. The integrands from (4.6) and (4.25) for BEM and PUBEM, resulting from collocating at the top left corner  $(0, 1)$ , of the abovementioned square are plotted over their respective first elements, shown as  $T(\xi)$  in Fig. 4.2.

This comparison highlights the fact that a PUBEM element can include many wavelengths and thus require many Gauss integration points.

### 4.3.1 Sub-divided integration

In the interest of accurately populating the system matrices, it is necessary to accurately perform the integration, because even a basis capable of capturing the underlying wave behaviour, this is of little use if the integration scheme is inadequate. This requirement for accuracy is particularly important for ill-conditioned systems that would be more than usually prone to giving erroneous solutions if matrix terms are not carefully computed. For this reason, unless stated otherwise, PUBEM elements are sub-divided into  $n$  integration

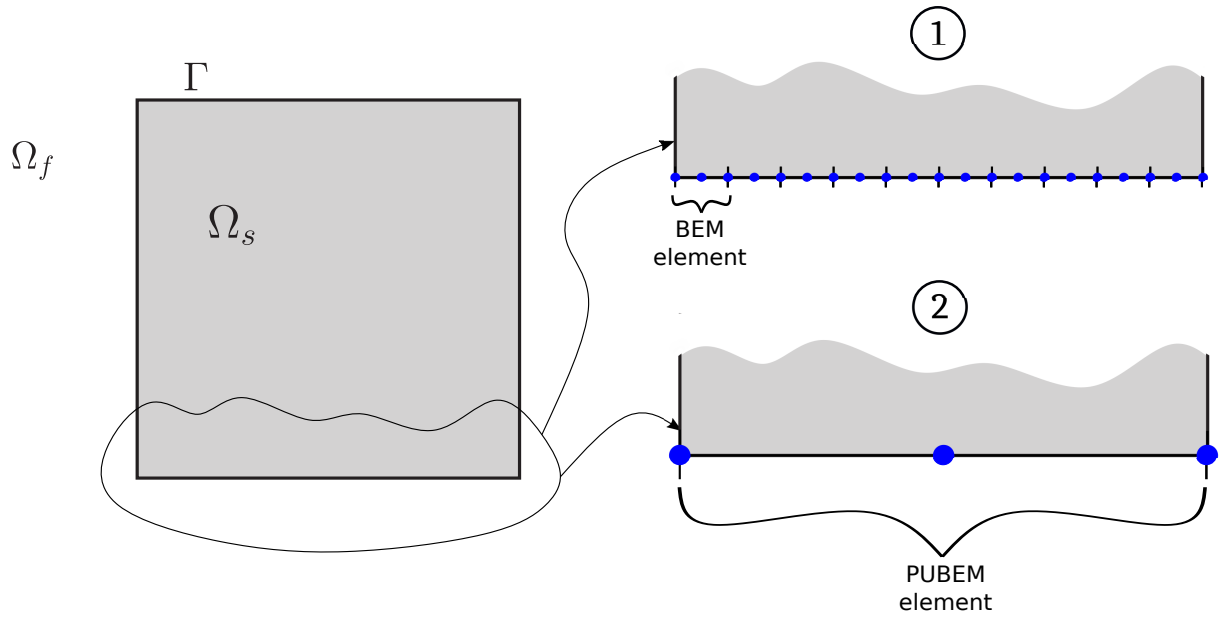


Figure 4.1: Example BEM discretisation (1) and PUBEM discretisation (2).

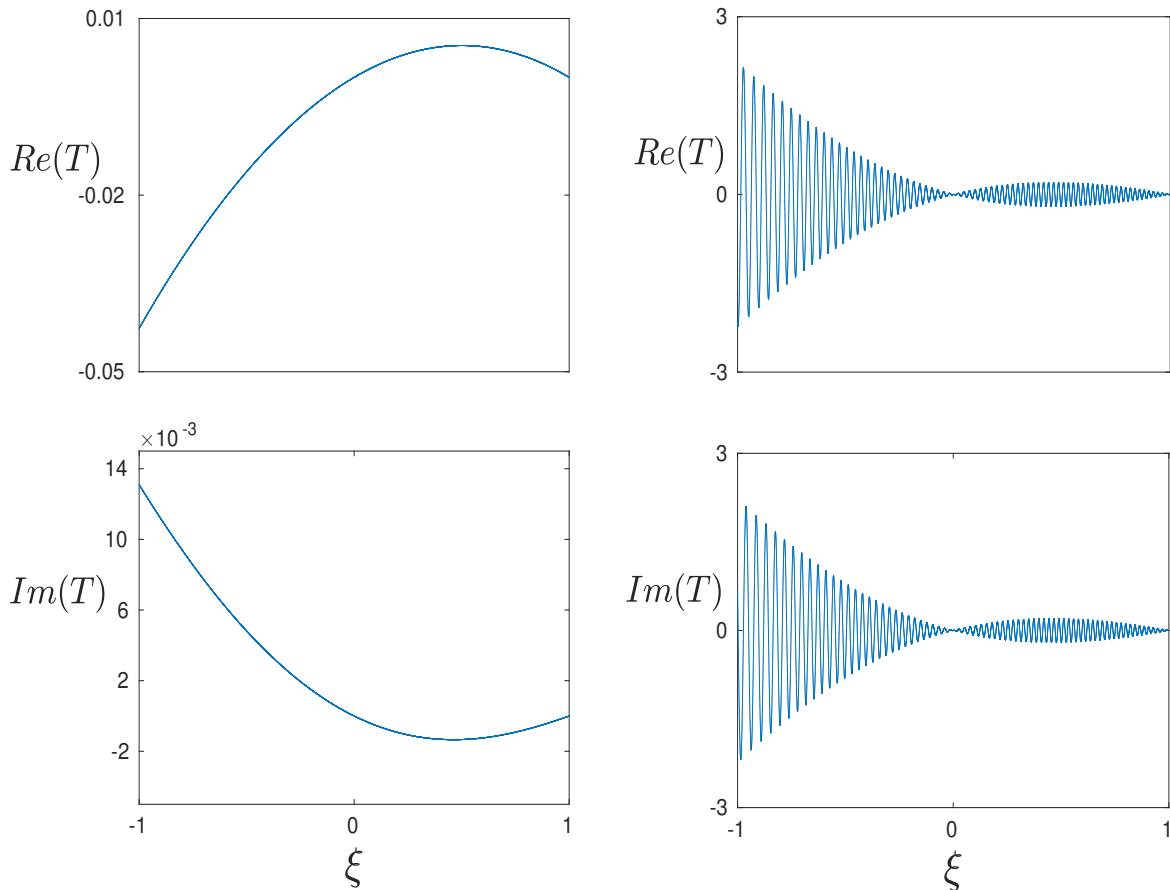


Figure 4.2: Comparison of the real and imaginary parts of a BEM integrand (left) and the real and imaginary parts of a PUBEM integrand (right). Both corresponding to the first element of the respective BEM and PUBEM discretisations of the unit square, both of which with a collocation point at  $(0, 1)$ ,  $k = 500$ .

cells, with Gauss-Legendre quadrature applied to each sub-division. This sub-division is a method of distributing integration points, and does not add further degrees of freedom to a system. To perform this sub-division over  $n$  cells, a coordinate transformation,

$$\int_{-1}^1 f(\xi) d\xi = \sum_{\hat{c}=1}^n \int_{-1}^1 f(\xi(\zeta_{\hat{c}})) \frac{d\xi}{d\zeta_{\hat{c}}} d\zeta_{\hat{c}} \quad (4.27)$$

is required, where  $\zeta$  is a parameter that varies across  $\lambda/4$ , i.e.  $\zeta \in [-1, 1]$  over an integration cell of length  $\lambda/4$ . shown in Fig. 4.3. This ensures that even for relatively large elements which include many wavelengths, it is still possible to integrate accurately by applying a fixed number of Gauss points per wavelength.

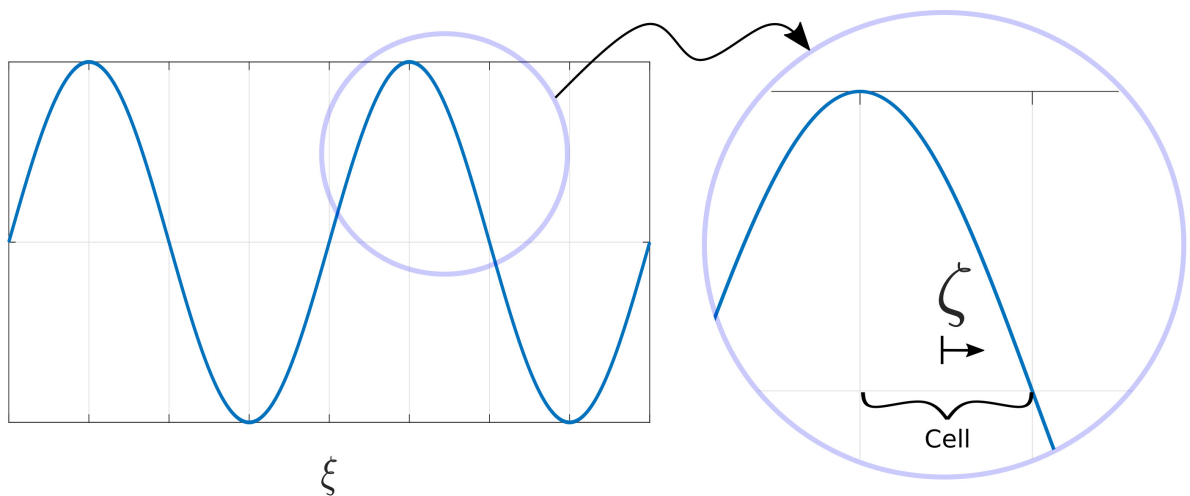


Figure 4.3: Wave sub-divided into integration cells of length  $\frac{\lambda}{4}$  using a coordinate change to  $\zeta$ .

### 4.3.2 Split Telles scheme

During the numerical experiments performed in this thesis, it was found that the standard Telles scheme was not converging for PUBEM integrals as readily as for BEM integrals. After some testing, it was found that the Telles scheme converges well for cases in which the singularity is located at  $\xi = -1, 0$  and  $\xi = 1$ , which correspond to the nodal locations of each quadratic element. Conveniently, for a standard BEM scheme, the collocation points usually share the same locations as the nodes. In PUBEM however, for  $J$  nodes per element and  $M$  plane waves per node, there are  $(J - 1)(M - 1)$  non-nodal collocation points. To evaluate these integrals, a split Telles scheme is employed which is found to converge well for all cases tested in this thesis. The scheme is implemented as follows.

The singular location is defined as  $\bar{\xi}$  and two portions, either side of the singularity, are defined as  $\eta_1 \in (-1, 1)$  and  $\eta_2 \in (-1, 1)$ . That is, by mapping  $\xi \in [-1, \bar{\xi}]$  to  $\eta_1$  and mapping  $\xi \in [\bar{\xi}, 1]$  to  $\eta_2$ . Taking the  $\eta_1$  as an example, for a straight line element, the

following parameterisation is used.

$$\xi = \frac{1}{2}[(1 + \bar{\xi})\eta_1 + \bar{\xi} - 1], \quad (4.28)$$

thus

$$\eta_1 = \frac{2\xi + 1 - \bar{\xi}}{1 + \bar{\xi}}. \quad (4.29)$$

$\eta_1$  is then equally split into  $N_1$  cells of length  $\lambda/4$ . A parameterisation  $\rho_1 \in (-1, 1)$  is applied across each cell, as follows.

$$\eta_1 = \frac{2j + \rho_1 - 1}{N_1} - 1, \quad (4.30)$$

thus

$$\rho_1 = N_1(1 + \eta_1) + 1 - 2j. \quad (4.31)$$

Finally, we apply a Telles scheme with the parameterisation  $\gamma_1 \in (-1, 1)$ , which requires a further coordinate transformation

$$\rho_1 = a\gamma_1^3 + b\gamma_1^2 + c\gamma_1 + d. \quad (4.32)$$

The same procedure is used for the  $\eta_2$  portion, but with the the variables  $\rho_2$  and  $\gamma_2$ . A given integral  $I$ , over a straight line element of length  $L$  would therefore be subject to the following process.

$$I = \int_{-1}^1 f(\eta_1) J_1 J_2 d\eta_1 + \int_{-1}^1 f(\eta_2) J_1 J_3 d\eta_2 \quad (4.33)$$

$$I = \sum_{j=1}^{N_1} \int_{-1}^1 f(\rho_1) J_1 J_2 J_4 d\rho_1 + \sum_{j=1}^{N_2} \int_{-1}^1 f(\rho_2) J_1 J_3 J_5 d\rho_2 \quad (4.34)$$

$$I = \sum_{j=1}^{N_1} \int_{-1}^1 f(\gamma_1) J_1 J_2 J_4 J_6 d\gamma_1 + \sum_{j=1}^{N_2} \int_{-1}^1 f(\gamma_2) J_1 J_3 J_5 J_7 d\gamma_2 \quad (4.35)$$

with the Jacobians defined as

$$J_1 = \frac{L}{2} \quad (4.36)$$

$$J_2 = \frac{1 + \bar{\xi}}{2} \quad (4.37)$$

$$J_3 = \frac{1 - \bar{\xi}}{2} \quad (4.38)$$

$$J_4 = \frac{1}{N_1} \quad (4.39)$$

$$J_5 = \frac{1}{N_2} \quad (4.40)$$

$$J_6 = \frac{3(\gamma_1 - \bar{\gamma}_1)^2}{1 + 3\bar{\gamma}_1^2} \quad (4.41)$$

$$J_7 = \frac{3(\gamma_2 - \bar{\gamma}_2)^2}{1 + 3\bar{\gamma}_2^2} \quad (4.42)$$

Resulting from this process are two Telles schemes, applied across sub-divided portions either side of the singularity, such that the singularity is always located at the end point of each scheme, thus allowing for greatly improved convergence. Note,  $J_1$  assumes a straight line element, an alternate Jacobian would likely be required for a general element.

## 4.4 Computation of error

In this chapter, and throughout this thesis, error is defined as  $\epsilon$ , which is taken to be relative error when analysing scalar results and  $L^2$  relative error when analysing a vector of results. The definition of  $\epsilon$  can be found in Appendix C.

### 4.4.1 Error in PUBEM integrals

Before presenting results, it is necessary to determine what level of accuracy is required from a PUBEM integration scheme, to compute acoustic potential to ‘engineering accuracy’ of 1%. Naturally, there is no true one-size-fits-all threshold that can be applied to every integral to be computed because the magnitude and profile of each integral required to form a PUBEM matrix can be unique. For example, relatively larger terms in the PUBEM matrix may have a larger contribution to resulting solution over the boundary. Nevertheless, in order to determine if the following integration schemes are candidates for computing PUBEM integrals, it is useful to know, generally, what level of accuracy is required in the integration scheme.

To estimate this threshold, a simple example of scattering by a unit circle being impinged by a plane-wave travelling in the positive  $x$ -direction is tested, with a relatively coarse discretisation (as is typical in PUBEM schemes) of 4 elements. When the PUBEM matrix, comprising the PUBEM integrals, is formed an artificial error is injected into each term. This error is a relative error of  $\pm 0.1\%$ ,  $1\%$ , or  $2\%$  wherein the polarity is

randomised. Firstly, a fixed frequency of  $k = 25$  is analysed, for a range of degrees of freedom per wavelength  $\tau$ ; secondly, a fixed number of degrees of freedom per wavelength is used ( $\tau \approx 5$ ) and the wavenumber  $k$  is varied, both sets of results can be seen in Fig. 4.4.

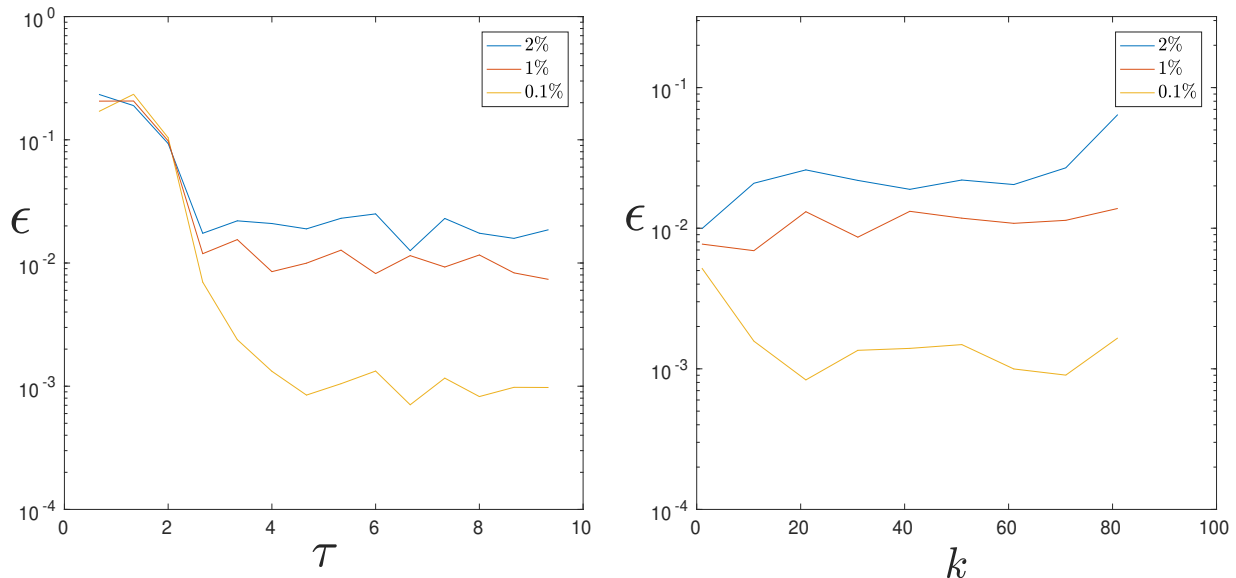


Figure 4.4: (left)  $L^2$  relative error  $\epsilon$  (in  $\phi$  over  $\Gamma$ ) vs.  $\tau$  for three test cases having  $\pm 0.1\%$ ,  $1\%$ , or  $2\%$  injected into the integrals;  $k = 25$ . (right)  $L^2$  relative error  $\epsilon$  (in  $\phi$  over  $\Gamma$ ) vs.  $k$  for three test cases having  $\pm 0.1\%$ ,  $1\%$ , or  $2\%$  injected into the integrals;  $\tau \approx 5$ . Notably, as can be seen

From Fig. 4.4, it can be seen that injecting a relative error of  $2\%$  into each integral results in an unacceptable level of error in the acoustic potential  $\phi$  computed over the boundary  $\Gamma$ . Notably, from the right hand side plot in Fig. 4.4,  $\epsilon$  appears to increase, slightly, as  $k$  increases, for fixed  $\tau$ . This is likely due to the combination of the injected error and the error associated with the choice of  $\tau$  becoming larger as  $k$  increases and  $\tau$  becomes insufficient. In contrast, from the left hand side plot in Fig. 4.4, increasing  $\tau$  does not seem to impact  $\epsilon$ . This is likely because, in this example, the injected error is the main source of error that is limiting the accuracy of the solution. Further, from Fig. 4.4 it can be seen that it may be possible in some cases to accept  $1\%$  error in the integrals and still achieve sub- $1\%$  error in the overall solution, though, not consistently. Finally, the integration error of  $0.1\%$  is shown to consistently result in an overall solution which is within the engineering accuracy range. For this reason, in the remainder of Section 4, integration error above  $1\%$  is presumed to be unacceptable.

## 4.5 Integration schemes for highly oscillatory integrals

As can be seen in Fig. 4.2 the plane-wave enrichment substantially impacts the integrand, and can result in a highly-oscillatory integrand, thus it is worth exploring an alternative to Gauss-Legendre for the PUBEM integrals. There exist a number of alternative integration approaches with the aim of evaluating highly oscillatory integrals, but to the authors' knowledge they are yet to be extended to PUBEM integrals (with the exception of Numerical Steepest Descent). A brief overview of some relevant methods is given here, before providing further depth and testing each method individually. The focus of much of the recent work in this field, and this thesis are Fourier-type integrals, given by

$$I = \int_a^b f(\xi)e^{ikg(\xi)}d\xi \quad (4.43)$$

where  $g(\xi)$  is the phase function,  $f(\xi)$  is slowly varying and smooth, and  $k$  is large. In much of the literature the frequency  $\omega$  is used in place of  $k$ , but they increase and decrease in tandem, so  $k$  can be treated the same way.

Perhaps the simplest of all of the approaches is the Asymptotic Method [70], which is achieved via repeated integration by parts. The literature states that this method is simple, but crude and only converges for very high frequency. The method of stationary phase [74] considers the leading contribution of the integral to be located in a window surrounding each of the stationary points in the oscillating function. Another alternative is the method of steepest descent also in [74], where the path of integration is deformed into the complex plane, removing the oscillatory behaviour from the kernel. This is developed further as the numerical steepest descent which applies quadrature methods to the integrals arising from the method of steepest descent. This was explored for PUBEM integrals in [68], with positive results for isolated examples, however, consistently determining the path of steepest descent in the presence of stationary points is challenging, and algorithms have not been developed to identify and accommodate singularities in the integrand in the complex plane. This prevents numerical steepest descent from becoming a robust alternative to Gauss-Legendre. Another class of alternatives are Levin-type methods [75] wherein the integrand is reformulated in terms of derivatives, and the result is approximated. Finally, there are the Filon-type methods, which approximate the slowly varying function  $f(\xi)$  with a suitable polynomial function allowing the evaluation of the resulting moments analytically.

### 4.5.1 PUBEM integral

The candidate integrals (4.25) that are tested in this chapter arise from (3.40), and are repeated here for convenience, in the general form

$$\int_a^b \frac{\partial G(p, q)}{\partial \mathbf{n}} \Psi_j e^{i\mathbf{k}\mathbf{d}\cdot\mathbf{q}} d\Gamma, \quad (4.44)$$

where the derivative of the Green's function is defined in (2.12), and the exponential term is a plane wave, with direction vector  $\mathbf{d}$ . At this point we note that the  $\alpha$  and  $\beta$  terms of (3.40), are also highly oscillatory but we focus on (4.44) because it appears in all PUBEM simulations, regardless of BCs applied. The cases with singularities are also important, but the regular integrals account for a large majority of the CPU time taken for an analysis and are therefore the focus of this work.

We begin by inserting the definition for the derivative of the Green's function, and the parameterisation into  $\xi$ , to produce

$$I = -\frac{ik}{4} \int_{-1}^1 H_1^{(1)}(kr) \Psi_j(\xi) e^{i\mathbf{k}\mathbf{d}_{jm}\cdot\mathbf{q}} \bar{J} \frac{\partial r}{\partial n} d\xi \quad (4.45)$$

where  $\bar{J}$  is the Jacobian associated with transforming into  $\xi$ . In order to manipulate (4.45) into a form similar to (4.43) we must approximate the Hankel function with its asymptotic expansion for a large argument [77] which is given by

$$H_v(kr) \approx \left( \frac{2}{\pi kr} \right)^{\frac{1}{2}} e^{i(kr - \frac{1}{2}v\pi - \frac{1}{4}\pi)} \sum_{s=0}^{\infty} i^s \frac{a_s(v)}{(kr)^s}, \quad (4.46)$$

with

$$a_s = \frac{(4v^2 - 1^2)(4v^2 - 3^2)\dots(4v^2 - (2s - 1)^2)}{s!8^s}, \quad a_0(v) = 1. \quad (4.47)$$

This approximation is sufficiently accurate, for the intended use of the current work as the majority of cases will contain a large argument. Even in cases where the argument is reduced (when  $r$  is small) the approximation error remains reasonable. This is highlighted in Fig. 4.5, where relative error  $\epsilon$  of the approximation of the Hankel function, using only the first two terms in the series, is plotted against  $k$  and  $r$ . Inserting (4.46) into (4.45) produces

$$I \approx -\frac{i}{4} \left( \frac{2}{\pi} \right)^{\frac{1}{2}} e^{-\frac{3i\pi}{4}} \bar{J} \sum_{s=0}^S i^s \frac{a_s(1)}{k^{s-\frac{1}{2}}} \int_{-1}^1 f(\xi, s) e^{ikg(\xi)} d\xi, \quad (4.48)$$

Now we have our PUBEM integral in a form (4.48), which is appropriate for highly oscillatory integration techniques. Notably,  $f(\xi, s)$  and  $g(\xi)$  will differ depending on the definition of each element, thus will be produced later in this section, before each example,

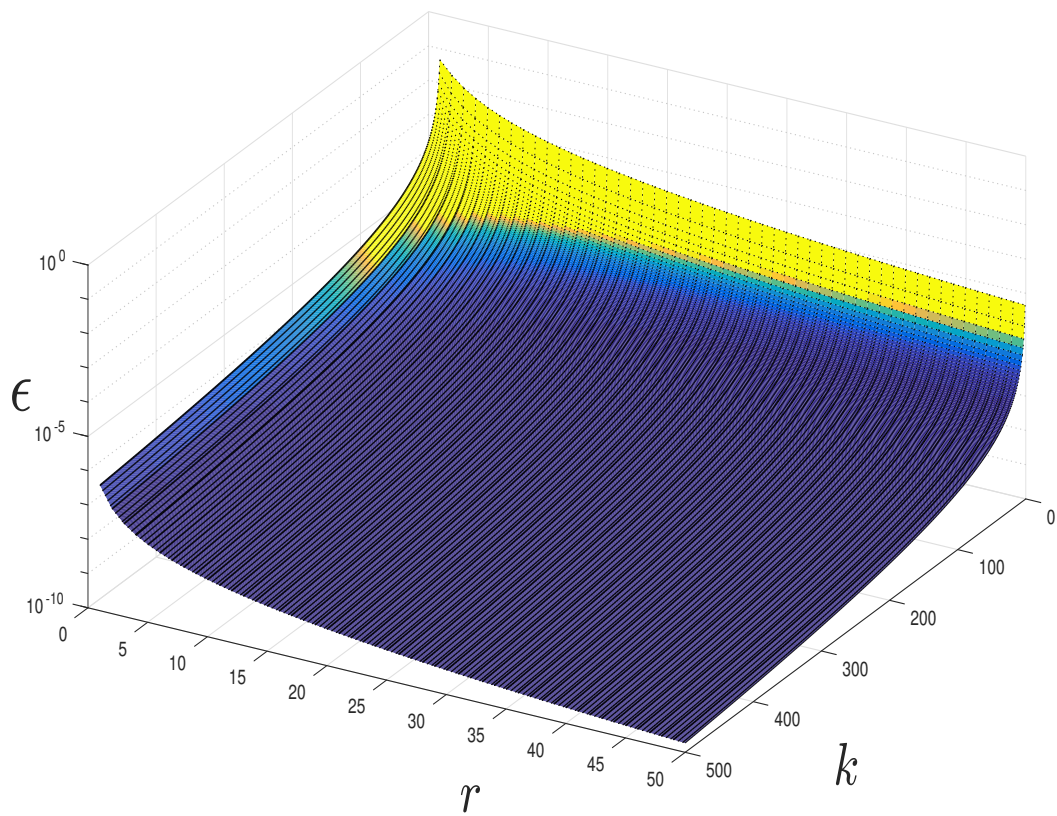


Figure 4.5: Error in the asymptotic approximation of  $H_1^{(1)}(kr)$ , using (4.46) with only the first two terms in the series, for small  $k$  and  $r$ , wherein  $k$  is the wavenumber and  $r$  is distance from the Hankel source point.

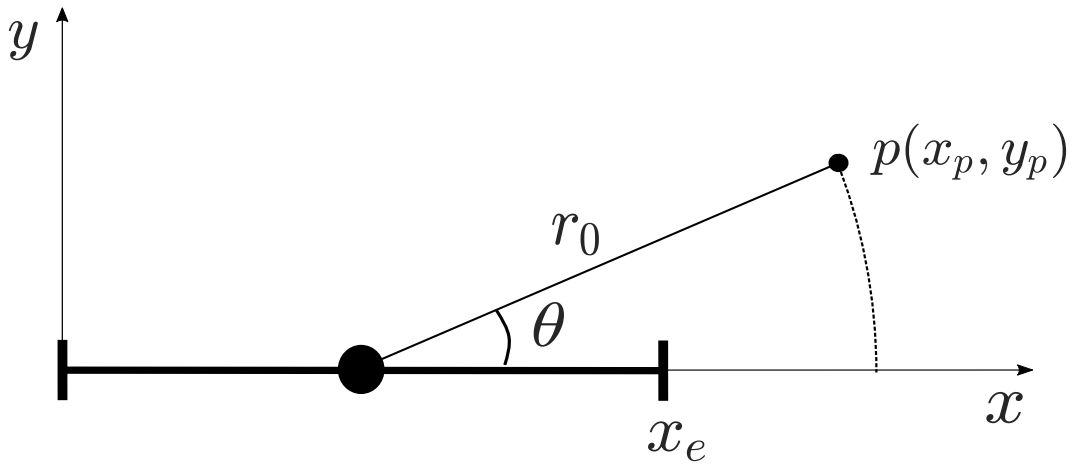


Figure 4.6: Variables used to define source point location.

and the Jacobian  $\bar{J}$  is assumed to be constant (appropriate for straight line elements and circular arc elements but not necessarily a general element). Before producing the numerical test results, a brief introduction to stationary points is required.

For the examples studied in this thesis  $g(\xi)$  is always monotonically increasing, or decreasing, either side of a ‘stationary point’. At such stationary points the derivative  $g'(\xi) \rightarrow 0$  and the behaviour of the integrand becomes non-oscillatory. These stationary points can cause additional difficulty for highly oscillatory integration schemes, as by definition they are not intended to evaluate non-oscillatory functions. This phenomenon will be discussed in detail later in the chapter, but for now a simple example is presented to highlight the impact that a stationary point has on the integrand.

Consider a flat element shown in Fig. 4.6, with  $x_e = 4$ . The integrand for two cases is plotted in Fig. 4.7, both having the same enrichment wave direction  $\bar{\phi}$  and the same wavenumber  $k = 100$ , but with different source point locations. Clearly the results differ significantly. Correspondingly, the following work will be split into two sections:

- Cases in the absence of stationary points
- Stationary point cases

The experimentation conducted in this chapter is performed on flat, straight line elements and circular arc elements.

## 4.5.2 In the absence of stationary points

### Straight line case

**Asymptotic method** The asymptotic method relies upon reformulating an integral, to produce:

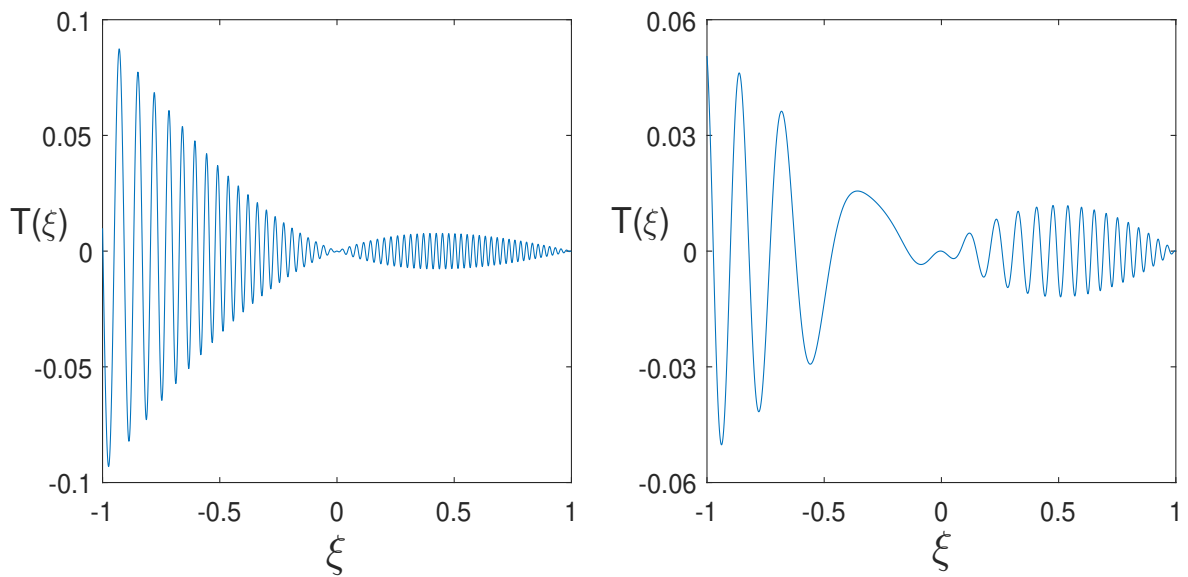


Figure 4.7: (left) Integrand in the absence of stationary points with  $k = 100$ ,  $\phi = 60^\circ$ ,  $x_p = 0.5$ ,  $y_p = 2.5$ . (right) Integrand containing a stationary point with  $k = 100$ ,  $\phi = 60^\circ$ ,  $x_p = 3$ ,  $y_p = 3$ .

$$I = \int_a^b f(\xi) e^{ikg(\xi)} d\xi = \frac{1}{ik} \int_a^b \frac{f(\xi)}{g'(\xi)} \frac{d}{d\xi} e^{ikg(\xi)} d\xi \quad (4.49)$$

and performing integration by parts on the result, as follows.

$$I = \frac{1}{ik} \left[ \frac{f(b)}{g'(b)} e^{ikg(b)} - \frac{f(a)}{g'(a)} e^{ikg(a)} \right] - \frac{1}{ik} \int_a^b \frac{d}{d\xi} \left[ \frac{f(\xi)}{g'(\xi)} \right] e^{ikg(\xi)} d\xi \quad (4.50)$$

where the final term can be thought of as the error incurred by only including information from the end points of the interval. This term, however, is also an oscillatory integral, on which we can repeat the integration by parts procedure; this may be repeated to an arbitrarily high order, resulting in the following expression

$$I_A = - \sum_s^S \sum_{v=1}^V \frac{1}{(-ik)^v} \left[ \frac{e^{ikg(b)}}{g'(b)} \sigma_{v-1}[f](b) - \frac{e^{ikg(a)}}{g'(a)} \sigma_{v-1}[f](a) \right] \quad (4.51)$$

in which

$$\sigma_0[f](\xi, s) = f(\xi, s), \quad (4.52)$$

$$\sigma_{v+1}[f](\xi, s) = \frac{d}{d\xi} \frac{\sigma_v[f](\xi, s)}{g'(\xi)}. \quad (4.53)$$

If we consider the PUBEM integral of (4.48), then it can be shown that

$$f(\xi, s) = \frac{\Psi_j(\xi)(y_q - y_p)}{r^{s+\frac{3}{2}}} \quad (4.54)$$

and

$$g(\xi) = r + \mathbf{d} \cdot \mathbf{q}(\xi) = \sqrt{(x_m(1 + \xi) - x_p)^2 + y_p^2} + x_m(1 + \xi) \cos(\bar{\phi}). \quad (4.55)$$

wherein  $\xi$  is the parametric variable that is used to describe the variation over each element and  $s$  refers to the index in the series form of the asymptotic approximation of the Hankel function.

**Filon method** In this section, the Filon method is outlined and implemented for a straight line element, in the absence of stationary points. The origin of the Filon method [76] dates back to 1928, but is greatly elaborated on by Iserles in [71] and [72], in which the ideas of Filon are extended to integrals of the form

$$I = \int_a^b f(\xi) e^{ikg(\xi)} d\xi, \quad (4.56)$$

where  $f(\xi)$  and  $g(\xi)$  are ‘smooth’ functions. For the PUBEM examples presented in this thesis there will also be the  $s$ -dependence from (4.48), i.e.  $f(\xi, s)$  and  $g(\xi, s)$ . There are a variety of Filon-type methods which have been derived from the original, but the premise remains the same in each;  $f(\xi)$  is approximated by a polynomial and the oscillatory kernel is multiplied by the coefficients of that polynomial. This means that the resulting integral may be evaluated analytically, by parts. The main difference between approaches under the umbrella term of Filon-type methods lies in the construction of the interpolating polynomial. A versatile method is that of the Filon-Clenshaw-Curtis Method (FCC) [73] where polynomial weights are pre-computed using the Fast Fourier Transform and the function is sampled at the classic Chebyshev locations. A benefit of this method is that no derivative information is required and the pre-computed weights allow applicability to a variety of problems without the requirement of reformulating and solving a new matrix.

The method chosen for this section is that of Iserles [69] is, where  $f(\xi, s)$  is sampled only at the end points of the interval. The degree of approximating polynomial is increased by providing derivative information rather than adding extra nodes as in the FCC method. An advantage of this method of construction is that it targets the end points which are the key locations in evaluating highly oscillatory integrals.

In order to use the Filon method, the coordinate in which oscillation takes place needs to be the same as the coordinate of integration, so we undertake a coordinate transformation of the integral (4.48) to integrate with respect to produce the following.

$$I_2 = \int_{g(a)}^{g(b)} f_2(g, s) e^{ikg} dg \quad (4.57)$$

where

$$f_2(g, s) = f(\xi, s) \frac{d\xi}{dg}. \quad (4.58)$$

which is approximated, resulting in the following.

$$I_2 \approx \int_{g(a)}^{g(b)} H_{s,m}(g) e^{ikg} dg. \quad (4.59)$$

where the approximating Hermite polynomial  $H_{s,m}$  of degree  $M$  is equal to

$$H_{s,m}(g) = h_{s,0} + h_{s,1}g + h_{s,2}g^2 + \dots + h_{s,M}g^M \approx f_s(\xi(g), s) \frac{d\xi}{dg} =: f_2(g, s). \quad (4.60)$$

For example a 3rd degree polynomial would be subject to the following interpolation

conditions:

$$H_{s,m}(a) = f_2(a, s) \quad (4.61)$$

$$H_{s,m}(b) = f_2(b, s) \quad (4.62)$$

$$H'_{s,m}(a) = f'_2(a, s) \quad (4.63)$$

$$H'_{s,m}(b) = f'_2(b, s). \quad (4.64)$$

For a general  $M$  the result is the following.

$$I \approx \sum_{s=0}^S \sum_{m=0}^M h_{s,m} \int_{g(a)}^{g(b)} g^m e^{ikg} dg. \quad (4.65)$$

The integrals in (4.65) are referred to as ‘Filon moments’, wherein the  $m_{th}$  Filon moment is defined as follows.

$$\mu_m = \int_{g(a)}^{g(b)} g^m e^{ikg} dg \quad (4.66)$$

which, for a general case, can be integrated analytically by parts

$$\mu_m = \sum_{m=0}^M -\binom{i}{k}^{M+1-m} \frac{m!}{M!} \left( g(b)^M e^{ikg(b)} - g(a)^M e^{ikg(a)} \right) \quad (4.67)$$

Thus, we require only the solution of a small system of equations to determine the Hermite coefficients  $h_{s,m}$  and compute the Filon moments for each value of  $s$ . The mapping  $\xi \rightarrow g$  can be evaluated analytically, using the following.

$$\xi = \frac{x_p - d_x g + \sqrt{g^2 + c_0 g + c_1}}{c_2} - 1 \quad (4.68)$$

$$\frac{d\xi}{dg} = \frac{1}{c_2} \left( -d_x + \frac{2g + c_0}{2\sqrt{g^2 + c_0 g + c_1}} \right) \quad (4.69)$$

$$\frac{d^2\xi}{dg^2} = \frac{1}{c_2 \sqrt{g^2 + c_0 g + c_1}} \left( 1 - \frac{(2g + c_0)^2}{4(g^2 + c_0 g + c_1)} \right) \quad (4.70)$$

$$c_0 = -2x_p d_x \quad (4.71)$$

$$c_1 = d_x^2 (x_p^2 + y_p^2) - y_2^2 \quad (4.72)$$

$$c_2 = x_m (1 - d_x^2) \quad (4.73)$$

The square root term in (4.68) - (4.73) is taken to be positive when  $dg/d\xi > 0$  and negative when  $dg/d\xi < 0$ . It is also worth noting that when  $d_x = \pm 1$ ,  $\xi \rightarrow \infty$  and the coordinate transformation needs to be replaced by

$$\xi = \frac{g^2 - x_p^2 - y_p^2}{2x_m(gd_x - x_p)} - 1 \quad (4.74)$$

$$\frac{d\xi}{dg} = \frac{d_x(g^2 - x_p^2 - y_p^2) - 2gx_p}{2x_m(gd_x - x_p)} \quad (4.75)$$

**Comparison** Take the case where  $x_e = 4$ ,  $\bar{\phi} = \frac{\pi}{3}$ ,  $x_p = -3$  and  $y_p = -3$ , with a quadratic, Langrangian basis and taking the  $N_1$  function. This is an example in which the integrand is oscillatory and does not contain a stationary point within the interval of integration, thus both the Asymptotic method and the Filon method perform well. The two are compared in Fig. 4.8, wherein  $k = 1-1000$ . For the Asymptotic method results, we take  $V = 1$  and  $V = 2$ , with the latter significantly outperforming the former; reducing the error by approximately 4 orders of magnitude. For the Filon method we compare a scheme which includes only the first derivative to define the Hermite polynomial, and a second scheme in which the second derivative is included. We notice a slight increase in performance when compared with the Asymptotic method, with the results following a similar, but shifted path.

Ultimately, the intention of employing highly oscillatory integration schemes is to reduce the run-time of PUBEM simulations. For this reason, it is beneficial to compare the resulting solution times with those of Gauss-Legendre. This comparison is shown for discrete examples of  $k$  in Table 4.1, with just the first derivative taken for the Filon Method and,  $V = 1$  for the Asymptotic method. In addition, Table 4.1 includes the timings for integration performed using the trapezium method, for an extra level of comparison. The highly-oscillatory schemes are faster than Gauss-Legendre for the frequencies shown and the solution time does not increase as a function of  $k$ , which is an important characteristic that is not shared by traditional quadrature schemes. Notably, as the frequency increases it is clear that the accuracy increases, due to the assumption that wave cancellation occurs within the interval of integration becoming more valid as more wavelengths are included within the interval of integration. This benefit is not present in the Gauss-Legendre results, and it is observable that the results remain relatively consistent due to the fact there are a fixed number of Gauss points applied per quarter wavelength.

Further, in the formulations of the Asymptotic method and the Filon method, in (4.50) and (4.59),  $k$  can be isolated. Therefore, once an integral has been evaluated, for a single  $k$ , using the Filon method or the asymptotic method it is possible to evaluate the same integral, but with different  $k$ , with very little computational expense. This can allow

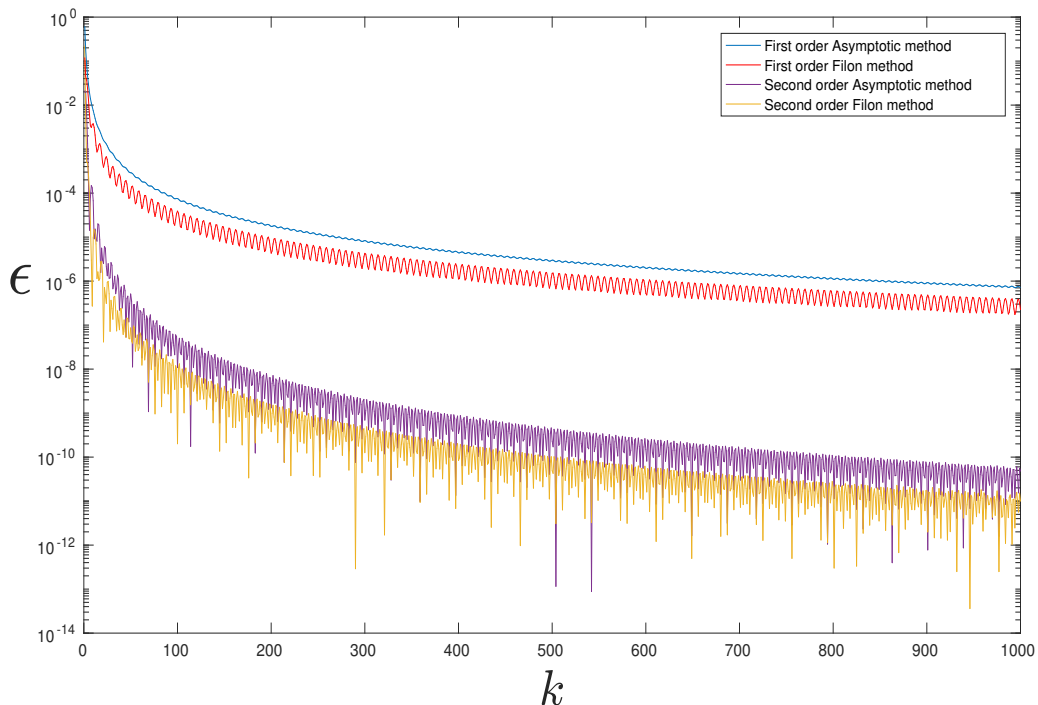


Figure 4.8: Relative error for a non-stationary case using the Asymptotic method with the 1st derivative (blue) and with the 2nd derivative (red).

accurate evaluation of ranges of integrals, provided there are no stationary points present within the interval of integration and the bottom end of the  $k$  range is still sufficiently high. Table 4.2 shows results for the same integrals as Table 4.1, but for ranges of  $k$ .

Whilst these results are very promising, this is a successful example in which the highly oscillatory integration schemes perform particularly well. Less successful cases will be presented and discussed later in this chapter. In addition, the frequencies tested are high, and it is clear that for this example Gauss-Legendre is competitive time-wise for  $k < 500$ , even though this example is cherry-picked to display the efficacy of Filon and the Asymptotic method.

$k$	Filon		Gauss		Trapezium	
	time	$\epsilon$	time	$\epsilon$	time	$\epsilon$
500	0.032	$1.506e - 06$	0.051	$1.07e - 07$	0.733	$1.04e - 07$
1000	0.035	$9.42e - 08$	0.079	$1.08e - 07$	1.412	$1.18e - 06$
2000	0.034	$2.33e - 08$	0.138	$1.07e - 07$	2.787	$1.72e - 06$
10000	0.033	$1.41e - 09$	0.594	$1.07e - 07$	13.792	$2.15e - 06$

Table 4.1: Solution time in seconds and relative error  $\epsilon$ .

	Gauss		Filon		Asymptotic	
$k$	time	$\epsilon$	time	$\epsilon$	time	$\epsilon$
500-1500	17.5	$1.42e-07$	0.23	$6.63e-07$	0.032	$7.83e-07$
1500-2500	32.9	$1.36e-07$	0.24	$9.42e-08$	0.031	$1.14e-07$
2500-3500	49.7	$1.65e-07$	0.22	$2.03e-08$	0.031	$3.81e-08$

Table 4.2: Time taken in seconds to evaluate varying ranges of integrals along with average relative error  $\epsilon$ .

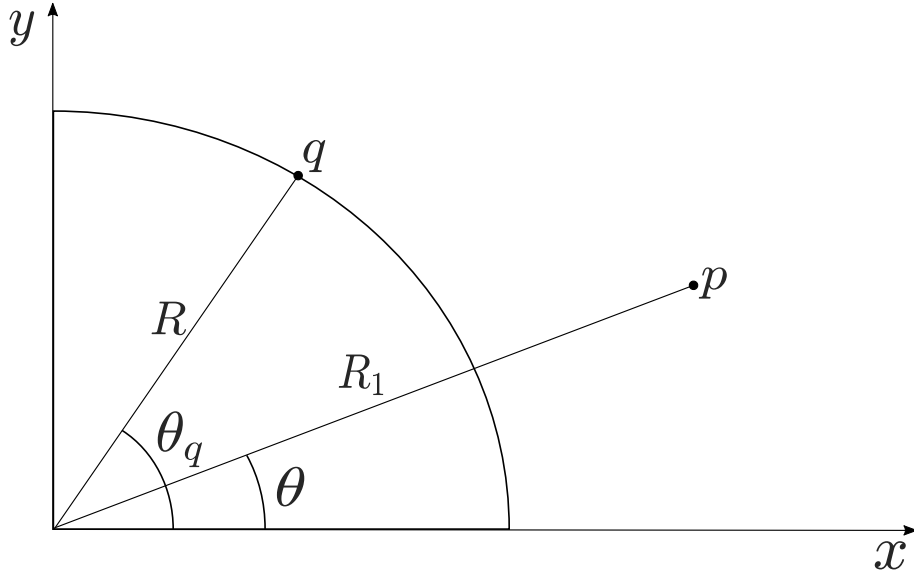


Figure 4.9: Location of source point  $p$  and field point  $q$  relative to the circular arc element (of radius  $R$  and spanning between the  $x$  and  $y$  axes) which can be thought of as forming one quarter of a unit circle scattering object.

### Circular arc case

The previous integrals were all evaluated over straight line elements, with substantial accuracy in the absence of stationary points. It is possible to extend the asymptotic method formulation to circular arc elements, which is detailed in the following. Consider an element spanning from the  $x$ -axis to the  $y$ -axis ( $\frac{\pi}{2}$  rads), as can be seen in Fig. 4.9. The arc element can be thought of as forming part of a unit circle scattering object. The source point (at this stage), may or may not be located on the circle traced by the radius of the given arc. Thus, the source point  $p$  and field point  $q$  are defined as follows

$$p = (R_1 \cos \theta, R_1 \sin \theta), \quad (4.76)$$

$$q = (R \cos \theta_q, R \sin \theta_q). \quad (4.77)$$

In order to use the definition in terms of the angle  $\theta_q$  as opposed to the variable  $\xi$  the mapping must be

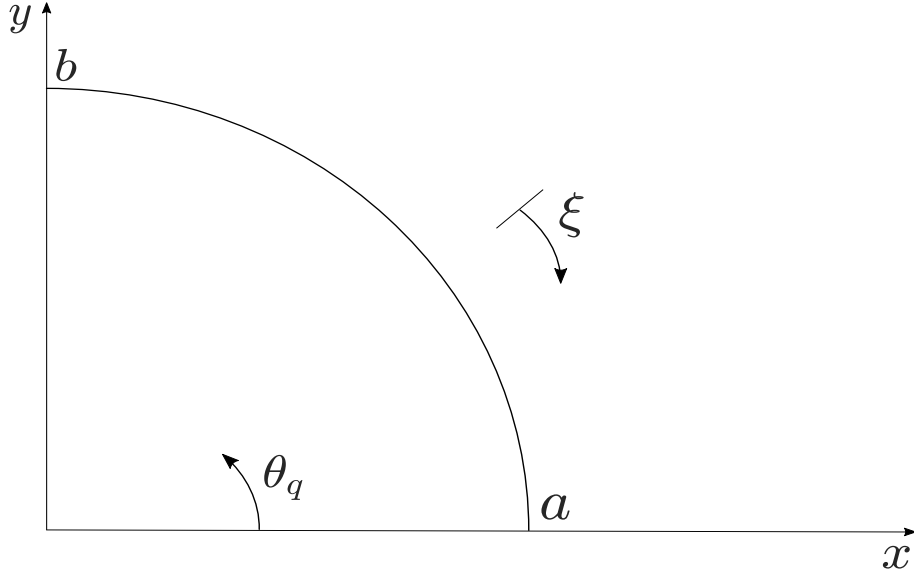


Figure 4.10: Mapping of  $\theta_q \mapsto \xi$  for the circular arc element spanning between the  $x$  and  $y$  axes which can be thought of as forming one quarter of a unit circle scattering object.

$$\theta_q = \frac{b+a}{2} - \frac{b-a}{2}\xi, \quad (4.78)$$

thus, the following can now be defined

$$\xi = \frac{b+a}{b-a} - \frac{2\theta_q}{b-a}, \quad (4.79)$$

where  $b = \frac{\pi}{2}$  and  $a = 0$  as shown in Fig. 4.10.

$$r = \sqrt{(R \cos(\theta_q) - R_1 \cos(\theta))^2 + (R \sin(\theta_q) - R_1 \sin(\theta))^2}, \quad (4.80)$$

$$\frac{\partial r}{\partial n(q)} = \frac{r_x}{r} n_x + \frac{r_y}{r} n_y, \quad (4.81)$$

in which  $n_x = -\cos(\theta_q)$ ,  $n_y = -\sin(\theta_q)$ ,  $r_x = x_q - x_p$  and  $r_y = y_q - y_p$ . This results in

$$\frac{\partial r}{\partial n(q)} = \frac{(R \cos \theta_q - R_1 \cos \theta)(-\cos \theta_q)}{r(\theta_q)} + \frac{(R \sin \theta_q - R_1 \sin \theta)(-\sin \theta_q)}{r(\theta_q)} \quad (4.82)$$

$$= \frac{1}{r(\theta_q)} (R_1 \cos(\theta - \theta_q) - R) \quad (4.83)$$

The plane wave can be defined in terms of the angle  $\phi$  as follows

$$\mathbf{d} = (d_x, d_y) = (\cos \bar{\phi}, \sin \bar{\phi}), \quad (4.84)$$

and therefore

$$g(\theta_q) = r + d_x R \cos \theta_q + d_y R \sin \theta_q. \quad (4.85)$$

The integral with the asymptotic approximation of the Hankel function included is presented again here, as follows

$$I = \frac{-iJ}{4} \left( \frac{2}{\pi} \right)^{\frac{1}{2}} e^{-\frac{3}{4}\pi i} \sum_{s=0}^{\infty} \frac{i^s a_s(1)}{k^{s-\frac{1}{2}}} \int_{-1}^1 f_2(\xi, s) e^{ikg(\theta_q)} d\xi, \quad (4.86)$$

where  $J$  can be treated as a constant because the element is a circular arc element. By converting back to  $\theta_q$  then we arrive at the following

$$I = \frac{-iJ}{4} \left( \frac{2}{\pi} \right)^{\frac{1}{2}} e^{-\frac{3}{4}\pi i} \sum_{s=0}^{\infty} \frac{i^s a_s(1)}{k^{s-\frac{1}{2}}} \int_a^b f_2(\theta_q, s) e^{ikg(\theta_q)} d\theta_q, \quad (4.87)$$

where

$$f_2(\theta_q, s) = \frac{N_j(\theta_q)(R_1 \cos(\theta - \theta_q) - R)}{(r(\theta_q))^{s+\frac{3}{2}}}, \quad (4.88)$$

and  $\theta_q$  is defined as in (4.79). As differentiation with respect to  $\theta_q$  is required the following definition is employed,

$$N_j(\theta_q) = N_j(\xi(\theta_q)) = N_j \left( \frac{-2\theta_q}{b-a} + \frac{b+a}{b-a} \right). \quad (4.89)$$

To demonstrate ability of the asymptotic method in this setting, we may use the asymptotic method with only a single derivative taken at the end points, to evaluate a typical integral that would arise when considering a unit circle being impinged by a plane-wave; the following parameters are used:  $R_1 = 1, R = 1, \theta = 3\pi/2, \phi = \pi, x_p = R_1 \cos \theta$  and  $y_p = R_1 \sin \theta$ . For  $k = 500$ , a relative error  $\epsilon = 1.46e - 05$  is produced. This is comparable with the level of accuracy obtained when using the asymptotic method for the straight line case. Unfortunately, for a typical enrichment wave direction and source point pairing, there will be at least 1, but up to 3 stationary points. This means that the positive result shown here would only be possible for a handful of cases. The location and frequency of stationary points for this case will be discussed further in section 4.5.3.

### 4.5.3 Stationary point cases

If we now allow the phase function to include stationary points i.e. where  $g'(\xi) = 0$ , then the formulation of high order integration schemes must be altered. The asymptotic method and the Filon method presented, so far, make the assumption that the oscillatory nature of the integrand in the middle portion of the element will cause cancellation, rendering its contribution negligible. This is no longer the case when stationary points

are included.

In order to determine the location of stationary points, for a straight line case wherein the element is laying flat on the  $x$ -axis. One can use the definition of  $g(\xi)$  from (4.55):

$$g(\xi) = r + \mathbf{d} \cdot \mathbf{q}(\xi) = \sqrt{(x_m(1 + \xi) - x_p)^2 + y_p^2} + x_m(1 + \xi) \cos(\bar{\phi}), \quad (4.90)$$

where  $x_m$  is the mid-point of the element,  $x_p$  and  $y_p$  are the  $x$  and  $y$  coordinates of the source point and the  $x$  coordinate of the field point is represented by the parametric mapping  $x_m(1 + \xi)$ , the  $y$  coordinate of the field point is zero because the element is laying on the  $x$ -axis. One can set  $g'(\xi) = 0$ , to produce

$$g'(\xi) = \frac{x_m(x_m(1 + \xi) - x_p)}{\sqrt{(x_m(1 + \xi) - x_p)^2 + y_p^2}} + x_m \cos \bar{\phi} = 0, \quad (4.91)$$

which can be rearranged to

$$x_m(1 + \xi) - x_p = -r \cos \bar{\phi}, \quad (4.92)$$

because  $r = \sqrt{(x_m(1 + \xi) - x_p)^2 + y_p^2}$ . Due to the fact that this example is limited to a straight line element laying on the  $x$ -axis, (4.92) can be reformulated to provide the stationary point locations  $\xi^*$ , as follows.

$$\xi^* = \frac{x_p \pm |y_p \cot \bar{\phi}|}{x_m} - 1. \quad (4.93)$$

If we define a source point as in Fig. 4.6, set  $\bar{\phi} = \pi/2$ ,  $x_e = 4$  and vary  $\theta$  and  $r$  it is possible to identify source point locations that will produce a stationary point within the interval of integration; the results of which are shown in Fig. 4.11, with cases in which a stationary point will occur within the interval of integration shown in yellow and cases in which a stationary point will not occur within the interval of integration shown in blue. The results from Fig. 4.11 indicate that a substantial number cases are stationary, especially as the source point moves closer to the element over which the integral is to be evaluated. Notably, stationary points occur when  $\theta = \pm \bar{\phi}$ , which is displayed in Fig. 4.12. Either side of  $\xi^*$ , it can be shown that  $g(\xi)$  is either monotonically increasing or decreasing. This means that for the straight line case there can only be a single stationary point within the interval of integration.

### Filon method

Consider a flat element, lying on the  $x$ -axis, defined according to Fig. 4.6. From (4.93) we can locate stationary points upon this flat element  $\xi^* \in (-1, 1)$ . In order to evaluate a stationary point case using the Filon method, a singularity subtraction method is

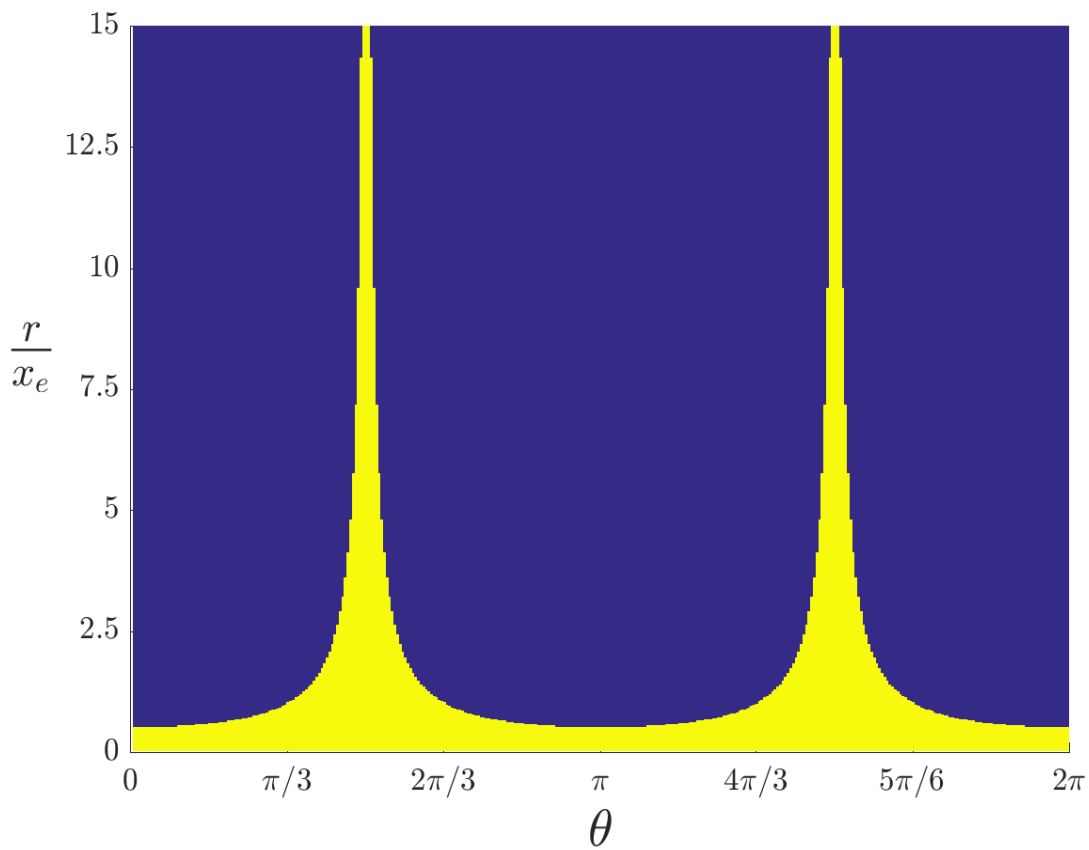


Figure 4.11: Source point locations which result in a stationary point within the interval of integration (yellow) and source point locations which result in a stationary point laying outside of the interval of integration (blue). Results are obtained by setting  $\bar{\phi} = \pi/2, x_e = 4$  and varying  $\theta$  and  $r$ .

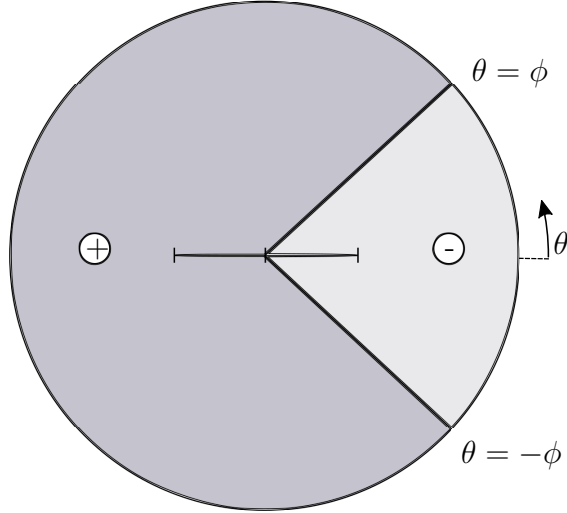


Figure 4.12: Polarity definition for  $g'(\xi)$  for an arbitrary fixed  $\phi$  and a flat straight line element, shown at  $\theta = \phi$  and  $\theta = -\phi$ . Positive and negative areas indicate the areas in which the  $g'(\xi)$  will be positive or negative respectively, thus,  $g'(\xi)$  behaves monotonically either side of a stationary point.

proposed. Filon scheme will then be applied to each side of the stationary point. For the stationary point case the interpolation conditions for the Hermite polynomial have an extra criterion, that we must include the stationary point as an interpolation point. Therefore the Hermite polynomial is defined as

$$H_{s,m}(\xi) = h_{s,0} + h_{s,1}\xi - \xi^* + h_{s,2}(\xi - \xi^*)^2 + \dots + h_{s,M}(\xi - \xi^*)^M \approx f_s(\xi, s) =: F_2(\xi, s). \quad (4.94)$$

If a 5th order Hermite polynomial is employed then the following interpolation conditions are required.

$$H_s(a) = F(a, s), \quad H'_s(a) = F'(a, s) \quad (4.95)$$

$$H_s(b) = F(b, s), \quad H'_s(b) = F'(b, s) \quad (4.96)$$

$$H_s(c) = F(c, s), \quad H'_s(c) = F'(c, s), \quad (4.97)$$

where  $a = -1$ ,  $b = \xi^*$  and  $c = 1$ . Note that in this case the polynomial approximation is made before any coordinate transformations have been performed because  $d\xi/dg$  is singular at the stationary point location. As the stationary point is subtracted, the Filon moments are shifted, to provide

$$\mu_l = \int_{-1}^1 (\xi - \xi^*)^l e^{ikg(\xi)} d\xi, \quad (4.98)$$

which is split into two intervals, either side of the stationary point. Thus each interval has a stationary point located at an end point. Thus, the overall result may be defined as the summation of the moments on either side as follows.

$$\mu_\ell = \left( \int_{-1}^{\xi^*} + \int_{\xi^*}^1 \right) (\xi - \xi^*)^\ell e^{ikg(\xi)} d\xi =: I_\alpha + I_\beta, \quad (4.99)$$

In order to compute the moments  $\mu_\ell$  a number of coordinate transformations are employed. Taking the  $I_\beta$  example and using an invertible mapping from  $\xi \mapsto g$  provides the following:

$$\int_{\xi^*}^1 (\xi - \xi^*)^\ell e^{ikg(\xi)} d\xi = \int_{g^*}^{g(1)} (g - g^*)^\ell \frac{dg}{dg} e^{ikg} dg \quad (4.100)$$

After some rearranging and the change of variables;  $\psi = g - x_p \cos \phi$ ,  $I_\beta$  becomes

$$I_\beta = \frac{e^{ikx_p \cos \phi}}{(x_m \sin^2 \phi)^\ell} \int_{|y_p \sin \phi|}^{g(1) - x_p \cos \phi} F(\psi) e^{ik\psi} d\psi \quad (4.101)$$

where

$$F(\psi) = \left( |y_p \sin(\phi) \cos(\phi)| - \cos(\phi)\psi + \sqrt{\psi^2 - y_p^2 \sin^2(\phi)} \right)^\ell \left( -\cos(\phi) + \frac{\psi}{\sqrt{\psi^2 - y_p^2 \sin^2(\phi)}} \right). \quad (4.102)$$

Using the binomial theorem it is possible to expand  $F(\psi)$  to produce a large expression which, in the interest of brevity, is detailed in Appendix A rather than here. The same process is followed for the  $I_\alpha$  interval. At the heart of evaluating the large expressions for  $I_\alpha$  and  $I_\beta$  is a set of four integrals. Firstly,  $\omega_\ell$  and  $\tilde{\omega}_\ell$  as follows.

$$\omega_\ell = \int_{|y_p \sin(\phi)|}^{g(1) - x_p \cos(\phi)} \psi^\ell e^{ik\psi} d\psi \quad (4.103)$$

$$\tilde{\omega}_\ell = \int_{g(-1) - x_p \cos(\phi)}^{|y_p \sin(\phi)|} \psi^\ell e^{ik\psi} d\psi. \quad (4.104)$$

which can simply be treated analytically by parts shown below for  $\omega_\ell$  using

$$\omega_\ell(a, b) = \sum_{j=0}^{\ell} \frac{(-1)^j j! \binom{\ell}{j} [b^{\ell-j} e^{ikb} - a^{\ell-j} e^{ika}]}{(ik)^{j+1}}, \quad (4.105)$$

where  $b = g(-1) - x_p \cos(\phi)$  and  $a = |y_p \sin(\phi)|$ ;  $\tilde{\omega}_\ell$  can be evaluated in the same way. Secondly there are the integrals which contain a singularity, and are defined as follows.

$$\rho = \int_{|y_p \sin(\phi)|}^{g(1)-x_p \cos(\phi)} \frac{\psi^{j_2+2j_3}}{\sqrt{\psi + |y_p \sin(\phi)|}} \frac{1}{\sqrt{\psi - |y_p \sin(\phi)|}} e^{ik\psi} d\psi \quad (4.106)$$

$$= e^{ik|y_p \sin(\phi)|} \int_0^{g(1)-x_p \cos(\phi)-|y_p \sin(\phi)|} \frac{(x + |y_p \sin(\phi)|)^{j_2+2j_3}}{\sqrt{x + 2|y_p \sin(\phi)|}} \frac{1}{\sqrt{x}} e^{ikx} dx \quad (4.107)$$

$$= e^{ik|y_p \sin(\phi)|} \int_0^{g(1)-x_p \cos(\phi)-|y_p \sin(\phi)|} B(x) \frac{1}{\sqrt{x}} e^{ikx} dx \quad (4.108)$$

where  $x = \psi - |y_p \sin(\phi)|$  and

$$B(x) = \frac{(x + |y_p \sin(\phi)|)^{j_2+2j_3}}{\sqrt{x + 2|y_p \sin(\phi)|}} \quad \text{or} \quad \frac{(x + |y_p \sin(\phi)|)^{j_2+2j_3+1}}{\sqrt{x + 2|y_p \sin(\phi)|}}. \quad (4.109)$$

And for the  $I_\alpha$  portion

$$\begin{aligned} \tilde{\rho} &= \int_{g(-1)-x_p \cos(\phi)}^{|y_p \sin(\phi)|} \frac{\psi^{j_2+2j_3}}{\sqrt{\psi + |y_p \sin(\phi)|}} \frac{1}{\sqrt{\psi - |y_p \sin(\phi)|}} e^{ik\psi} d\psi \\ &= e^{ik|y_p \sin(\phi)|} \int_{g(-1)-x_p \cos(\phi)-|y_p \sin(\phi)|}^0 \frac{(x + |y_p \sin(\phi)|)^{j_2+2j_3}}{\sqrt{x + 2|y_p \sin(\phi)|}} \frac{1}{\sqrt{x}} e^{ikx} dx \\ &= e^{ik|y_p \sin(\phi)|} \int_{g(-1)-x_p \cos(\phi)-|y_p \sin(\phi)|}^0 B(x) \frac{1}{\sqrt{x}} e^{ikx} dx, \end{aligned} \quad (4.110)$$

where

$$B(x) = \frac{(x + |y_p \sin(\phi)|)^{j_2+2j_3}}{\sqrt{x + 2|y_p \sin(\phi)|}} \quad \text{or} \quad \frac{(x + |y_p \sin(\phi)|)^{j_2+2j_3+1}}{\sqrt{x + 2|y_p \sin(\phi)|}} \quad (4.111)$$

Since  $\rho$  and  $\tilde{\rho}$  are in fact oscillatory integrals, it is possible to apply a Filon scheme. This requires the computation of the moments  $\nu_j$  and  $\tilde{\nu}_j$  as follows.

$$\nu_j = \int_0^b x^{j-\frac{1}{2}} e^{ikx} dx \quad (4.112)$$

$$= - \sum_{\ell=0}^{j-1} \frac{\prod_{n=1}^{\ell} (j - (n-1) - \frac{1}{2})}{(-ik)^{\ell+1}} b^{j-\ell-\frac{1}{2}} e^{ikb} + \frac{\prod_{n=1}^j (j - (n-1) - \frac{1}{2})}{(-ik)^j} \nu_0 \quad (4.113)$$

where

$$\nu_0 = \int_0^b \frac{e^{ikx}}{\sqrt{x}} dx = \frac{\sqrt{\pi} \operatorname{erf}(\sqrt{-ik} \sqrt{b})}{\sqrt{-ik}} \quad (4.114)$$

for  $j = 0, 1, \dots$ . The same process is followed for  $\tilde{\nu}_j$

$$\tilde{\nu}_j = \int_{\tilde{b}}^0 x^{j-\frac{1}{2}} e^{ikx} dx \quad (4.115)$$

$$= \sum_{\ell=0}^{j-1} \frac{\prod_{n=1}^{\ell} (j - (n-1) - \frac{1}{2})}{(-ik)^{\ell+1}} \tilde{b}^{j-\ell-\frac{1}{2}} e^{ik\tilde{b}} + \frac{\prod_{n=1}^j (j - (n-1) - \frac{1}{2})}{(-ik)^j} \tilde{\nu}_0. \quad (4.116)$$

$$(4.117)$$

wherein the following expression from [78] is employed

$$\tilde{\nu}_0 = -\frac{\sqrt{\pi} \operatorname{erf}\left(\sqrt{-ik} \sqrt{\tilde{b}}\right)}{\sqrt{-ik}} \quad (4.118)$$

for  $j = 0, 1, \dots$ . This is made possible by the error function of a complex argument, which facilitates the computation of the singular  $\nu_0$  and  $\tilde{\nu}_0$  integrals.

**Numerical example** Consider the case when  $x_p = 5$ ,  $y_p = 7$ ,  $\bar{\phi} = 60$ . Using (4.93) we find that there is a stationary point located at  $\xi^* = -0.5207259$ . Thus, to implement the Filon method for this example we must include  $\xi = -0.5207259$  as one of the interpolation points, when fitting the Hermite polynomials. A Hermite polynomial must be constructed for each  $s$ , in this case we take  $S = 2$ , which requires the construction of 3 Hermite polynomials. The fit for the  $s = 0$  case is shown in Fig. 4.13. Results for this example are shown in Fig. 4.14, wherein  $k = 1-1000$  and the conditions of (4.97) are expanded on, by using higher order derivatives to construct the Hermite polynomial. It is clear that the method has the capability to produce accurate results, and that the error can be reduced by including more information to form the interpolating polynomial. The main drawback with this method is the run-time, in particular when using higher order derivatives in the construction. Table 4.3 shows the times taken for the Filon schemes vs. the Gauss schemes. As the motivation for employing integration schemes designed for highly oscillatory functions is speed, it is clear from the run-times that this scheme is not a viable alternative to Gauss-Legendre, for the frequency range that we require.

$k$	Time(s)			
	$Filon_1$	$Filon_2$	$Filon_3$	Gauss
500	0.28	0.35	0.46	0.051
1000	0.27	0.35	0.46	0.079
2000	0.28	0.35	0.44	0.138
10000	0.29	0.35	0.45	0.594

Table 4.3: Solution time in seconds for Gauss-Legendre and for 3 Filon stationary point Filon schemes wherein the subscript (1, 2, 3) refers to the number of derivatives taken at end point and stationary point locations.

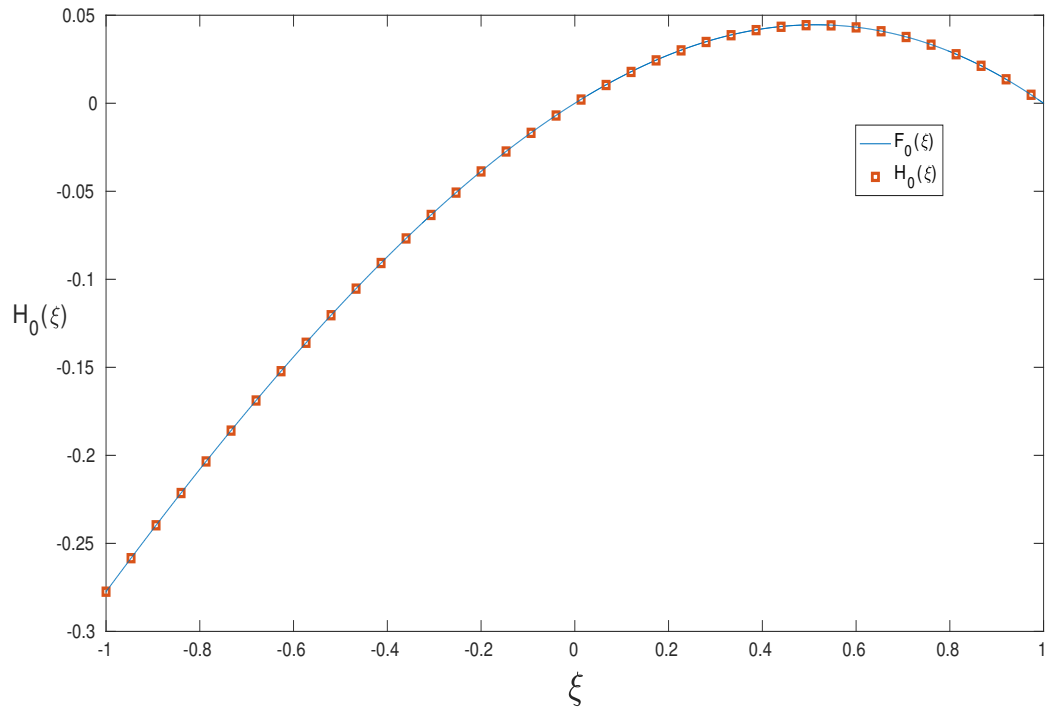


Figure 4.13: Hermite polynomial fit.

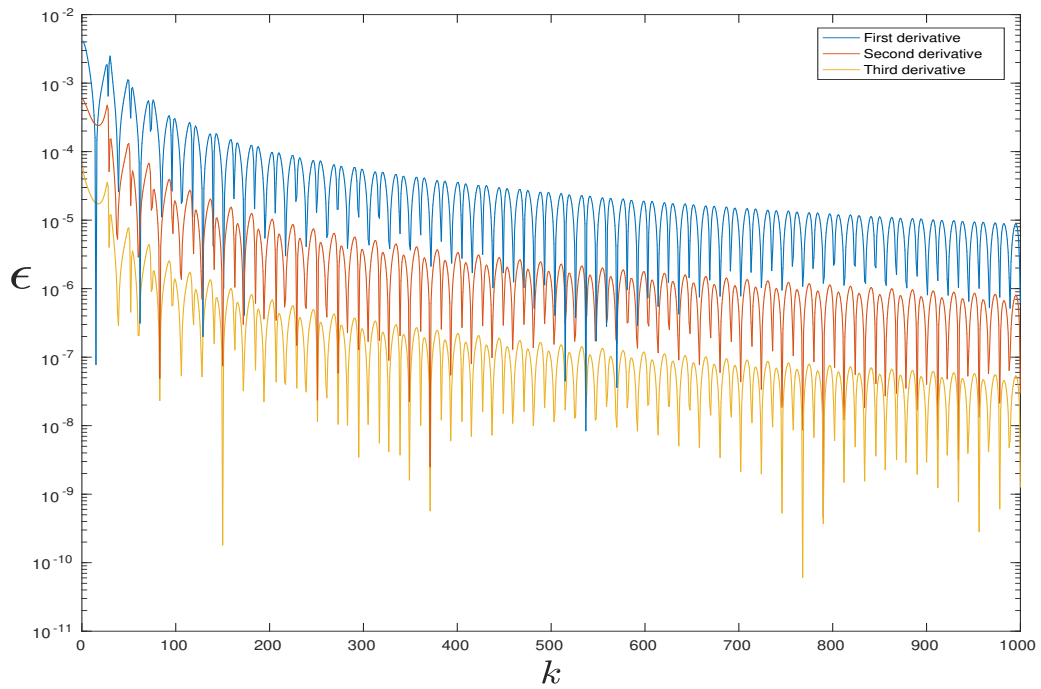


Figure 4.14:  $L^2$  error for a first order stationary point Filon scheme (blue), a second order scheme (red) and a third order scheme (orange).

## Method of stationary phase

The Method of Stationary Phase (MSP) considers small intervals including stationary point locations to provide the most important contribution to the overall value of the integral. The formula for MSP [74] is

$$I \approx f(x^*) \sqrt{\frac{2\pi}{k|g''(x^*)|}} e^{ikg(x^*)} e^{\pm \frac{i\pi}{4}}, \quad (4.119)$$

in which  $x^*$  represents a stationary point. This can be used to reformulate the PUBEM integral (4.48), to produce

$$I \approx \gamma \sum_{s=0}^S \frac{i^s a_s(1)}{k^{s-\frac{1}{2}}} f(\xi^*, s) \sqrt{\frac{2\pi}{k|g''(\xi^*)|}} e^{ikg(\xi^*)} e^{\pm \frac{i\pi}{4}}, \quad (4.120)$$

where

$$\gamma = \frac{-iJ}{4} \left( \frac{2}{\pi} \right)^{\frac{1}{2}} e^{-\frac{3}{4}\pi i}. \quad (4.121)$$

As with the Filon and asymptotic method, this expression is independent of  $k$ . When compared with the Filon-type method proposed to tackle stationary point locations, the method of stationary phase has the benefit of simplicity and speed.

**Straight line case** Some preliminary test results are presented here, wherein the method of stationary phase is used to integrate (4.48) for a flat straight line element. Initial testing, with PUBEM elements using quadratic Lagrangian functions, shows moderate accuracy for the  $N_2$  case, but a reduction in accuracy for the  $N_1$  and  $N_3$  cases which indicates that the stationary point location is not the only location that provides a significant contribution to the overall value of the integral. For example, taking an element of length 4, laying on the  $x$ -axis with  $\bar{\phi} = \frac{-\sqrt{3}}{2}$ ,  $k = 500$ ,  $x_p = -2$  and  $y_p = -2$  and integrating using the MSP produces a relative error of  $\epsilon = 5.8e - 04$  for the  $N_2$  shape function, but  $\epsilon = 0.028$  and  $\epsilon = 0.019$  for the  $N_1$  and  $N_3$  respectively. This is unsurprising because at the end of the interval there is no cancellation between the positive and negative parts of the oscillation. It is possible though, to include information at the end points by employing the asymptotic method via repeated integration by parts. In order to do this, consider 3 smooth functions ( $F_A$ ,  $F_B$  and  $F_C$ ) diagrammatically shown in Fig. 4.15.

These blending functions are constructed using portions of sine waves, and defined in terms of the following points along the  $\xi$ -axis such that  $-1 < \xi_A < \xi_B < \xi_C < 1$ , where  $\xi_B$  denotes the stationary point.  $F_B$  takes the value of 1 in the neighbourhood of the stationary point, tapering down to 0 at the end points.  $F_A(-1) = 1$  and  $F_C(1) = 1$ , also

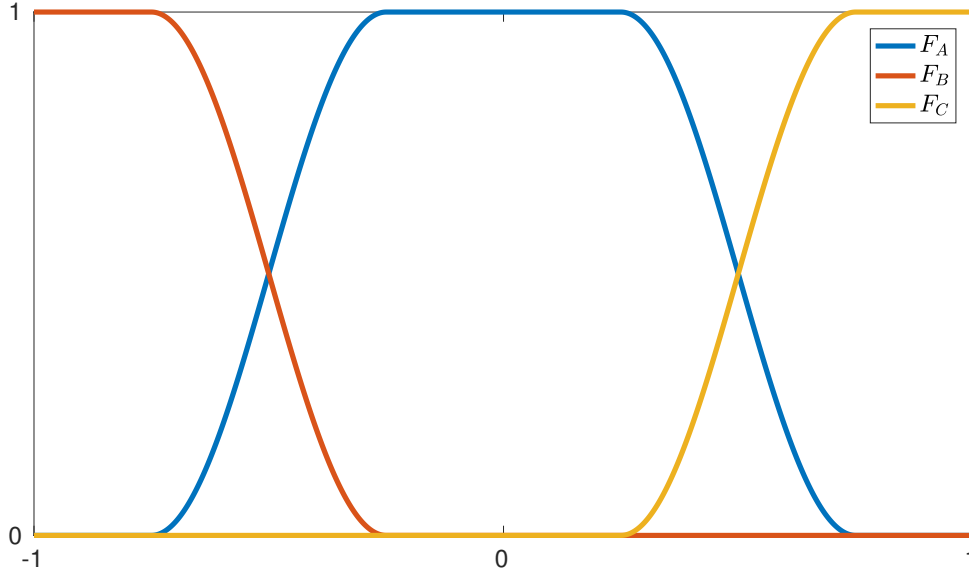


Figure 4.15: Smooth blending functions for including the end point contributions to the MSP formulation.

tapering to 0 at opposite end locations. Due to the partition of unity the integral (4.48) may be written as

$$I = \int_{-1}^1 (F_A(\xi) + F_B(\xi) + F_C(\xi))f(\xi, s)e^{ikg(\xi)} d\xi \quad (4.122)$$

Which may be treated separately as

$$I = I_A + I_B + I_C, \quad (4.123)$$

where

$$I_A = \int_{-1}^A F_A(\xi)f(\xi, s)e^{(ikg(\xi))} d\xi \quad (4.124)$$

$$I_B = \int_{-1}^1 F_B(\xi)f(\xi, s)e^{(ikg(\xi))} d\xi \quad (4.125)$$

$$I_C = \int_B^1 F_C(\xi)f(\xi, s)e^{(ikg(\xi))} d\xi. \quad (4.126)$$

The only integral which contains stationary points is  $I_B$  which means that  $I_A$  and  $I_C$  may be evaluated using the Asymptotic Method as follows

$$I_A = \frac{1}{ik} \left[ \frac{F_A(\xi(A))f(\xi(A), s)}{g'(\xi(A))} e^{ikg(\xi(A))} - \frac{F_A(-1)f(\xi(-1), s)}{g'(-1)} e^{ikg(-1)} \right] + \mathcal{O}(k^{-2}), \quad (4.127)$$

$$I_C = \frac{1}{ik} \left[ \frac{F_C(1)f(1, s)}{g'(1)} e^{ikg(1)} - \frac{F_C(\xi(C))f(\xi(C), s)}{g'(\xi(C))} e^{ikg(\xi(C))} \right] + \mathcal{O}(k^{-2}), \quad (4.128)$$

whereas  $I_B$  can be evaluated using the MSP

$$I_B \approx F_B(\xi(B))f(\xi(B), s) \sqrt{\frac{2\pi}{k|g''(\xi(B))|}} e^{ikg(\xi(B))} e^{\pm \frac{i\pi}{4}}. \quad (4.129)$$

Now the above mentioned element, of length 4 is considered with the same enrichment wave direction but focusing on results for the case including the  $N_1$  shape function (the  $N_3$  can be omitted because it mirrors the  $N_1$  case). It can be seen for a range of  $k$  in Fig. 4.16 that if the end point information is included via asymptotic expansion, then the accuracy in computing the integral containing  $N_1$  shape function becomes comparable to the accuracy in computing the integral containing the  $N_2$  shape function, thus resolving the issue.

Whilst the preliminary results appear positive, the error is still relatively large for the lower  $k$  range, and the example chosen is far from the most challenging. In fact, stationary points located near the end points of the interval of integration cause the most difficulty for the MSP. This is highlighted in Fig. 4.17 for a range of  $k$ , wherein error clearly increases as  $\xi^*$  approaches  $-1$  and  $1$ , i.e. the ends of the element.

As each element contains  $j = 1, \dots, J$  shape functions, each integral contains a shape function  $N_j$ . If  $J = 3$  is selected (i.e. quadratic elements), the highest errors will occur in the integrals containing the  $N_1$  and  $N_3$  shape functions wherein the stationary point is located near the end of the interval of integration. A possible remedy to this is to employ the trigonometric basis functions of [65] which are produced by the following equations.

$$N_1(\xi) = -\frac{1}{4} \cos(\pi\xi) - \frac{1}{2} \sin\left(\frac{\pi}{2}\xi\right) + \frac{1}{4}, \quad (4.130)$$

$$N_2(\xi) = \frac{1}{2} \cos(\pi\xi) + \frac{1}{2}, \quad (4.131)$$

$$N_3(\xi) = -\frac{1}{4} \cos(\pi\xi) + \frac{1}{2} \sin\left(\frac{\pi}{2}\xi\right) + \frac{1}{4}. \quad (4.132)$$

These functions are shown in Fig. 4.18, with their extension past the interval of the element represented using a dashed line. This choice is made because considering integrating over the support of  $N_j$  is more useful than integrating element-by-element. Though, the

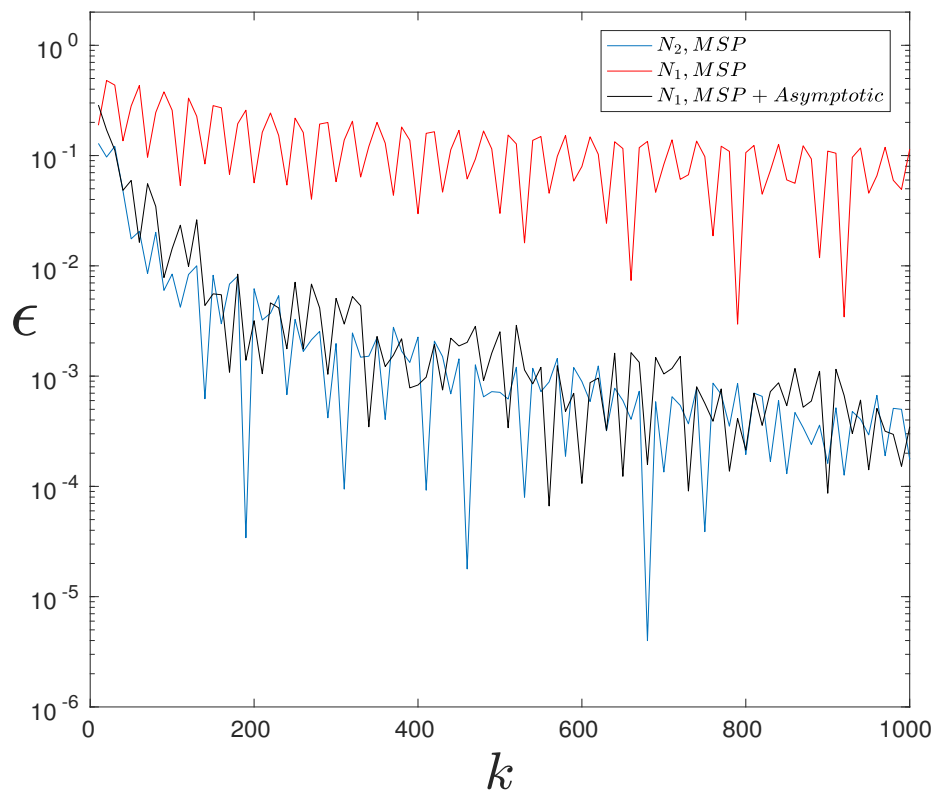


Figure 4.16:  $L_2$  error for the integral containing the  $N_2$  shape function, and a comparison of the  $L_2$  error of the integral containing the  $N_1$  shape function evaluated with and without including the end point contributions.

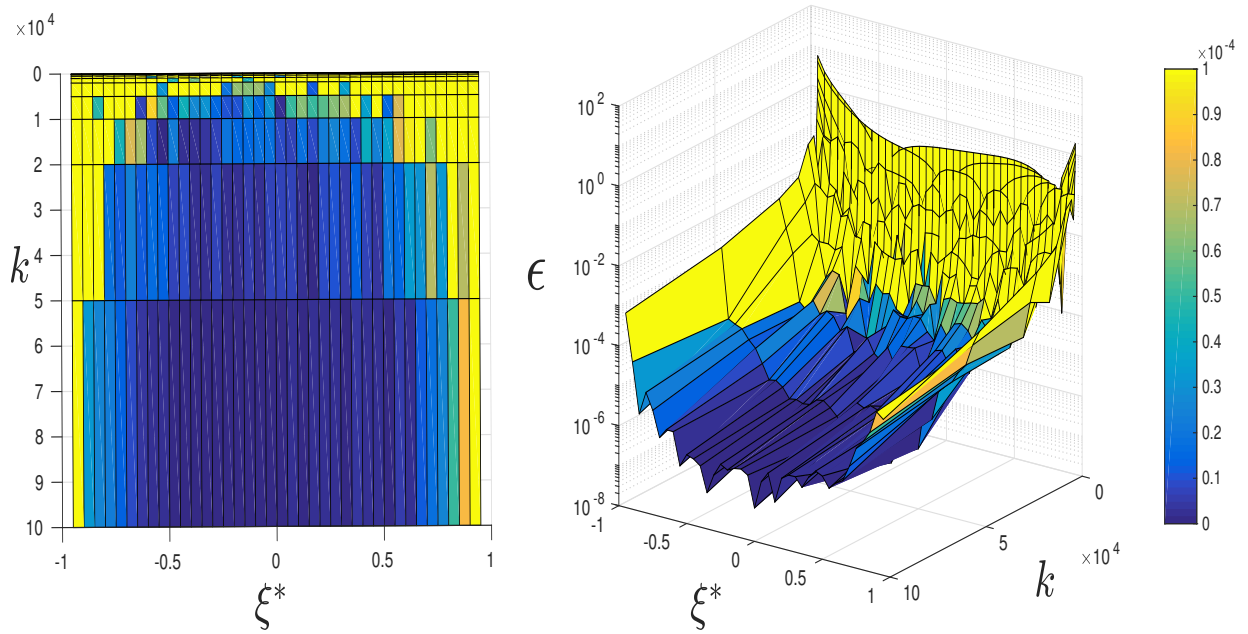


Figure 4.17:  $L_2$  error incurred by MSP for stationary points  $\xi^*$  located across a straight line flat element for a range of  $k$ .

continuity between functions across element ends is important and conventional piecewise Lagrange polynomial functions exhibit only  $C^0$  continuity at the shared node. Contrast this with the trigonometric shape functions which exhibit  $C^1$  continuity generally, but this improves to  $C^\infty$  continuity if the lengths of the adjacent elements are the same. Furthermore the slowly varying function  $F(\xi)$  goes to zero at the ends of the interval, as does  $F'(x)$  which negates the need to include end-point information.

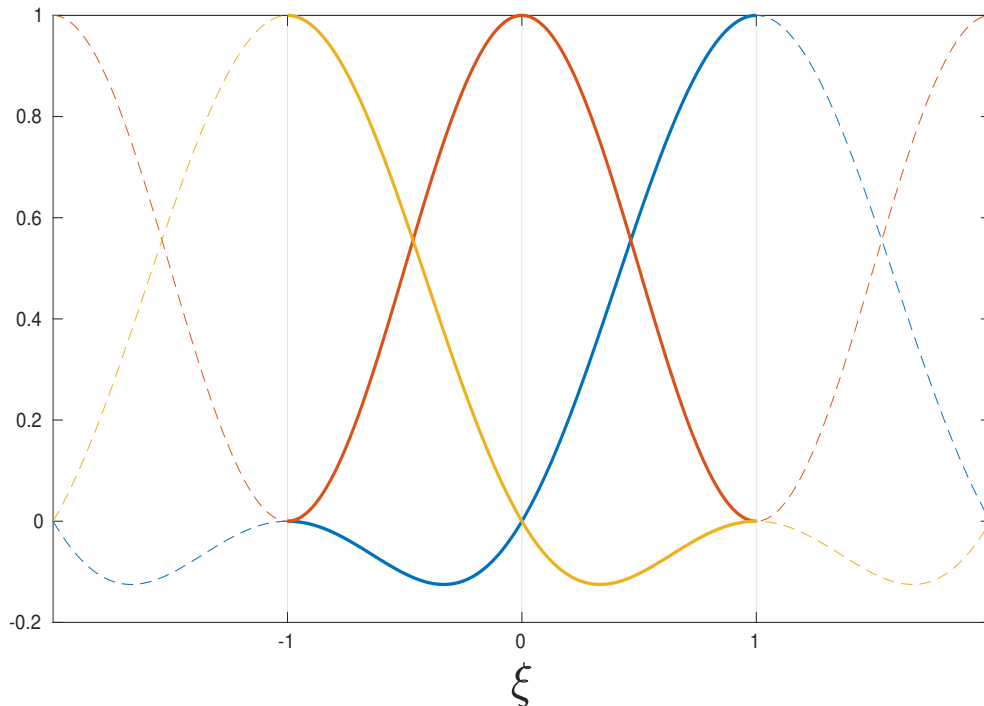


Figure 4.18: Trigonometric shape functions.

To illustrate this, we take an example from a circular scattering object, discretised into 4 elements, shown in Fig. 4.19. We find a case which would normally cause difficulty with stationary behaviour near the end of an element by setting  $(x_p, y_p) = (\cos(\frac{7\pi}{6}), \sin(\frac{7\pi}{6}))$  and  $\bar{\phi} = \frac{11\pi}{18}$ . Consider elements  $e_1$  and  $e_2$  which together span  $\theta = [0, \pi]$ , with a stationary point  $\theta^* = \frac{29\pi}{54}$  it is possible to integrate over the support of the shape function for the shared node shown in Fig. 4.19 in terms of  $\theta$  as follows.

$$I = \int_0^\pi F(\theta) e^{ikg(\theta)} d\theta \quad (4.133)$$

The basis functions of elements 1 and 2 are combined to form a composite shape function (which can be considered as a single basis function) for the shared node. Varying  $k$  and comparing the integral over the described support with a reference value, computed using a converged Gauss-Legendre integration scheme, the results of Fig. 4.20 are produced. These results indicate a reasonable level of accuracy, which increases as  $k$  increases.

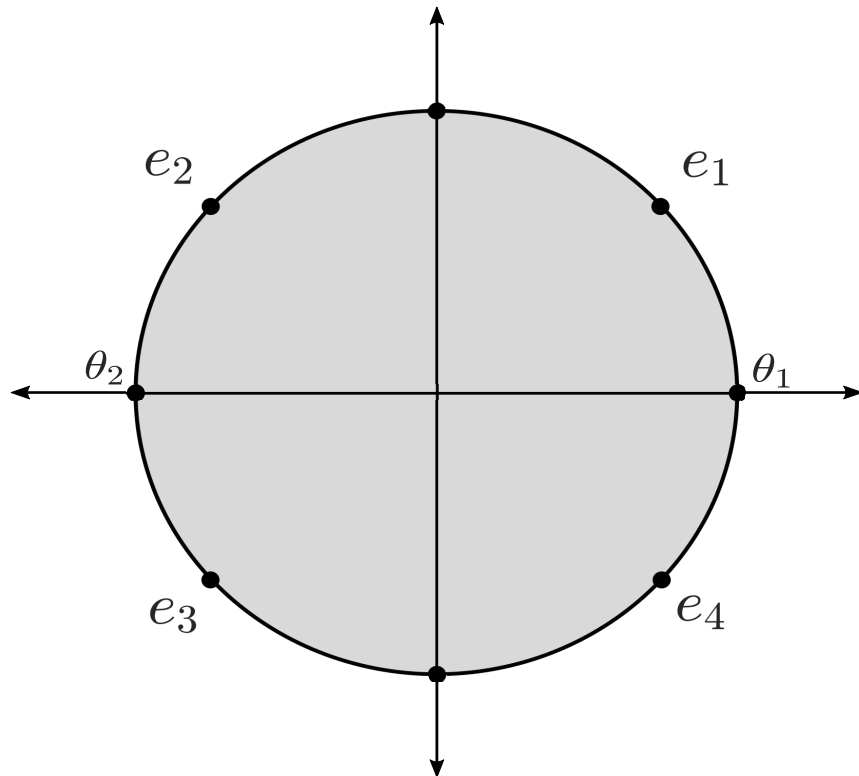
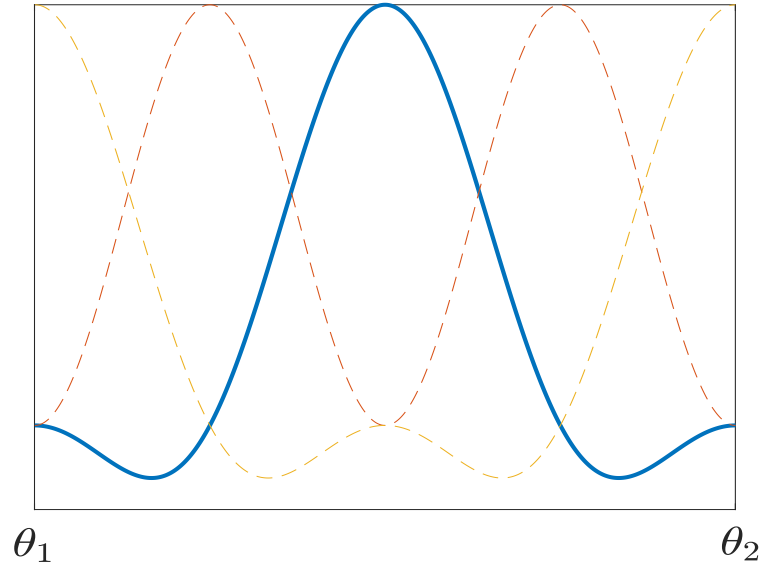


Figure 4.19: Test elements from a circular scattering object with trigonometric support.

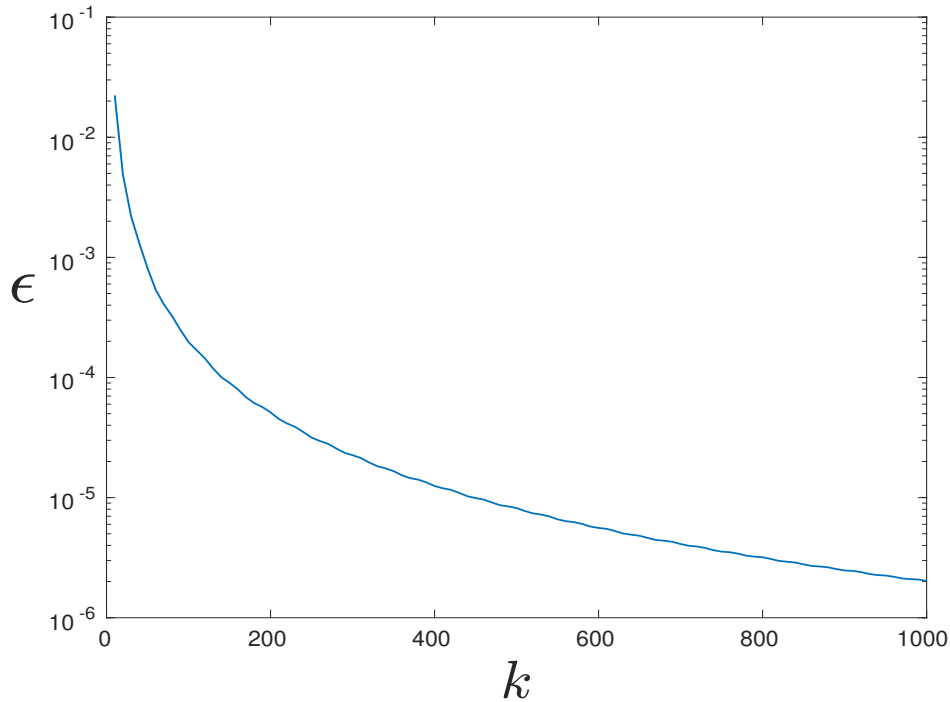


Figure 4.20: Relative error in the integration over the trigonometric support of the shared node between element 1 and 2 plotted against  $k$ .

### Targeted Gauss-Legendre

A final approach tested is a so-called targeted Gauss-Legendre scheme, which locates window functions around stationary point locations and the end points of elements, as these areas provide the leading order behaviour to the overall value of the integrand. In order to distinguish this algorithm from the previous algorithms,  $\rho$  is used in place of  $\xi$  as the parametric variable across the element. Thus we define a set of window functions having the dimensions defined according to Fig. 4.21 wherein the window functions are set equal to 1 at focal points which are located at the ends of the element if considering the  $N_1$  or  $N_2$  functions and  $\rho^*$  if there is a stationary point. Each function is tapered using a sine curve of width  $\delta$  to produce a smoothing effect. The width  $\bar{\rho}$  represents the portion of the window which is set equal to 1 and is halved for the end point contributions. This scheme differs from the other approaches that we have observed thus far because it still applies traditional quadrature, but only over a portion of the element. A simple example to illustrate the core of this method is shown in Fig. 4.22 which considers an  $N_2$  shape function with  $k = 500$ ,  $x_e = 4$  and  $\bar{\phi} = \theta = \frac{\pi}{2}$  to enforce a central stationary point  $\rho^*$ . The width of the window function  $\bar{\rho}$  is then widened with the resulting relative error observed. It was found that including the end point contributions for  $N_2$  functions offered no improvement, but was necessary for  $N_1$  and  $N_3$  functions which agrees with

previous results from the MSP testing. Fixing the window size and varying  $k$ , produces the results of Fig. 4.23, which are shown for  $N_1$  and  $N_2$ . Both sets of results improve as  $k$  increases with the results for  $N_1$  being more accurate, though double the Gauss points are required for  $N_1$  and  $N_3$ .

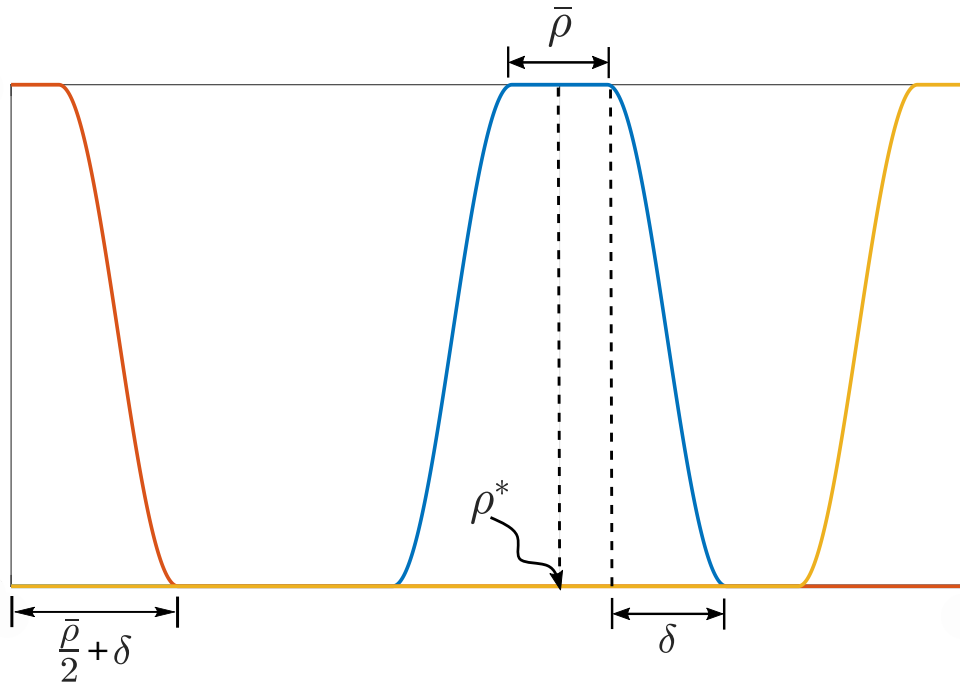


Figure 4.21: Window functions for targeted Gauss-Legendre.

#### 4.5.4 Problems with using integration schemes for highly oscillatory integrals

##### Non-stationary cases

For each method discussed above, a number of examples are presented in which the error is relatively low, to show that there is potential for benefit in certain cases, and that impressive results may be obtained with very little computational expense. Whilst it is possible to find many of these cases, by varying  $k$ ,  $\bar{\phi}$ ,  $\theta$ ,  $r$  and  $x_e$  to suit, due to the general nature of PUBEM, cases will often arise wherein the results are far from optimal. This is because, for example,  $\bar{\phi}$  is dictated by  $M$  and  $x_e$  is dictated by  $E$ .

The results of Fig. 4.8 represent a particularly favourable case; by moving the source point to a new location, defined by  $\theta = \frac{\pi}{6}$  and  $r = 4$  but maintaining the same element size and considering the same variation in  $k$  the results of Fig. 4.26 are produced, in which the Filon method fails completely and the results of the Asymptotic method are nearly 8 orders of magnitude less accurate than those shown in Fig. 4.8. Unfortunately, problem cases arise frequently as a result of stationary and near stationary behaviour. This can be

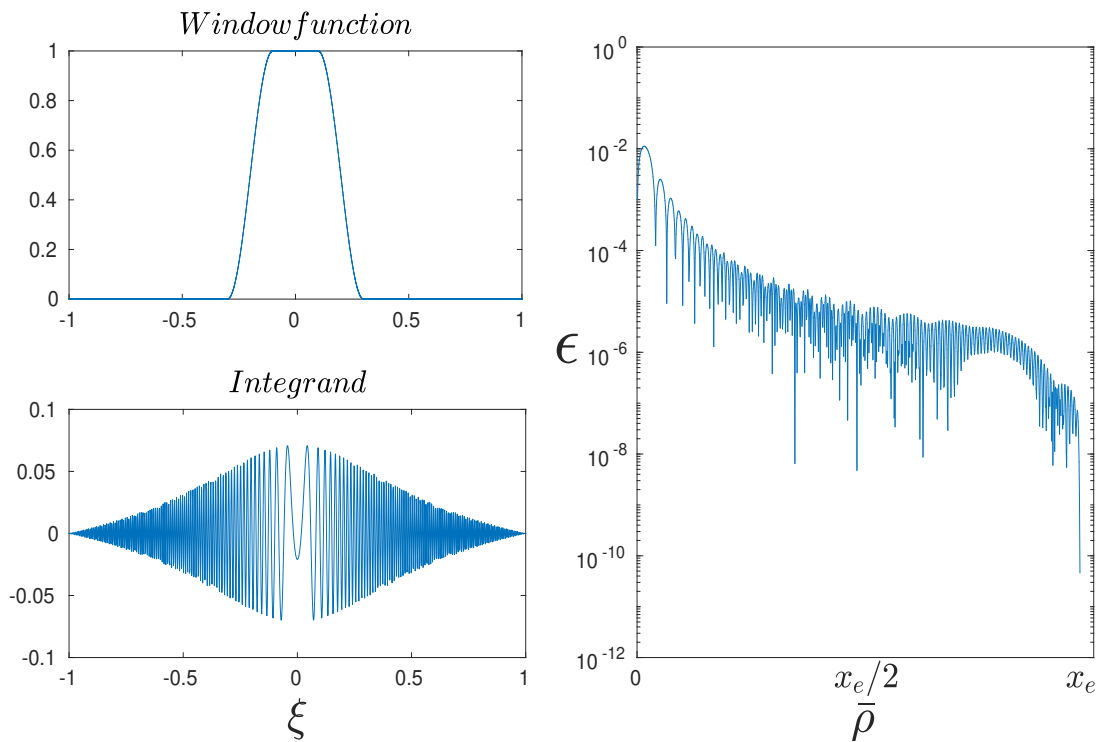


Figure 4.22: (left) Example of a window function and associated integrand for  $N_2$  with a stationary point at  $\xi = 0$ , (right)  $L_2$  error vs.  $\bar{\rho}$  for the same case.

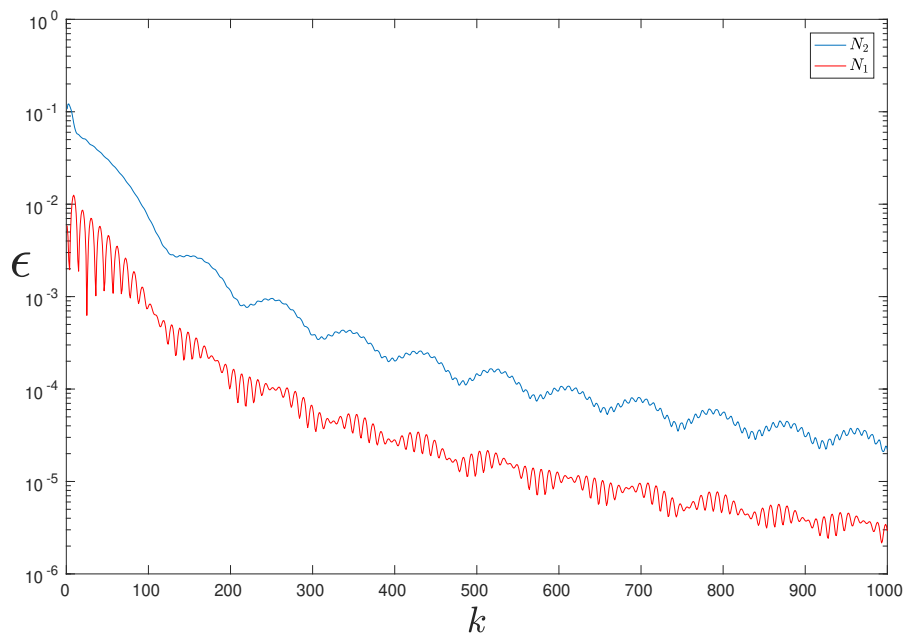


Figure 4.23:  $L_2$  error for the  $N_1$  and  $N_2$  shape functions using targeted Gauss-Legendre integration with  $\bar{\rho} = 0.2$  and  $\delta = 0.15$ .

shown by employing a second-order Asymptotic scheme for the original more favourable example and fixing  $k = 500$  then varying  $\theta$  and  $r$ , which produces the results of Fig. 4.27 wherein the majority of cases have unacceptable error levels, comfortably above 1%. In addition, the timings shown in Table 4.1 and Table. 4.2 are for first-order schemes which produce such acceptable levels of error in favourable cases, though a second-order Filon scheme has a run-time of approximately 0.097s per integral and approximately 0.061s per integral for a second-order Asymptotic scheme.

Further, near-stationary cases, i.e. cases where a stationary point is adjacent to the interval of integration, can cause difficulty, even for the second order asymptotic method. This problem is highlighted in Fig. 4.24 wherein a second order asymptotic integration scheme is employed to integrate over a straight line element of length  $x_e = 4$  with varying  $r_0$  and  $\theta$ , and with  $k = 100$ . The white regions in Fig. 4.24 are areas in which the relative error  $\epsilon$  exceeds 0.01. Still further, for this example, Gauss-Legendre is actually faster than using the second order asymptotic scheme, and will produce reliable results for every  $r_0$ - $\theta$  combination. These near-stationary cases cause even greater difficulty for Targeted Gauss-Legendre and the Filon method.

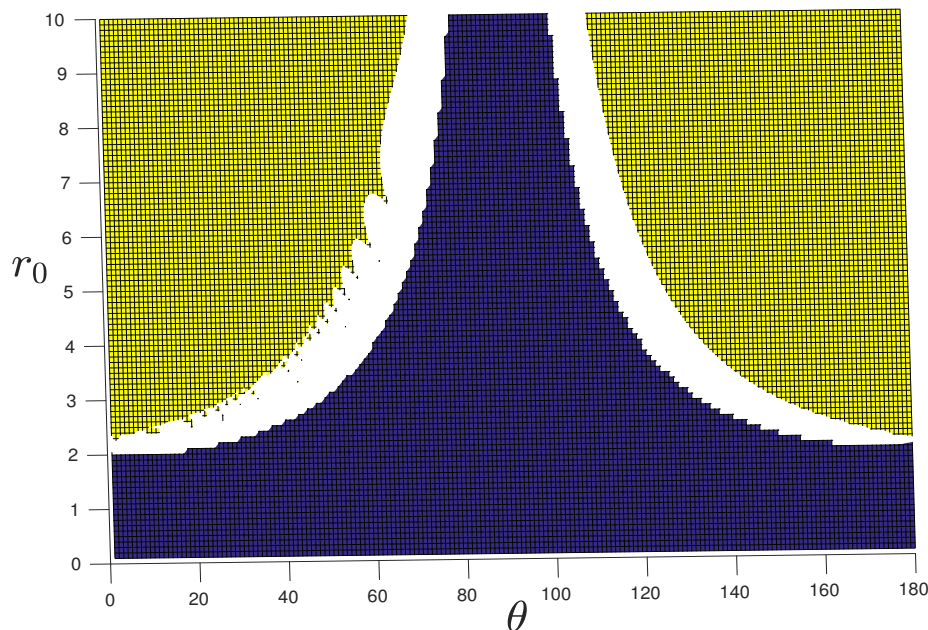


Figure 4.24: Regions of relative error  $\epsilon$  for second order asymptotic method integrals with varying  $r_0$  and  $\theta$ ,  $k = 100$ ; yellow regions show  $\epsilon < 0.001$ , blue regions show stationary point locations, and the white regions show near-stationary locations wherein  $\epsilon > 0.01$ .

As with the other methods presented there are a number of cases wherein targeted Gauss does not perform well. For example, Fig. 4.25 shows results with varying  $\theta$  and  $r_0$  with  $k = 500$ ,  $\bar{\phi}, \bar{\rho} = 0.2$  and  $\delta = 0.15$ . It is evident from the results that the error in

computing integrals containing the  $N_1$  shape function is over 1% for most combinations of  $r_0$  and  $\theta$  and for almost all combinations the error in computing the  $N_2$  shape functions is over 1%.

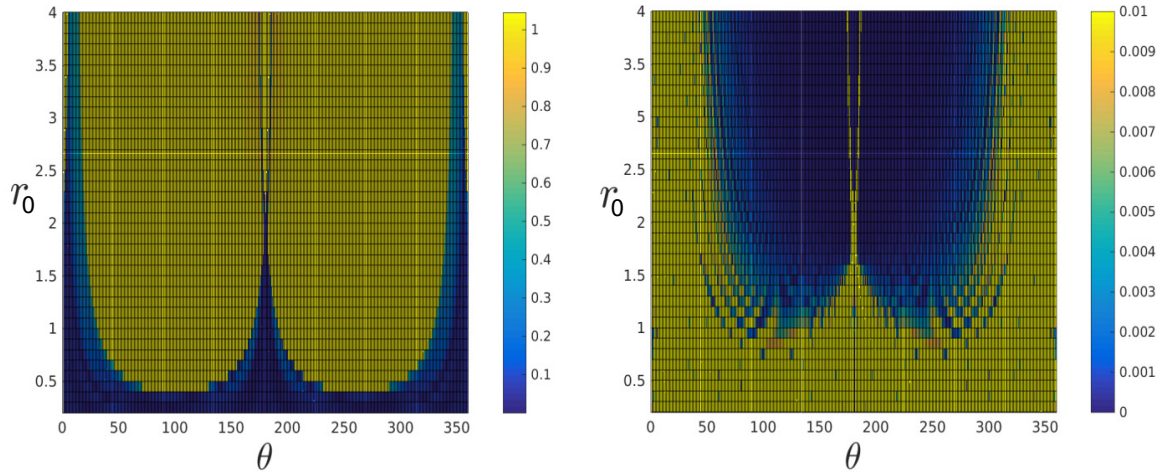


Figure 4.25:  $L_2$  error for the  $N_2$  case (left) and the  $N_1$  case (right), both with  $\bar{\phi} = \frac{\pi}{18}$ ,  $k = 500$ ,  $\bar{\rho} = 0.2$ ,  $\delta = 0.15$ , varying  $\theta$  and  $r_0$ .

It is important to note at this point that although large  $k$  has been considered for the geometries that are analysed in this thesis that much of the PUBEM literature is devoted to much lower  $k$ , typically in the mid-high frequency range where PUBEM performs well. Furthermore, to consider a single flat, straight line element is to give strong advantage to the Filon method and the Asymptotic method as there are far fewer stationary points than for an arc element, for example. In addition, the stationary points are predictable with the simple equation (4.93). Another consideration is the element length  $x_e$  (which has been set as  $x_e = 4$  in the previous examples) would vary subject to requirements of conditioning. Naturally, the integration schemes, which are designed to treat highly oscillatory integrals, perform best when there is more oscillation contained within the interval of integration, due to more cancellation occurring. Reducing  $x_e$  is tantamount to reducing the effective  $k$ , i.e.  $kx_e$  is the important parameter, because this provides a good indication of the amount of oscillation contained within the interval of integration. This can be seen in Fig. 4.28 wherein  $k$  and  $x_e$  are varied to produce the same apparent  $k$ .

### Stationary point cases

As with the non-stationary case there are also a number of issues with stationary point cases. A reasonable level of accuracy can be obtained using the adapted Filon method as can be seen in Fig. 4.14, but the algorithm is large. This means that the method is not a suitable alternative to Gauss-Legendre as the run-times seen in Table 4.3 far exceed that

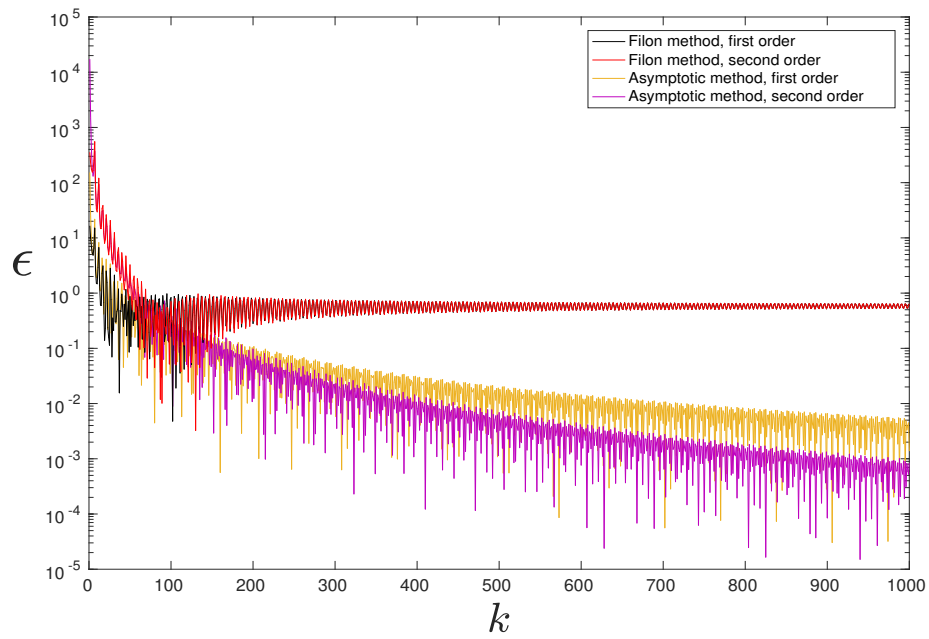


Figure 4.26: Relative error using a second order Asymptotic scheme with  $\theta$  and  $r$  varying for the case when  $x_e = 4$  and  $\bar{\phi} = \frac{\pi}{3}$ .

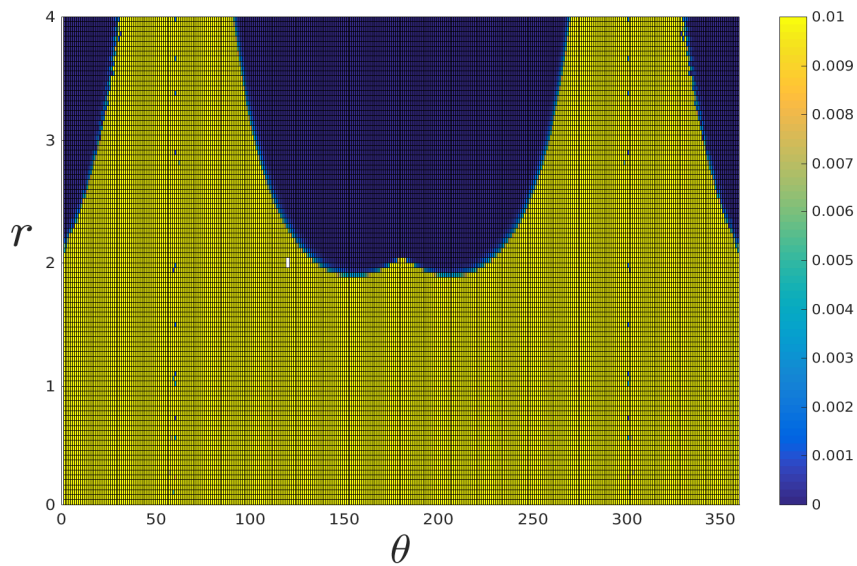


Figure 4.27: Relative error using a second order Asymptotic scheme with  $\theta$  and  $r$  varying for the case when  $x_e = 4$  and  $\bar{\phi} = \frac{\pi}{3}$ .

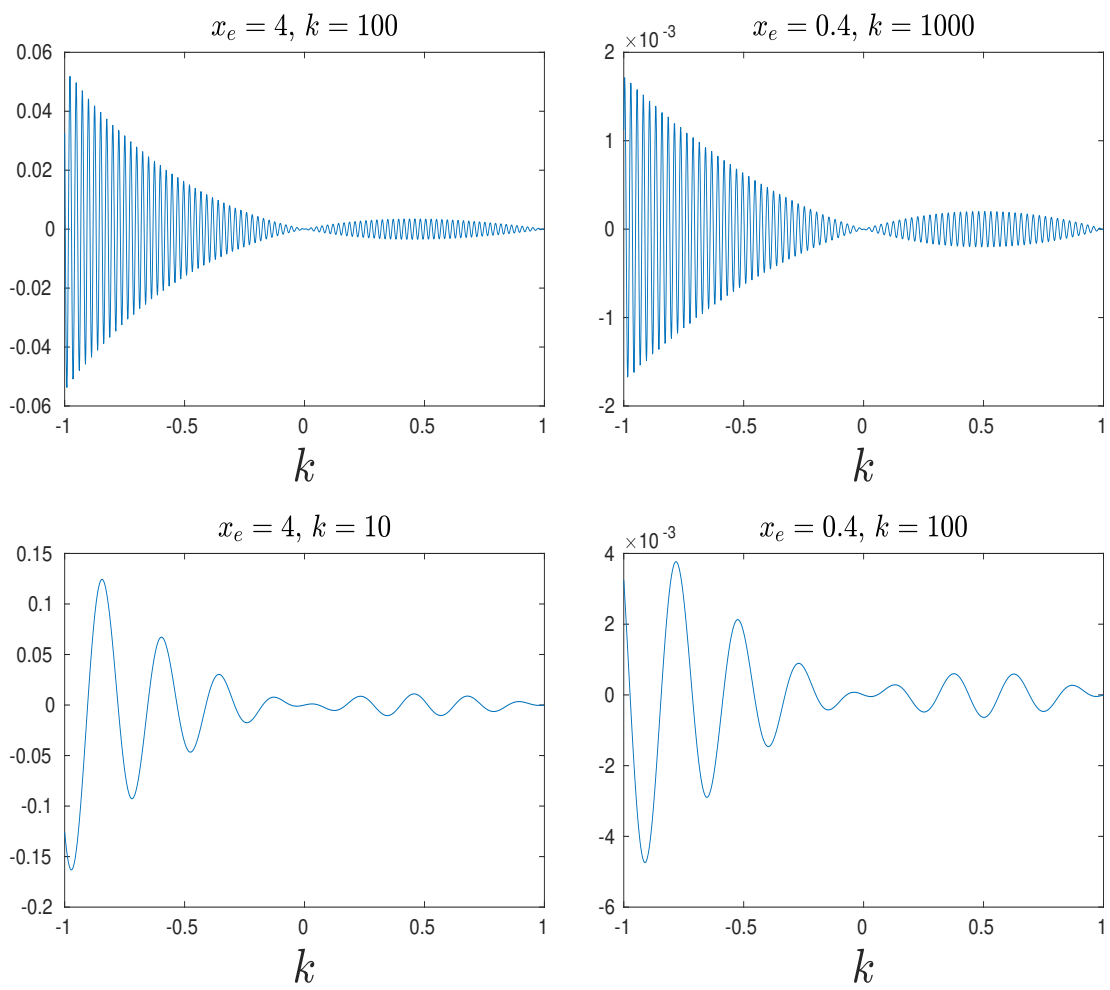


Figure 4.28: Integrands resulting from different combinations of  $x_e$  and  $k$ .

of Gauss-Legendre. Targeted Gauss has also been shown to be ineffective for stationary cases in Fig. 4.25.

This leaves the MSP which produced some promising results, though in reality not all cases behave this way. In fact, if MSP is employed to solve a full scattering example there are a number of challenges. Firstly, there is the requirement to effectively locate stationary points before integrating, which is possible via a bisection method but this introduces a considerable computational expense. This problem would be magnified with more complex geometries which are not constructed of simple straight line or circular arc elements. To illustrate this, we consider the simple example of a unit circle scattering object again, with  $k = 100\pi$ ,  $E = 4$  and  $M = 157$ , with the stationary points located according to [66]. The resulting relative errors across the system matrix are shown in Fig. 4.29, highlighting the large portion of integrals which are inaccurately computed using the MSP. There are a number of cases within the matrix which are simply not evaluated

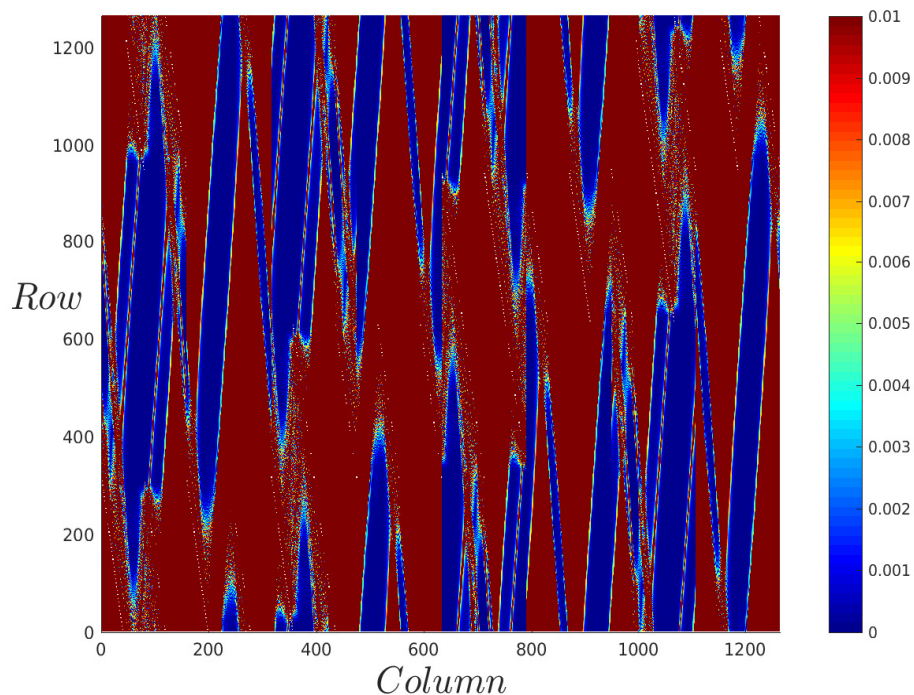


Figure 4.29: Relative error in matrix terms for a circular scattering object,  $k = 100\pi$ ,  $E = 4$  and  $M = 157$ .

accurately by the MSP, though many of the errors are incurred as a result of the MSP setting integrals, for which there is no stationary point within the interval of integration, equal to zero even if the integral is significant in magnitude. If a stationary point occurs near end point locations where the basis functions are very close to zero, the negative effect is minimised, though that is not the case if the near stationary point is towards the centre of the interval of integration. This is possible in cases wherein the source point

lies within the interval of integration, causing a sharp change in the phase function  $g(\xi)$ . An example of this from the above discretisation of a circular scattering object where  $(x_p, y_p) = (\cos(1.28), \sin(1.28))$ ,  $\bar{\phi} = 2.86$  and with an element spanning from the positive  $x$ -axis to the positive  $y$ -axis is shown in Fig. 4.30. Fig. 4.30 shows  $g(\xi)$  and resulting integrand, which is near stationary and the integral would be set equal to zero using MSP when in reality it is equal to  $0.03161 - 0.09879i$ .

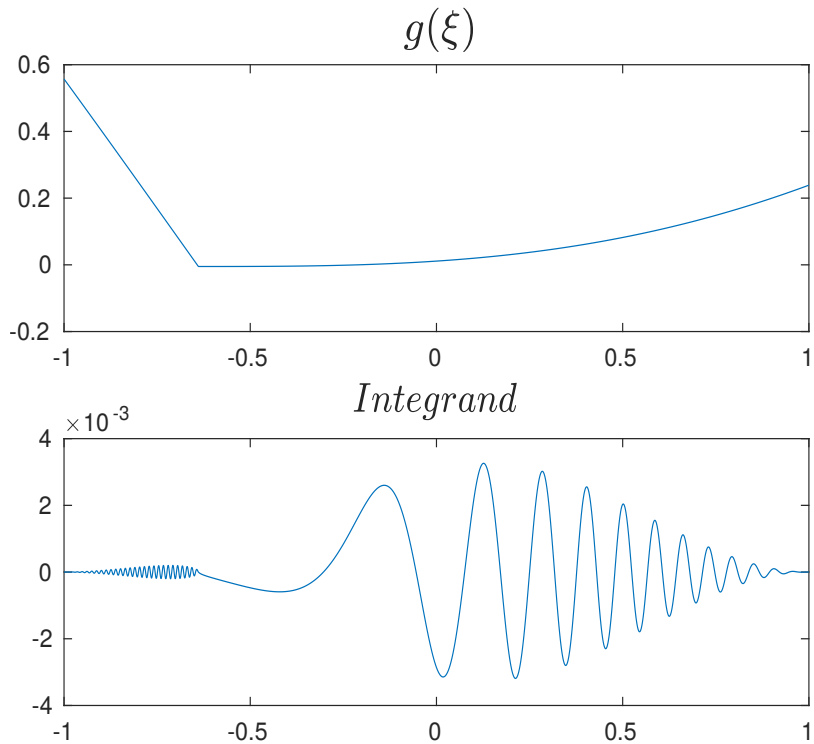


Figure 4.30:  $g(\xi)$  and the resulting integrand for a near stationary case.

To summarise, there are some choice cases for which any of the above highly-oscillatory integration schemes can produce very accurate results. Though, in PUBEM, it is likely that the majority of cases will result in unacceptable error. This is due to:

- multiple stationary points within the interval of integration and stationary points adjacent to the interval of integration
- small  $r$
- small  $kx_e$

The cases considered have been very simple geometrically (straight line elements, for example); to be able to consider general convex objects one would be required to tackle cases with multiple stationary points which provide considerable difficulty for the above methods. Further, the small  $r$ , resulting from source points close-to or on the interval

of integration increases the likelihood of encountering stationary and near stationary points, and for a typical object considered in the thesis there will be many of these cases. Small elements and low- $k$  have the same, undesirable, effect of diminishing the oscillation in the integrand. With all of the above issues considered, it is difficult to imagine a robust implementation solely relying on any of the high-oscillatory integration techniques presented. That is, apart from very large  $k$  problems which may tread into the territory of ray-tracing and optics methods. One could consider using highly oscillatory integration techniques to speed up integration for favourable cases and using conventional Gauss-Legendre in the (more common) less favourable cases, though this would require implementation of an algorithm to decide where it is appropriate to use Gauss-Legendre, which itself will require computational expense. Further, if the Gauss points have been placed once, many of the integration variables will have been computed at those points which means that it may be favourable to simply re-use them.

All is not lost though, as it appears that creating a robust alternative to Gauss-Legendre is so difficult because Gauss-Legendre is not actually very expensive, when optimally designed for PUBEM integrals. For this reason, the following section explores its use for the PUBEM integrals, more specifically: how many Gauss points per wavelength are required.

## 4.6 Gauss-Legendre tailored for PUBEM integrals

Much of the literature on PUBEM is focused on numerical performance of a plane-wave basis and comparing its efficacy against more conventional bases. As a result of this, there is yet to be a thorough quantification of the integration techniques performed and the order of integration required. For this reason, coupled with the difficulties outlined in Section 4.5, the performance of Gauss-Legendre tailored for PUBEM integrals is studied in this section. A number of examples are presented, including polygonal and smooth objects, with the aim of determining how many Gauss points are required to achieve engineering accuracy. The Gauss-Legendre schemes tested are applied over integration cells of the interval of integration, and the number of Gauss points per interval, along with interval size are evaluated.

### 4.6.1 Straight line element

To begin, consider a flat straight line element, of length 1, lying on the  $x$ -axis, with the starting point  $(x_s, y_s) = (0, 0)$  and end point  $(x_e, y_e) = (1, 0)$  and the following parameters: enrichment wave direction  $\bar{\phi} = 60^\circ$ ; source point located at an angle of  $\theta = 10^\circ$ ; and a radius of  $r_0 = 1$  (as defined in Fig. 4.6) from the centre of the element  $(x_c, y_c) = (0.5, 0)$ . For ease of plotting,  $|\log_{10}(\epsilon)|$  is taken wherein  $\epsilon$  is the relative error incurred by each integral, which is shown in Fig. 4.31, plotted against the number of

Gauss points per cell  $ngp$  and the number of cells employed per wavelength. It can be seen that an ‘engineering accuracy’ of 1% is achieved with relatively few Gauss points, in fact using a single integration cell per wavelength with 10 Gauss points per cell produces an error  $< 10^{-15}$ . This is however, a single example and the accuracy achieved will differ according to variables such as  $k$ ,  $\bar{\phi}$ ,  $\theta$  and  $r_0$ . Notably,  $\epsilon$ , in the yellow region, wherein the results are most accurate, appears to be limited to  $\approx 10^{-15}$ . Such limitation is likely due to reaching the capacity of machine precision. This effect is also shown in subsequent figures.

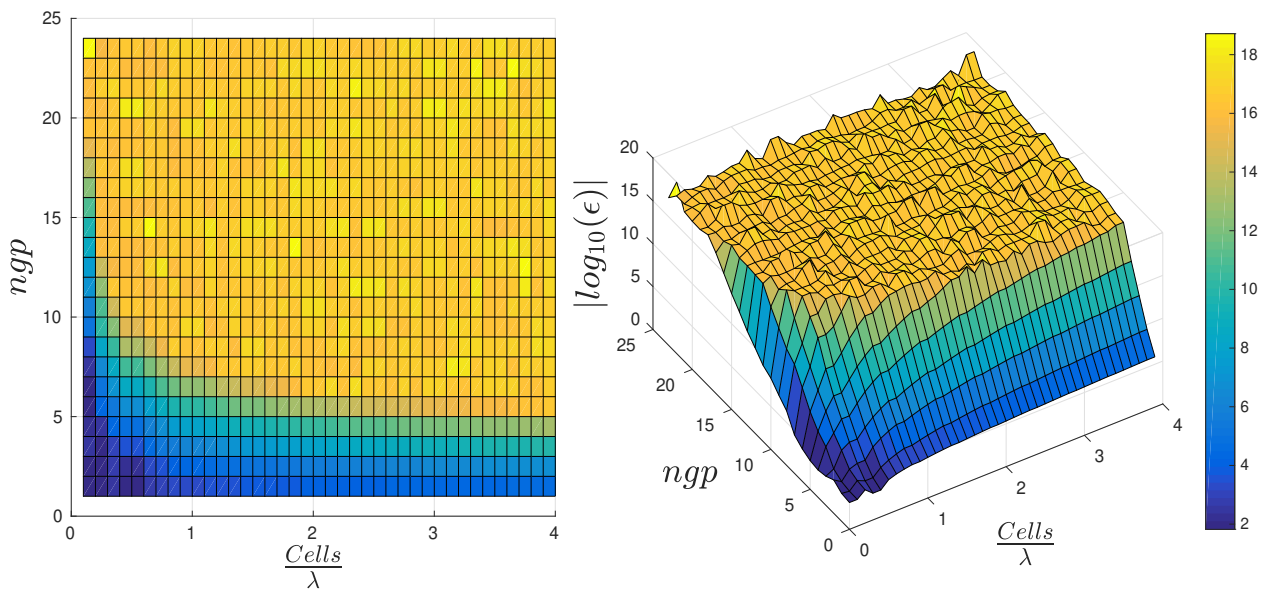


Figure 4.31:  $|Log_{10}(\epsilon)|$  for a straight line element having the starting point  $(x_s, y_s) = (0, 0)$  and end point  $(x_e, y_e) = (1, 0)$ ,  $\theta = 10^\circ$ ,  $r_0 = 1$ ,  $\bar{\phi} = 60^\circ$  and  $k = 100$ .

Firstly, to study the impact that  $k$  has on the accuracy of this example,  $k$  is varied from 1-1000 with cells equal in size to the wavelength and 10 Gauss points are applied over each cell. The results are shown in Fig. 4.32 wherein the relative error  $\epsilon$  gradually increases as  $k$  increases. Note that in the plots in this section, a reduction in the quantity plotted indicates an increase in error. This could become significant for very large  $k$ , but due to the fact that most of the problems of interest do not exceed  $k = 100$  the difference in accuracy experienced as a result of varying  $k$  can be considered to be negligible.

Next, the angle between the source point and the positive  $x$ -direction is fixed, such that  $\theta = 90^\circ$ , but  $\bar{\phi}$  and  $r_0$  are varied, in order to determine what happens to the relative error

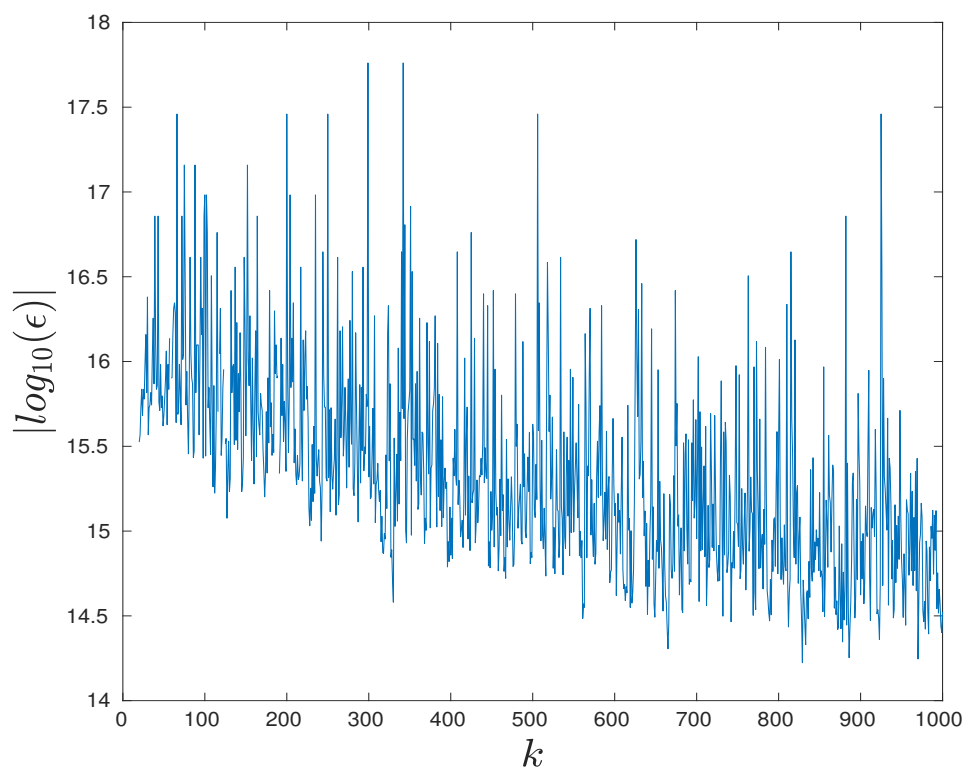


Figure 4.32:  $|Log_{10}(\epsilon)|$  for a straight line element having having the starting point  $(x_s, y_s) = (0, 0)$  and end point  $(x_e, y_e) = (1, 0)$ ,  $\theta = 10^\circ$ ,  $r_0 = 1$ ,  $\bar{\phi} = 60^\circ$  and  $k = 1 - 1000$ .

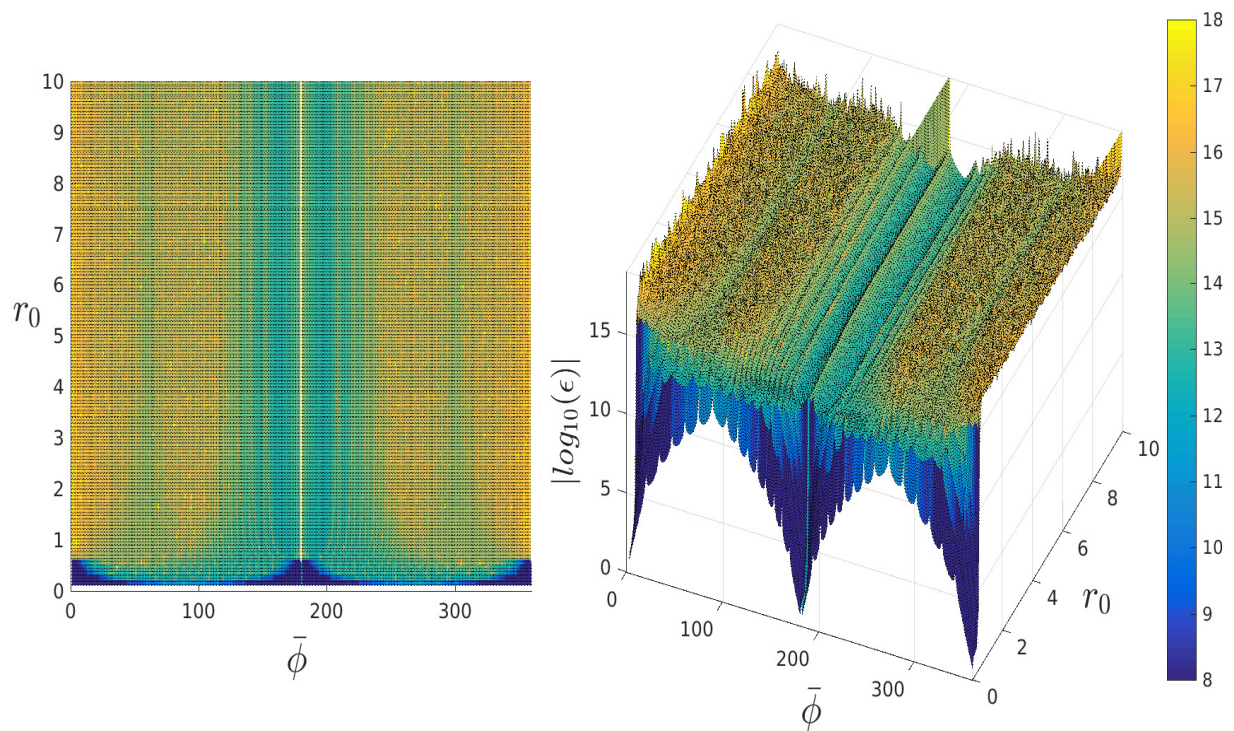


Figure 4.33:  $|\text{Log}_{10}(\epsilon)|$  for a straight line element having the starting point  $(x_s, y_s) = (0, 0)$  and end point  $(x_e, y_e) = (1, 0)$ ,  $0 < \bar{\phi} < 360^\circ$ ,  $r_0 = 1 - 10$ .

$\epsilon$  at different source point locations. The results from this testing are shown in Fig. 4.33, and it is evident that the source point location relative to the element has a substantial impact on the accuracy. For example, as  $r_0$  becomes small the integration error becomes more significant, and unacceptable in some cases. This is expected because the integral becomes near singular as  $r_0$  decreases. Though, as  $r_0$  decreases relative to the  $x_e$  the less oscillatory the integrand becomes. In addition the error reduces where  $\theta = \bar{\phi}$ , which could be a result of cancellation between the enrichment wave and the Green's function. From Fig. 4.33 we can infer the influence of the relationship between  $\bar{\phi}$  and  $\theta$ , i.e. it can be seen that relative error is reduced wherein  $\bar{\phi} = \theta$  due to the cancellation occurring between the enrichment wave and the Green's function. In order to explore this relationship further, a modification is made to the example to use the following parameters:  $x_e = 4$ , with a source point fixed at  $r_0 = 4$  and  $\theta = 90^\circ$  with  $\bar{\phi} = 0-180^\circ$ . The results for this example with  $k = 100$  are shown in Fig. 4.34, and it is clear that whilst using a larger number of Gauss points, the error remains unchanged as  $\bar{\phi}$  varies, but when fewer points are used, the integration error for stationary point cases wherein  $\theta = \bar{\phi}$  is clearly smaller, with the highly oscillatory portions providing a challenge. Notably, for this example it is beneficial to integrate over larger cells, and increase the number of Gauss points to compensate, rather than applying multiple cells per wavelength and relatively fewer Gauss points per cell.

## 4.6.2 Scattering by a square

In order to confirm the number of Gauss points required in a typical scattering simulation, using straight line elements we consider scattering by a unit square. For this example,  $k = 20$  and a single element is employed per side with  $M = 12$  to produce  $\tau \approx 3.8$ . Results for this example are shown in Fig. 4.35 where  $\epsilon$  is the  $L^2$  relative error of the acoustic potential  $\phi$  at a vector of points over the boundary  $\Gamma$  of the square and  $ngp$  is the number of Gauss points per cell. It is clear from Fig. 4.35 that an acceptable level of error is reached comfortably by using a single cell per wavelength with 10 Gauss points in each cell.

In order to determine if there is a 'sweet spot' for  $ngp$  vs.  $\frac{Cells}{\lambda}$  the error is scaled by the total number of Gauss points employed per element (which is equal to  $(ngp)(Cells)$ ), which is shown in Fig. 4.36 by dividing the error by the Gauss points employed per element. A slight benefit is seen by increasing  $ngp$  (rather than decreasing the cell size), but this is less substantial than for the specific single element case shown in Fig. 4.34.

## 4.6.3 Circular arc element

The results above are all based on straight line elements, which have been shown to have fewer stationary points than arc elements, for example. For this reason, attention is turned

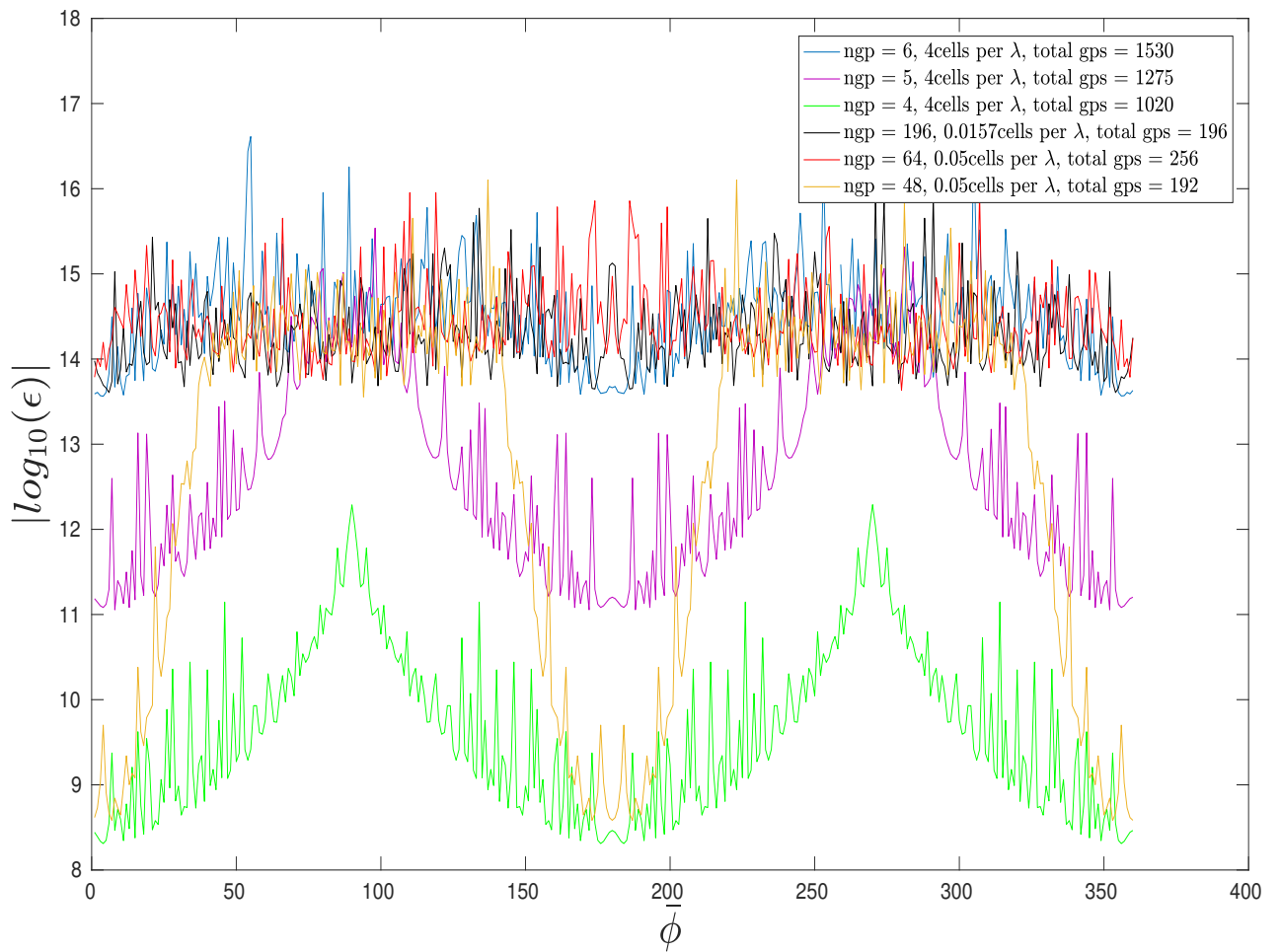


Figure 4.34:  $|Log_{10}(\epsilon)|$  for a straight line element having the starting point  $(x_s, y_s) = (0, 0)$  and end point  $(x_e, y_e) = (4, 0)$ ,  $\theta = 90^\circ$ ,  $r_0 = 4$ ,  $0 < \bar{\phi} < 360^\circ$  and  $k = 100$ .

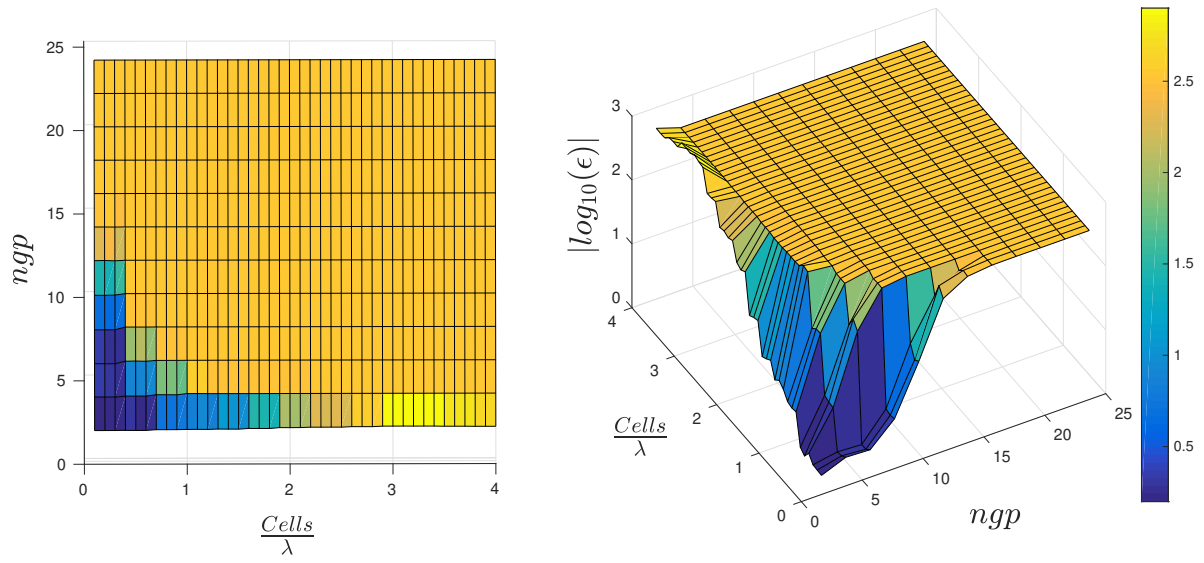


Figure 4.35:  $|Log_{10}(\epsilon)|$  for a square scattering object,  $k = 20$ .

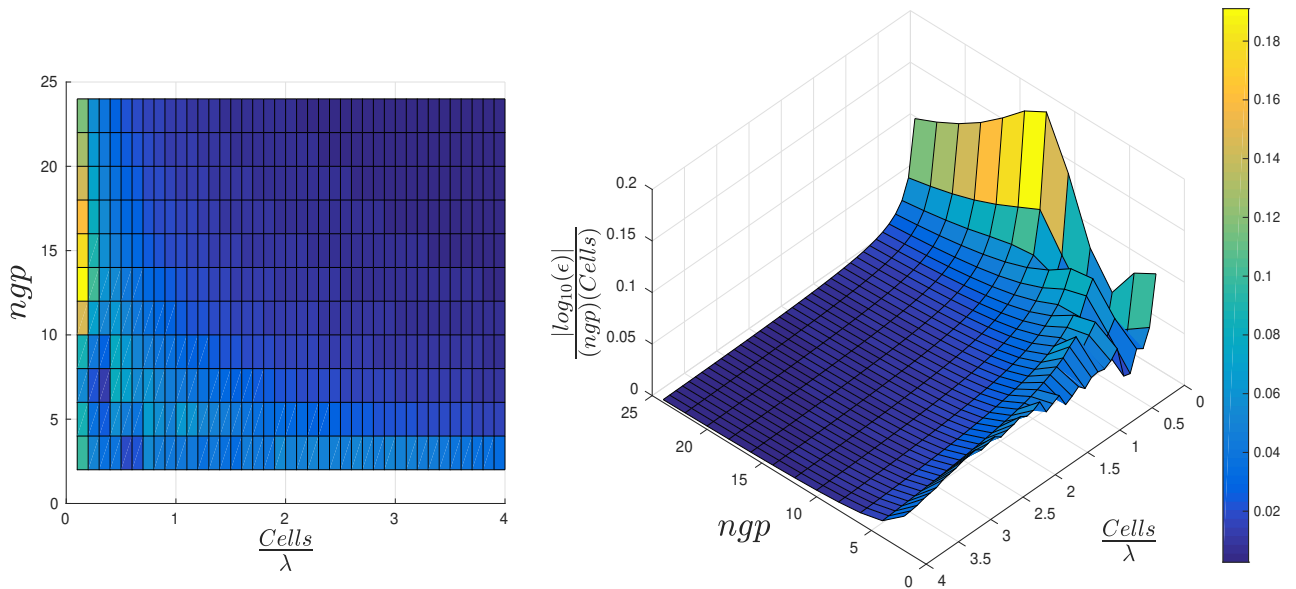


Figure 4.36:  $|Log_{10}(\epsilon)|$  scaled for a square scattering object,  $k = 20$ .

to circular arc elements, to study the difference in numerical behaviour; thus, consider a circular arc element, with a unit radius, of length  $\frac{\pi}{4}$  spanning from the positive  $x$ -direction to the positive  $y$ -direction, with the source point fixed at  $(x_p, y_p) = (10, 10)$  and  $k = 100$ . Results for this case are plotted in Fig. 4.37, which shows similar convergence of relative error  $\epsilon$  as the straight line element results, where again, using larger cells (and  $ngp$ ) shows benefit.

For further insight and as was studied with the straight line element,  $\bar{\phi}$  is varied and the results observed in Fig. 4.38, wherein a very small number of Gauss points is seen to produce very accurate results. Again, there are clear regions in which the integrals computed using relatively fewer Gauss points struggle and this is likely due to more oscillatory behaviour resulting from constructive interference between the Green's function and the enrichment wave.

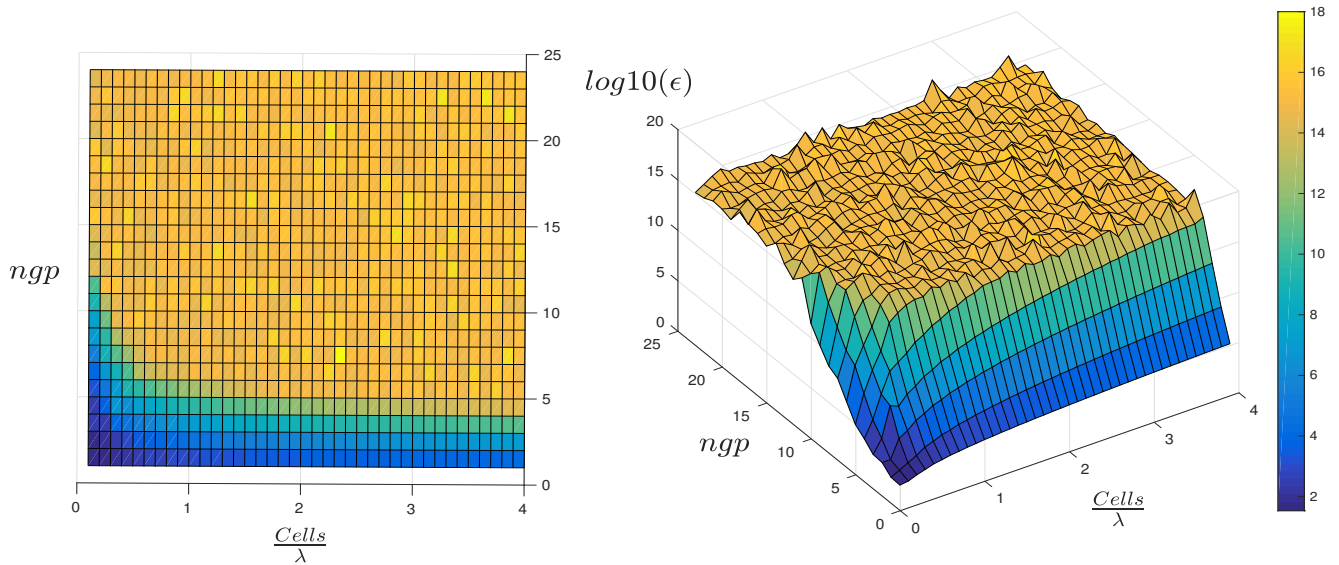


Figure 4.37:  $\text{Log}_{10}(\epsilon)$  for a circular arc element, with a unit radius, of length  $\frac{\pi}{4}$  spanning from the positive  $x$ -direction to the positive  $y$ -direction and having  $x_p, y_p = (10, 10)$ ,  $R = 1$ ,  $\bar{\phi} = 60^\circ$  and  $k = 100$ .

#### 4.6.4 Scattering from a circle

Circular arc elements are now combined to produce an example of scattering by a unit circle. A relatively coarse discretisation is employed, using only 2 elements with  $M = 32$ , and setting  $k = 50$ . This produces  $\lambda = 0.1257$  and  $\tau = 2.5$ . Results are displayed in Fig. 4.39 where  $\epsilon$  is the  $L^2$  relative error of the acoustic potential  $\phi$  at a vector of points over the boundary  $\Gamma$  of the circular scattering object. As can be seen in Fig. 4.39, engineering

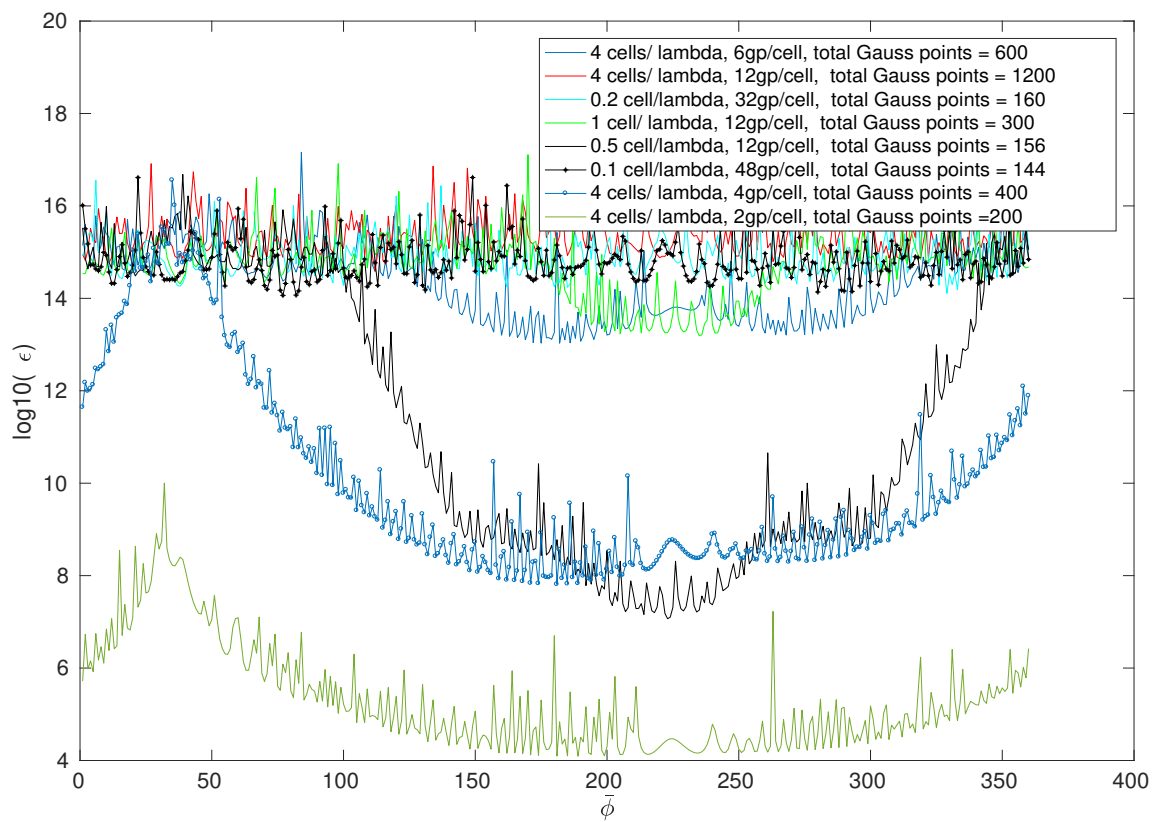


Figure 4.38:  $\text{Log}_{10}(\epsilon)$  for a circular arc element spanning from  $(-1, 0)$  to  $(0, 1)$  and having  $(x_p, y_p) = (10, 10)$ ,  $R = 1$ ,  $0 < \bar{\phi} < 360^\circ$  and  $k = 100$ .

accuracy is comfortably achieved with a single cell per wavelength and 10 Gauss points are used per cell. The error appears to be limited at approximately  $\epsilon = 10^{-3}$ , but that is a limitation of the relatively low  $\tau$ . In order to try and determine a sweet-spot, in a similar manner to the square example, the results in Fig. 4.40 show the error scaled by dividing by the number of Gauss points used per element, which indicates that using larger cells with more Gauss points per cell is beneficial, although this seems less pronounced than when considering only a single element. This confirms the finding of the straight line element and square example.

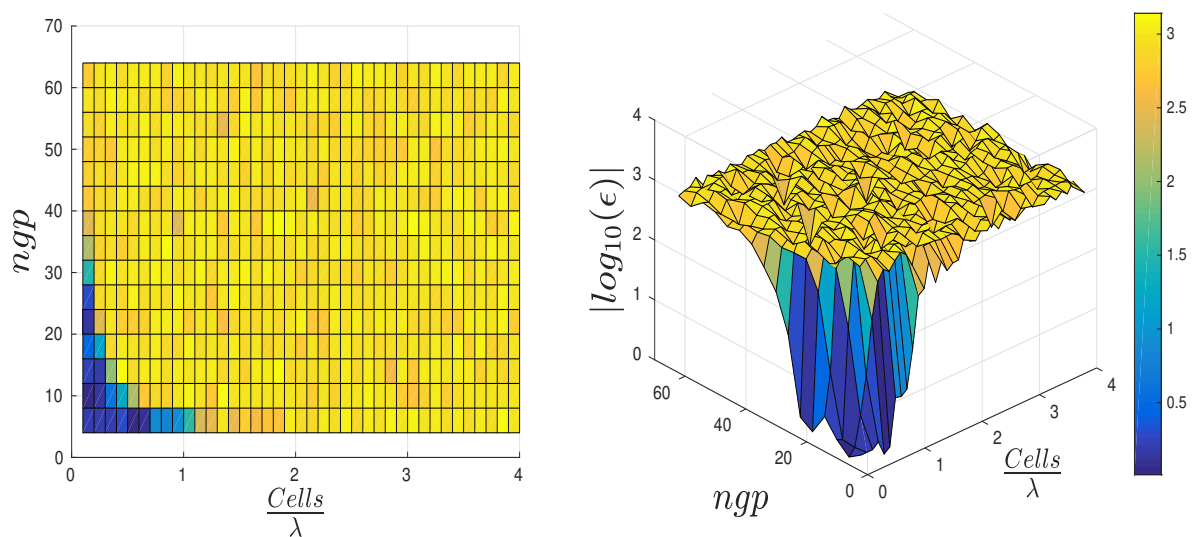


Figure 4.39:  $\text{Log}_{10}(\epsilon)$  for a circular scattering object,  $k = 50$ .

Table 4.4 shows the overall  $L_2$  error for a circular scattering object being impinged by a plane wave, with 4 elements,  $M = 32$  and  $k = 50$ . By varying the number of Gauss points used per cell, along with the cell size we see variations in error, and can use the total number of Gauss points as a marker for how efficient each scheme is. It is evident from Table 4.4 that there is benefit in using larger cells, though the benefit is less pronounced than when considering only a single element. As it was observed that reducing the distance between the source point and the interval of integration can cause a dramatic drop in accuracy, it is necessary to inspect the system matrix. The matrix can be computed by using a highly refined Gauss scheme, then a scheme with fewer points and noting where the largest errors are incurred, to see if there is a pattern or a dependence on  $r$ . This is shown in Fig. 4.41 wherein the diagonal terms contain the largest errors, which

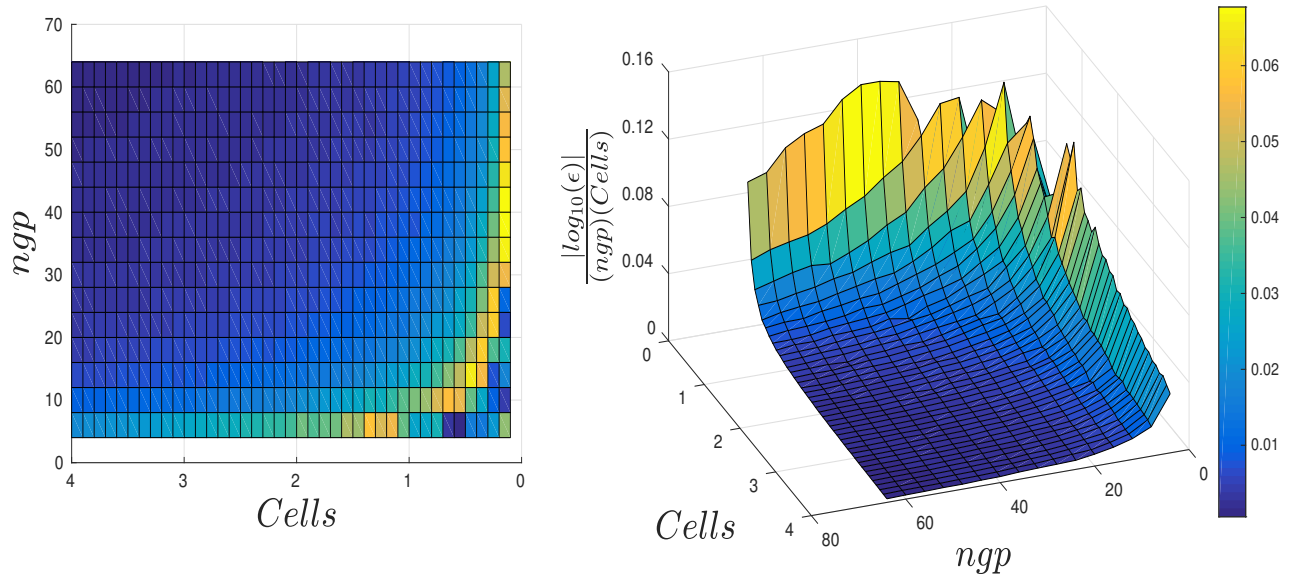


Figure 4.40:  $\text{Log}_{10}(\epsilon)$  scaled for a circular scattering object,  $k = 50$ .

$ngp$	$Cells/elem$	Total Gauss points	Points/ $\lambda$	$L_2error$
84	2	672	13.44	$1.0358e - 05$
64	2	512	10.24	$6.2163e - 05$
48	2	384	7.68	$1.1070e - 04$
32	2	256	5.12	$3.1524e - 04$
24	2	192	3.84	0.0031
48	1	192	3.84	0.0041
6	50	1200	24	$1.7693e - 06$
4	50	800	16	$5.4995e - 06$
2	50	400	8	$7.1584e - 05$
2	38	304	6.08	$2.6526e - 04$
2	25	200	4	0.0488

Table 4.4:  $L_2$  error for circular scattering object,  $k = 50$ ,  $E = 4$ ,  $M = 32$ .

could suggest that the reduction in  $r$  (i.e. the distance between the source point and the field point) is driving the overall error. Though, the diagonal terms in the matrix are typically the larger terms, thus one might expect the errors to be larger, we may mitigate the impact of the varying magnitude of the matrix terms by using a relative error. This relative error is shown in Fig. 4.42, in which there are still larger errors clustered around the diagonal terms.

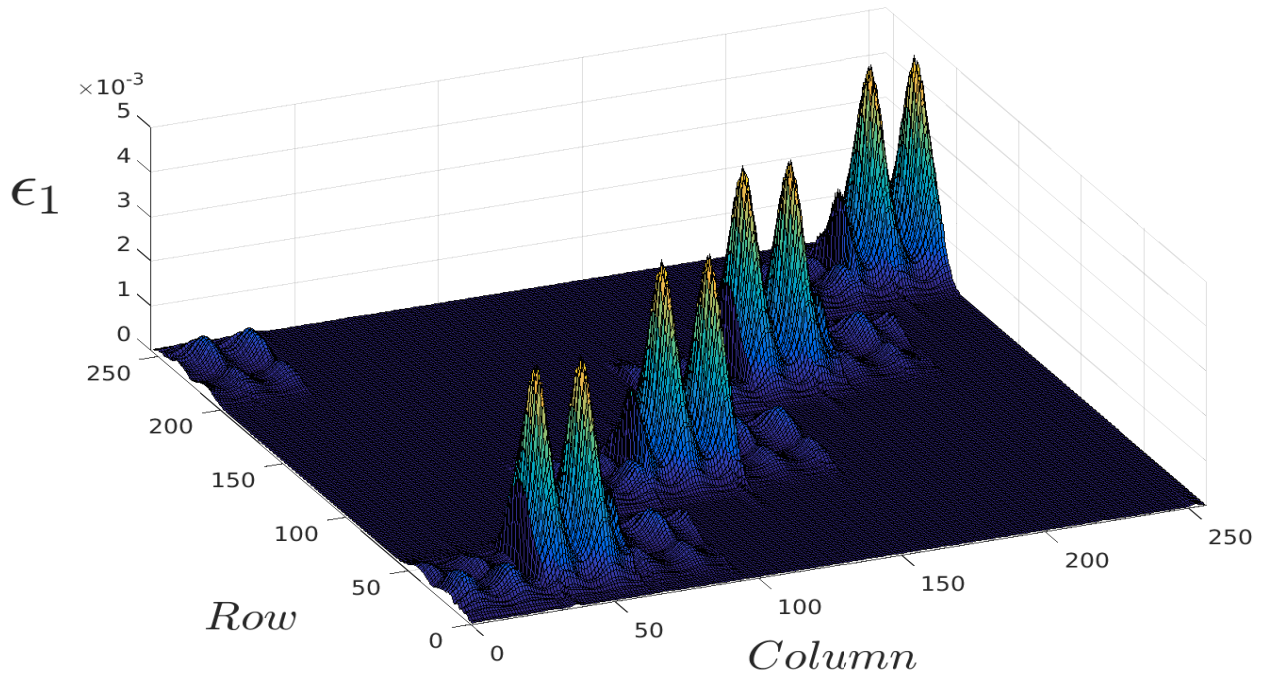


Figure 4.41: Absolute error in matrix terms for scattering by a circle, with  $E = 4$ ,  $M = 32$  and  $k = 50$ .

In order to reduce the impact that the dominant terms in the matrix have on the overall error we may apply additional Gauss points to cases wherein the source point lies within the interval of integration; i.e., increasing  $ngp$  or reducing the cell size. The result of including extra Gauss points in these key areas can be seen in Table 4.5 wherein  $ngp_{extra}$  represents the number of Gauss points employed when the source point is within the element of interest. Four schemes are compared and improved results are presented, such as, a requirement of only 3.12 Gauss points being required to achieve engineering accuracy by using a sufficiently large  $ngp$  and  $ngp_{extra}$  with a relatively large cell size.

To add an extra level of analysis, the schemes described in Table 4.5 are employed for varying  $k$ , with the results shown in Table 4.6. The results show that even whilst varying  $k$  the accuracy is relatively consistent, which of course, is important.

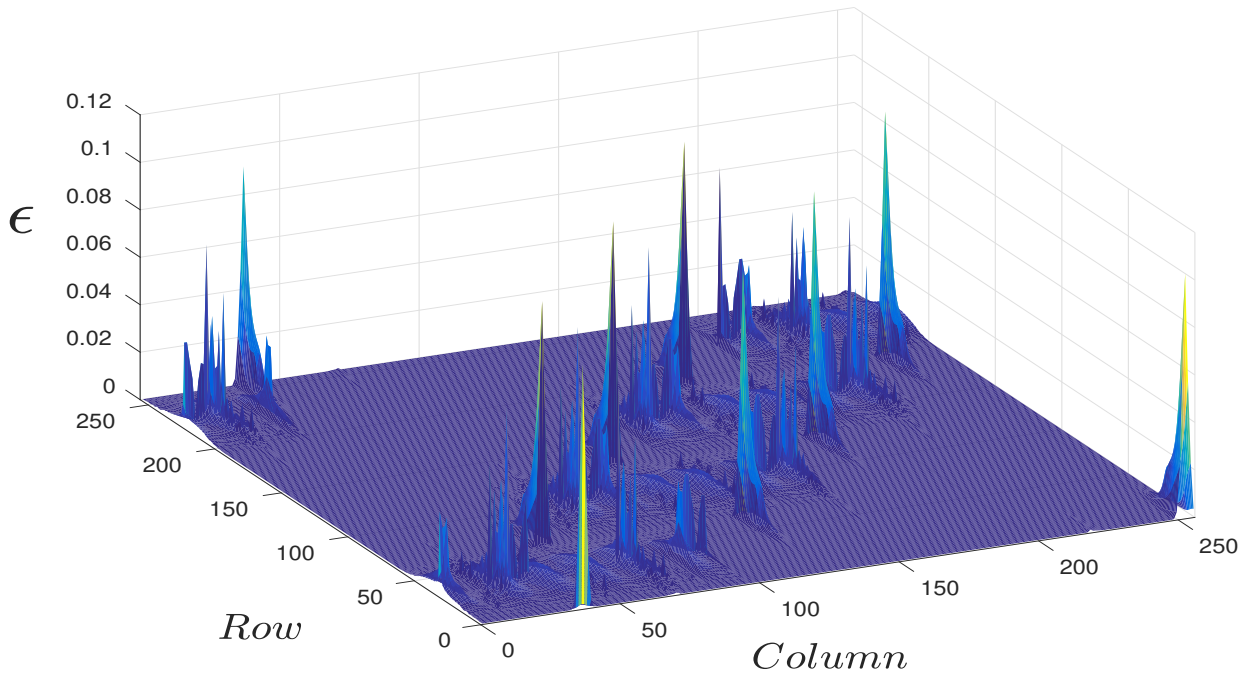


Figure 4.42: Relative error in matrix terms for scattering by a circle, with  $E = 4$ ,  $M = 32$  and  $k = 50$ .

<i>scheme</i>	<i>ngp</i>	<i>ngp<sub>extra</sub></i>	<i>Cells/elem</i>	Total Gauss points	Points/ $\lambda$	$L_2error$
1	48	64	1	208	4.16	$2.4006e - 04$
2	24	48	2	240	4.8	$1.3676e - 04$
3	24	32	2	208	4.16	$1.7810e - 04$
4	18	24	2	156	3.12	0.0043

Table 4.5:  $L_2$  error for circular scattering object,  $k = 50$ ,  $E = 4$ ,  $M = 32$ .

<i>k</i>	<i>scheme1</i>	<i>scheme2</i>	<i>scheme3</i>	<i>scheme4</i>
60	$2.5282e - 04$	$8.0090e - 05$	$1.6653e - 04$	0.0050
70	$1.9697e - 04$	$5.1083e - 05$	$7.6694e - 05$	0.0021
80	$1.5642e - 04$	$7.7985e - 05$	$8.1775e - 05$	0.0019
90	$1.9892e - 04$	$3.2763e - 05$	$5.3659e - 05$	0.0014
100	$7.0376e - 05$	$6.0350e - 05$	$7.6733e - 05$	0.0011

Table 4.6:  $L_2$  error for circular scattering object,  $k = 60 - 100$ ,  $E = 4$ ,  $M = 38 - 64$ .

### 4.6.5 Scattering by a capsule

A final example of scattering by a capsule is presented. The capsule is defined according to Fig. 4.43 wherein  $R = 1$ . The  $\phi_{inc} = 0$  is studied with with the following parameters:  $E = 4$ ,  $M = 32$ , and  $k = 50$  which results in  $\tau \approx 2.6$ . The real part and absolute value of the total potential are shown in Fig. 4.44. Using similar Gauss-Legendre schemes to the schemes employed for the circle, the results of Table 4.7 are produced, which are not quite as accurate as the results for the circle, though it is clear that achieving engineering accuracy with approximately 4 Gauss points per wavelength is possible.

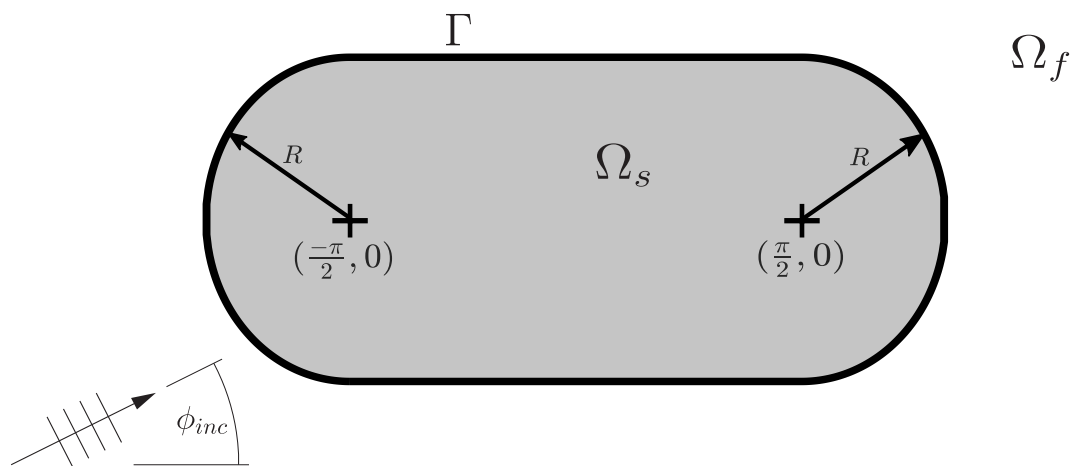


Figure 4.43: Capsule geometry.

<i>scheme</i>	<i>ngp</i>	<i>ngp<sub>extra</sub></i>	<i>Cells/elem</i>	Total Gauss points	Points/ $\lambda$	$L_2error$
1	48	64	1	400	4.0	$5.8286e - 04$
2	28	48	2	448	4.8	$5.5610e - 04$
3	26	32	2	428	4.28	$5.6831e - 04$
4	42	48	2	342	3.42	0.0134

Table 4.7:  $L_2$  relative error  $\epsilon$  for scattering by a capsule,  $R = 1$   $k = 50$ ,  $E = 8$ ,  $M = 32$ .

### 4.6.6 Conclusion

From the above results, it appears that relatively few Gauss points are required (somewhere in the region of 4 per wavelength) to achieve engineering accuracy. This is a positive result due to the fact that it is difficult to construct a robust alternative to Gauss-Legendre. These results are for full scattering problems, including a variety of elements and a suitable range of plane-wave enrichment directions. For special cases wherein  $\theta$  and  $\bar{\phi}$  combine favourably, highly accurate results can be achieved with significantly few Gauss points, but as seen in the results for the highly-oscillatory integration

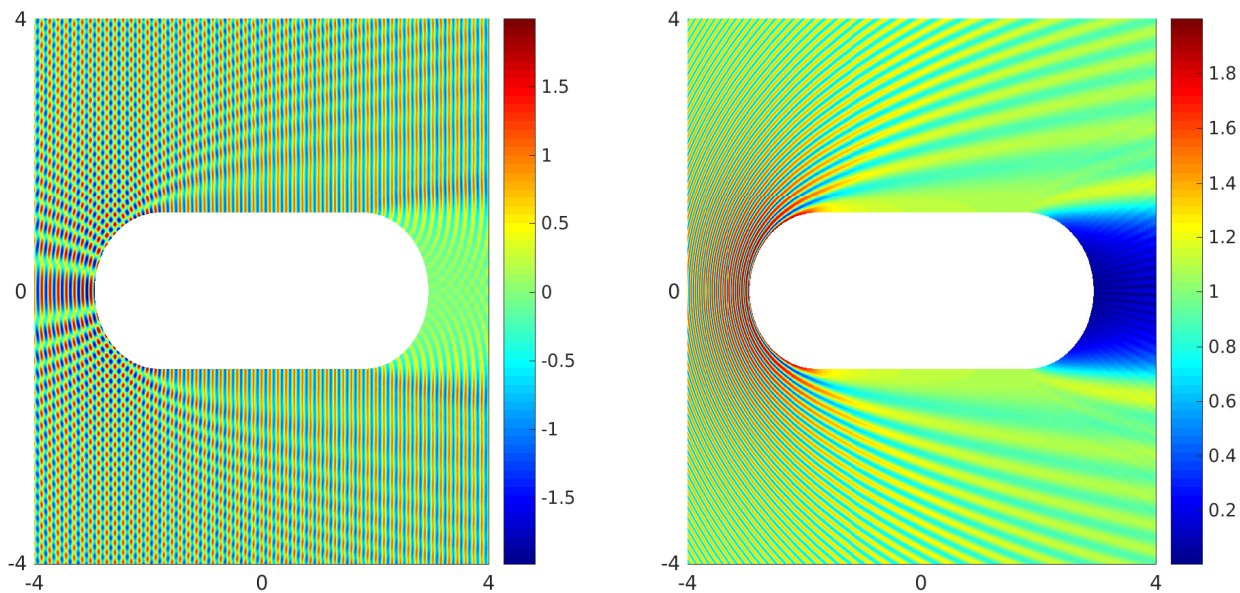


Figure 4.44: (left) Real part of the total potential, (right) absolute value of total potential. Capsule scatterer for the case  $k = 50$ .

schemes, there will usually exist some more challenging cases, which dictate the overall results.

## 4.7 Summary

In this chapter, integration schemes which are designed specifically for evaluating highly oscillatory integrals, such as the Filon method, the asymptotic method, the method of stationary phase, and a targeted Gauss-Legendre implementation, have been tested for PUBEM integrals over straight line and circular arc elements. These integration schemes performed very well for particular integrals tested, namely when  $\lambda$  is small relative to the element length, or in the absence of stationary points. Though, for the majority of cases, these methods will not evaluate integrals with sufficient precision to achieve engineering accuracy of 1% in the overall solution. A common feature of the problematic cases is the presence of a stationary point near the end of an element. Further, the cases tested in this chapter involve relatively simple geometries comprising straight line and circular arc elements. One might expect more complicated geometries to cause further difficulty for integration schemes designed specifically for evaluating highly oscillatory integrals for two reasons. Firstly, because there would likely be an increase in the number of stationary points, and the location of these stationary points may only be retrievable via an iterative method. Secondly, the formulation of the integration schemes will become more complicated, for example, the coordinate transformation and computation of derivatives

required for the Filon method are simple for a straight line element, but for generalised elements,  $g(\xi)$  would likely be more complicated and it may not be possible to evaluate required derivatives analytically.

Further testing in section 4.6 revealed the efficacy of traditional Gauss-Legendre integration for PUBEM integrals. Specifically, a tailored Gauss-Legendre integration scheme, such tailoring involving using multiple integration cells per element. The impact that integration cell size and the number of Gauss points per integration cell has on the overall solution has been tested for smooth and polygonal geometries. It is possible to achieve engineering accuracy for some geometries using fewer than 4 Gauss points per wavelength, but for general cases the results of section 4.6 suggest that using very high-order Gauss integration over a small number of cells can be sufficient to achieve engineering accuracy.

# Chapter 5

## Singular enrichment functions for wave scattering by polygons

### 5.1 Introduction

In previous chapters, wave scattering problems have been presented and solved, predominantly for smooth scattering objects. Introducing corners into scattering problems, for example wave scattering from polygonal objects, such as that shown in Fig. 5.1, provides additional difficulty for numerical solvers. This additional difficulty arises because the corner locations introduce singular behaviour into the scattered fields. A conventional BEM basis comprising polynomial shape functions does not contain any singular behaviour, thus typically requires relatively small elements at corner locations. Similarly, whilst well suited to high frequency problems, the plane-wave basis of PUBEM does not include singular behaviour.

Numerical methods, outside of BEM, have been developed to tackle the increase in degrees of freedom required that is associated with singularities. This is seen, for example, in the eXtended Finite Element Method (XFEM) in which localised enrichment using singular functions enhances the computational efficiency in solving fracture mechanics problems. The asymptotic singular behaviour at corner locations is known and can be inserted into the approximation space to improve efficiency. This approach has been taken for Laplace operators [81]; in a UVWF setting [82]; in an MFS setting [83, 84], and in an FEM setting [85] where the effect of corner singularities on pollution is studied. As mentioned, when using a conventional set of basis functions without enrichment, relatively small elements will likely be required, though only in locations in which the effect of singular behaviour is present in the solution, i.e. not at locations remote from corners. With this knowledge, alternate schemes have been developed to reduce the number of degrees of freedom required for geometries containing corners, for example, using a graded mesh along with a preconditioning strategy [79] and utilising a fast solver [80].

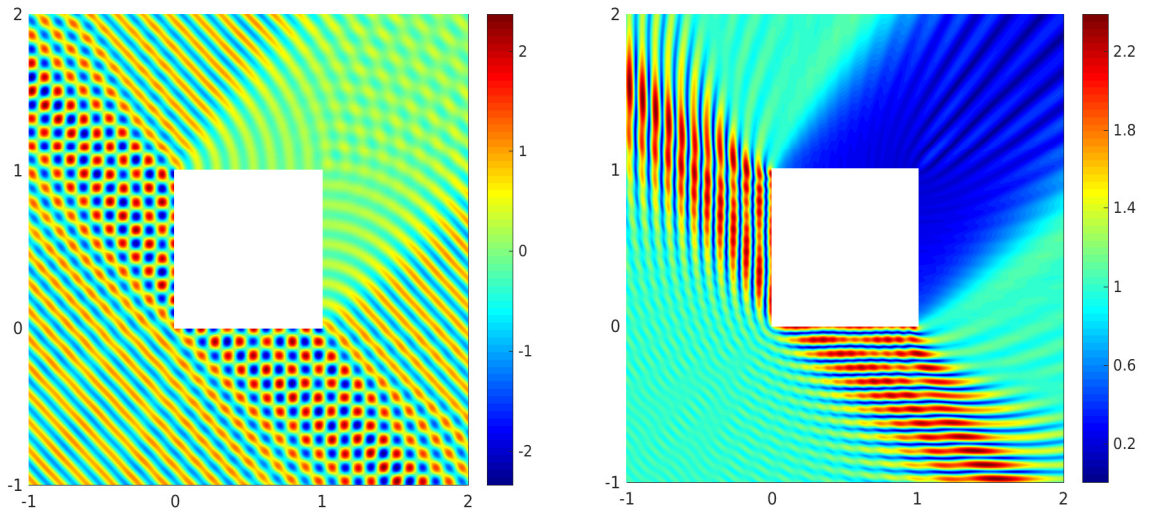


Figure 5.1: (left) Real part of the total potential, (right) absolute value of total potential. Unit square scatterer for the case  $k = 50$ .

In this chapter, the BEM and PUBEM basis functions, described in sections 3.4 and 3.5 respectively, are extended to include further enrichment which is geared towards modelling scattering from corners. The aim of this further enrichment is to increase the efficiency, from a  $\tau$  standpoint, with which BEM and PUBEM can solve the Helmholtz equation in the presence of corners. The further enriched BEM formulation will be referred to herein as eXtended Boundary Element Method (XBEM) and the further enriched PUBEM formulation will be referred to herein as Partition of Unity eXtended Boundary Element Method (PUXBEM).

The Helmholtz problems considered in this section involve scattering from sound-hard objects, with corners. Each polygonal object is defined as  $\Omega_s \subset \mathbb{R}^2$  and with a boundary  $\Gamma$ . To form the requisite BIEs for XBEM and PUXBEM, the Neumann Sound-hard boundary condition is used, wherein

$$\nabla\phi(\mathbf{x}) \cdot \mathbf{n} = 0, \quad \mathbf{x} \in \Gamma \quad (5.1)$$

where  $\mathbf{n}$  is the unit normal at  $\mathbf{x}$ .

## 5.2 XBEM formulation

To form the XBEM BIE, including the singular enrichment, we begin with the BIE for exterior domains (3.25) then apply the Neumann sound-hard boundary condition (5.1) to produce the following

$$c(\mathbf{p})\phi(\mathbf{p}) + \int_{\Gamma} \frac{\partial G(\mathbf{p}, \mathbf{q})}{\partial \mathbf{n}} \phi(\mathbf{q}) d\Gamma_q = \phi^{inc}(\mathbf{p}), \quad \mathbf{p}, \mathbf{q} \in \Gamma \quad (5.2)$$

where  $c(p)$  at corner locations is defined by the exterior angle associated with the corner, as shown in Fig. 3.3, elsewhere  $c(p) = \frac{1}{2}$ . The incident wave, which is being scattered by polygon  $\Omega_s$ , is denoted  $\phi^{inc}$ . In a conventional BEM formulation, as described in section 3.4, a polynomial basis is employed, to describe the acoustic potential  $\phi$  over each element as follows,

$$\phi = \sum_{j=1}^J \Psi_j(\xi) \phi_j^e, \quad (5.3)$$

wherein  $\phi$  is described at node  $j$  of element  $e$  and  $\xi \in [-1, 1]$ . It is common to take  $J = 3$ , and employ Lagrangian shape functions, which take the form

$$\Psi_1 = \frac{1}{2}\xi(\xi - 1) \quad (5.4)$$

$$\Psi_2 = (1 - \xi)(1 + \xi) \quad (5.5)$$

$$\Psi_3 = \frac{1}{2}\xi(\xi + 1). \quad (5.6)$$

Discretising  $\Gamma$  into  $E$  elements and applying the description of  $\phi$  shown in (5.3) over each element in the discretisation produces

$$c(\mathbf{p})\phi(\mathbf{p}) + \sum_{e=1}^E \sum_{j=1}^J \int_{-1}^1 \frac{\partial G(\mathbf{p}, \mathbf{q})}{\partial \mathbf{n}} \Psi_j(\xi) J^e d\xi \phi_j^e = \phi^{inc}(\mathbf{p}), \quad \mathbf{p}, \mathbf{q} \in \Gamma \quad (5.7)$$

where  $J^e$  is the Jacobian of the geometric mapping  $(x, y) \rightarrow \xi$ . In order to include the singular enrichment required to form XBEM, we augment the polynomial expansion (5.3) to include additional functions  $\psi$ , as follows

$$\phi = \sum_{j=1}^J \Psi_j(\xi) \phi_j^e + \sum_{l=1}^L \psi_l(\xi) \tilde{\phi}_l^e \quad (5.8)$$

wherein  $\psi_l$  represents term  $l$  in an expansion including a total of  $L$ , not yet defined, singular shape functions. Including this enrichment in the discretised BIE (5.7) produces

the XBEM discretisation

$$\begin{aligned}
c(\mathbf{p})\phi(\mathbf{p}) + \sum_{e=1}^E \sum_{j=1}^J \int_{-1}^1 \frac{\partial G(\mathbf{p}, \mathbf{q})}{\partial \mathbf{n}} \Psi_j(\xi) J^e d\xi \phi_j^e \\
+ \sum_{e=1}^E \sum_{l=1}^L \int_{-1}^1 \frac{\partial G(\mathbf{p}, \mathbf{q})}{\partial \mathbf{n}} \psi_l(\xi) J^e d\xi \tilde{\phi}_l^e = \phi^{inc}(\mathbf{p})
\end{aligned} \tag{5.9}$$

which can be solved in the same way that a conventional BIE can be solved, though now, over  $\Gamma$ , the potential  $\phi$  will be recovered from the combination of functions, shown in (5.8).

### 5.3 PUXBEM formulation

To form the PUXBEM BIE, including the singular enrichment, we first remember the form of PUBEM basis (3.39) from section 3.5, as follows

$$\phi = \sum_{j=1}^J \sum_{m=1}^M \Psi_j(\xi) A_{jm}^e e^{ik\mathbf{d}_{jm} \cdot \mathbf{q}}, \tag{5.10}$$

wherein  $\phi$  is described over the element  $e$ ,  $M$  is the total number of plane-waves per node,  $\xi \in [-1, 1]$ , and

$$\mathbf{d}_{jm} = (\cos \bar{\phi}_{jm}, \sin \bar{\phi}_{jm}), \quad \bar{\phi}_{jm} = \frac{2\pi(m-1)}{M}. \tag{5.11}$$

Therefore, the discretised PUBEM BIE for exterior problems, with the Neumann sound-hard condition (5.1) condition imposed, is

$$c(\mathbf{p})\phi(\mathbf{p}) + \sum_{e=1}^E \sum_{j=1}^J \sum_{m=1}^M \int_{-1}^1 \frac{\partial G(\mathbf{p}, \mathbf{q})}{\partial \mathbf{n}} \Psi_j(\xi) e^{ik\mathbf{d}_{jm} \cdot \mathbf{q}} J^e d\xi A_{jm}^e = \phi^{inc}(\mathbf{p}), \quad \mathbf{p}, \mathbf{q} \in \Gamma \tag{5.12}$$

which forms our starting point for PUXBEM. In order to include the singular enrichment required to form PUXBEM, we augment the PUBEM basis (5.10) to include the additional functions  $\psi$ , as follows

$$\phi = \sum_{j=1}^J \sum_{m=1}^M \Psi_j(\xi) A_{jm}^e e^{ik\mathbf{d}_{jm} \cdot \mathbf{q}} + \sum_{l=1}^L \psi_l(\xi) B_l^e, \tag{5.13}$$

wherein  $\psi_l$  corresponds to the  $\psi_l$  from (5.8) in the XBEM formulation. Including this enrichment in the discretised PUBEM BIE (5.12) produces the PUXBEM discretisation,

as follows

$$\begin{aligned}
c(\mathbf{p})\phi(\mathbf{p}) + \sum_{e=1}^E \sum_{j=1}^J \sum_{m=1}^M \int_{-1}^1 \frac{\partial G(\mathbf{p}, \mathbf{q})}{\partial \mathbf{n}} \Psi_j(\xi) e^{ik\mathbf{d}_{jm} \cdot \mathbf{q}} J^e d\xi A_{jm}^e \\
+ \sum_{e=1}^E \sum_{l=1}^L \int_{-1}^1 \frac{\partial G(\mathbf{p}, \mathbf{q})}{\partial \mathbf{n}} \psi_l(\xi) J^e d\xi B_l^e = \phi^{inc}(\mathbf{p}), \quad \mathbf{p}, \mathbf{q} \in \Gamma
\end{aligned} \tag{5.14}$$

where  $B_l^e$  can be thought of as amplitudes of the singular enrichment functions.

## 5.4 Modified basis functions

So far, the process of forming the XBEM and PUXBEM BIEs has been presented, which involves augmenting each BIE to include singular functions  $\psi_l$ , though the function itself has not been defined. As mentioned, the local behaviour of the solution at corner location is known, or rather the asymptotic behaviour can be represented by a series solution [91], as

$$\phi(r_b, \theta_b) \approx \sum_{n=1}^N J_{n\alpha}(kr_b) \cos n\alpha\theta_b, \quad 0 < \frac{\pi}{\alpha} < 2\pi, \tag{5.15}$$

for the Neumann case, where  $J_{n\alpha}$  are Bessel functions which are of fractional order due to the combination of  $\alpha$  and  $n$ .  $r_b$  is the Euclidean distance from a corner to a given point and  $\theta_b$  is the angle from a planar surface adjacent to the corner to given point, both  $r_b$  and  $\theta_b$  are shown in Fig. 5.2. The variable  $\alpha$  can be defined in terms of the exterior angle at the corner which is  $\pi/\alpha$ . Consider the example of a right-angle, such as a corner of a square,  $\alpha = 2/3$  as dictated by the above definition. If one takes  $k = 20$ , for the same example, and plots the first six terms in the series Fig. 5.3 is produced. From this plot of the family of Bessel functions, it is clear that, at  $r_b = 0$ , only the first term ( $J_{2/3}(kr_b)$ ) in the series contains a singular gradient. Therefore, this term is the candidate for use as an enrichment function. Thus, as opposed to some of the literature, such as Luostari et al. [82] and Barnett & Betcke [83], only the first term is used as enrichment for XBEM and PUXBEM. This is due to the target of efficient solution using small  $\tau$ , i.e. including more terms in the series (that are not singular) will add to the total number of degrees of freedom used, though not substantially contribute to capturing the singular behaviour at corner locations. A second alternative  $r_b^\alpha$  is also considered as a candidate for  $\psi_l$  because the asymptotic behaviour of the Bessel function candidate, for a small argument, is of the form  $r_b^\alpha$ . Therefore, the two candidate enrichment functions  $\psi_{1,l}$  and  $\psi_{2,l}$  are defined as follows

$$\psi_{1,l} = r_b^\alpha \cos l\alpha\theta_b \tag{5.16}$$

$$\psi_{2,l} = J_{l\alpha}(kr_b) \cos l\alpha\theta_b. \tag{5.17}$$

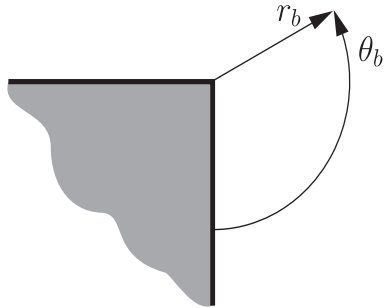


Figure 5.2: Polar coordinate system local to a corner.

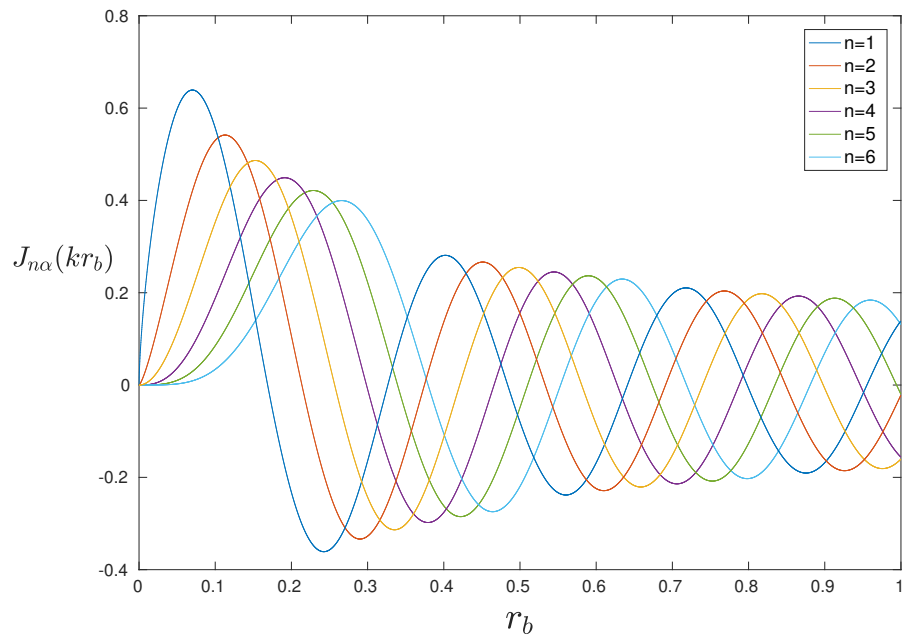


Figure 5.3: Bessel functions with  $n = 1-6$ ,  $\alpha = \frac{2}{3}$  and  $k = 20$ .

As the evaluation of  $\psi_{1,l}$  and  $\psi_{2,l}$  is only required on the boundary  $\Gamma$ ,  $\theta_b$  will be a constant on each planar surface, adjacent to the corner of interest. As an example, consider two planar surfaces of a square, meeting at a right-angle, substantially corresponding to those shown in Fig. 5.2,  $\theta_b$  would take one of two values:  $\theta_b = 0$  and  $\theta_b = 3\pi/2$ . This provides two options for implementation of the enrichment: formulation *A* wherein two degrees of freedom are associated with each singular enrichment function, i.e. a separate degree of freedom corresponding to each of the edges meeting at the corner in question; and formulation *B* wherein a single degree of freedom is associated with each enrichment function.

The cosine term in (5.15)-(5.17) describes the smooth variation in potential in the circumferential direction in the vicinity of the corner. While this is of great importance in finite element and UWVF implementations, we note that in a BEM context we are required to evaluate only the trace of the functions on the boundary, i.e. inserting  $\theta_b$  into the argument, which will take the value of either 0 or  $3\pi/2$ , for a right-angled corner. For clarity, formulation *A* and formulation *B* are laid out below. Formulation *A*:

$$\bar{u}_L^e \neq \bar{u}_1^{e+1} \quad (5.18)$$

$$B_L^e \neq B_1^{e+1} \quad (5.19)$$

Formulation *B*:

$$\bar{u}_L^e = \bar{u}_1^{e+1} \quad (5.20)$$

$$B_L^e = B_1^{e+1} \quad (5.21)$$

Notably, similarly to the plane-wave basis of PUBEM, enriching with Bessel functions can introduce the requirement to evaluate highly oscillatory integrals. As the focus of this study into singular enrichment is the efficacy of the functions themselves, a subdivided Gauss-Legendre integration scheme is employed with a sufficient number of cells and Gauss points per cell to remove any integration error from the results.

In subsequent sections,  $L^2$  error  $\epsilon$  is computed for a number of Helmholtz problems.  $\epsilon$  is taken to be relative error when analysing scalar results and  $L^2$  relative error when analysing a vector of results. The definition of  $\epsilon$  can be found in Appendix *C*. The reference solutions with which the XBEM and PUXBEM are compared against are obtained by using converged BEM or PUBEM schemes, depending on the problem. This requirement to produce accurate reference solutions restricts the analysis to problems in the low-mid frequency range.

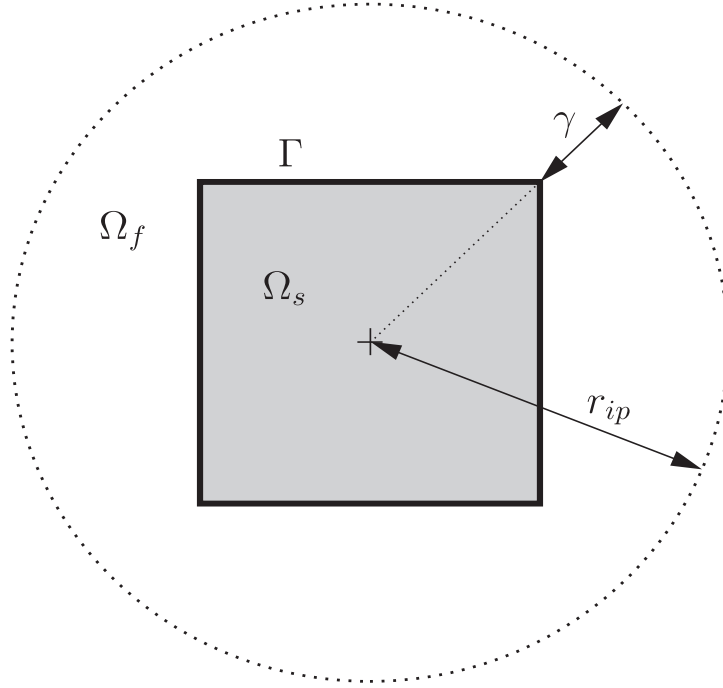


Figure 5.4: Internal point locations for a square scattering object.

### 5.4.1 Square scattering object

A first example is presented here, comprising a unit square scattering object, a schematic representation of which is shown in Fig. 5.4 wherein a ring of internal points is presented. This ring of internal points is defined in terms of a radius  $r_{ip}$  from the centre of the square scattering object, and the distance  $\gamma$  with which the radius extends past the corners of the square scattering object, i.e.  $r_{ip} = \sqrt{0.5^2 + 0.5^2} + \gamma$  for the unit square. In this example, the square scattering object is impinged by a plane-wave  $\phi^{inc}$  propagating at an angle of  $\frac{\pi}{4}$  from the positive  $x$ -axis, with  $k = 20$  and  $\gamma = 1$ . The acoustic potential  $\phi$  is evaluated over the boundary  $\Gamma$  then at the ring of internal points, according to section 3.4, using BEM, XBEM and PUXBEM. The results of this analysis can be seen in Fig. 5.5, where the degrees of freedom (DoF) are varied and the corresponding  $L^2$  relative error  $\epsilon$  is plotted.  $\psi_1$  and  $\psi_2$  represent the different singular enrichment functions, as defined in section 5.4.

From Fig. 5.5, it is clear that, per DoF, the enriched schemes significantly outperform standard BEM. XBEM using either form of singular enrichment function significantly outperforms standard BEM. The PUXBEM schemes, which include both singular enrichment and plane-wave enrichment offer further improvement, with reduction in  $\epsilon$  of over two orders of magnitude. Notably, for both XBEM and PUXBEM, the form of singular enrichment, i.e.  $\psi_1$  and  $\psi_2$  perform similarly, though  $\psi_2$  which contains the fractional order Bessel functions consistently (but marginally) outperforms  $\psi_1$ .

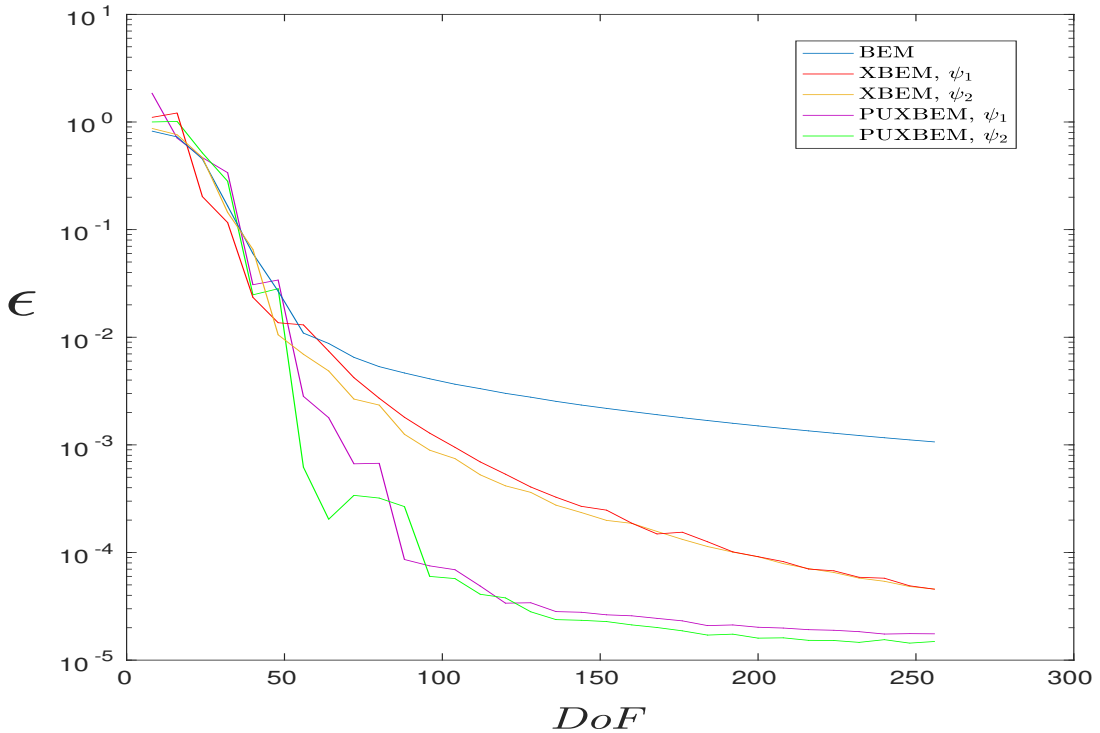


Figure 5.5:  $L^2$  relative error  $\epsilon$  vs. DoF,  $k = 20$ .

In order to produce the plot shown in Fig. 5.5, the wavenumber  $k$  was fixed, which restricts the analysis to a single frequency, but allows analysis of the effect that the number of degrees of freedom has on the solution, using the differing schemes. To provide further insight, the number of degrees of freedom are fixed at 128, for the same geometry and angle of incidence but with varying  $k$ . The results of which, evaluated at the same ring of internal points, i.e.  $\gamma = 1$  are shown in Fig. 5.6. In this example we find that, again, the enriched schemes XBEM and PUXBEM are substantially more accurate than standard BEM. Further, it can be seen in Fig. 5.6 that the  $\psi_2$  enriched schemes outperform the  $\psi_1$  enriched schemes.

Notably, from Fig. 5.6, for low  $k$  XBEM schemes are the most accurate, though, the  $L^2$  relative error incurred by the XBEM schemes creeps up towards that of the BEM scheme, as  $k$  increases. This increase in error is not entirely surprising because when  $k$  increases, the singularity will become less dominant in comparison to the multiple wavelengths across the edge of the scattering object. Therefore, at large  $k$ , each scheme must be able to represent the comparatively higher frequency behaviour across each edge, and the XBEM scheme is similarly equipped to the standard BEM scheme, i.e. comprising a (predominantly) polynomial basis. Whereas the PUXBEM basis includes plane-waves which can maintain accuracy more easily as frequency increases. Therefore, it can be understood, from Fig. 5.6 that XBEM is the superior scheme for low  $k$  and PUXBEM is

likely superior for larger  $k$ .

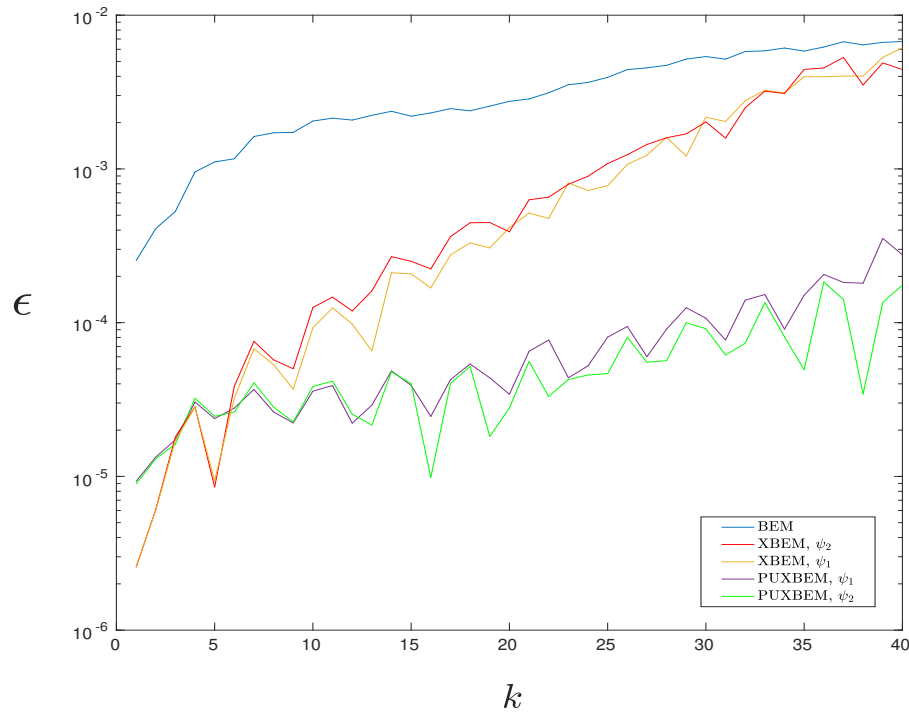


Figure 5.6:  $L^2$  relative error vs.  $k$  using 128 DoF.

For additional comparison, the internal points at which the  $L^2$  relative error is evaluated are moved, by varying  $\gamma$ . Results of this variation are presented in Table 5.1 for  $\gamma = 1-5$ , with the number of degrees of freedom fixed at 128, for  $k = 20$ . The singular enrichment employed for the XBEM and PUXBEM results in Table 5.1 is the  $\psi_2$  function. Notably, the benefit from using the singular enrichment is seen, at least for the  $\gamma$  range tested, to be present further afield. This means that the benefit is not restricted to areas local to the corners.

$\gamma$	BEM	XBEM	PUXBEM
1	$2.8354e - 03$	$4.3427e - 04$	$2.7960e - 05$
2	$2.2018e - 03$	$3.4139e - 04$	$2.1726e - 05$
3	$1.8703e - 03$	$2.9102e - 04$	$1.8458e - 05$
4	$1.6527e - 03$	$2.5755e - 04$	$1.6312e - 05$
5	$1.4947e - 03$	$2.3311e - 04$	$1.4753e - 05$

Table 5.1: Relative error  $\epsilon$  using 128 DoF for  $\gamma = 1-5$ .

Henceforth, the XBEM and PUXBEM results presented will employ the  $\psi_2$  singular enrichment functions, this is for ease of plotting as the  $\psi_2$  schemes have been shown to consistently outperform the corresponding  $\psi_1$  schemes.

## Use of blending functions

In the results presented in this chapter, so far, there has been no attempt made to enforce continuity of the singular enrichment functions at the ends of elements. This is because, as described in (5.8) and (5.13), the singular enrichment functions, multiplied by shape functions, do not typically provide continuity of the potential solution.

From Fig. 5.3 it can be seen that the fractional order Bessel functions are equal to 0 at  $r_b = 0$ , which will be located at one end of the element which is immediately adjacent to a corner at which two edges of a polygon meet in an XBEM or PUXBEM scheme.

Though, considering the variation of the Bessel functions over the edges associated with the same corner, there is no guarantee that the same Bessel functions will be equal to 0 at the opposite ends of the edges, i.e. at  $r_b = L$ . This introduces a discontinuity into the formulation. Whilst there are methods which successfully employ discontinuous basis functions, such as PWDG [37, 38] and DEM [39], it is useful to determine the impact of the discontinuity in the basis of the XBEM and PUXBEM schemes.

The impact that the discontinuity of the singular enrichment functions has on the overall solution is tested here by enforcing continuity of the functions, at both end points. Firstly, an edge of a polygon is defined as having length  $L$  wherein  $0 < r_b < L$ , with  $r_b = 0$  at the corner that is being enriched. It is possible to include a blending function  $w(\eta)$  in  $\psi_2$ , which tapers towards zero at  $r_b = L$ . Including  $w(\eta)$  in this way enforces  $\psi_2 = 0$  at  $r_b = L$ . Therefore,  $\psi_2$  can be written as follows,

$$\psi_{2,l} = J_{l\alpha}(kr_b) \cos(l\alpha\theta_b)w(\eta) \quad (5.22)$$

with the following definition of  $\eta$

$$\eta = \frac{2r_b}{L - \beta} - \frac{L + \beta}{L - \beta} \quad (5.23)$$

where  $\beta$  represents the span in which  $w(\eta)$  is equal to 1, defined as follows

$$w(\eta) = \begin{cases} 1, & \text{if } r_b < \beta \\ 0.25(1 - \eta)^2(2 + \eta), & \text{otherwise} \end{cases} \quad (5.24)$$

which is a Hermite function. This Hermite function can be seen in Fig. 5.7, plotted against  $r_b$  for  $0 < r_b < L$ .  $\beta$  can be seen clearly in Fig. 5.7 along with the tapering of the Hermite function. On the right hand side of Fig. 5.7 the blended version of  $\psi_2$  from (5.22) is shown tapering to zero, thus enforcing continuity of the basis. Fig. 5.8 shows the  $L^2$  relative error  $\epsilon$ , taken over a ring of internal points with  $\gamma = 1$ , against the number of degrees of freedom for a unit square scattering object being impinged by a plane-wave  $\phi^{inc}$

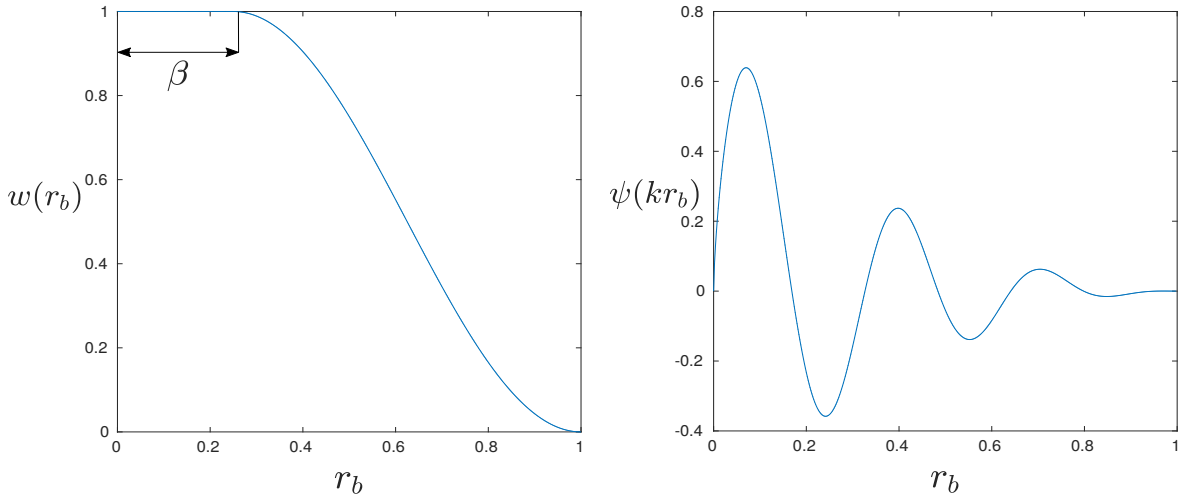


Figure 5.7: (left) Hermite blending function, (right) Blended Bessel function with  $n = 1$ ,  $k = 20$  and  $\alpha = \frac{2}{3}$ .

propagating at an angle of  $\frac{\pi}{4}$  from the positive  $x$ -axis, with  $k = 20$ . The 5 sets of results of shown in Fig. 5.8 correspond to 5 different  $\beta$  spans and indicate that it is actually more accurate to set  $\beta = L$ , i.e. not blend.

Fig. 5.9 shows results for the for the same square scattering object as Fig. 5.8 but with  $k$  varying and the number of degrees of freedom fixed at 128. These results confirm that the singular enrichment functions perform best without blending functions. Notably, from Fig. 5.8 and Fig. 5.9, it appears that including blending functions also reduces the stability of the results, thus, from hereon the blending functions are not included and the discontinuity of  $\psi_2$  is accepted.

### Accuracy locally at a corner

In Table 5.1 it is shown that increasing  $\gamma$  has little impact on the benefits of including singular enrichment functions. Though, even at  $\gamma = 1$  the internal points, at which the the error is computed, are relatively remote from the corners (the square has sides of length 1). In order to study the impact of singular enrichment functions locally at corners the internal points are arranged to surround each corner much more closely than  $\gamma = 1$  as can be seen in Fig. 5.10. In the case of the square scattering object this means that the internal points are taken over four arcs, each of radius  $\gamma$ , the union of these four sets of points forms a complete contour, defined as follows

$$\Gamma_R = \bigcup_{i=1}^{i=4} \Gamma_R^i. \quad (5.25)$$

Fig. 5.11 shows the  $L^2$  relative error  $\epsilon$ , taken over  $\Gamma_R$ , against  $\gamma$  (for a range of  $\gamma = 0.01$ -0.2) for a unit square scattering object being impinged by a plane-wave  $\phi^{inc}$  propagating

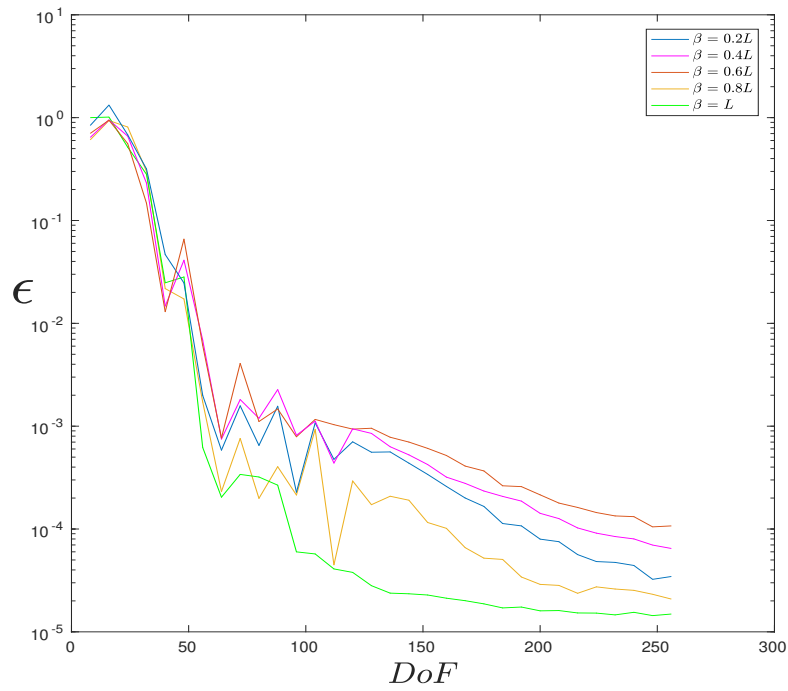


Figure 5.8: Relative error vs. DoF for  $\gamma = 1$ , varying  $\beta$  where  $L$  is the element length.

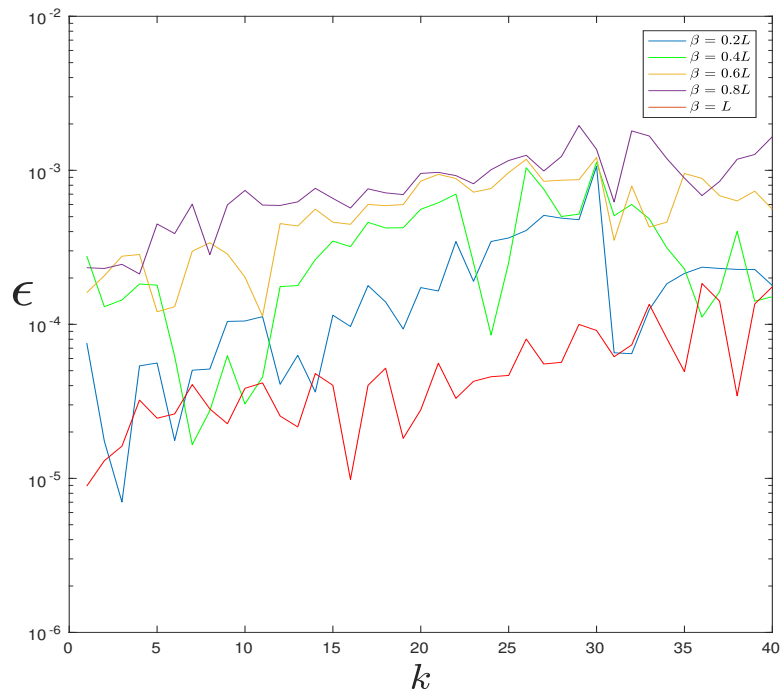


Figure 5.9: Relative error vs.  $k$  using 128 DoF, varying  $\beta$  where  $L$  is the element length.

at an angle of  $\frac{\pi}{4}$  from the positive  $x$ -axis with  $k = 20$ . The results of Fig. 5.11 indicate that the standard BEM scheme begins to fail as the evaluation points approach the corner locations whereas the enriched schemes remain within the engineering accuracy range.

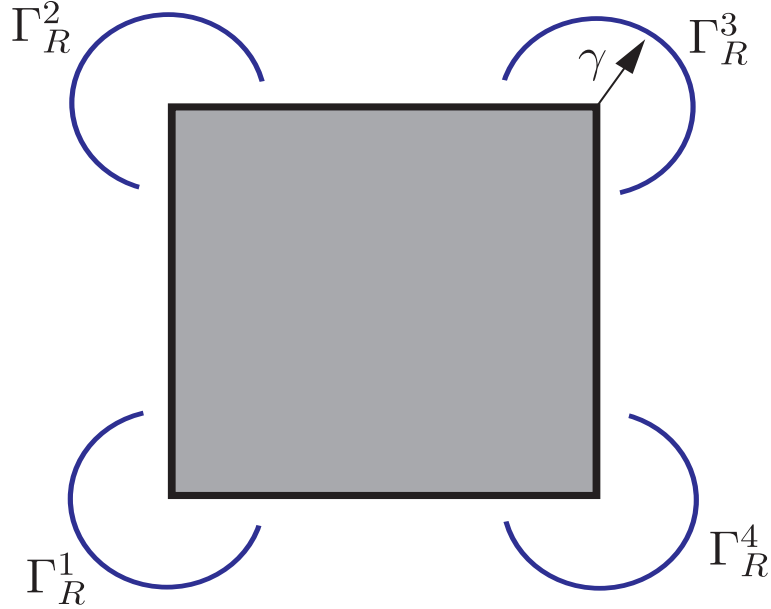


Figure 5.10: Internal point locations for single square scattering object.

### Conditioning

When including enrichment functions, such as in PUBEM, it is well-known that the the resulting system of equations can become ill-conditioned [52]. In particular, this ill-conditioning increases as the number of enrichment wave directions  $M$  increases relative to the number of elements  $E$ . To reduce the condition number of a PUBEM system, the ratio of  $M$  to  $E$  can be adjusted by reducing  $M$  and increasing  $E$  accordingly. Notably, alternate schemes have been designed to tackle the ill-conditioning in a plane-wave basis [92], but it has been found that, typically, a suitable solver can be employed to overcome the ill-conditioning in PUBEM systems.

In this section, the condition number, defined as  $\kappa$ , is tested for BEM, XBEM, and PUXBEM. Fig. 5.12 presents  $\kappa$  against the number of degrees of freedom for the unit square being impinged by a plane-wave  $\phi^{inc}$  propagating at an angle of  $\frac{\pi}{4}$  from the positive  $x$ -axis with  $k = 20$ . The results shown in Fig. 5.12 indicate that the conditioning of PUXBEM is substantially worse than that of BEM and XBEM, though, this is actually consistent with the literature on PUBEM and as mentioned above, a suitable solver can reach an accurate solution. Thus, even with this increase in condition number, PUXBEM is considerably more accurate than XBEM, so the cost of this enrichment from a conditioning standpoint seems to be negated by the accuracy gained by employing the enrichment. Fig. 5.12 also shows that including the relatively few degrees of freedom associated the

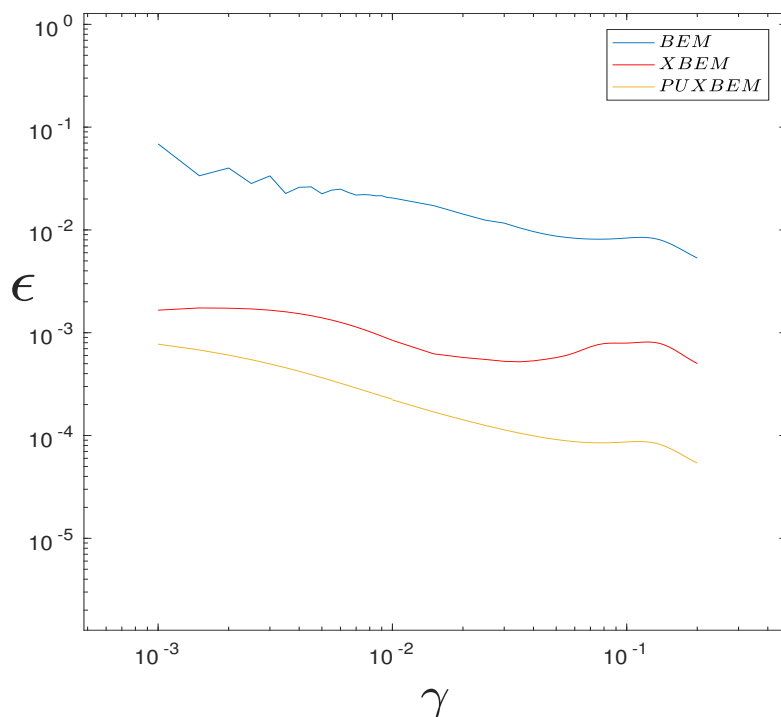


Figure 5.11: Relative error vs.  $\gamma$  using 128 DoF.

singular enrichment of XBEM is enough to increase the condition number of the system by nearly two orders of magnitude.

### Single degree of freedom per Bessel function

As presented in section 5.4 there are two possible formulations for the XBEM and PUBEM enrichment: *formulation A* and *formulation B*. One might expect that *formulation B*, i.e. including the corner enrichment as a single degree of freedom would provide the most accurate solution because *formulation B* includes the cosine term  $\cos \lambda \alpha \theta_b$  to unify the enrichment at each corner whereas *formulation A* does not account for the variation in the circumferential direction. Though the results presented in this chapter, so far, for XBEM and PUXBEM have all used *formulation A* because it has been found to be more accurate. In this section, a comparison is made between *formulation A* and *formulation B* to verify that *formulation A* is more accurate.

Fig. 5.13 presents  $L^2$  relative error against  $k$  for a square scatterer being impinged by a plane-wave  $\phi^{inc}$  propagating at an angle of  $\frac{\pi}{4}$  from the positive  $x$ -axis. The results shown in Fig. 5.13 indicate that using *formulation B*, whilst more stable, is consistently outperformed by *formulation A* for the range of  $k$  tested. Therefore, with the exception of the results shown in Fig. 5.13, *formulation A* is employed to generate XBEM and PUXBEM results.

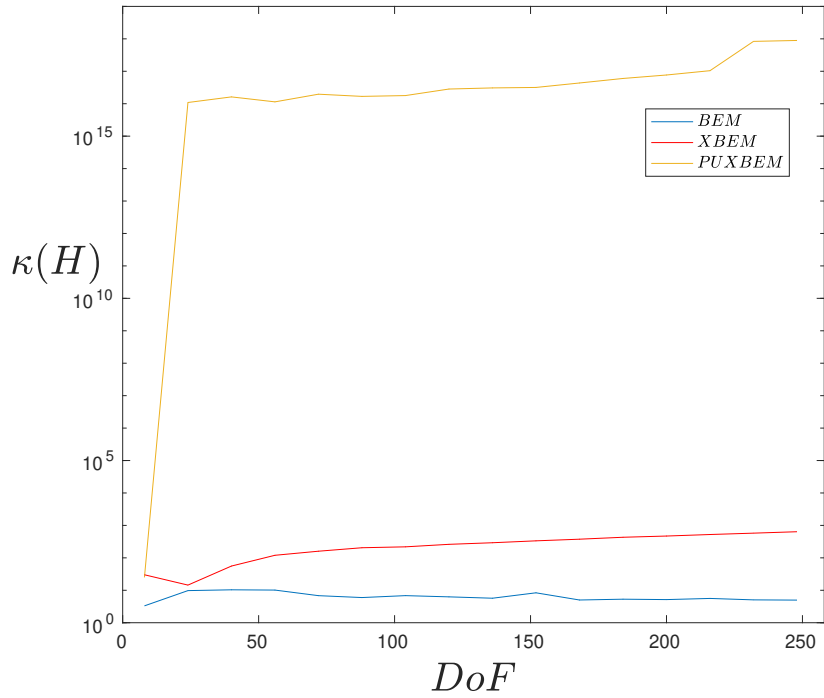


Figure 5.12: Condition number  $\kappa$  of the  $H$  matrix vs. degrees of freedom.

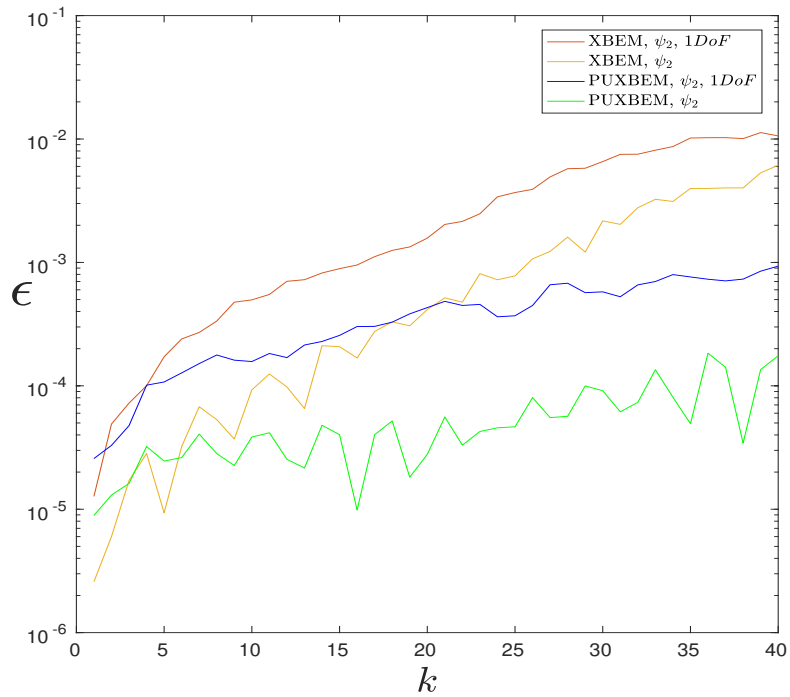


Figure 5.13: Relative error vs. DoF using a single DoF per  $\psi_2$ , marked  $1DoF$  and using a DoF for each edge. The single DoF results were obtained using 124 DoF and the two DoF results used 128 DoF.

## 5.4.2 Multiple square scattering

For numerical schemes which aim to solve general Helmholtz problems, it is important to be able to model reflections. These reflections can of course occur in interior Helmholtz problems, but relevant to the the focus of this chapter, these reflections can also occur when considering non-convex scattering objects or multiple scattering objects. It is useful to determine if XBEM and PUXBEM can still add benefit in the presence of these reflections.

Up until now, in this chapter, and in this thesis, examples have been presented for single scattering objects only. In this section a scattering arrangement is considered, which includes two unit square scattering objects being impinged by a plane-wave  $\phi^{inc}$  propagating at an angle of  $\frac{\pi}{4}$  from the positive  $x$ -axis with  $k = 20$ . The square objects are positioned according to Fig. 5.15 which shows the real part of the total potential of the resulting acoustic field, with reflections clearly visible. In order to compare BEM, XBEM, and PUXBEM, a set of internal points is defined according to Fig. 5.14 with eight arcs, each of radius  $\gamma$  and centered around one of the eight corners. This choice of internal point locations is made because using a single ring of internal points would require a relatively large radius to include both square objects. Using such a large ring would result in many of the internal points being remote from the corners of the squares that one might expect would experience the majority of the reflections, i.e. located centrally in the square scattering arrangement. Accordingly, the set of internal points  $\Gamma_R$  is defined as follows

$$\Gamma_R = \bigcup_{i=1}^{i=8} \Gamma_R^i \quad (5.26)$$

For this example the convergence of BEM, XBEM and PUXBEM is compared using an  $L^2$  norm  $Q$  taken of the solution vector, defined as follows

$$Q = \|\phi\|_{L_2(\Gamma_R)}. \quad (5.27)$$

Fig. 5.16 shows the convergence of  $Q$  against number of degrees of freedom for the multiple scattering object arrangement with  $\gamma = 0.01$ . Fig. 5.16 indicates that XBEM and PUXBEM converge very quickly, towards the same result, using relatively few degrees of freedom, whereas BEM slowly oscillates towards the same result, requiring a much greater number of degrees of freedom. Therefore, even in the presence of reflections, there is substantial benefit in employing singular enrichment functions.

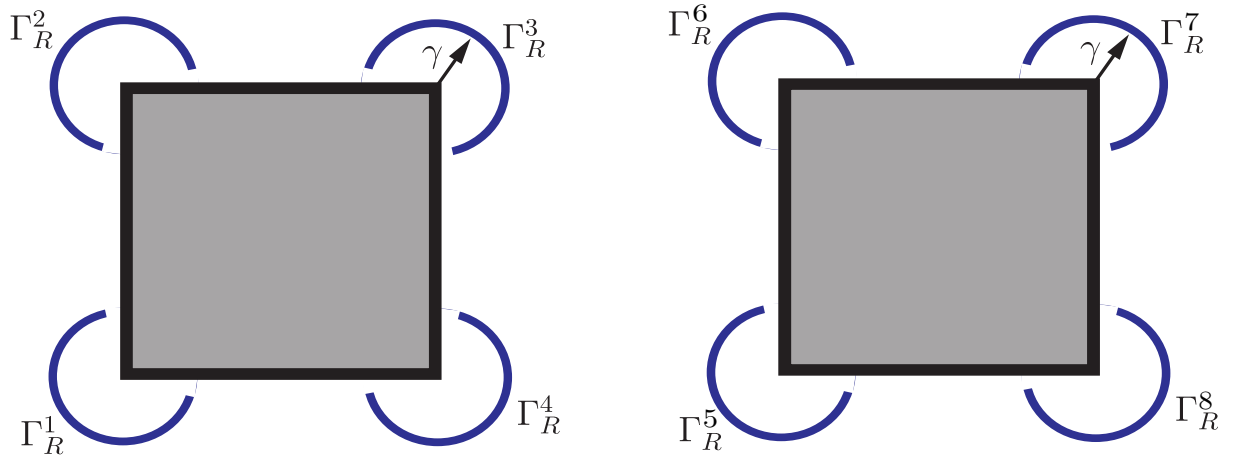


Figure 5.14: Internal point locations for the two square scattering arrangement.

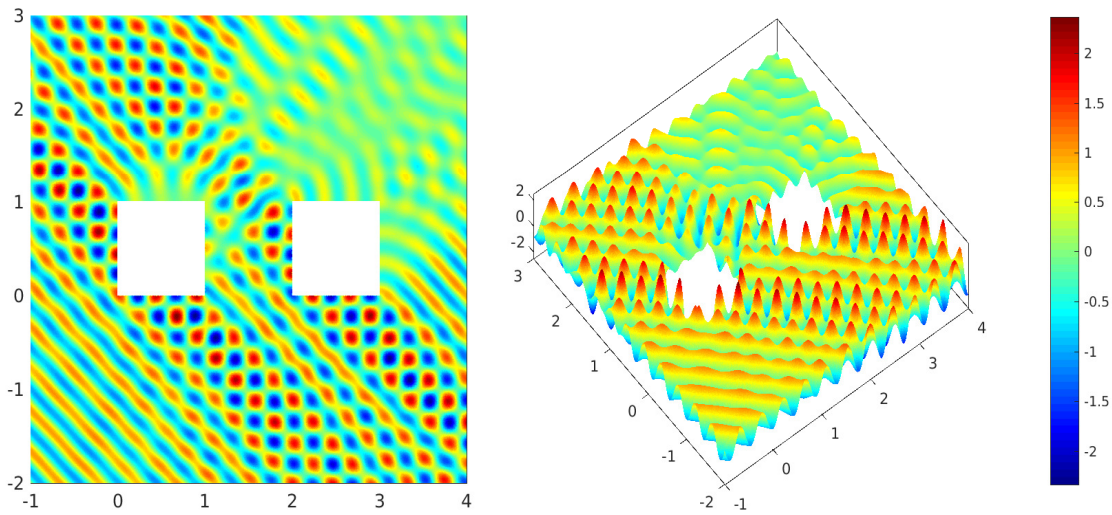


Figure 5.15: Real part of total potential field resulting from a configuration of two squares being impinged by an  $\phi_{inc} = \frac{\pi}{4}$ .

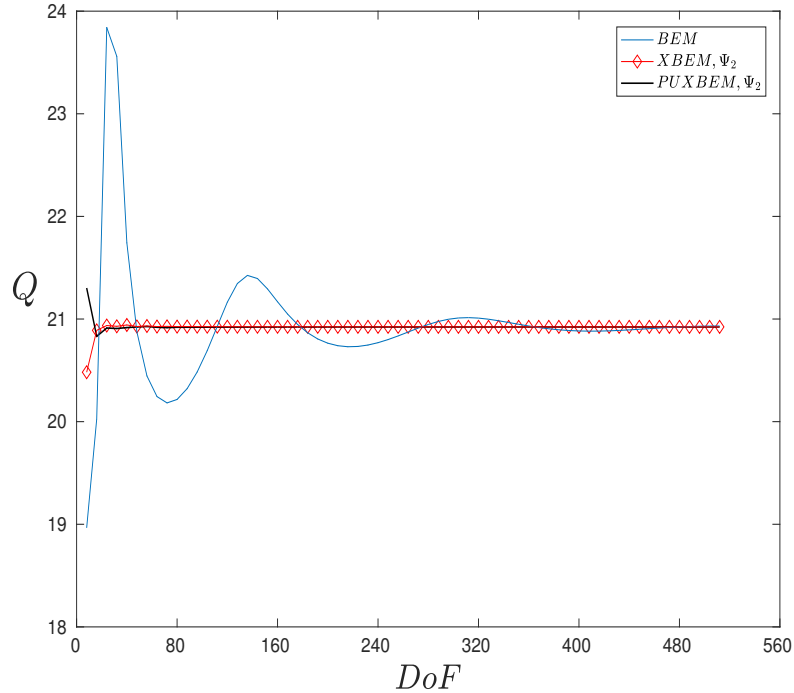


Figure 5.16:  $L_2$  norm vs. DoF at internal points around two square scattering objects, where  $\gamma = 0.01$ .

### 5.4.3 Triangular scattering object

In the above sections, varying singular enrichment functions have been tested, along with varying  $k$ , use of blending functions, numbers of degrees of freedom and multiple scattering object arrangements. The previous arrangements have included right angles. In this section, final testing is performed to verify that singular enrichment is suitable for alternate geometries.

The geometry used for this example is schematically represented in Fig. 5.17, which shows the internal point locations around a vertex of a unit equilateral triangle, defined in terms of  $\gamma$  where  $\gamma = 0.1$ . As it has been found from the results presented in Fig. 5.6 that XBEM is the superior scheme for low  $k$  and PUXBEM is superior as  $k$  becomes larger, two examples are presented in this section: the first is BEM vs. XBEM for scattering from the triangle with  $k = 2$  and the second is PUBEM vs. PUXBEM for scattering from the triangle with  $k = 20$ . For both examples,  $L^2$  relative error  $\epsilon$  is plotted against the number of degrees of freedom and the triangular scattering object is being impinged by a plane-wave travelling directly downwards, in the negative  $y$ -direction.

Fig. 5.18 shows the BEM vs. XBEM results and Fig. 5.19 shows the PUBEM vs. PUXBEM results. From both of these figures, it is clear that there is benefit in including the singular enrichment, reductions in  $\epsilon$  of up to two orders of magnitude. Notably, the

results for XBEM and, in particular, PUXBEM are less stable than BEM and PUBEM respectively. This test confirms that the corner enrichment works for  $60^\circ$  corners, as well as right angles, giving confidence in the use of different enrichment functions as informed by the value of  $\alpha$  at each corner.

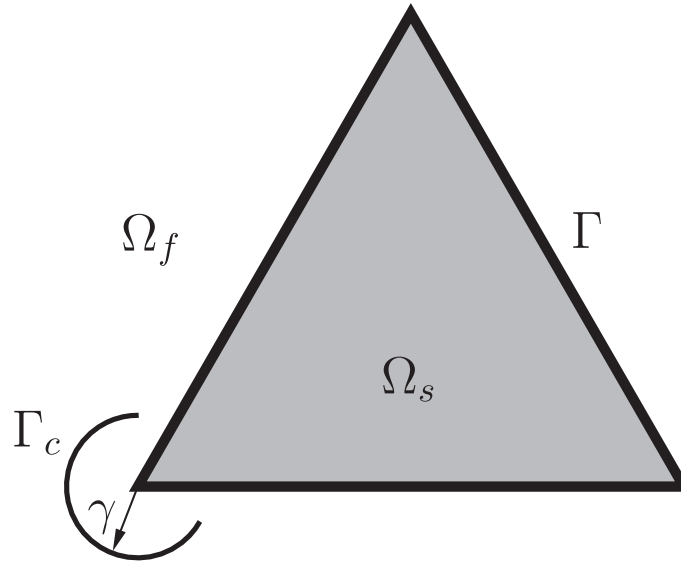


Figure 5.17: Internal point locations for single triangular scattering object.

## 5.5 Conclusions

In this chapter, singular enrichment functions have been presented for Helmholtz scattering problems in BEM and PUBEM settings, with the resulting singular enriched schemes being introduced as XBEM and PUXBEM respectively. The aim of the singular enrichment is to reduce the number of degrees of freedom required in BEM analysis for scattering from corners. To test the singular enrichment functions, multiple examples have been presented, including: square and triangular geometries wherein  $k$  has been varied; the number of degrees of freedom have been varied, and multiple scattering objects have been considered. Further, two candidate forms of enrichment  $\psi_1$  and  $\psi_2$  have been tested, along with the use of blending functions.

The outcome from tests undertaken in this chapter is that there is substantial benefit in including singular enrichment functions in a BEM or PUBEM setting. Though, XBEM is slightly more accurate than PUXBEM for low  $k$  and PUXBEM is more accurate for larger  $k$  problems. It was found that blending to enforce continuity at end points has a detrimental effect on the accuracy of the results obtained using singular enrichment functions. Further, it was found that including a separate singular enrichment function per side is favourable over just using a single degree of freedom associated with each

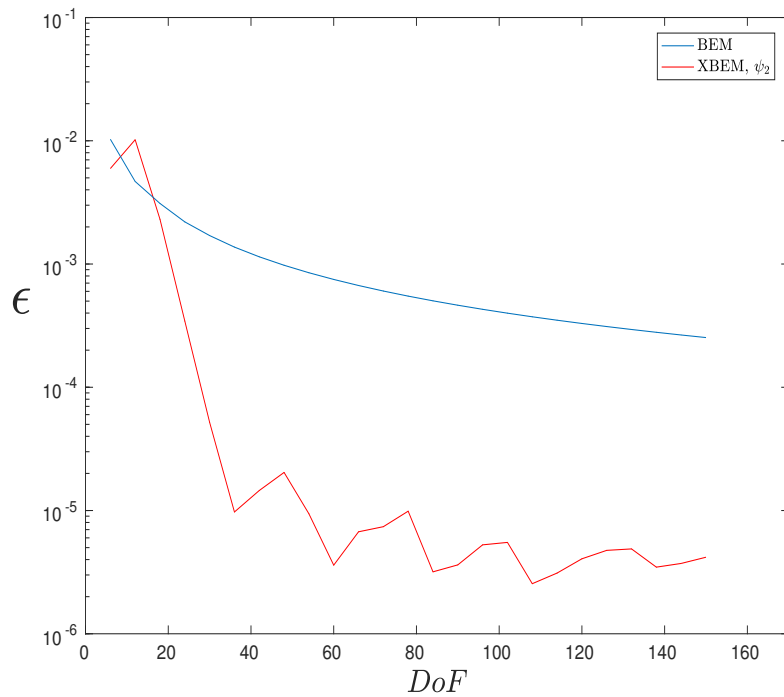


Figure 5.18: Relative error vs. DoF for a triangular scattering object with  $\gamma = 0.1$ ,  $k = 2$ .

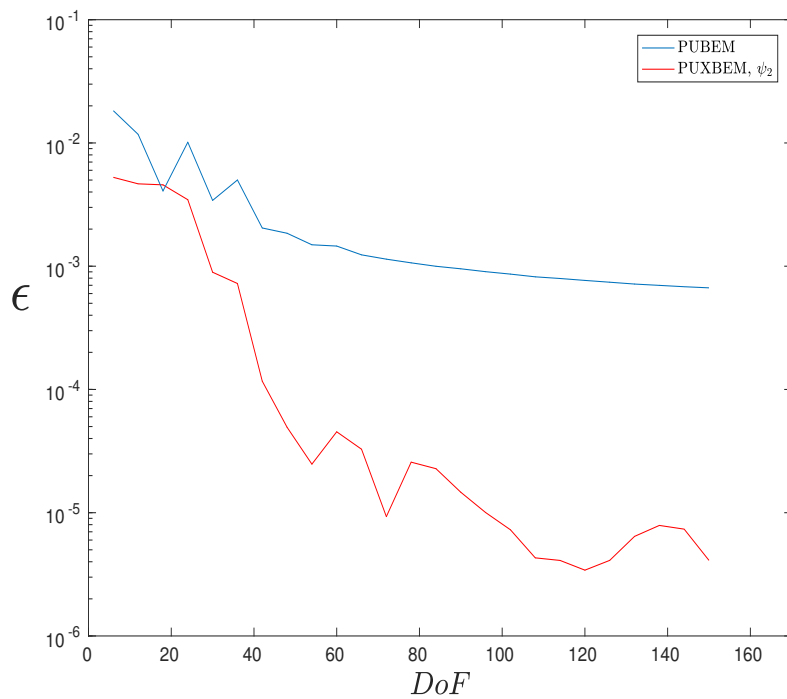


Figure 5.19: Relative error vs. DoF for a triangular scattering object with  $\gamma = 0.1$ ,  $k = 20$ .

corner.

# Chapter 6

## High-order basis functions

### 6.1 Introduction

Classical BEM implementations are typically constructed around a low order, piecewise polynomial basis. Similarly, for isogeometric formulations, typically low order NURBS basis functions are used. The requirement to model short wave problems (i.e. where the wavelength is short in comparison to the domain/scatterer size) motivates a different approach. It has been shown in earlier parts of this thesis that the use of plane waves is an attractive option to enhance computational efficiency. In this chapter an alternative approach is tested, which is the use of high-order polynomial or NURBS basis functions in order to capture highly oscillatory acoustic fields. Outside of BEM, high-order bases have been studied in detail, such as in spectral methods and FEM [19–24], and in an IGAFEM setting [18, 102]. Further, outside of BEM, useful comparisons between high-order methods and Trefftz methods have been made [25, 26]. Though, it appears that there is yet to be a thorough analysis of high-order Lagrange functions or high-order NURBS in a BEM setting. Such analysis, along with the comparison of high-order bases against PUBEM, is the focus of this chapter. Further, the pollution effect which is well-studied in FEM, observed in a PWDG setting [105], and is known as an error that cannot be resolved via local mesh refinement and therefore accumulates in other regions of the model, has recently been demonstrated and quantified for a number of low-order basis functions [103]. It appears that the pollution effect is yet to be studied for PUBEM, thus, a section in this chapter is devoted to examining pollution in both high-order BEM and PUBEM.

The problems considered in this chapter include internal problems, for which a Robin boundary condition is required which results in the discretised BIE (3.35), presented here for convenience:

$$\begin{aligned}
c(\mathbf{p})\phi(\mathbf{p}) + \sum_{e=1}^E \sum_{j=1}^J \int_{-1}^1 \left[ \frac{\partial G(\mathbf{p}, \mathbf{q})}{\partial \mathbf{n}} - \alpha G(\mathbf{p}, \mathbf{q}) \right] \Psi_j(\xi) J^e d\xi \phi_j^e \\
= \int_{\Gamma} \beta G(\mathbf{p}, \mathbf{q}) d\Gamma(\mathbf{q}) + \phi^{inc}(\mathbf{p}), \quad \mathbf{p}, \mathbf{q} \in \Gamma.
\end{aligned} \tag{6.1}$$

### 6.1.1 Lagrange basis

In this chapter, the Lagrange basis, that was presented in chapter 3, is extended to include higher order terms. As mentioned in chapter 3, it is common to use a quadratic basis comprised of 3 basis functions, as follows

$$\Psi_1 = \frac{1}{2}\xi(\xi - 1) \tag{6.2}$$

$$\Psi_2 = (1 - \xi)(1 + \xi) \tag{6.3}$$

$$\Psi_3 = \frac{1}{2}\xi(\xi + 1), \tag{6.4}$$

though, linear and constant elements can also be employed. In this chapter multiple bases will be tested, so a superscript  $L$  is used to indicate a Lagrange basis, such that acoustic potential  $\phi$  over element  $e$  with  $J$  Lagrangian basis functions can be written as follows

$$\phi = \sum_{j=1}^J \Psi_j^L(\xi) \phi_j^e, \tag{6.5}$$

for which there is a convenient expansion to produce  $\Psi_j^L(\xi)$ , as follows

$$\Psi_j^L(\xi) := \prod_{\substack{0 \leq m \leq J \\ m \neq j}} \frac{\xi - \xi_m}{\xi_j - \xi_m} = \frac{(\xi - \xi_0)}{(\xi_j - \xi_0)} \cdots \frac{(\xi - \xi_{j-1})}{(\xi_j - \xi_{j-1})} \frac{(\xi - \xi_{j+1})}{(\xi_j - \xi_{j+1})} \cdots \frac{(\xi - \xi_J)}{(\xi_j - \xi_J)}. \tag{6.6}$$

To produce the results in this chapter, four Lagrange bases are compared: 3 basis functions per element; six basis functions per element; nine basis functions per element; and, twelve basis functions per element. These bases can be seen, plotted for  $\xi \in [-1, 1]$ , in Fig. 6.1.

### 6.1.2 NURBS

As indicated in section 6.1, NURBS bases are also tested in this chapter. The concept of using NURBS as a basis in IGAFEM and IGABEM was introduced in chapter 3, though, a short introduction to Isogeometric analysis is provided here, before presenting the actual

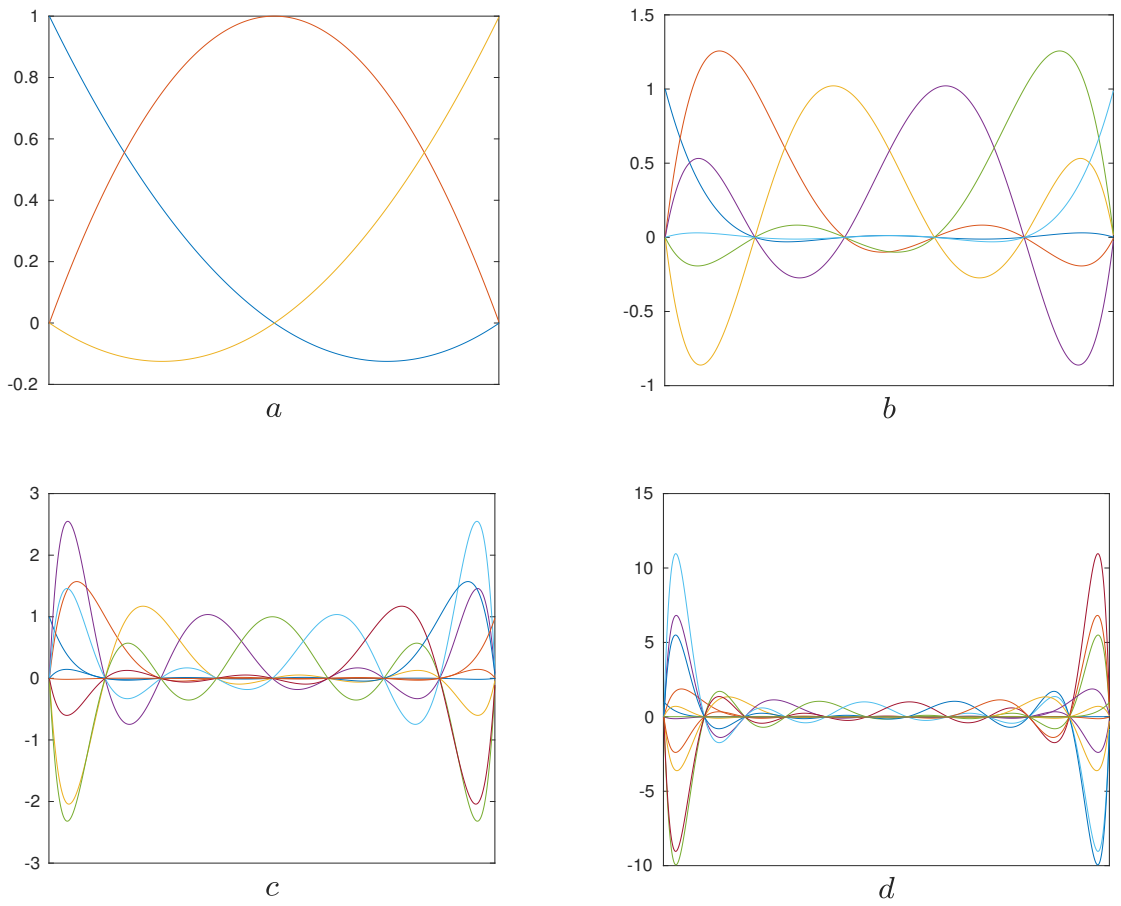


Figure 6.1: Lagrangian basis functions with  $a, b, c$  and  $d$  showing  $S = 3, 6, 9$  and  $12$  respectively.

NURBS functions.

NURBS are B-Splines with non-uniform weightings and are often employed in the creation of CAD geometries. NURBS can provide a convenient choice of basis because they can be readily imported from CAD software. In this way, the same functions that are used to describe a given geometry can, for example, be used to describe variation in acoustic potential over that geometry. This is the core concept of Isogeometric Analysis (IGA) [93]. NURBS provide further benefit by virtue of being smooth and non-negative. IGA is now a very popular numerical method [94–96], and has been studied in a BEM setting (termed IGABEM) [97, 98, 106] along with an example using T-splines for acoustics problems [99]. Notably, the importation of a NURBS geometry from CAD to be used for numerical analysis is well-suited to BEM, when compared with FEM, because NURBS are used to describe the edges of a geometry in  $2D$  or the surface of a geometry in  $3D$  which, conveniently, is all that is required for BEM analysis, whereas in FEM an additional volumetric description would be required. A final note, enriched NURBS bases have also been successfully employed [100, 101] to form the eXtended Isogeometric Boundary Element Method (XIBEM).

Thus, the second basis studied in this chapter is a NURBS basis, which describes  $\phi$  as follows.

$$\phi = \sum_{j=0}^{J-1} \Psi_{j,p}^B(\xi) \phi_j^e, \quad (6.7)$$

in which the superscript  $B$  is used to indicate the NURBS basis, and where

$$\Psi_{j,p}^B(\xi) := \frac{N_{j,p}(\xi)w_j}{\sum_{i=0}^J N_{i,p}(\xi)w_i} \quad (6.8)$$

and  $w_j$  are a set of weights,  $N_{j,p}$  are  $p$ th-degree B-spline basis functions, which can be represented for  $p > 0$

$$N_{j,p}(\xi) = \frac{\xi - \xi_j}{\xi_{j+p} - \xi_j} N_{j,p-1}(\xi) + \frac{\xi_{j+p+1} - \xi}{\xi_{j+p+1} - \xi_{j+1}} N_{j+1,p-1}(\xi), \quad (6.9)$$

and for  $p = 0$

$$N_{0,j}(\xi) = \begin{cases} 1, & \text{if } \xi_j \leq \xi \leq \xi_{j+1} \\ 0, & \text{otherwise} \end{cases} \quad (6.10)$$

Similarly to the orders of Lagrangian basis chosen, four NURBS bases are compared: 3 basis functions per element; six basis functions per element; nine basis functions per element; and, twelve basis functions per element. These bases can be seen, plotted for  $\xi \in [-1, 1]$ , in Fig. 6.2.

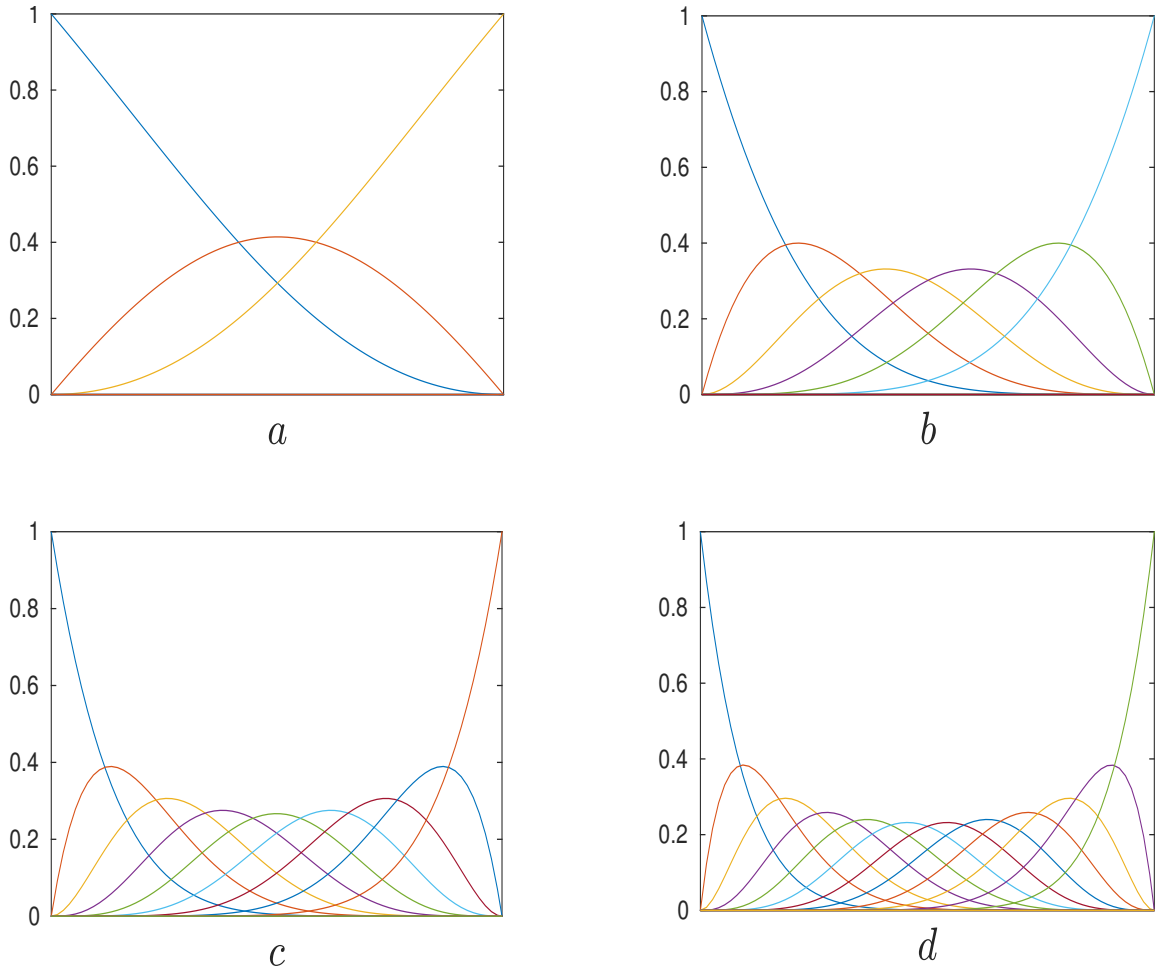


Figure 6.2: NURBS basis functions with all weights  $w_j = 1$ ;  $a, b, c$  and  $d$  show  $J = 3, 6, 9$  and  $12$  respectively.

### 6.1.3 Plane waves.

In contrast to the high-order bases presented above, the third and final basis that is employed in this chapter is the PUBEM basis which is comprised of a set of plane-waves propagating at equispaced angles. The PUBEM basis is presented in chapter 3, but shown here as a reminder.

In PUBEM, the set of plane-waves, typically, is multiplied by a quadratic Lagrangian basis, as follows

$$\phi = \sum_{j=1}^J \sum_{m=1}^M \Psi_j^L(\xi) A_{jm} e^{ik \mathbf{d}_{jm} \cdot \mathbf{q}}, \quad (6.11)$$

in which the superscript  $L$  is used to indicate that the plane-waves are multiplied by Lagrange functions, and

$$\mathbf{d}_{jm} = (\cos \theta_{jm}, \sin \theta_{jm}), \quad \theta_{jm} = \frac{2\pi(m-1)}{M} \quad (6.12)$$

where  $M$  represents the number of plane waves per node,  $i = \sqrt{-1}$  and  $\mathbf{d}_{jm}$  are the unit direction vectors of propagation of the plane waves. The modified version of (3.35) is as follows,

$$\begin{aligned} c(\mathbf{p})\phi(\mathbf{p}) + \sum_{e=1}^E \sum_{j=1}^S \sum_{m=1}^M \int_{-1}^1 \left[ \frac{\partial G(\mathbf{p}, \mathbf{q})}{\partial \mathbf{n}} - \alpha G(\mathbf{p}, \mathbf{q}) \right] \Psi_j^L(\xi) e^{ik \mathbf{d}_{jm} \cdot \mathbf{q}} J^e d\xi A_{jm}^e \\ = \int_{\Gamma} G(\mathbf{p}, \mathbf{q}) \beta d\Gamma_{\mathbf{q}} + \phi^{inc}(\mathbf{p}), \end{aligned} \quad (6.13)$$

the solution of which produces a set of unknown amplitudes  $A_{jm}$  from which the acoustic potential  $\phi$  can be recovered, according to (6.11).

## 6.2 Numerical testing

### 6.2.1 Implementation

In this section high-order NURBS and Lagrange polynomial bases are compared with PUBEM, error  $\epsilon$  is taken to be relative error when analysing scalar results and  $L^2$  relative error when analysing a vector of results. The definition of  $\epsilon$  can be found in Appendix C. Computational efficiency will be presented in terms of the number of degrees of freedom per wavelength  $\tau$ . The condition number,  $\kappa$ , of each resulting system of equations is also observed. Three test cases are considered: scattering by a single cylinder, scattering by multiple cylinders and a plane wave propagating along the length of a duct, all of which have analytical solutions. For the exterior scattering problems, the cylindrical obstacles

are assumed to be perfectly reflecting or ‘sound-hard’, and for the duct the relevant boundary conditions will be presented. Numerical integration is performed using a subdivided Gauss-Legendre quadrature scheme with a sufficient number of integration points to ensure that the integration error is negligible. A range of discretisations and wave numbers are tested, with an additional pollution study for the duct case. The number of degrees of freedom used is denoted  $N_d$ .

### 6.2.2 Scattering by a cylinder

Scattering by a sound-hard cylinder (i.e. a circular obstacle in  $2D$ ) in an infinite domain is a benchmark problem having an analytical solution [2] which is used in this section to provide reference scattered potential  $\phi_{ref}$ . The scattered potential  $\phi_{ref}$  at a point  $\bar{\mathbf{p}}$  can be represented by a series solution comprised of Bessel functions, as follows.

$$\phi_{ref}(\bar{\mathbf{p}}) = \frac{J'_0(ka)}{H'_0(ka)} H_0(kr) - 2 \sum_{n=1}^{\infty} i^n \frac{J'_n(ka)}{H'_n(ka)} H_n(kr) \cos(n\theta), \quad \bar{\mathbf{p}} \in \Omega_f \quad (6.14)$$

For example, to represent this example using BEM the BIE (6.1) is used and a sound-hard Neumann boundary condition is applied on  $\Gamma$ , defined by

$$\frac{\partial \phi(\mathbf{q})}{\partial \mathbf{n}} = 0, \quad \mathbf{q} \in \Gamma. \quad (6.15)$$

This reduces (6.1) to

$$c(\mathbf{p})\phi(\mathbf{p}) + \sum_{e=1}^E \sum_{s=1}^S \int_{-1}^1 \frac{\partial G(\mathbf{p}, \mathbf{q})}{\partial \mathbf{n}} \Psi_s(\xi) J^e d\xi \phi_s^e = \phi^{inc}(\mathbf{p}). \quad (6.16)$$

In this section, a unit cylinder is considered, as a scattering object, being impinged by a plane-wave travelling in the positive  $x$ -direction. The real part and the absolute value of acoustic potential scattered by this unit cylinder  $k = 2\pi$  is shown in Fig. 6.3. A circular contour, over which error  $\epsilon$  is evaluated, is defined by  $\Gamma_\epsilon = \{(x, y) : x = 2 \cos \theta, y = 2 \sin \theta, \theta \in (0, 2\pi)\}$ . For the Lagrange polynomial basis and the NURBS basis four orders 2, 5, 8 and 11 (as shown in Fig. 6.1 and Fig. 6.2) are considered. For the PUBEM basis, a fixed number of elements,  $E = 4$  is used, increasing  $N_d$  by incrementing the number plane waves per node,  $M$ .

A first example is presented, in which the wavenumber is fixed at  $k = 2\pi$  but  $N_d$  is varied up to  $\approx 250$ , which corresponds to  $\tau \approx 40$ . Whilst this  $\tau$  vastly exceeds the  $\tau \approx 2.5$  required by PUBEM (or any of the bases tested in this chapter) to achieve engineering accuracy, increasing it to this extent offers valuable insight into the broader numerical behaviour of the basis. The results for this example, presented in Fig. 6.4, show a clear improvement in computational efficiency from using higher order functions. These results

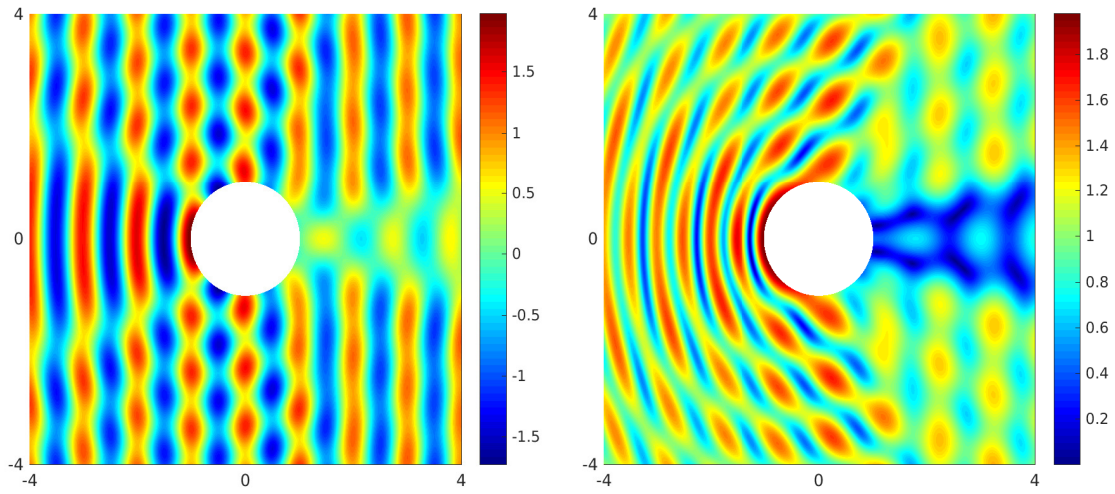


Figure 6.3: (left) Real part of the total potential, (right) absolute value of total potential, for scattering by a unit cylinder,  $k = 2\pi$ .

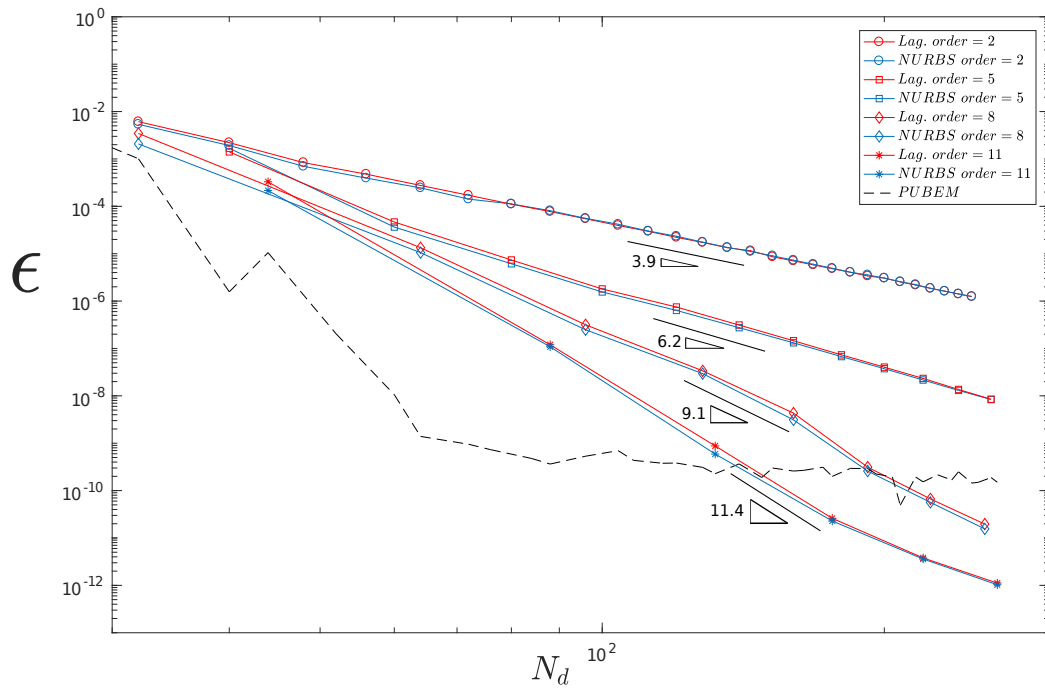


Figure 6.4:  $L^2$  relative error  $\epsilon$  vs.  $N_d$  for scattering by a unit cylinder,  $k = 2\pi$ .

are somewhat expected as in [106] increase in accuracy is seen as a result of increasing the order of a NURBS basis from 2-3, for elasticity problems. It is evident that the Lagrange and NURBS bases offer similar numerical performance, and that the NURBS basis does not offer the clearer improvement that has been seen in other, predominantly low-order, IGABEM applications. Though, 3rd order NURBS and Lagrange shape functions are shown to converge at a similar rate for acoustic scattering by a torus in [99]. An explanation might be as follows. IGABEM can be expected to give improvements over the classical piecewise polynomial basis for two reasons: (i) the exact geometric description, and (ii) the smoother, non-negative basis. As long as the geometric error produced by the Lagrange basis functions is small in comparison with the wavelength, the implications geometric error on the solution error will be limited. Once the Lagrange models in this study are sufficiently refined to observe the heuristic rule on the required  $\tau$ , the geometric description is certainly of sub-wavelength accuracy, so the difference in the errors is likely to reduce to the effect of the improved smoothness and non-negativity of the NURBS basis. It can be seen that this effect is a mild one, so that the errors produced by high order Lagrange and NURBS bases are rather similar.

In the results shown in Fig. 6.4, PUBEM is seen to quickly achieve a higher level of accuracy, but is eventually overtaken by the higher order NURBS and Lagrange bases with the increased severity of ill-conditioning in the PUBEM linear system at large  $\tau$  [49]. For comparison, the condition number  $\kappa$  is plotted for the Lagrange and NURBS systems in Fig. 6.5. These plots indicate that whilst increasing the order of basis functions employed does increase  $\kappa$ , increasing  $N_d$  has no detrimental impact on the condition number.

In contrast, the condition number of PUBEM appears to increase in response to an increase in the the number of degrees of freedom, as can be seen in Fig. 6.6 which shows a direct comparison between  $\kappa$ ,  $N_d$  and  $\epsilon$  for the PUBEM case. Further, from Fig. 6.6, it can be seen that limitations of the solver restrict the accuracy of the solution. However, it is clear that, as long as a suitable solver is chosen that can deal with such ill-conditioned matrices, the most accurate PUBEM solutions are to be found from the most poorly conditioned systems because these systems benefit from the most enriched approximation space.

Testing, so far, has been restricted to a relatively low  $k$  which is not favourable for PUBEM, because PUBEM performs best in the mid-high frequency range. In order to provide an extra level of comparison, that may favour PUBEM, another example is tested for the single cylinder case, in which  $N_d$  is fixed, but  $k$  varies. It is not possible to force the number of degrees of freedom used for each basis to equal one another, but for each discretisation  $N_d \in [220, 224]$ ; the results are displayed in Fig. 6.7. These results show that, as expected, PUBEM outperforms the other methods at high frequency, but, importantly, it is evident that the high-order methods function optimally at large  $\tau$  (i.e. at

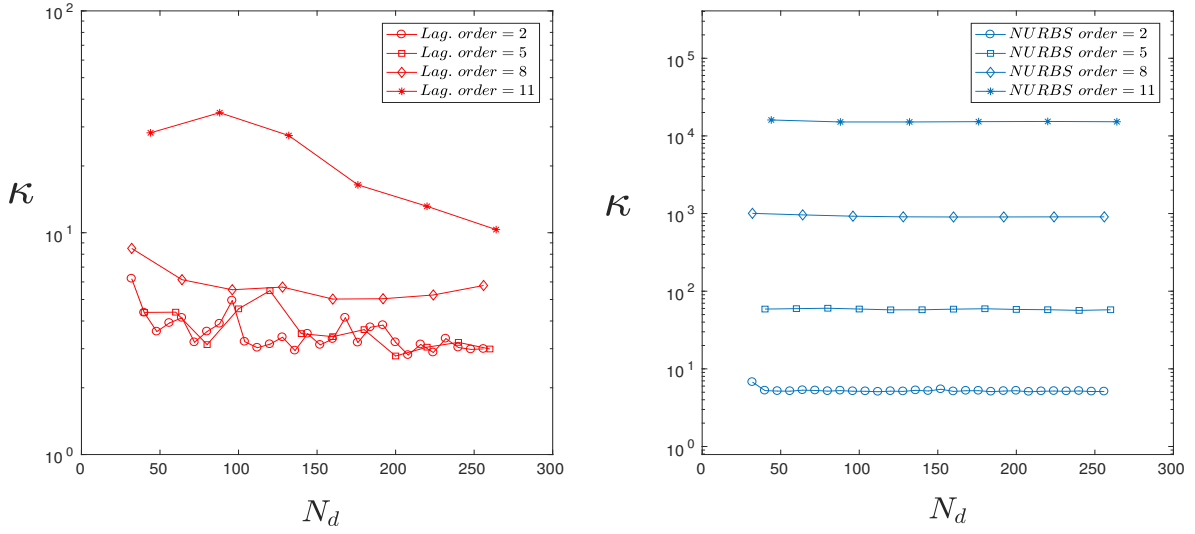


Figure 6.5: (Left) Condition number  $\kappa$  vs.  $N_d$  for Lagrange basis, (Right) Condition number  $\kappa$  vs.  $N_d$  for NURBS basis, for scattering by a unit cylinder,  $k = 2\pi$ .

small  $k$  when  $N_d$  is fixed) whereas the converse is true for PUBEM.

### 6.2.3 Scattering by three cylinders

In this section, a multiple scattering arrangement is considered, to test the efficacy of each basis in the presence of reflections. Specifically, the example chosen comprises 3 sound-hard circular cylinders in an infinite domain, being impinged by an incident plane-wave. This problem is selected because it has an analytical solution [104], wherein the scattered potential  $\phi_{ref}$  for a set of  $N$  cylinders can be represented on the boundary of the  $v$ th cylinder by a series solution comprised of Hankel functions,

$$\phi_{ref}(a_v, \theta_v) = -\frac{2i}{\pi k a_v} \sum_{n=-\infty}^{\infty} \frac{A_n^v}{H_n'(k a_v)} e^{in\theta_v}, \quad (6.17)$$

where  $a_v$  is the radius of the  $v$ th cylinder,  $\theta_v$  is the angle from the positive  $x$ -axis of the  $v$ th cylinder to the point of evaluation and  $H_n$  is a Hankel function of the first kind and order  $n$ . The infinite series can be truncated, with  $A_n^v$  obtained according to [104]. The boundary of each cylinder can be denoted as  $\Gamma_1, \Gamma_2$  and  $\Gamma_3$  and evaluate the error norm evaluated over the union  $\epsilon$  so that  $\Gamma_\epsilon = \bigcup_{v=1}^3 \Gamma_v$ .

The three unit cylinders are located at a radius of 3 from the origin  $(0, 0)$  with centres at angles of  $0, \frac{2\pi}{3}$  and  $\frac{4\pi}{3}$ , being impinged by a plane wave travelling in the positive  $x$ -direction. The total potential for this example with  $k = 4\pi$  is shown in Fig. 6.8. It is

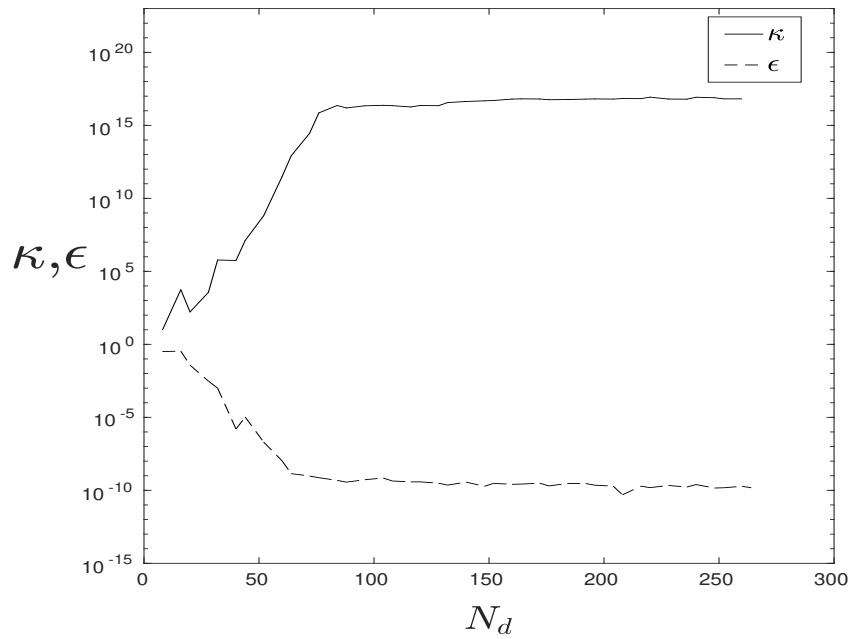


Figure 6.6: PUBEM  $L^2$  relative error  $\epsilon$  and condition number  $\kappa$  for scattering by a unit cylinder,  $k = 2\pi$ .

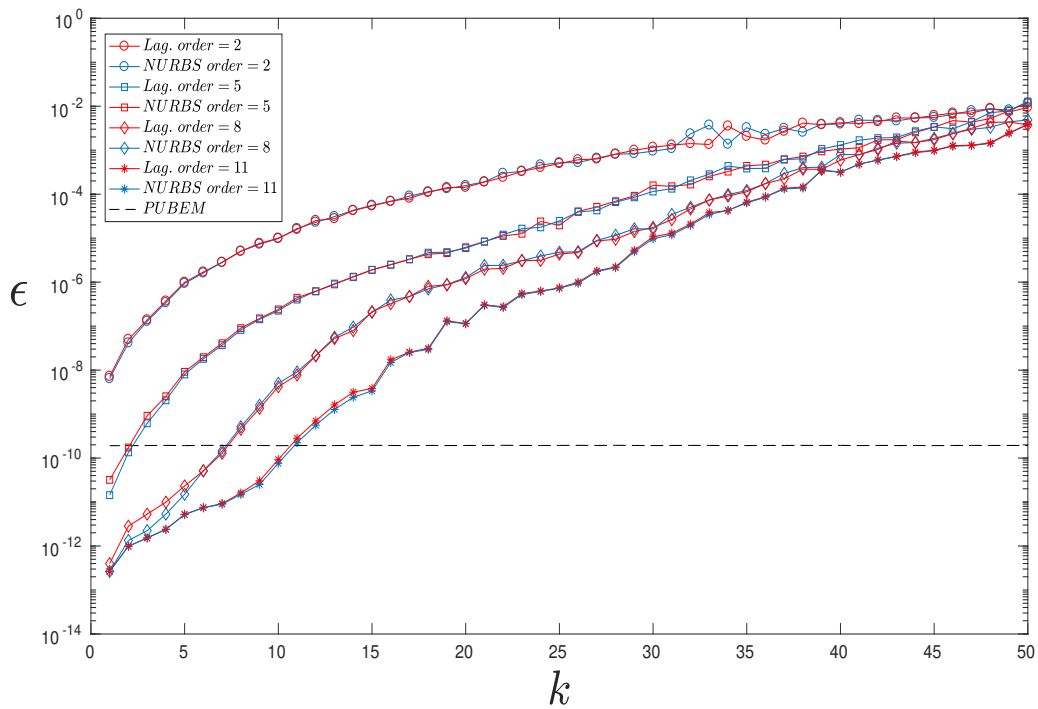


Figure 6.7:  $L^2$  relative error  $\epsilon$  for scattering by a unit cylinder, with  $N_d \in 220-224$ .

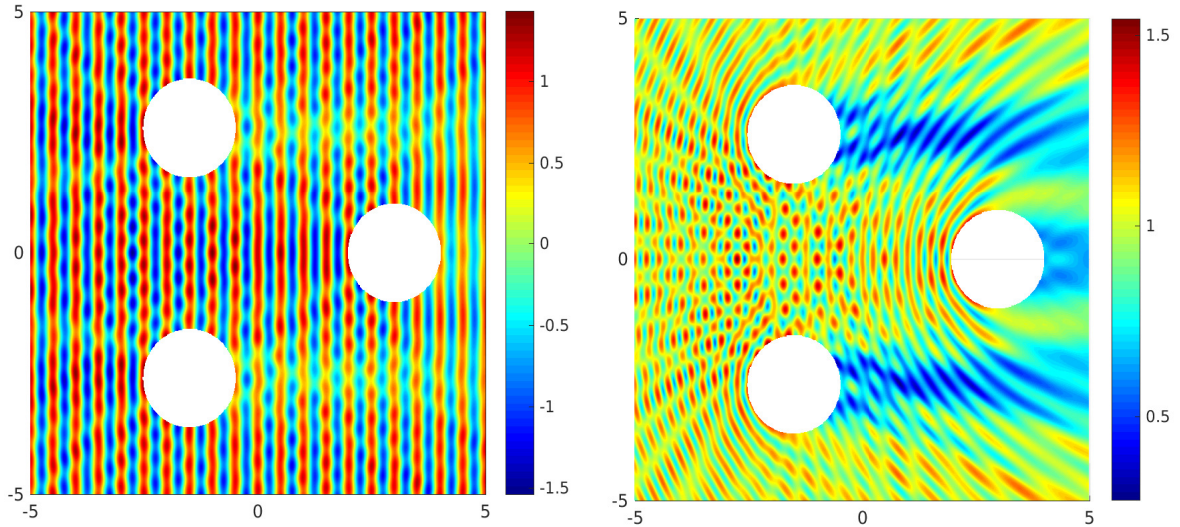


Figure 6.8: (left) Real part of the total potential, (right) absolute value of total potential, for scattering by three unit cylinders,  $k = 4\pi$ .

evident that with the inclusion of reflections, the solution is more complicated than that of the single cylinder.

For each cylinder in this example, the same selection of basis functions and discretisations, used for the single cylinder example, are applied. As with the single cylinder example the wavenumber is fixed at  $k = 4\pi$ , and the degrees of freedom per circle vary up to  $\approx 250$ . The results for this example are presented in Fig. 6.9 which appear very similar to those obtained for the single cylinder. It can be seen in Fig. 6.9 that there is a clear benefit in using high-order basis functions and, again, the Lagrange results are in close agreement with the NURBS results. It can also be seen in Fig. 6.9 that the PUBEM results are similar to those obtained for the single cylinder example; reaching a high level of accuracy quickly, before gradually being overtaken by the high-order NURBS and Lagrange functions, due to conditioning limitations. This happens slightly later (at  $N_d \approx 210$ ) than for the single cylinder case ( $N_d \approx 140$ ), which can be attributed to the increase in  $k$ , because this produces a  $\tau$  range that is more favourable for PUBEM. The respective condition numbers of the resulting systems of equations are shown in Fig. 6.10 for the Lagrange and NURBS basis, with the PUBEM condition number in Fig. 6.11. It is clear that the behaviour is similar to the previous example again, as the lowest condition numbers are seen in the Lagrange basis, with a slight increase associated with the NURBS basis and a substantial increase for PUBEM. It is worth noting that using PUBEM offers an improvement in  $\epsilon$  of 4-5 orders of magnitude over the conventional quadratic Lagrange polynomial basis for much of the range of problem sizes tested.

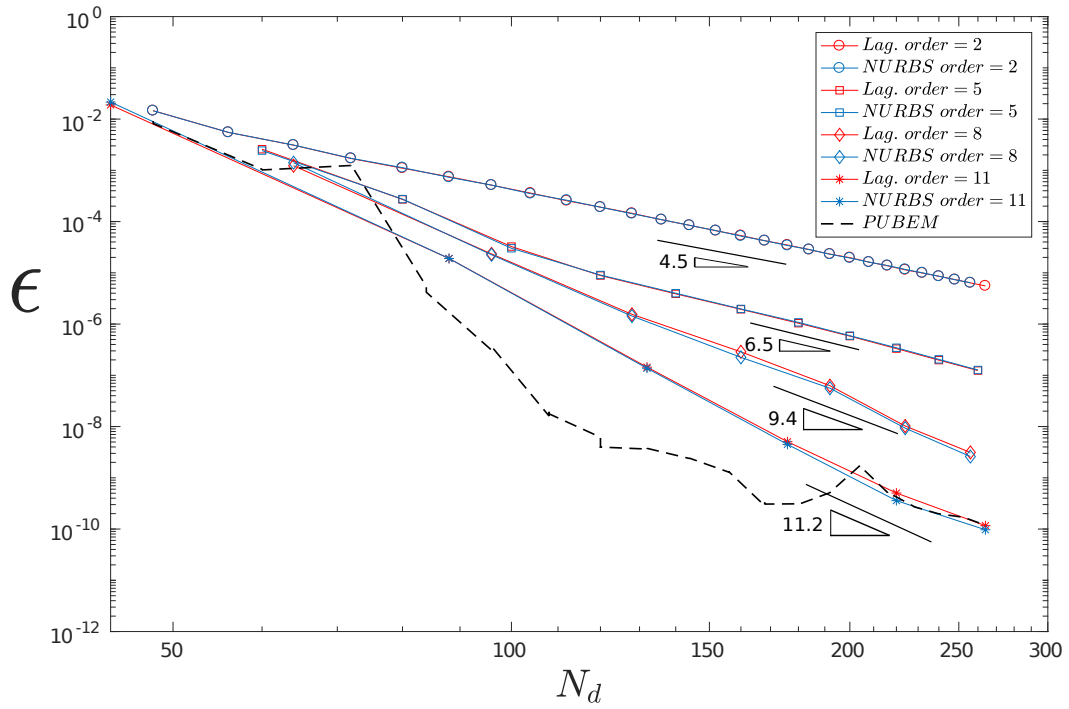


Figure 6.9:  $L^2$  relative error  $\epsilon$  vs  $N_d$  (per cylinder) for scattering by three unit cylinders,  $k = 4\pi$ .

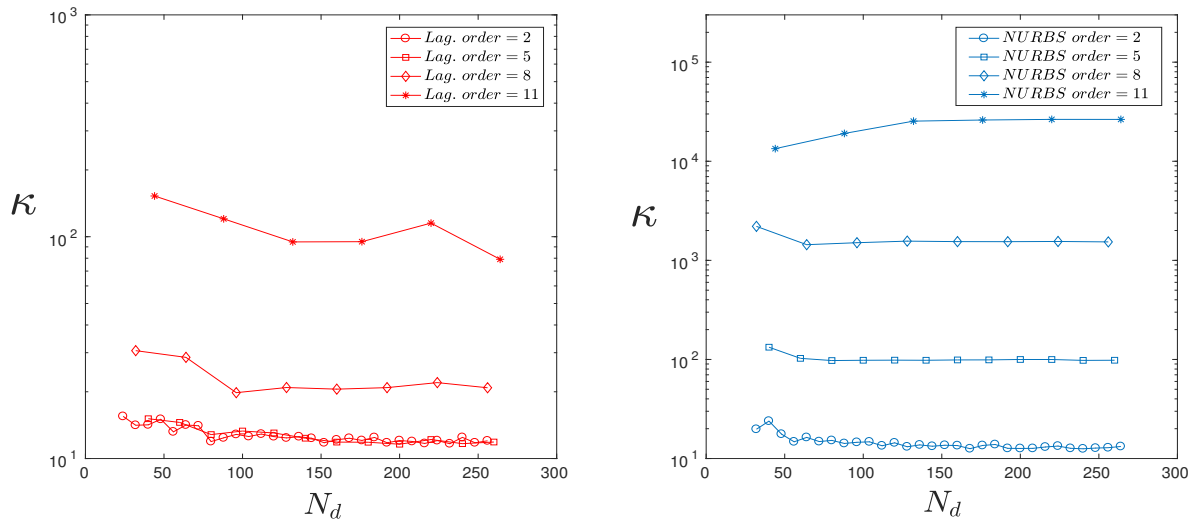


Figure 6.10: (Left) Condition number  $\kappa$  vs.  $N_d$  for Lagrange basis, (Right) Condition number  $\kappa$  vs.  $N_d$  for NURBS basis, for scattering by three unit cylinders,  $k = 4\pi$ .

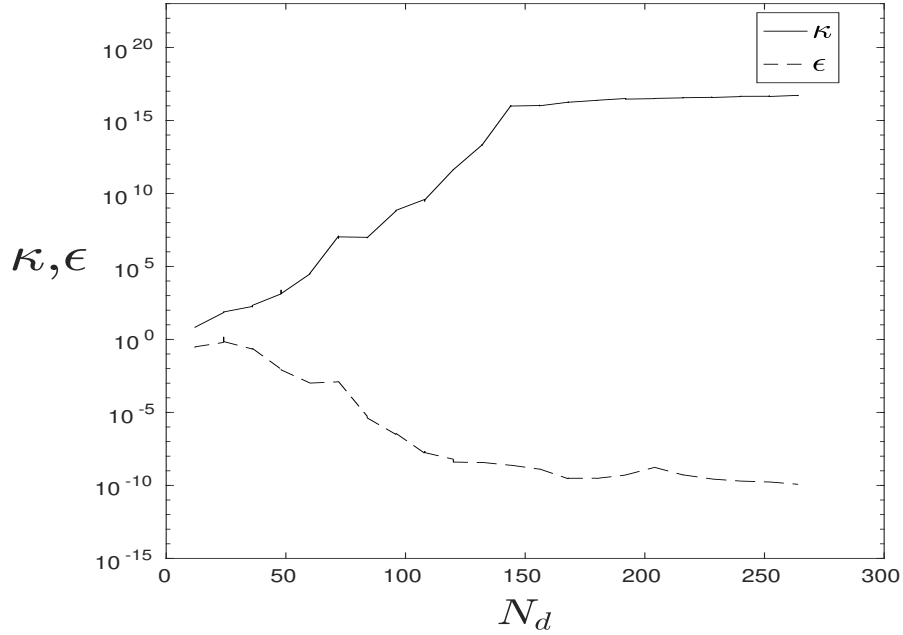


Figure 6.11: PUBEM  $L^2$  relative error  $\epsilon$  and condition number  $\kappa$  for scattering by three unit cylinders,  $k = 4\pi$ .

#### 6.2.4 Plane wave propagating along the length of a duct

In this section, a third example is considered wherein a plane-wave is propagating along the length of a duct, which is in essence a  $1D$  problem, but is being analysed here in  $2D$ . As with the other examples in this chapter, the motivation behind selection of this example is the fact that it has an analytical solution, in this case wherein the potential at a point  $\bar{\mathbf{p}}$  is given by

$$\phi_{ref}(\bar{\mathbf{p}}) = e^{ikx(\bar{\mathbf{p}})}, \quad \bar{\mathbf{p}} \in \Omega_f. \quad (6.18)$$

This example is considered as an acoustic cavity problem with Robin boundary conditions  $\alpha = 0, \beta = -ik$  prescribed on the left hand side of the duct, and  $\alpha = ik, \beta = 0$  on the right hand side; these can be seen along with relevant dimensions in Fig. 6.12. Along the horizontal boundaries  $\alpha = 0$  is prescribed and  $\beta = 0$ , corresponding to the ‘sound-hard’ condition. The  $L^2$  relative error  $\epsilon$  is evaluated over a straight line of points  $\Gamma_\epsilon = \{(x, y) : x \in (0, L), y = W/2\}$ . Results from a test case in a short duct of dimensions  $L = 1, W = 1$ , with  $k = 4\pi$ , are displayed in Fig. 6.13, and it is evident that the error  $\epsilon$  follows a similar pattern to that in the previous examples. That is, increasing the order of basis functions employed causes a reduction in error, with Lagrange polynomials and NURBS offering similar performance.

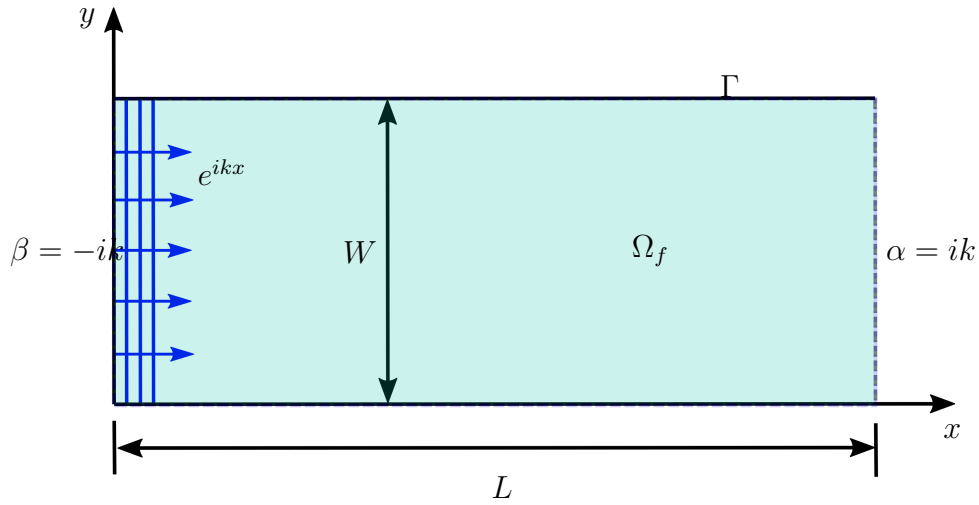


Figure 6.12: Duct boundary conditions and domain.

To generate the plots showing the  $L^2$  relative errors  $\epsilon$  for the Lagrange and NURBS schemes in Fig. 6.13, the discretisation process is straightforward; first select the order of basis to be employed, then increase the number of elements to give the required total number of degrees of freedom. Though, the PUBEM discretisation for the same example is slightly more involved. Before discussing the PUBEM discretisation of the duct, the discretisation of the first two examples of exterior scattering from cylinders, is described; a coarse discretisation of 4 elements per cylinder was used, with  $M$  chosen to provide the required number of degrees of freedom,  $N_d$ . Therefore, in PUBEM there are two options, one can increase the total number of elements,  $E$  (i.e.  $h$ -refinement), or increase the number of plane waves  $M$  included per node (a process akin to  $p$ -refinement, and sometimes called  $Q$ -refinement). It has been shown that the latter is favourable [50], until  $\tau$  becomes sufficiently large to cause severe ill-conditioning, at which point an increase in the number of elements,  $E$ , with an associated reduction in the number of plane waves  $M$ , becomes the favourable option. This is similar to the  $hp$ -refinement schemes commonly found in the finite element literature.

In this duct problem, one would expect that including enrichment in the  $x$ -direction would be of benefit because, obviously, then the solution to the problem is contained in the approximation space and it would be expected that a solution with very low errors would be obtained. Testing, shows that this indeed the case, and one can also reduce  $M$  to 1 (i.e. including only the  $x$ -direction and no other directions in the plane wave basis). This is demonstrated in Table 6.1, which displays  $\epsilon$  for a range of ducts of length  $L$  up to  $200\lambda$  for the case  $k = 4\pi$ , with only a single element used on each side of the duct. It is evident that a high level of accuracy is consistently achieved for this coarsest of meshes,

independently of  $L$ .

As mentioned, the exact solution is contained in the approximation space, therefore, high accuracy for such a small number of degrees of freedom shown in Table 6.1 comes as no surprise. Though, it is perhaps more useful to investigate the performance of PUBEM where  $M > 1$  and the  $x$ -direction is *not* contained in the basis. It is well known that a linear combination of (a sufficient number of) plane-waves can reproduce any solution of the Helmholtz equation, and here the behaviour of PUBEM is explored with this multiple wave expansion in approximating the plane-wave propagating through the duct. The results shown in Fig. 6.13 were produced using this set of plane-waves, propagating in directions (not including  $\theta = 0$ ). From these results, it is clearly still possible to recover the acoustic potential with high accuracy.

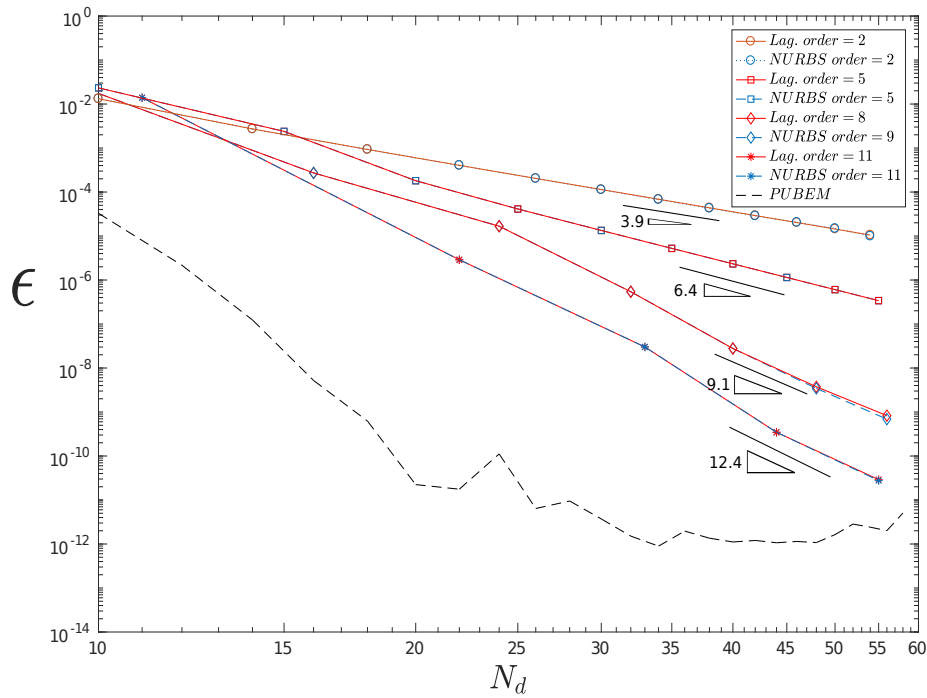


Figure 6.13:  $L^2$  error  $\epsilon$  vs.  $N_d$  per side for a travelling wave in a duct,  $k = 4\pi$ .

$L/\lambda$	2	20	100	200
$\tau$	1	0.1	0.02	0.01
$\epsilon$	$3.0996e - 13$	$3.5676e - 13$	$3.5802e - 13$	$3.4503e - 13$

Table 6.1: Relative error  $\epsilon$  with  $M = 1$  using only a single element per side,  $k = 4\pi$ .

### Pollution error in the duct.

In FEM, pollution error is a commonly studied numerical aspect, though, this is not the case for BEM. In fact the pollution effect has only recently been investigated for

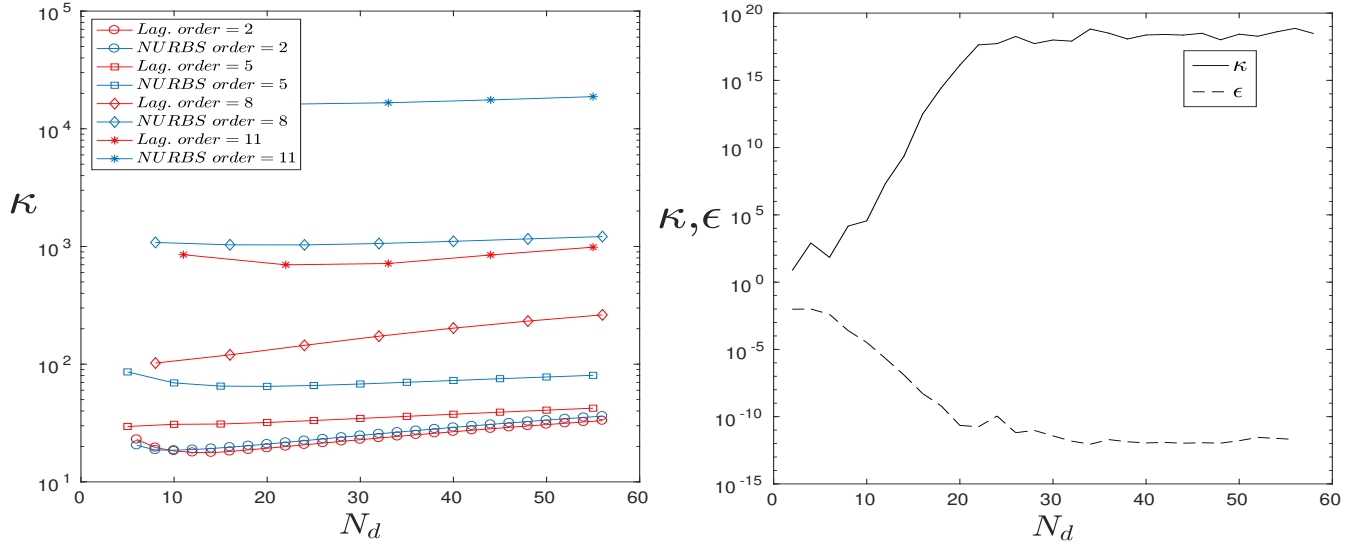


Figure 6.14: (left) Condition number  $\kappa$  for the Lagrange and NURBS basis, (right) Condition number  $\kappa$  and  $L^2$  error  $\epsilon$  for the plane wave basis, for a travelling wave in a duct,  $k = 4\pi$ .

BEM by Marburg [103], who used a discretisation comprising piecewise constant, linear and quadratic basis functions in a BEM approximation of propagation of a plane-wave along a long, slender, air-filled duct to show the pollution effect. Marburg showed that the pollution error is an error that increases along the length of the duct and cannot be resolved by refining the mesh towards the end of the duct. In this section, the same duct is tested, with the same number of degrees of freedom per side as the finest of Marburg's discretisations, but using high-order and plane-wave enriched basis functions. The dimensions of this example are  $W = 0.2$  m and  $L = 54.4$  m, with the speed of sound in air taken to be 340 m/s and a frequency of 750 Hz.

The first example considered here is produced by including 1632 degrees of freedom along each of the long sides of the duct. A local absolute error  $\epsilon_1 = |\phi - \phi_{ref}|$ , is computed over  $\Gamma_\epsilon$ . The local absolute error  $\epsilon_1$  is shown in Fig. 6.15; it is clear that both the Lagrange and NURBS bases are subject to a pollution effect manifested in degradation in accuracy with increasing coordinate  $x$ . Increasing the order of basis employed does reduce the overall error, but the error is seen to increase as a function of  $x$ . Again, the results of the Lagrange and NURBS bases are very similar (the condition numbers for this example are shown in Table 6.2, which shows the conditioning is benign in both cases). The PUBEM discretisations employed are  $M = 1, 8, 10$  and 12, with the corresponding number of elements,  $E$ , to provide the required number of degrees of freedom per side.

Lagrange		NURBS		PUBEM	
Order	$\kappa$	Order	$\kappa$	$M$	$\kappa$
2	50.3	2	51.5	1	49.6
5	47.8	5	72.8	8	$1.9e + 18$
8	90.6	8	1137.3	10	$1.3e + 19$
11	1341.6	11	1972.4	12	$3.6e + 18$

Table 6.2: Condition number  $\kappa$  for the duct with  $L = 54.4m$ ,  $W = 0.2m$  and  $f = 750Hz$

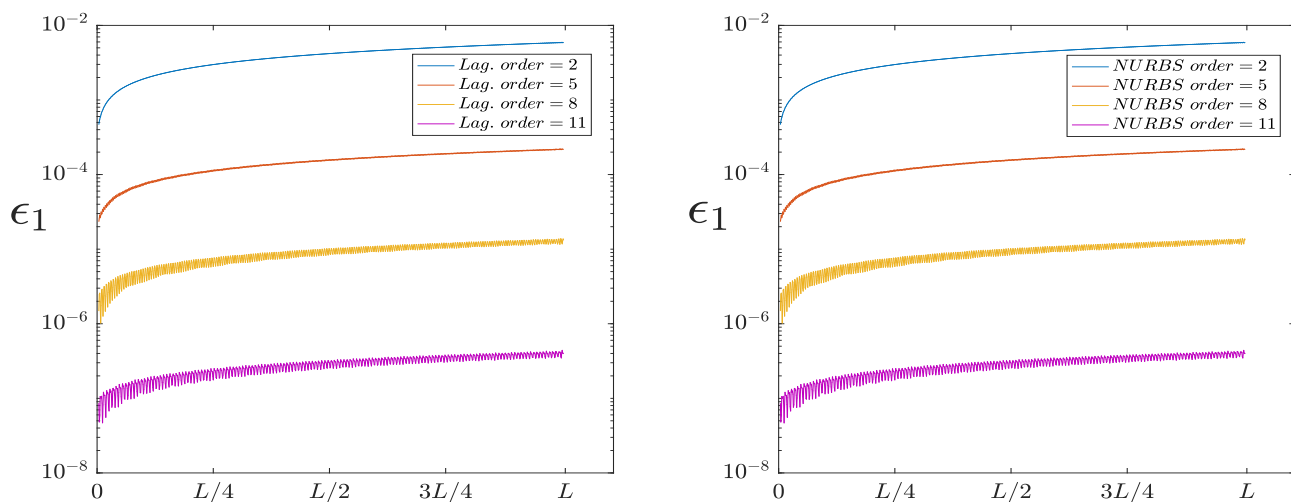


Figure 6.15: (left) Local error  $\epsilon_1$  for the Lagrange basis, (right) Local error  $\epsilon_1$  for the NURBS basis for a travelling wave in a duct having  $L = 54.4$ ,  $f = 750Hz$ , and including 1632 degrees of freedom on each long side.

For the  $M = 8, 10$  and  $12$  discretisations the plane wave directions are equispaced, but the  $x$ -direction is explicitly excluded from the basis, whereas for the  $M = 1$  case, it is the only direction included in the basis. Fig 6.16 displays the variation in error  $\epsilon_1$  incurred, by the PUBEM schemes, with position in the duct. For the case  $M = 1$  the errors are consistently very small, and there is no evidence of any meaningful pollution error. For  $M = 8, 10, 12$  the errors are highly oscillatory in  $x$ , which may perhaps be expected for errors in the range  $10^{-9}$  to  $10^{-11}$ , but a small underlying positive gradient is visible that suggests there is a mild pollution effect when using a plane wave basis. These results for pollution errors in the PUBEM are consistent with the observations of Gittelsohn for the plane-wave enriched Discontinuous Galerkin (PWDG) method [105].

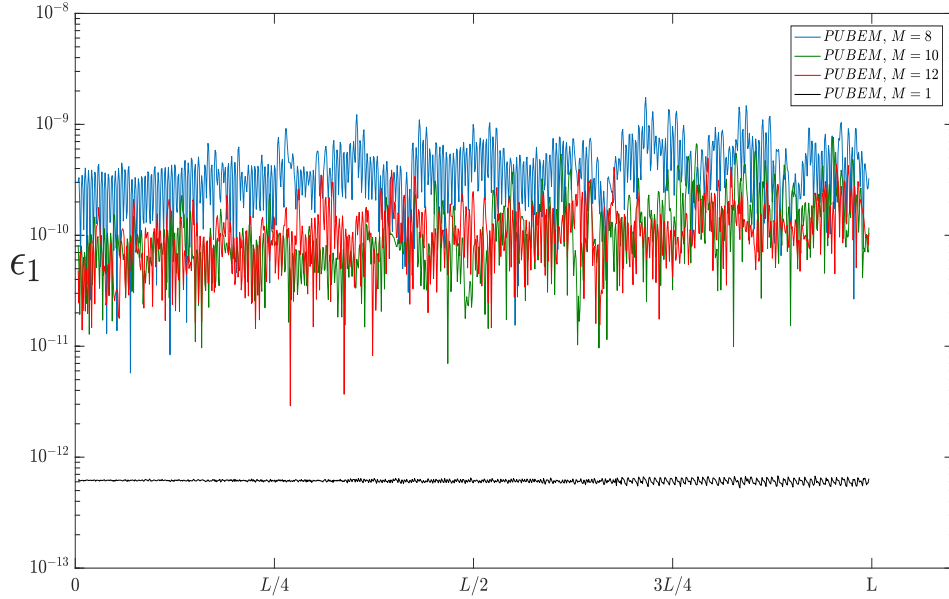


Figure 6.16: Local error  $\epsilon_1$  for the PUBEM basis for a travelling wave in a duct having  $L = 54.4$ ,  $f = 750Hz$ , and including 1632 degrees of freedom on each long side.

### 6.3 Conclusions

In this chapter, numerical performance of high-order NURBS and Lagrange polynomial bases has been compared with the plane-wave basis of PUBEM for three benchmark problems. It has been shown that a marked improvement in accuracy can be achieved by the order of NURBS and Lagrange polynomial bases, with a reduction in error of up to 6 orders of magnitude. The resulting condition number of the system of equations increases along with the order, but for the examples studied (up to 11th order functions per element), both systems are well conditioned and the accuracy of the solution is not adversely affected. The NURBS and Lagrange bases provide very similar numerical solutions in the relative  $L^2$  error norm, though, NURBS prove to be slightly more accurate. PUBEM has been shown to consistently outperform the lower order bases, but for large  $\tau$  the 11th order Lagrange and NURBS bases generate better conditioned linear systems and can achieve greater accuracy. Additionally, the pollution error in BEM has been observed for high-order and PUBEM discretisations in an example of a travelling wave in a long duct. The overall error in the duct can be reduced by increasing the order of the basis functions, or by enriching it, but a pollution error will still develop for waves propagating over a long distance.

# Chapter 7

## Optimal selection of basis for PUBEM

The results of Chapter 6 provided insight into the order of BEM bases employed, in particular, indicating that a relatively high-order basis can provide greater accuracy per degree of freedom than a standard quadratic basis. It is common to employ a standard basis such as quadratic shape functions or NURBS of order 2 with a plane wave basis, because it is understood that the plane-waves are doing most of the work in representing the solution. For this reason, there is yet to be a study into the order of the underlying basis functions which serve to interpolate the amplitudes of the plane-wave basis.

In this chapter, PUBEM is implemented using a variety of elements, from constant to order 4. The circular scattering object has proven useful, not just due the analytical solution, but due to the fact that the results from the circle have been shown to be a good indicator of performance for other geometries, such as the capsule, and multiple scatterer arrangements. Thus, a single geometry of a circular scattering object is considered here, which negates the requirement to repeat many results.

Earlier chapters of this thesis have demonstrated that the accuracy of the solution, including the management of the system conditioning, can be controlled by making an appropriate choice of the number of degrees of freedom per wavelength,  $\tau$ . Therefore, for a given problem for a scatterer of some known perimeter and for a given wavenumber  $k$ , it becomes a simple matter to determine the optimal number of degrees of freedom to use in our PUBEM analysis. The total number of degrees of freedom is  $N_d = (J - 1)EM$ , where  $E$  is the number of elements,  $M$  is the number of plane wave directions per node and  $J$  is the number of conventional basis functions used per element. Thus, there is considerable freedom in our choice of  $E, M, J$  to accumulate the desired total number of degrees of freedom. The optimisation of this decision making is the subject of this chapter. Before presenting the results, note that: the total number of degrees of freedom

is defined as  $N_d$ ;  $\epsilon$  is an  $L^2$  relative error as defined in Appendix C;  $p$  is the order of basis ( $p = 0$  is a constant element), and  $\kappa$  is the condition number of the resulting system of equations. Due to the requirement of repeating results for each order of basis, there appear to be a large number of results are presented here, but there are essentially only two tests performed: varying  $k$  and varying  $N_d$ .

## 7.1 Varying $k$

Firstly the number of degrees of freedom is fixed as follows  $N_d = 192$  and the number of elements is varied as follows  $E = 2, 4, 8, 16$ , then results are compared for each order of basis function, i.e.,  $p = 0-4$ . Implicit within the variation of  $E$  with a fixed  $N_d$  is the requirement that  $M$  varies accordingly, and naturally, as  $E$  increases  $M$  decreases and vice versa. Results are shown for each  $E$ - $M$  combination for the  $p = 0$  case in Fig. 7.1 wherein  $k$  is varied from 1-100 and the resulting error  $\epsilon$  and condition number  $\kappa$  are plotted. Predictably,  $\kappa$  increases as more plane-waves and larger elements are used, with the lowest  $\kappa$  achieved by the  $E = 16$  discretisation. The error seems to be highest for  $E = 16$ , even though it is the most well-conditioned, with the accuracy generally increasing, until  $E$  drops as low as 2, which produces slightly less accurate results than the  $E = 4$  case. The accuracy of these results is substantial, considering that the elements are constant, which means that the plane-waves are doing the vast majority of the work.

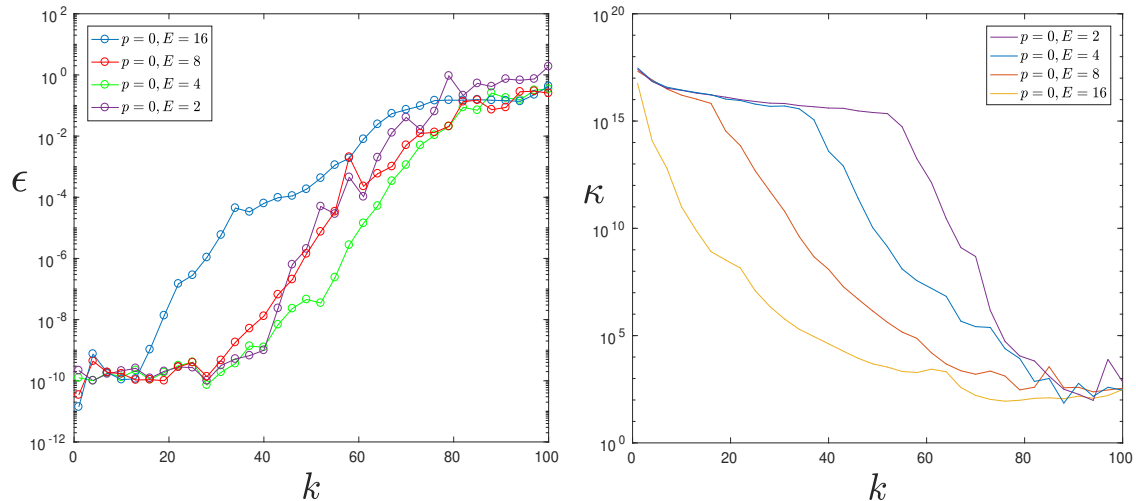


Figure 7.1:  $L^2$  relative error epsilon and the corresponding condition number  $\kappa$ , for basis functions of order  $p = 0$ .

The error and condition number with  $k$  varying are plotted, for  $p = 1-4$ , in Figs. 7.2-7.5 respectively. Overall, the results bear resemblance to the  $p = 0$  case, though, it appears

that from  $p \geq 2$  the fewer elements the better, with the  $E = 2$  case outperforming the  $E = 4$  case.

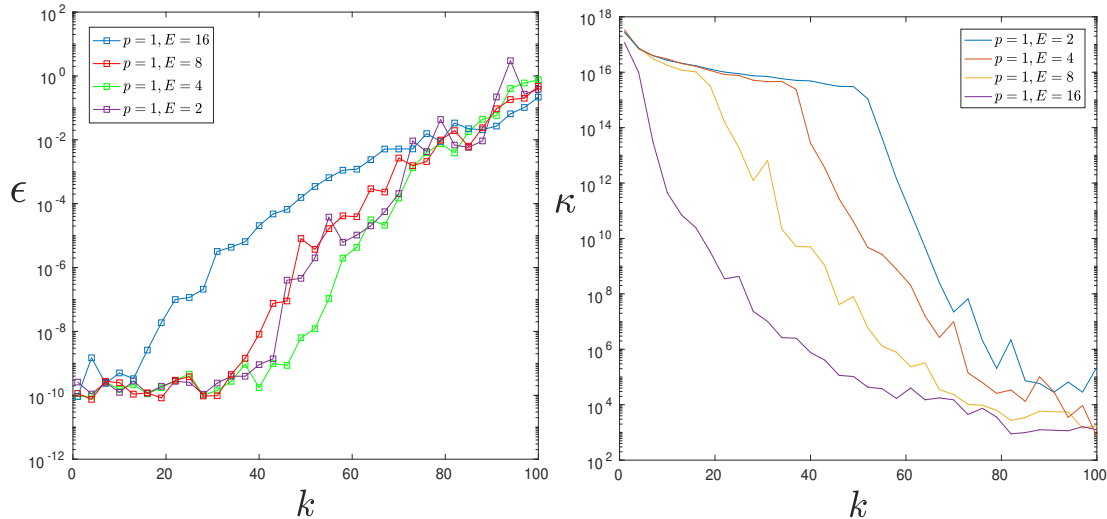


Figure 7.2:  $L^2$  relative error epsilon and the corresponding condition number  $\kappa$ , for basis functions of order  $p = 1$ .

## 7.2 Varying the number of degrees of freedom

In Fig. 7.6 results are shown for a fixed wavenumber  $k = 50$  and  $N_d$  varied by increasing  $M$ , again for  $E = 2, 4, 8, 16$  and  $p = 0-4$ . Again, it is noted that the condition number is lowest for the  $E = 16$  case and highest for the  $E = 2$  case. Further, we notice that for this constant element case  $E = 4$  outperforms  $E = 2$ .

The error and condition number with  $N_d$  varying for  $p = 1-4$  are plotted in Figs. 7.7-7.10 respectively. Overall, the results bear resemblance to the  $p = 0$  case, though, it appears that again, from  $p \geq 2$  the fewer elements the better, with the  $E = 2$  case outperforming the  $E = 4$  case. Thus, it appears that for quadratic or higher-order elements, it is optimal to employ as few elements as possible, whereas extra care is required for constant and linear elements.

## 7.3 Comparison

The results above are difficult to compare directly, so Fig. 7.11 is provided to present the most accurate discretisation for each order and compare the error resulting from varying  $k$  and  $N_d$ . The results in Fig. 7.11 confirm that above with regards to  $E = 2$  and  $E = 4$ , but generally shows very similar levels of error for each  $p$ , meaning that the simplicity of a constant element, coupled with the accuracy that is possible could provide a strong benefit over quadratic PUBEM elements.

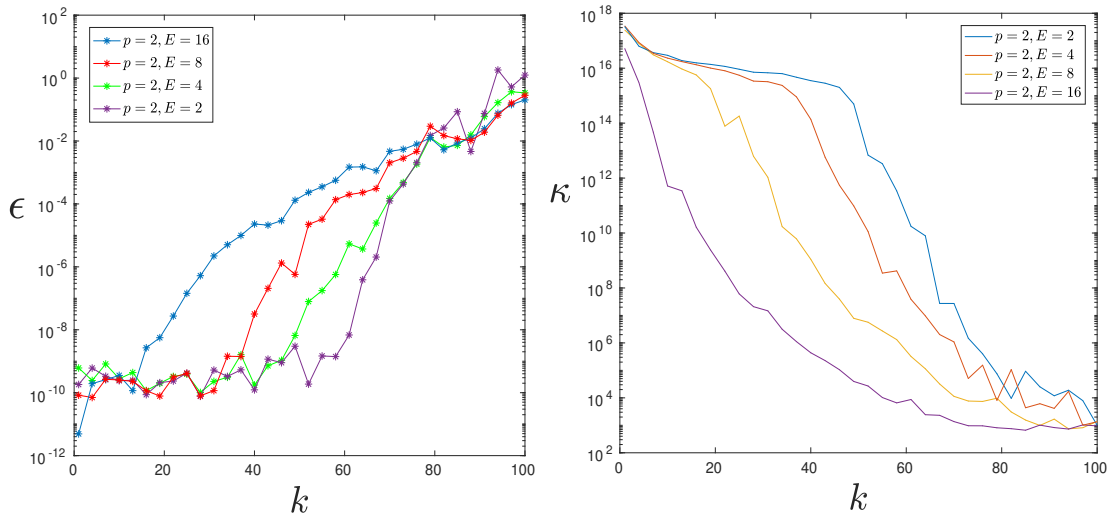


Figure 7.3:  $L^2$  relative error  $\epsilon$  and the corresponding condition number  $\kappa$ , for basis functions of order  $p = 2$ .

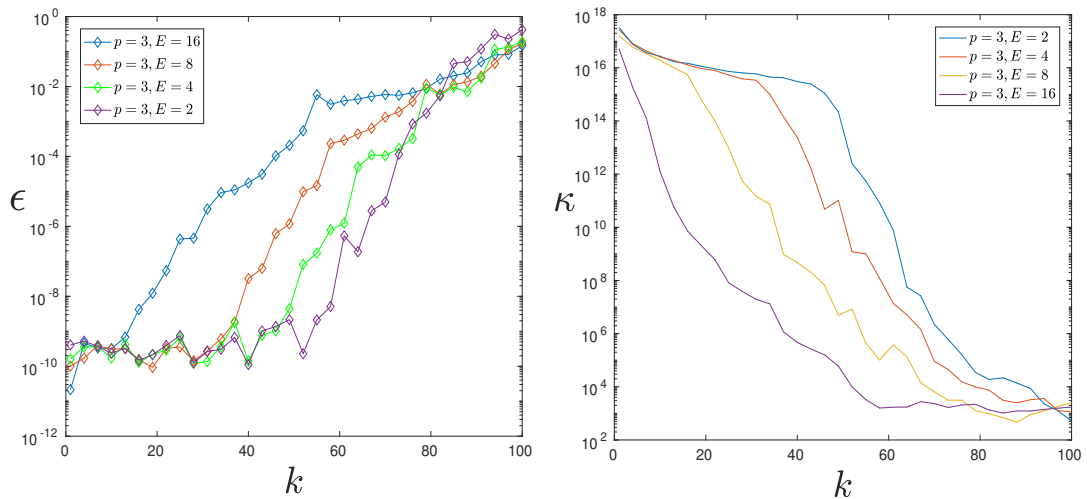


Figure 7.4:  $L^2$  relative error  $\epsilon$  and the corresponding condition number  $\kappa$ , for basis functions of order  $p = 3$ .

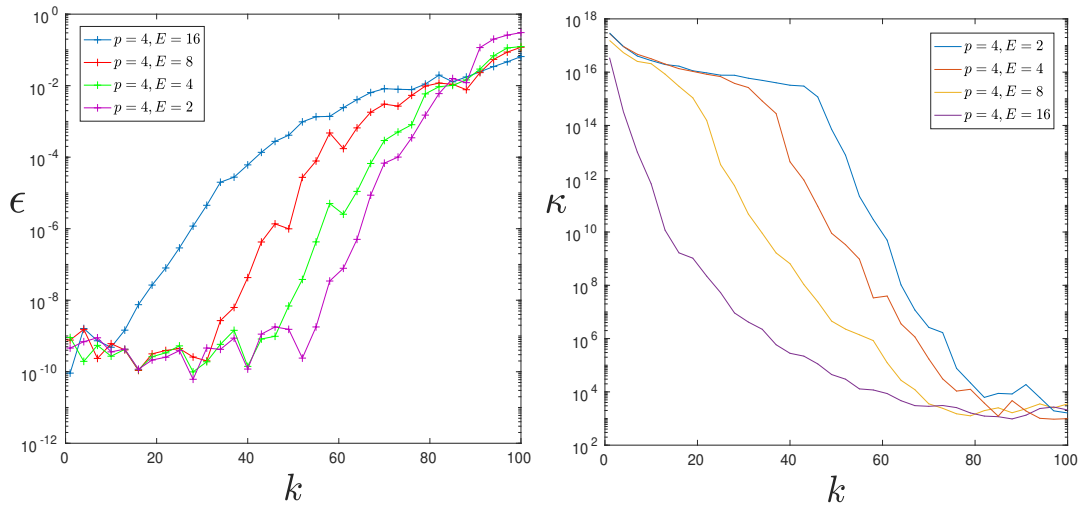


Figure 7.5:  $L^2$  relative error  $\epsilon$  and the corresponding condition number  $\kappa$ , for basis functions of order  $p = 4$ .

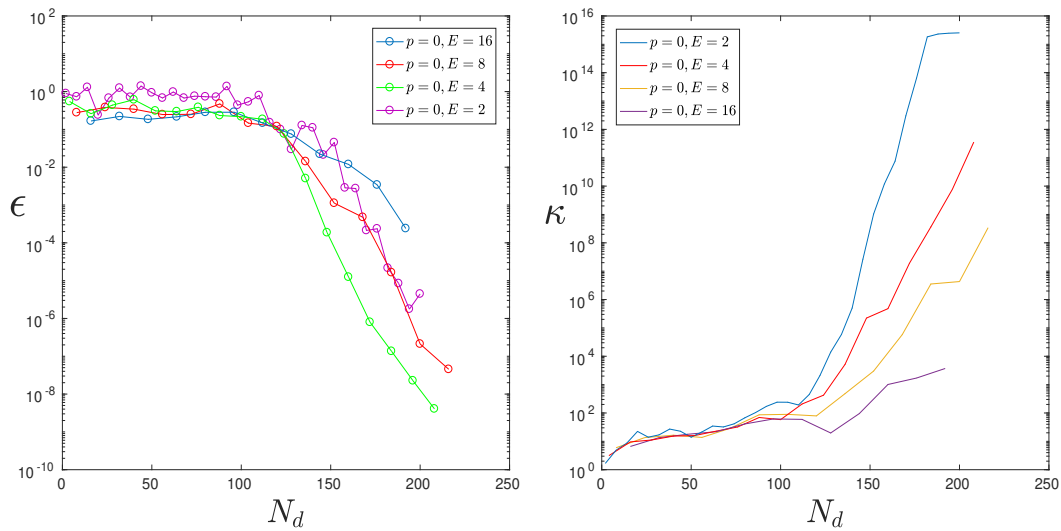


Figure 7.6:  $L^2$  relative error  $\epsilon$  and the resulting condition number  $\kappa$  vs.  $N_d$  for discretisations including a total number of elements  $E = 2, 4, 8, 16$ .  $k = 50$  and  $N_d$  is increased by increasing  $M$ ,  $p = 0$ .

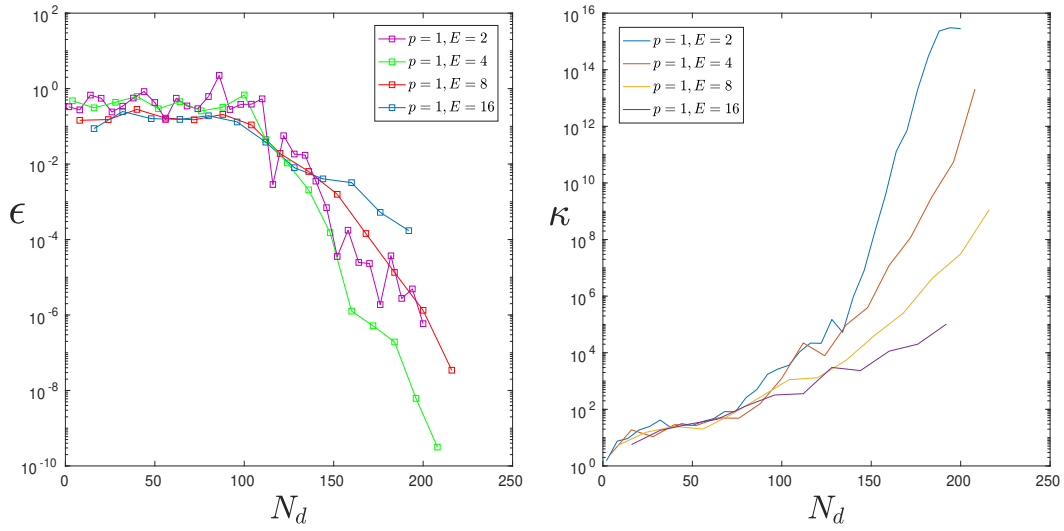


Figure 7.7:  $L^2$  relative error  $\epsilon$  and the resulting condition number  $\kappa$  vs.  $N_d$  for discretisations including a total number of elements  $E = 2, 4, 8, 16$ .  $k = 50$  and  $N_d$  is increased by increasing  $M$ ,  $p = 1$ .

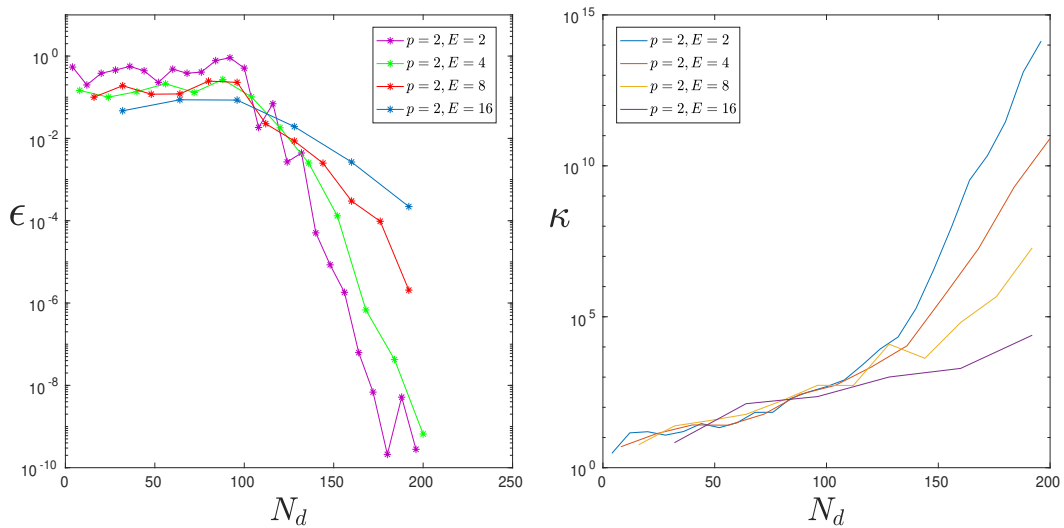


Figure 7.8:  $L^2$  relative error  $\epsilon$  and the resulting condition number  $\kappa$  vs.  $N_d$  for discretisations including a total number of elements  $E = 2, 4, 8, 16$ .  $k = 50$  and  $N_d$  is increased by increasing  $M$ ,  $p = 2$ .

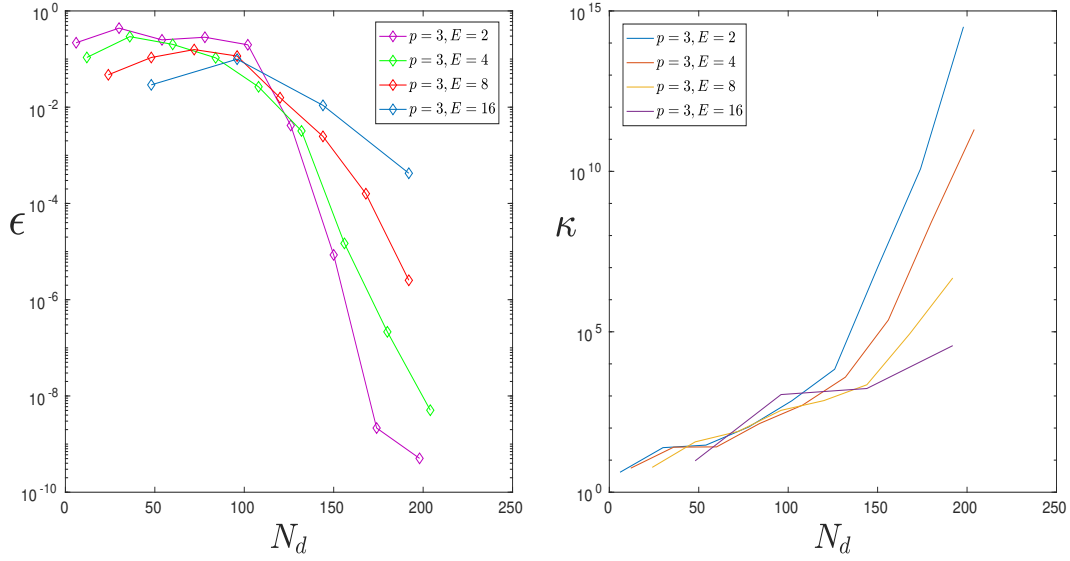


Figure 7.9:  $L^2$  relative error  $\epsilon$  and the resulting condition number  $\kappa$  vs.  $N_d$  for discretisations including a total number of elements  $E = 2, 4, 8, 16$ .  $k = 50$  and  $N_d$  is increased by increasing  $M$ ,  $p = 3$ .

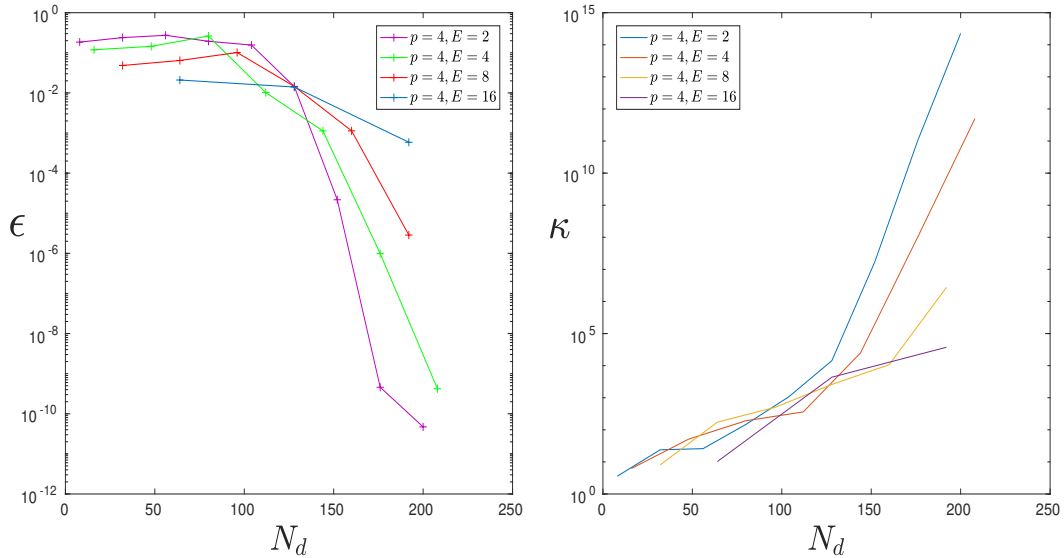


Figure 7.10:  $L^2$  relative error  $\epsilon$  and the resulting condition number  $\kappa$  vs.  $N_d$  for discretisations including a total number of elements  $E = 2, 4, 8, 16$ .  $k = 50$  and  $N_d$  is increased by increasing  $M$ ,  $p = 4$ .

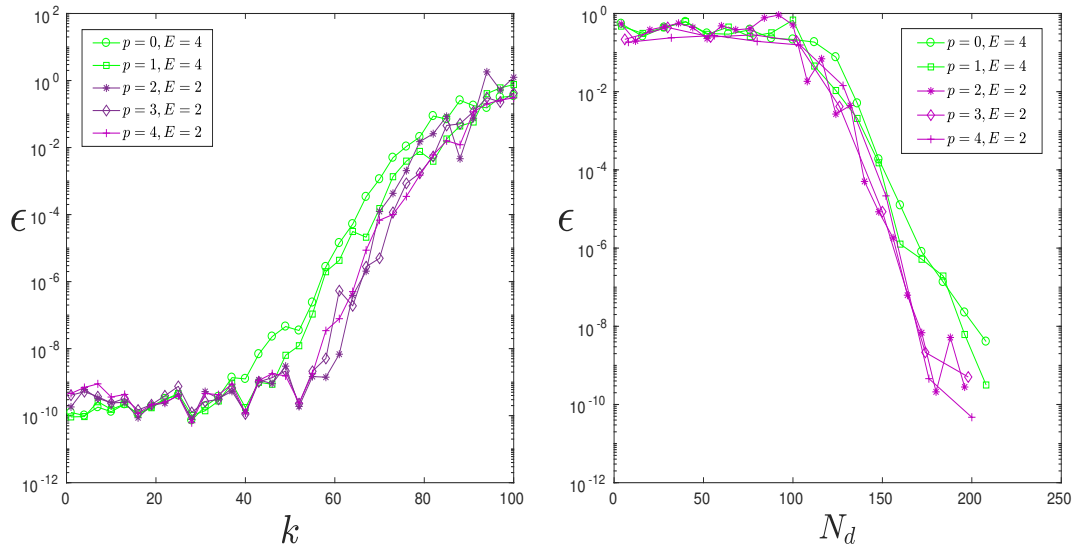


Figure 7.11:  $L^2$  relative error  $\epsilon$  vs.  $k$  for the most accurate example for each  $p$  taken from the above results (left).  $L^2$  relative error  $\epsilon$  vs.  $N_d$  for the most accurate example for each  $p$  taken from the above results (right).

## 7.4 Conclusion

In summary, it seems that for the circular scatterer,  $E = 2$  with larger  $M$  is the most accurate, apart from whilst using the constant or linear elements. For more complicated geometries, more than 2 elements would need to be used but the general indication from this analysis is that a smaller number of elements tends to be preferable over a large number of elements. This implies that if we wish to employ  $E \leq 2$  then  $p \geq 2$  would be ideal, though the constant and linear elements are still very accurate, and this slight increase in error could be offset by improved integration speed achieved by use of simpler functions.

Even with the results of this section highlighting the efficacy of using large elements with relatively low order basis functions, a more thorough analysis including more complicated geometries or multiple objects would likely be required to develop a one-size-fits-all rule for determining an optimal number of elements to use; optimal order of basis functions; and, the corresponding optimal number of plane waves to use per node, for a given wavenumber.

# Chapter 8

## Conclusions and further work

### 8.1 Conclusions

The work presented in this thesis has been a broad study of the use of oscillatory basis functions in acoustic modelling. There have been three major aspects that have been studied in which novel work has been undertaken, these are:

- 1 Integration schemes for PUBEM
- 2 Singular basis functions for scattering from corners
- 3 High-order Lagrange and NURBS schemes

Together, these studies provide a comprehensive investigation of numerical performance of schemes based on these novel basis functions.

In addition, a short study of the optimal number of elements  $E$  vs. the number of plane waves included per node  $M$  was performed. The results showed that highly accurate results could be achieved using constant elements and a coarse discretisation, as long as a sufficient number of plane waves were employed.

#### 8.1.1 Integration schemes for PUBEM

The following highly-oscillatory integration schemes were tested:

- 1 Filon method
- 2 Asymptotic method
- 3 Method of stationary phase
- 4 Targeted Gauss-Legendre
- 5 Optimised Gauss-Legendre

All of these integration schemes produced highly accurate results for some cases, but none produced highly accurate results in all cases. This led to a study of a standard Gauss-Legendre scheme with the results suggesting that only around 4 Gauss points are required per wavelength for PUBEM integrals. Some of this work was published in *Journal of Computational Mathematics (JCM)*.

A common feature of the problematic cases is the presence of a stationary point close to the end of an element. In a typical PUBEM analysis, tens of thousands of integrals could be performed. The ill-conditioning of these systems of equations means that it is important to evaluate our integrals to a prescribed accuracy because even a relatively small number of inaccurately evaluated integrals can impact on the overall accuracy of the solution. It is concluded that a scheme giving robust evaluation of all integrals is important and this is only provided by Gauss-Legendre. However, results from testing of the Optimised Gauss-Legendre scheme show that relatively few Gauss points per wavelength are required. In particular, there is benefit in using relatively large integration cells, with high-order quadrature.

### **8.1.2 Singular basis functions for scattering from corners**

A study into the numerical behaviour of PUBEM and BEM at corner locations was presented and additional enrichment functions developed to increase accuracy. The resulting enriched schemes are termed XBEM and PUXBEM and produce substantial improvement. For example, the results show that an increase in accuracy of two orders of magnitude is possible for scattering by polygonal objects, simply by including a fractional order Bessel function at each corner. A range of  $k$  was tested and the number of degrees of freedom were varied. Also, the resulting condition numbers were observed. This work was published in *International Journal for Numerical Methods in Engineering (IJNME)*.

This scheme was shown to work for  $90^\circ$  and  $60^\circ$  corners and it is confidently predicted that the scheme would perform well for other angles.

### **8.1.3 High-order Lagrange and NURBS schemes**

High-order basis functions were explored for scattering problems including multiple cylinders in  $2D$  and wave propagation along the length of a duct. A variety of frequencies and discretisations were tested, with Lagrange and NURBS bases. Further, the results were compared with PUBEM schemes. Furthermore, the pollution effect was observed for PUBEM in the duct example. This work was published in *Engineering Analysis with Boundary Elements (EABE)*.

It was shown that a reduction in error of up to 6 orders of magnitude can be achieved by increasing the orders of the Lagrange and NURBS bases. Notably the condition numbers of the resulting systems of equations increased with the order of the bases, though this

does not appear to adversely impact the results. A mild pollution effect was observed in the PUBEM results; this is the first time that this has been demonstrated.

For Larger problems, the high-order Lagrange and NURBS schemes appear to be competitive with PUBEM because they converge consistently and their matrix systems are comparatively well-conditioned.

#### **8.1.4 Optimal selection of basis functions for PUBEM**

A PUBEM scheme was implemented, to analyse scattering from a circle, using a variety of elements, from constant to order 4, with a variety discretisations each having differing ratios of total number of elements  $E$  to number of plane waves per node  $M$ . It was shown that, at least for a circular scattering object, that generally, using relatively few elements in combination with a relatively large number of plane waves is optimal for accuracy. This was true even with linear and constant elements with the exception the very coarsest discretisation of only two elements on the boundary.

## **8.2 Recommendations for further work**

### **8.2.1 Integration**

The integration schemes that were not based on quadrature, whilst interesting, did not produce a robust alternative to Gauss-Legendre quadrature for highly oscillatory integrals for  $k$  in the mid-high frequency range for which most of the PUBEM literature is focused. Though, it would be interesting to apply the integration techniques presented in this thesis for genuine high-frequency problems and to compare the resulting PUBEM solution with, for example, optics or ray-tracing solutions.

Further, the investigations into the Filon method, the asymptotic method and MSP were based on quadratic shape functions which are standard in the PUBEM literature. In light of the possible advantages of the low-order shape functions, it would be interesting to investigate these schemes, in particular the Filon and asymptotic schemes, for PUBEM integrals. This would simplify the expressions (in particular for the Filon and Asymptotic method) which would reduce computation time; and, the more simple slowly varying function could dampen the underlying end point behaviour which could result in a more accurate results (remembering how important the end point behaviour is).

Finally, it would be interesting to explore a second-order term in the method of stationary phase. This could potentially evaluate integrals in which a stationary point is closer to the end of an element than is allowable with a first-order scheme. Although, there would likely, still, be cases that are problematic, it may be that these are so small in number that the overall accuracy of the analysis is acceptable.

### 8.2.2 Singular enrichment functions

The singular enrichment functions were a great success, resulting in a substantial increase in accuracy. This benefit may be transferable to  $3D$ , for polyhedral objects, where similar enrichment from edges could be applied. It is not immediately clear how the enrichment functions would be defined at the vertices. Though, there are asymptotic solutions for scattering from vertices.

### 8.2.3 High-order basis functions

It was shown that using high-order basis functions provided a reduction in error of 6 orders of magnitude in some cases. It would be interesting to see how this translates to  $3D$ . Further, the pollution effect in BEM was discussed, but only for a single example. It would be worth exploring this in depth, and comparing with PUBEM, but it is not straightforward to find appropriate problems to solve. Test problems base on a Hankel source present challenges because to test pollution effect, one needs many wavelengths and the decay in the Hankel source over the required number of wavelengths means that the potentials become too small in the area of interest for meaningful conclusions to be drawn.

### 8.2.4 Optimal selection of basis functions for PUBEM

It would be interesting to perform a more thorough analysis of the optimal order of basis to be used for PUBEM, in order to develop a one-size-fits-all rule for determining an optimal number of elements to use; optimal order of basis functions; and, the corresponding optimal number of plane waves to use per node, for a given wavenumber. Such analysis should include more complicated geometries or multiple objects.

# Appendices

# Appendix A

## Stationary points algorithm

To integrate using the Filon method, when stationary points are included within the interval of integration, it is necessary to perform a number of coordinate transformations, in order to produce an expression which is amenable to the method. This begins with the inversion of  $g(\xi)$  such that  $v = g(\xi)$ ; from the expression of  $g(\xi)$ , it can be derived directly that

$$\xi = h(v) = -1 + \frac{x_p - v \cos(\phi) \pm \sqrt{(v - x_p \cos(\phi))^2 - y_p^2 \sin^2(\phi)}}{x_m \sin^2(\phi)}, \quad (\text{A.1})$$

and

$$\frac{d\xi}{dv} = h'(v) = \frac{-\cos(\phi)}{x_m \sin^2(\phi)} \pm \frac{v - x_p \cos(\phi)}{x_m \sin^2(\phi) \sqrt{(v - x_p \cos(\phi))^2 - y_p^2 \sin^2(\phi)}}. \quad (\text{A.2})$$

Further, it can be shown that

$$v^* = g(\xi^*) = x_p \cos(\phi) + |y_p| |\sin(\phi)|. \quad (\text{A.3})$$

One can focus on the  $I_\beta$  portion of the interval with  $\xi \in (\xi^*, 1)$  and rewrite in terms of the variable  $v$  as

$$I_\beta = \int_{\xi^*}^1 (\xi - \xi^*)^\ell e^{ikg(\xi)} d\xi = \int_{v^*}^{g(1)} (h(v) - \xi^*)^\ell h'(v) e^{ikv} dv, \quad (\text{A.4})$$

where

$$(h(v) - \xi^*) = \frac{-\cos(\phi)(v - x_p \cos(\phi)) + |y_p \cos(\phi)| |\sin(\phi)| + \sqrt{(v - x_p \cos(\phi))^2 - y_p^2 \sin^2(\phi)}}{x_m \sin^2(\phi)}, \quad (\text{A.5})$$

and  $h'(v)$  is given in (A.2). The  $h'(v)$  term is singular at  $v^*$  and in order to convert this into a form which is easier to treat, a further coordinate transformation  $\psi = v - x_p \cos(\phi)$  is applied which yields

$$I_\beta = \int_{v^*}^{g(1)} (h(v) - h(v^*))^\ell h'(v) e^{ikv} dv = \frac{e^{ikx_p \cos(\phi)}}{(x_m \sin^2(\phi))^\ell} \int_{|y_p \sin(\phi)|}^{g(1) - x_p \cos(\phi)} F(\psi) e^{ik\psi} d\psi \quad (\text{A.6})$$

which produces

$$F(\psi) = \left( \pm |y_p \cos(\phi)| |\sin(\phi)| - \cos(\phi)\psi + \sqrt{\psi^2 - y_p^2 \sin^2(\phi)} \right)^\ell \quad (\text{A.7})$$

$$\left( -\cos(\phi) + \frac{\psi}{\sqrt{\psi^2 - y_p^2 \sin^2(\phi)}} \right) \quad (\text{A.8})$$

which can be represented using the binomial theorem  $(A + B)^\ell = \sum_{i=0}^{\ell} \binom{\ell}{i} A^{\ell-i} B^i = \sum_{i=0}^{\ell} \binom{\ell}{i} A^i B^{\ell-i}$ ,  $\binom{\ell}{i} = \frac{\ell!}{i!(\ell-i)!}$  as

$$\begin{aligned} F(\psi) &= \sum_{j_1=0}^{\ell} \binom{\ell}{j_1} (\pm |y_p \cos(\phi)| |\sin(\phi)| - \cos(\phi)\psi)^{\ell-j_1} \left( \sqrt{\psi^2 - y_p^2 \sin^2(\phi)} \right)^{j_1} \\ &\quad \left( -\cos(\phi) + \frac{\psi}{\sqrt{\psi^2 - y_p^2 \sin^2(\phi)}} \right) \\ &= \sum_{j_1=0}^{\ell} \binom{\ell}{j_1} \sum_{j_2=0}^{\ell-j_1} \binom{\ell-j_1}{j_2} (\pm |y_p \cos(\phi)| |\sin(\phi)|)^{\ell-j_1-j_2} (-\cos(\phi))^{j_2} \psi^{j_2} \\ &\quad \left( \sqrt{\psi^2 - y_p^2 \sin^2(\phi)} \right)^{j_1} \left( -\cos(\phi) + \frac{\psi}{\sqrt{\psi^2 - y_p^2 \sin^2(\phi)}} \right) \\ &= \sum_{j_1=0}^{\ell} \binom{\ell}{j_1} \sum_{j_2=0}^{\ell-j_1} \binom{\ell-j_1}{j_2} (\pm |y_p \cos(\phi)| |\sin(\phi)|)^{\ell-j_1-j_2} \\ &\quad \left[ (-\cos(\phi))^{j_2+1} \psi^{j_2} \left( \sqrt{\psi^2 - y_p^2 \sin^2(\phi)} \right)^{j_1} + (-\cos(\phi))^{j_2} \psi^{j_2+1} \left( \sqrt{\psi^2 - y_p^2 \sin^2(\phi)} \right)^{j_1-1} \right]. \end{aligned} \quad (\text{A.9})$$

(A.10)

The sum  $\sum_{j_1=0}^{\ell}$  is split into two separate sums for odd and even  $j_1$ , to produce

$$\begin{aligned}
F(\psi) &= \left( \sum_{\substack{n=0 \\ j_1 \text{ taking } 2n}}^{\lfloor \frac{\ell}{2} \rfloor} + \sum_{\substack{n=1 \\ j_1 \text{ taking } 2n-1}}^{\lfloor \frac{\ell+1}{2} \rfloor} \right) \binom{\ell}{j_1} \sum_{j_2=0}^{\ell-j_1} \binom{\ell-j_1}{j_2} \\
&\quad (\pm |y_p \cos(\phi)| |\sin(\phi)|)^{\ell-j_1-j_2} \left[ (-\cos(\phi))^{j_2+1} \psi^{j_2} \times \right. \\
&\quad \left. \left( \sqrt{\psi^2 - y_p^2 \sin^2(\phi)} \right)^{j_1} + (-\cos(\phi))^{j_2} \psi^{j_2+1} \left( \sqrt{\psi^2 - y_p^2 \sin^2(\phi)} \right)^{j_1-1} \right] \\
&= \sum_{\substack{n=0 \\ j_1=2n}}^{\lfloor \frac{\ell}{2} \rfloor} \binom{\ell}{2n} \sum_{j_2=0}^{\ell-2n} \binom{\ell-2n}{j_2} (\pm |y_p \cos(\phi)| |\sin(\phi)|)^{\ell-2n-j_2} \\
&\quad \left[ (-\cos(\phi))^{j_2+1} \psi^{j_2} (\psi^2 - y_p^2 \sin^2(\phi))^n \right. \\
&\quad \left. + \frac{(-\cos(\phi))^{j_2} \psi^{j_2+1} (\psi^2 - y_p^2 \sin^2(\phi))^n}{\sqrt{\psi + |y_p \sin(\phi)|}} \frac{1}{\sqrt{\psi - |y_p \sin(\phi)|}} \right] \\
&\quad + \sum_{\substack{n=1 \\ j_1=2n-1}}^{\lfloor \frac{\ell+1}{2} \rfloor} \binom{\ell}{2n-1} \sum_{j_2=0}^{\ell-(2n-1)} \binom{\ell-(2n-1)}{j_2} (\pm |y_p \cos(\phi)| |\sin(\phi)|)^{\ell-(2n-1)-j_2} \\
&\quad \left[ \frac{(-\cos(\phi))^{j_2+1} \psi^{j_2} (\psi^2 - y_p^2 \sin^2(\phi))^n}{\sqrt{\psi + |y_p \sin(\phi)|}} \frac{1}{\sqrt{\psi - |y_p \sin(\phi)|}} \right. \\
&\quad \left. + (-\cos(\phi))^{j_2} \psi^{j_2+1} (\psi^2 - y_p^2 \sin^2(\phi))^{n-1} \right],
\end{aligned}$$

where the  $\lfloor \cdot \rfloor$  represent the floor. After this, the binomial expansion

$$(\psi^2 - y_p^2 \sin^2(\phi))^n = \sum_{j_3=0}^n \binom{n}{j_3} (-y_p^2 \sin^2(\phi))^{n-j_3} \psi^{2j_3},$$

is used to provide

$$\begin{aligned}
I_\beta &= \frac{e^{ikx_p \cos(\phi)}}{(x_m \sin^2(\phi))^\ell} \int_{|y_p \sin(\phi)|}^{g(1)-x_p \cos(\phi)} F(\psi) e^{ik\psi} d\psi \\
&= \frac{e^{ikx_p \cos(\phi)}}{(x_m \sin^2(\phi))^\ell} \sum_{n=0}^{\lfloor \frac{\ell}{2} \rfloor} \binom{\ell}{2n} \sum_{j_2=0}^{\ell-2n} \binom{\ell-2n}{j_2} \sum_{j_3=0}^n \binom{n}{j_3} (\pm 1)^{\ell-2n-j_2} (-1)^{n-j_3+j_2+1} \\
&\quad (|y_p| |\sin(\phi)|)^{\ell-j_2-2j_3} |\cos(\phi)|^{\ell-2n-j_2} \cos^{j_2+1}(\phi) \omega_{j_2+2j_3} \\
&+ \frac{e^{ikx_p \cos(\phi)}}{(x_m \sin^2(\phi))^\ell} \sum_{n=0}^{\lfloor \frac{\ell}{2} \rfloor} \binom{\ell}{2n} \sum_{j_2=0}^{\ell-2n} \binom{\ell-2n}{j_2} \sum_{j_3=0}^n \binom{n}{j_3} (\pm 1)^{\ell-2n-j_2} (-1)^{n-j_3+j_2} \\
&\quad (|y_p| |\sin(\phi)|)^{\ell-j_2-2j_3} |\cos(\phi)|^{\ell-2n-j_2} (\cos(\phi))^{j_2} \\
&\quad \int_{|y_p \sin(\phi)|}^{g(1)-x_p \cos(\phi)} \frac{\psi^{j_2+2j_3+1}}{\sqrt{\psi + |y_p \sin(\phi)|} \sqrt{\psi - |y_p \sin(\phi)|}} e^{ik\psi} d\psi \\
&+ \frac{e^{ikx_p \cos(\phi)}}{(x_m \sin^2(\phi))^\ell} \sum_{n=1}^{\lfloor \frac{\ell+1}{2} \rfloor} \binom{\ell}{2n-1} \sum_{j_2=0}^{\ell-(2n-1)} \binom{\ell-(2n-1)}{j_2} \sum_{j_3=0}^n \binom{n}{j_3} (\pm 1)^{\ell-(2n-1)-j_2} \\
&\quad (-1)^{n-j_3+j_2+1} (|y_p| |\sin(\phi)|)^{\ell-j_2-2j_3+1} |\cos(\phi)|^{\ell-(2n-1)-j_2} (\cos(\phi))^{j_2+1} \\
&\quad \int_{|y_p \sin(\phi)|}^{g(1)-x_p \cos(\phi)} \frac{\psi^{j_2+2j_3}}{\sqrt{\psi + |y_p \sin(\phi)|} \sqrt{\psi - |y_p \sin(\phi)|}} e^{ik\psi} d\psi \\
&+ \frac{e^{ikx_p \cos(\phi)}}{(x_m \sin^2(\phi))^\ell} \sum_{n=1}^{\lfloor \frac{\ell+1}{2} \rfloor} \binom{\ell}{2n-1} \sum_{j_2=0}^{\ell-(2n-1)} \binom{\ell-(2n-1)}{j_2} \sum_{j_3=0}^{n-1} \binom{n-1}{j_3} (\pm 1)^{\ell-(2n-1)-j_3} \\
&\quad (-1)^{n-j_3+j_2-1} (|y_p| |\sin(\phi)|)^{\ell-j_2-2j_3-1} |\cos(\phi)|^{\ell-(2n-1)-j_2} (\cos(\phi))^{j_2} \omega_{j_2+2j_3+1}.
\end{aligned}$$

An equivalent process is used to produce a similar expansion for the  $I_\alpha$  portion of the integral. Before discussing the specific treatment of the resulting integrals, the  $I_\alpha$  expansion is presented here.

$$I_\alpha = \int_{-1}^{\xi^*} (\xi - \xi^*)^\ell e^{ikg(\xi)} d\xi = \int_{g(-1)}^{v^*} (h(v) - h(v^*))^\ell h'(v) e^{ikv} dv. \quad (\text{A.11})$$

This is transformed into  $\psi$  and the binomial expansion employed to produce the following expression.

$$\begin{aligned}
I_\alpha &= \frac{e^{ikx_p \cos(\phi)}}{(x_m \sin^2(\phi))^\ell} \int_{g(-1)-x_p \cos(\phi)}^{|y_p \sin(\phi)|} \tilde{F}(\psi) e^{ik\psi} d\psi \\
&= \frac{e^{ikx_p \cos(\phi)}}{(x_m \sin^2(\phi))^\ell} \sum_{n=0}^{\lfloor \frac{\ell}{2} \rfloor} \binom{\ell}{2n} \sum_{j_2=0}^{\ell-2n} \binom{\ell-2n}{j_2} \sum_{j_3=0}^n \binom{n}{j_3} (\pm 1)^{\ell-2n-j_2} (-1)^{n-j_3+j_2+1} \\
&\quad (|y_p| |\sin(\phi)|)^{\ell-j_2-2j_3} |\cos(\phi)|^{\ell-2n-j_2} \cos^{j_2+1}(\phi) \tilde{\omega}_{j_2+2j_3} \\
&- \frac{e^{ikx_p \cos(\phi)}}{(x_m \sin^2(\phi))^\ell} \sum_{n=0}^{\lfloor \frac{\ell}{2} \rfloor} \binom{\ell}{2n} \sum_{j_2=0}^{\ell-2n} \binom{\ell-2n}{j_2} \sum_{j_3=0}^n \binom{n}{j_3} (\pm 1)^{\ell-2n-j_2} (-1)^{n-j_3+j_2} \\
&\quad (|y_p| |\sin(\phi)|)^{\ell-j_2-2j_3} |\cos(\phi)|^{\ell-2n-j_2} (\cos(\phi))^{j_2} \\
&\quad \int_{g(-1)-x_p \cos(\phi)}^{|y_p \sin(\phi)|} \frac{\psi^{j_2+2j_3+1}}{\sqrt{\psi + |y_p \sin(\phi)|}} \frac{1}{\sqrt{\psi - |y_p \sin(\phi)|}} e^{ik\psi} d\psi \\
&- \frac{e^{ikx_p \cos(\phi)}}{(x_m \sin^2(\phi))^\ell} \sum_{n=1}^{\lfloor \frac{\ell+1}{2} \rfloor} \binom{\ell}{2n-1} \sum_{j_2=0}^{\ell-(2n-1)} \binom{\ell-(2n-1)}{j_2} \sum_{j_3=0}^n \binom{n}{j_3} \\
&\quad (\pm 1)^{\ell-(2n-1)-j_2} (-1)^{n-j_3+j_2+1} (|y_p| |\sin(\phi)|)^{\ell-j_2-2j_3+1} |\cos(\phi)|^{\ell-(2n-1)-j_2} (\cos(\phi))^{j_2+1} \\
&\quad \int_{g(-1)-x_p \cos(\phi)}^{|y_p \sin(\phi)|} \frac{\psi^{j_2+2j_3}}{\sqrt{\psi + |y_p \sin(\phi)|}} \frac{e^{ik\psi}}{\sqrt{\psi - |y_p \sin(\phi)|}} d\psi \\
&+ \frac{e^{ikx_p \cos(\phi)}}{(x_m \sin^2(\phi))^\ell} \sum_{n=1}^{\lfloor \frac{\ell+1}{2} \rfloor} \binom{\ell}{2n-1} \sum_{j_2=0}^{\ell-(2n-1)} \binom{\ell-(2n-1)}{j_2} \sum_{j_3=0}^{n-1} \binom{n-1}{j_3} (\pm 1)^{\ell-(2n-1)-j_2} \\
&\quad (-1)^{n-j_3+j_2-1} (|y_p| |\sin(\phi)|)^{\ell-j_2-2j_3-1} |\cos(\phi)|^{\ell-(2n-1)-j_2} (\cos(\phi))^{j_2} \tilde{\omega}_{j_2+2j_3+1}.
\end{aligned}$$

# Appendix B

## Method of Fundamental Solutions

The Method of Fundamental Solutions (MFS) is a numerical technique which can be employed to solve Helmholtz problems. Consider the total acoustic potential to be equal to the sum of the scattered and the incident potential, as follows.

$$\phi(\mathbf{x}) = \phi^{scat}(\mathbf{x}) + \phi^{inc}(\mathbf{x}), \quad \mathbf{x} \in \Omega_s. \quad (\text{B.1})$$

Considering the derivatives of B.1 and applying the sound-hard boundary condition provides

$$\frac{\partial \phi^{scat}}{\partial n} = -\frac{\partial \phi^{inc}}{\partial n}, \quad \mathbf{x} \in \partial\Omega_s. \quad (\text{B.2})$$

The MFS places  $\bar{\alpha} = 1, \dots, \bar{m}$  source points (shown in Fig. B.1) within the scattering object in order to express the scattered potential as a linear combination of fundamental solutions

$$\phi^{scat}(\mathbf{x}) = \sum_{\bar{\alpha}}^{\bar{m}} A_{\bar{\alpha}} G(\bar{\alpha}, \bar{\beta}), \quad (\text{B.3})$$

where  $A_{\bar{\alpha}}$  are the unknown amplitudes which may be found by collocating at  $\bar{\beta} = 1, \dots, \bar{B}$  points over the boundary  $\partial\Omega$  and solving the resulting system of equations, with the following being true at each point  $\bar{\beta} \in \partial\Omega$

$$\frac{\partial \phi^{scat}}{\partial n} = A_{\bar{\alpha}} \frac{\partial G(\bar{\alpha}, \bar{\beta})}{\partial n}, \quad \mathbf{x} \in \partial\Omega. \quad (\text{B.4})$$

Though, in order to minimise the residual error  $Q$  a least squares scheme can be employed, wherein

$$Q := \sum_{\bar{\beta}}^{\bar{B}} \left[ \frac{\partial \phi^{inc}(\mathbf{x}_{\bar{\beta}})}{\partial n} - \sum_{\bar{\alpha}}^{\bar{m}} A_{\bar{\alpha}} \frac{\partial G(\bar{\alpha}, \bar{\beta})}{\partial n} \right]^2. \quad (\text{B.5})$$

The amplitudes  $A_{\bar{\alpha}}$  may be used to recover the scattered potential and combined with the incident potential, to recover the total potential.

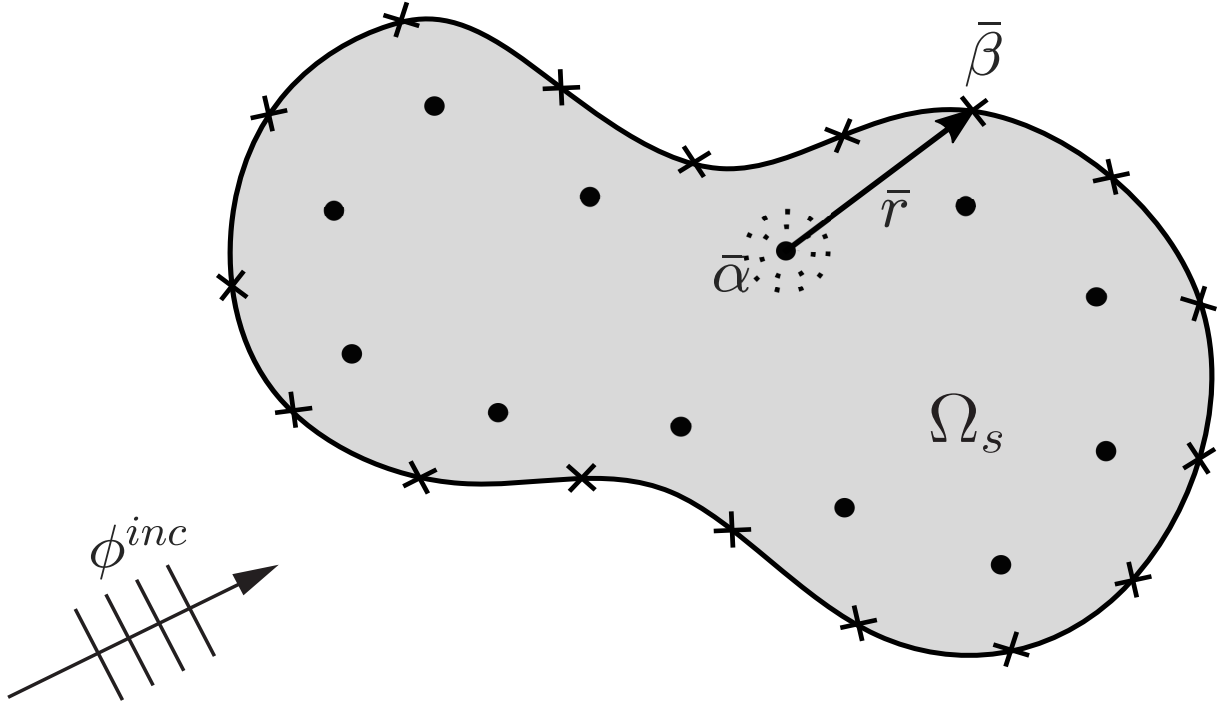


Figure B.1: MFS source point  $\bar{\alpha}$  and sample point  $\bar{\beta}$ , where  $\bar{r}$  is the Euclidian distance between them.

# Appendix C

## Quantification of errors

Throughout this thesis, a number of numerical methods are tested, such as, novel integration techniques or novel enrichment functions. In order to verify the efficacy of a given numerical method, it is important to be able to calculate the error with respect to an reference solution. In this thesis error is defined as  $\epsilon$  which can be thought of as a relative error, though, the method of determining  $\epsilon$  differs depending on whether it is being calculated for a vector of results or a scalar result. When error is calculated for a vector, an  $L^2$  relative error is employed; for example,  $\epsilon$  for a vector of acoustic potential  $\phi$  evaluated at a vector of points over the boundary  $\Gamma$  is defined as follows

$$\epsilon(\phi; \Gamma_\epsilon) = \frac{\|\phi - \phi_{ref}\|_{L_2(\Gamma_\epsilon)}}{\|\phi_{ref}\|_{L_2(\Gamma_\epsilon)}}, \quad (\text{C.1})$$

where  $\phi_{ref}$  is a reference solution in vector form. Whereas, for a scalar value such as single integral  $I$  the relative error  $\epsilon$  is defined as follows

$$\epsilon = \frac{I - I_{ref}}{I_{ref}} \quad (\text{C.2})$$

where  $I_{ref}$  is a reference solution.

# References

- [1] Bowman, J.J., Senior, T.B. and Uslenghi, P.L., 1987. *Electromagnetic and acoustic scattering by simple shapes*. Hemisphere, New York, USA, 1987.
- [2] Jones, D.S., 1986. *Acoustic and electromagnetic waves*, Oxford/New York, Clarendon Press/Oxford University Press.
- [3] Ihlenburg, F., 2006. *Finite element analysis of acoustic scattering (Vol. 132)*. Springer Science & Business Media.
- [4] Bouillard, P. and Ihlenburg, F., 1999. Error estimation and adaptivity for the finite element method in acoustics: 2D and 3D applications. *Computer methods in applied mechanics and engineering*, 176(1-4), pp.147-163.
- [5] Giorgiani, G., Modesto, D., Fernández-Méndez, S. and Huerta, A., 2013. High-order continuous and discontinuous Galerkin methods for wave problems. *International Journal for numerical methods in Fluids*, 73(10), pp.883-903.
- [6] Thompson, L.L., 2006. A review of finite-element methods for time-harmonic acoustics. *The Journal of the Acoustical Society of America*, 119(3), pp.1315-1330.
- [7] Ihlenburg, F. and Babuška, I., 1995. Finite element solution of the Helmholtz equation with high wave number Part I: The h-version of the FEM. *Computers & Mathematics with Applications*, 30(9), pp.9-37.
- [8] Ihlenburg, F. and Babuška, I., 1997. Finite element solution of the Helmholtz equation with high wave number part II: the hp version of the FEM. *SIAM Journal on Numerical Analysis*, 34(1), pp.315-358.
- [9] Harari, I., 2006. A survey of finite element methods for time-harmonic acoustics. *Computer methods in applied mechanics and engineering*, 195(13-16), pp.1594-1607.
- [10] Astley, R.J., 2009. Numerical methods for noise propagation in moving flows, with application to turbofan engines. *Acoustical science and technology*, 30(4), pp.227-239.

- [11] Ciskowski, R.D. and Brebbia, C.A. eds., 1991. Boundary element methods in acoustics. Springer.
- [12] Atak, O., Bergen, B., Huybrechs, D., Pluymers, B. and Desmet, W., 2014. Coupling of Boundary Element and Wave Based Methods for the efficient solution of complex multiple scattering problems. *Journal of Computational Physics*, 258, pp.165-184.
- [13] Chen, K., Cheng, J. and Harris, P.J., 2009. A new study of the Burton and Miller method for the solution of a 3D Helmholtz problem. *IMA journal of applied mathematics*, 74(2), pp.163-177.
- [14] Li, S. and Huang, Q., 2011. A fast multipole boundary element method based on the improved Burton-Miller formulation for three-dimensional acoustic problems. *Engineering Analysis with Boundary Elements*, 35(5), pp.719-728.
- [15] Babuška, I., Ihlenburg, F., Paik, E.T. and Sauter, S.A., 1995. A generalized finite element method for solving the Helmholtz equation in two dimensions with minimal pollution. *Computer methods in applied mechanics and engineering*, 128(3-4), pp.325-359.
- [16] Babuška, I.M. and Sauter, S.A., 1997. Is the pollution effect of the FEM avoidable for the Helmholtz equation considering high wave numbers?. *SIAM Journal on numerical analysis*, 34(6), pp.2392-2423.
- [17] Antoine, X. and Geuzaine, C., 2009. Phase reduction models for improving the accuracy of the finite element solution of time-harmonic scattering problems I: General approach and low-order models. *Journal of Computational Physics*, 228(8), pp.3114-3136.
- [18] Khajah, T., Antoine, X. and Bordas, S., 2016. Isogeometric finite element analysis of time-harmonic exterior acoustic scattering problems. arXiv preprint arXiv:1610.01694.
- [19] Petersen, S., Dreyer, D. and von Estorff, O., 2006. Assessment of finite and spectral element shape functions for efficient iterative simulations of interior acoustics. *Computer methods in applied mechanics and engineering*, 195(44-47), pp.6463-6478.
- [20] Bériot, H., Prinn, A. and Gabard, G., 2016. Efficient implementation of high-order finite elements for Helmholtz problems. *International Journal for Numerical Methods in Engineering*, 106(3), pp.213-240.
- [21] Boyd, J.P., 2001. Chebyshev and Fourier spectral methods. Courier Corporation.

- [22] Solin, P., Segeth, K. and Dolezel, I., 2003. Higher-order finite element methods. CRC Press.
- [23] Ainsworth, M., 2004. Discrete dispersion relation for hp-version finite element approximation at high wave number. *SIAM Journal on Numerical Analysis*, 42(2), pp.553-575.
- [24] Vos, P.E., Sherwin, S.J. and Kirby, R.M., 2010. From h to p efficiently: Implementing finite and spectral/hp element methods to achieve optimal performance for low-and high-order discretisations. *Journal of Computational Physics*, 229(13), pp.5161-5181.
- [25] El Kacimi, A., Laghrouche, O., Mohamed, M.S. and Trevelyan, J., 2018. Bernstein-Bézier based finite elements for efficient solution of short wave problems. *Computer Methods in Applied Mechanics and Engineering*.
- [26] Lieu, A., Gabard, G. and Bériot, H., 2016. A comparison of high-order polynomial and wave-based methods for Helmholtz problems. *Journal of Computational Physics*, 321, pp.105-125.
- [27] Laghrouche, O. and Bettess, P., 2000. Short wave modelling using special finite elements. *Journal of Computational Acoustics*, 8(01), pp.189-210.
- [28] Kechroud, R., Soulaïmani, A. and Antoine, X., 2009. A performance study of plane wave finite element methods with a padè-type artificial boundary condition in acoustic scattering. *Advances in Engineering Software*, 40(8), pp.738-750.
- [29] Giladi, E. and Keller, J.B., 2001. A hybrid numerical asymptotic method for scattering problems. *Journal of Computational Physics*, 174(1), pp.226-247.
- [30] Chandler-Wilde, S., Graham, I.G., Langdon, S. and Spence, E.A., 2012. Numerical-asymptotic boundary integral methods in high-frequency acoustic scattering. *Acta numerica*, 21, pp.89-305.
- [31] Babuška, I. and Melenk, J.M., 1997. The Partition of Unity Method. *International Journal for Numerical Methods in Engineering*, 40(4), pp.727-758.
- [32] Melenk, J.M. and Babuška, I., 1996. The partition of unity finite element method: basic theory and applications. In *Research Report/Seminar für Angewandte Mathematik (Vol. 1996, No. 01)*. Eidgenössische Technische Hochschule, Seminar für Angewandte Mathematik.
- [33] Laghrouche, O., Bettess, P. and Astley, R.J., 2002. Modelling of short wave diffraction problems using approximating systems of plane waves. *International Journal for Numerical Methods in Engineering*, 54(10), pp.1501-1533.

- [34] Laghrouche, O., Bettess, P., Perrey-Debain, E. and Trevelyan, J., 2005. Wave interpolation finite elements for Helmholtz problems with jumps in the wave speed. *Computer Methods in Applied Mechanics and Engineering*, 194(2-5), pp.367-381.
- [35] Ortiz, P. and Sanchez, E., 2001. An improved partition of unity finite element model for diffraction problems. *International Journal for Numerical Methods in Engineering*, 50(12), pp.2727-2740.
- [36] Ladevèze, P., Arnaud, L., Rouch, P. and Blanzé, C., 2001. The variational theory of complex rays for the calculation of medium-frequency vibrations. *Engineering Computations*, 18(1/2), pp.193-214.
- [37] Hiptmair, R., Moiola, A. and Perugia, I., 2011. Plane wave discontinuous Galerkin methods for the 2D Helmholtz equation: analysis of the p-version. *SIAM Journal on Numerical Analysis*, 49, pp.264-284.
- [38] Gabard, G., 2007. Discontinuous Galerkin methods with plane waves for time-harmonic problems. *Journal of Computational Physics*, 225, pp.1961-1984.
- [39] Farhat, C., Harari, I. and Franca, L.P., 2001. The discontinuous enrichment method. *Computer Methods in Applied Mechanics and Engineering*, 190(48), pp.6455-6479.
- [40] Cessenat, O. and Despres, B., 1998. Application of an ultra weak variational formulation of elliptic PDEs to the two-dimensional Helmholtz problem. *SIAM Journal on Numerical Analysis*, 35(1), pp.255-299.
- [41] Huttunen, T., Gamallo, P. and Astley, R.J., 2009. Comparison of two wave element methods for the Helmholtz problem. *Communications in Numerical Methods in Engineering*, 25(1), pp.35-52.
- [42] Baumeister, K.J., 1977. Finite-difference theory for sound propagation in a lined duct with uniform flow using the wave envelope concept (Vol. 1001). National Aeronautics and Space Administration.
- [43] Lyon, R.H., DeJong, R.G. and Heckl, M., 1995. Theory and application of statistical energy analysis.
- [44] Gordon, W., 1975. Far-field approximations to the Kirchoff-Helmholtz representations of scattered fields. *IEEE Transactions on Antennas and Propagation*, 23(4), pp.590-592.
- [45] Lian, H., Simpson, R.N. and Bordas, S.P., 2013. Stress analysis without meshing: Isogeometric boundary-element method. *Proceedings of the Institution of Civil Engineers-Engineering and Computational Mechanics*, 166(2), pp.88-99.

- [46] Simpson, R.N., Bordas, S.P., Lian, H. and Trevelyan, J., 2013. An isogeometric boundary element method for elastostatic analysis: 2D implementation aspects. *Computers Structures*, 118, pp.2-12.
- [47] Simpson, R.N., Bordas, S.P., Trevelyan, J. and Rabczuk, T., 2012. A two-dimensional isogeometric boundary element method for elastostatic analysis. *Computer Methods in Applied Mechanics and Engineering*, 209, pp.87-100.
- [48] Ciskowski, R.D. and Brebbia, C.A. eds., 1991. *Boundary element methods in acoustics*. Springer.
- [49] Perrey-Debain, E., Trevelyan, J. and Bettess, P., 2004, 2002. New special wave boundary elements for short wave problems. *Communications in Numerical Methods in Engineering*, 18(4), pp.259-268.
- [50] Perrey-Debain, E., Trevelyan, J. and Bettess, P., 2004. Wave boundary elements:a theoretical overview presenting applications in scattering of short waves, *Eng. Anal Bound. Elem.*, 28: 131–141.
- [51] Perrey-Debain, E., Laghrouche, O., Bettess, P. and Trevelyan, J., 2004. Plane-wave basis finite elements and boundary elements for three-dimensional wave scattering. *Philosophical Transactions of the Royal Society of London A: Mathematical, Physical and Engineering Sciences*, 362(1816), pp.561-577.
- [52] Perrey-Debain, E., Trevelyan, J. and Bettess, P., 2003. Plane wave interpolation in direct collocation boundary element method for radiation and wave scattering: numerical aspects and applications. *Journal of sound and vibration*, 261(5), pp.839-858.
- [53] Chandler-Wilde, S.N. and Langdon, S., 2007. A Galerkin boundary element method for high frequency scattering by convex polygons. *SIAM Journal on Numerical Analysis*, 45(2), pp.610-640.
- [54] Groth, S.P., Hewett, D.P. and Langdon, S., 2015. Hybrid numerical-asymptotic approximation for high-frequency scattering by penetrable convex polygons. *IMA Journal of Applied Mathematics*, 80(2), pp.324-353.
- [55] Colton, D. and Kress, R. 1993 , *Integral Equation Methods in Scattering Theory*, Springer.
- [56] Nédélec, J.C., 2013. *Acoustic and electromagnetic equations: integral representations for harmonic problems (Vol. 144)*. Springer Science Business Media.

- [57] Coifman, R., Rokhlin, V. and Wandzura, S., 1993. The fast multipole method for the wave equation: A pedestrian prescription. *IEEE Antennas and Propagation Magazine*, 35(3), pp.7-12.
- [58] Darve, E., 2000. The fast multipole method: numerical implementation. *Journal of Computational Physics*, 160(1), pp.195-240.
- [59] Darbas, M., Darrigrand, E. and Lafranche, Y., 2013. Combining analytic preconditioner and fast multipole method for the 3-D Helmholtz equation. *Journal of Computational Physics*, 236, pp.289-316.
- [60] Liu, Y., 2009. *Fast multipole boundary element method: theory and applications in engineering*. Cambridge university press.
- [61] Bebendorf, M., 2000. Approximation of boundary element matrices. *Numerische Mathematik*, 86(4), pp.565-589.
- [62] van't Wout, E., Gélat, P., Betcke, T. and Arridge, S., 2015. A fast boundary element method for the scattering analysis of high-intensity focused ultrasound. *The Journal of the Acoustical Society of America*, 138(5), pp.2726-2737.
- [63] Perrey-Debain, E., Trevelyan, J. and Bettess, P., 2001, September. Using wave boundary elements in BEM for high frequency scattering. In *Proceedings of Third UK Conference on Boundary Integral Methods*, University of Brighton.
- [64] Perrey-Debain, E., Trevelyan, J. and Bettess, P., 2003, September. Numerical aspects of single wave basis boundary elements for acoustic scattering. In *Proceedings of the fourth UK conference on boundary integral methods*. Ed. Sia Amini. The University of Salford. Salford. UK.
- [65] Peake M.J., Trevelyan, J. and Coates, G., 2013. Novel basis functions for the partition of unity boundary element method for Helmholtz problems. *International Journal for Numerical Methods in Engineering*, 93(9), pp.905-918.
- [66] Bruno, O.P., Geuzaine, C.A., Monro Jr, J.A. and Reitich, F., 2004. Prescribed error tolerances within fixed computational times for scattering problems of arbitrarily high frequency: the convex case. *Philosophical Transactions of the Royal Society of London. Series A: Mathematical, Physical and Engineering Sciences*, 362(1816), pp.629-645.
- [67] Telles, J.C.F., 1987. A self-adaptive co-ordinate transformation for efficient numerical evaluation of general boundary element integrals. *International journal for numerical methods in engineering*, 24(5), pp.959-973.

- [68] Honnor, M.E., Trevelyan, J. and Huybrechs, D., 2010. Numerical evaluation of the two-dimensional partition of unity boundary integrals for Helmholtz problems. *Journal of computational and applied mathematics*, 234(6), pp.1656-1662.
- [69] Iserles, A. and Nørsett, S.P., 2004. On quadrature methods for highly oscillatory integrals and their implementation. *BIT Numerical Mathematics*, 44(4), pp.755-772.
- [70] Iserles, A. and Nørsett, S.P., 2005. Efficient quadrature of highly oscillatory integrals using derivatives. *Proceedings of the Royal Society A: Mathematical, Physical and Engineering Sciences*, 461(2057), pp.1383-1399.
- [71] Iserles, A., 2004. On the numerical quadrature of highly-oscillating integrals I: Fourier transforms. *IMA Journal of Numerical Analysis*, 24(3), pp.365-391.
- [72] Iserles, A., 2005. On the numerical quadrature of highly-oscillating integrals II: Irregular oscillators. *IMA journal of numerical analysis*, 25(1), pp.25-44. *Anal.*, 25 (2004), 25–44.
- [73] Dominguez, V., Graham, I.G. and Smyshlyaev, V.P., 2011. Stability and error estimates for Filon-Clenshaw-Curtis rules for highly oscillatory integrals. *IMA journal of numerical analysis*, 31(4), pp.1253-1280.
- [74] Olver, F.W.J., 1974. *Asymptotics and Special Functions* (New York: Academic).
- [75] Levin, D., 1982. Procedures for computing one-and two-dimensional integrals of functions with rapid irregular oscillations. *Mathematics of Computation*, 38(158), pp.531-538.
- [76] Filon, L.N.G., 1930. III. On a quadrature formula for trigonometric integrals. *Proceedings of the Royal Society of Edinburgh*, 49, pp.38-47.
- [77] Olver, F.W., Lozier, D.W., Boisvert, R.F. and Clark, C.W. eds., 2010. *NIST handbook of mathematical functions* hardback and CD-ROM. Cambridge university press.
- [78] Gao, J., Condon, M., Iserles, A., Gilvey, B.D. and Trevelyan, J., 2021. Quadrature methods for highly oscillatory singular integrals. *Journal of computational mathematics.*, 39(2), pp.227-260.
- [79] Helsing, J. and Ojala, R., 2008. Corner singularities for elliptic problems: Integral equations, graded meshes, quadrature, and compressed inverse preconditioning. *Journal of Computational Physics*, 227(20), pp.8820-8840.

- [80] Śmigaj, W., Betcke, T., Arridge, S., Phillips, J. and Schweiger, M., 2015. Solving boundary integral problems with BEM++. *ACM Transactions on Mathematical Software (TOMS)*, 41(2), p.6.
- [81] Platte, R.B. and Driscoll, T.A., 2004. Computing eigenmodes of elliptic operators using radial basis functions. *Computers Mathematics and Applications*, 48(3-4), pp.561-576.
- [82] Luostari, T., Huttunen, T. and Monk, P., 2012. The ultra weak variational formulation using Bessel basis functions. *Communications in Computational Physics*, 11(2), pp.400-414.
- [83] Barnett, A.H. and Betcke, T., 2010. An exponentially convergent nonpolynomial finite element method for time-harmonic scattering from polygons. *SIAM Journal on Scientific Computing*, 32(3), pp.1417-1441.
- [84] Antunes, P.R.S. and Valtchev, S.S., 2010. A meshfree numerical method for acoustic wave propagation problems in planar domains with corners and cracks. *Journal of Computational and Applied Mathematics*, 234(9), pp.2646-2662.
- [85] Chaumont-Frelet, T. and Nicaise, S., 2018. High-frequency behaviour of corner singularities in Helmholtz problems. *ESAIM: Mathematical Modelling and Numerical Analysis*, 52(5), pp.1803-1845.
- [86] A. A. Becker, 1992. *The boundary element method in engineering: a complete course*, McGraw-Hill, Maidenhead.
- [87] Schenck, H.A., 1968. Improved integral formulation for acoustic radiation problems. *The journal of the acoustical society of America*, 44(1), pp.41-58.
- [88] Burton, A.J. and Miller, G.F., 1971. The application of integral equation methods to the numerical solution of some exterior boundary-value problems. *Proc. R. Soc. Lond. A*, 323(1553), pp.201-210.
- [89] Li, S. and Huang, Q., 2010. An improved form of the hypersingular boundary integral equation for exterior acoustic problems. *Engineering Analysis with Boundary Elements*, 34(3), pp.189-195.
- [90] Liu, Y. and Rizzo, F.J., 1997. Scattering of elastic waves from thin shapes in three dimensions using the composite boundary integral equation formulation. *The Journal of the Acoustical Society of America*, 102(2), pp.926-932.

- [91] Descloux, J. and Tolley, M., 1983. An accurate algorithm for computing the eigenvalues of a polygonal membrane. *Computer Methods in Applied Mechanics and Engineering*, 39(1), pp.37-53.
- [92] Antunes, P.R.S., 2018. A numerical algorithm to reduce the ill conditioning in meshless methods for the Helmholtz equation. *Numerical Algorithms*, 79(3), pp.879-897.
- [93] Hughes, T. J. R., Cottrell, J. A. and Bazilevs, Y., 2005. Isogeometric analysis: CAD, finite elements, NURBS, exact geometry and mesh refinement. *Computer Methods in Applied Mechanics and Engineering*, 194, pp.4135-4195.
- [94] Bazilevs, Y., Calo, V.M., Hughes, T.J. and Zhang, Y., 2008. Isogeometric fluid-structure interaction: theory, algorithms, and computations. *Computational mechanics*, 43(1), pp.3-37.
- [95] Buffa, A., Sangalli, G. and Vázquez, R., 2010. Isogeometric analysis in electromagnetics: B-splines approximation. *Computer Methods in Applied Mechanics and Engineering*, 199(17-20), pp.1143-1152.
- [96] Cottrell, J.A., Reali, A., Bazilevs, Y. and Hughes, T.J., 2006. Isogeometric analysis of structural vibrations. *Computer methods in applied mechanics and engineering*, 195(41-43), pp.5257-5296.
- [97] Politis, C., Ginnis, A.I., Kaklis, P.D., Belibassakis, K. and Feurer, C., 2009, October. An isogeometric BEM for exterior potential-flow problems in the plane. In 2009 SIAM/ACM Joint Conference on Geometric and Physical Modeling (pp. 349-354).
- [98] Li, K. and Qian, X., 2011. Isogeometric analysis and shape optimization via boundary integral. *Computer-Aided Design*, 43(11), pp.1427-1437.
- [99] Simpson, R.N., Scott, M.A., Taus, M., Thomas, D.C. and Lian, H., 2014. Acoustic isogeometric boundary element analysis. *Computer Methods in Applied Mechanics and Engineering*, 269, pp.265-290.
- [100] Peake, M.J., Trevelyan, J. and Coates, G., 2013. Extended isogeometric boundary element method (XIBEM) for two-dimensional Helmholtz problems. *Computer Methods in Applied Mechanics and Engineering*, 259, pp.93-102.
- [101] Peake, M.J., Trevelyan, J. and Coates, G., 2015. Extended isogeometric boundary element method (XIBEM) for three-dimensional medium-wave acoustic scattering problems. *Computer Methods in Applied Mechanics and Engineering*, 284, pp.762-780.

- [102] Diwan, G.C. and Mohamed, M.S., 2019. Pollution studies for high order isogeometric analysis and finite element for acoustic problems. *Computer Methods in Applied Mechanics and Engineering*, 350, pp.701-718.
- [103] Marburg, S., 2018. A pollution effect in the boundary element method for acoustic problems. *Journal of theoretical and computational acoustics*, 26(02), p.1850018.
- [104] Linton, C.M. and Evans, D.V., 1990. The interaction of waves with arrays of vertical circular cylinders. *Journal of fluid mechanics*, 215, pp.549-569.
- [105] Gittelsohn, C.J. and Hiptmair, R., 2014. Dispersion analysis of plane wave discontinuous Galerkin methods. *International Journal for Numerical Methods in Engineering*, 98(5), pp.313-323.
- [106] Simpson, R.N., Bordas, S.P., Trevelyan, J. and Rabczuk, T., 2012. A two-dimensional isogeometric boundary element method for elastostatic analysis. *Computer Methods in Applied Mechanics and Engineering*, 209, pp.87-100.